Kumulative Dissertation

From Ripples to Relics:
Multi-messenger studies of compact binaries

zur Erlangung des akademischen Grades

doctor rerum naturalium (Dr. rer. nat.)

in der Wissenschaftsdisziplin

Theoretische Astrophysik

eingereicht von

Nina Kunert

am

25. März 2025

an der

Mathematisch-Naturwissenschaftlichen Fakultät

Institut für Physik und Astronomie

an der Universität Potsdam

Ort und Datum der Disputation:

Potsdam, 1. Juli 2025

Supervisors:

Prof. Dr. Tim Dietrich
Institute of Physics and Astronomy, University of Potsdam, Germany

Prof. Dr. Philipp Richter
Institute of Physics and Astronomy, University of Potsdam, Germany

Reviewers:

Prof. Dr. Tim Dietrich
Institute of Physics and Astronomy, University of Potsdam, Germany

Prof. Dr. Jocelyn Read
Department of Physics, California State University Fullerton, United States of America

Prof. Dr. Patricia Schmidt
School of Physics and Astronomy, University of Birmingham, United Kingdom

Published online on the
Publication Server of the University of Potsdam:
https://doi.org/10.25932/publishup-68297
https://nbn-resolving.org/urn:nbn:de:kobv:517-opus4-682976

Abstract

Multi-messenger astronomy explores the universe using a multitude of signals, including electromagnetic radiation, gravitational waves, and high-energy particles, providing a more complete understanding of cosmic events than any single method alone. Binary neutron star mergers serve as ideal laboratories for multi-messenger studies and reveal remarkable versatility as probes of fundamental physics and potentially for phenomena beyond Standard Model particle physics, such as dark matter. On August 17, 2017, the detection of GW170817, along with the gamma-ray burst GRB170817A and the kilonova AT2017gfo, marked the first multi-messenger observation of a binary neutron star merger, providing unprecedented insights into astrophysics, nuclear physics, and cosmology.

However, significant challenges remain. On the one hand, the impact of systematic, model-dependent errors on the measurement of fundamental parameters is not yet fully understood and quantified. On the other hand, the limited number of detected gravitational wave events of this kind still presents a challenge. Furthermore, key questions persist regarding their potential to constrain the unknown neutron star equation of state of dense nuclear matter and to unveil the nature of dark matter. To study astronomical phenomena with complex signatures, this work relies on Bayesian statistical methods. In particular, using a Bayesian nuclear-physics and multi-messenger astrophysics code, it is demonstrated that a joint statistical analysis of different messengers representing distinct astrophysical processes could provide deeper insights into compact binary mergers.

The presented studies, targeting the investigation of gravitational waveform model-dependent systematic biases, indicate that multiple observations of binary neutron star mergers with current-generation detectors can introduce significant biases in neutron star radius inference, highlighting the need for improved waveform model accuracy. In contrast, waveform model systematics have a negligible impact on determining the cosmic expansion rate.

Motivated by the limited number of observed binary neutron star mergers in gravitational waves, the presented Bayesian multi-wavelength analysis of a gamma-ray burst and its afterglow demonstrates a complementary approach to identifying and characterizing such events. Expanding this method to a broader range of astrophysical scenarios can provide deeper insights into gamma-ray burst progenitors and their connections with compact binaries, including binary neutron star mergers, especially during periods when gravitational-wave detections are not available.

Addressing one of the fundamental open questions regarding the unknown neutron star equation of state, the findings demonstrate that gravitational-wave observations of binary neutron star mergers from future observatories could differentiate between three-nucleon interaction models. Hence, these insights provide a better understanding of the behavior of nuclear matter, describing how three-nucleon forces, arising from interactions involving a third nucleon that modifies two-body forces, influence the equation of state of neutron star matter. In addition, observations with next-generation gravitational-wave detectors can be expected to yield improved constraints on microphysical parameters governing the behavior of nuclear matter at extreme densities within neutron stars.

Similarly, dark matter constitutes a major unresolved question. The presented analyses of simulated gravitational-wave data from dark-matter-admixed binary neutron star mergers indicate that next-generation detectors may have limited sensitivity to test for or exclude the presence of dark matter in binary neutron star mergers. The results of this study disfavor the presence of dark matter within the framework of the model considered, and no constraints on its properties or underlying nature could be derived.

Zusammenfassung

Die Multimessenger-Astronomie untersucht das Universum mithilfe verschiedener Signale, darunter elektromagnetische Strahlung, Gravitationswellen und hochenergetische Teilchen. Durch die Kombination dieser Daten entsteht ein deutlich umfassenderes Verständnis kosmischer Ereignisse im Vergleich zu einer einzelnen Messmethode. Besonders die Verschmelzung zweier Neutronensterne, ein sogenanntes binäres Neutronensternsystem, eignet sich für solche Studien, da sie all diese Signale emittieren und wertvolle Einblicke in fundamentale physikalische Fragen liefern können. Darüber hinaus wird vermutet, dass diese Systeme mit Phänomenen außerhalb des Standardmodells, wie dunkler Materie, in Verbindung stehen könnten und demnach wertvolle neue Erkenntnisse liefern könnten. Die erste Entdeckung eines solchen Systems gelang am 17. August 2017, als sowohl das Gravitationswellensignal GW170817 als auch elektromagnetische Strahlung in Form des Gammablitzes GRB170817A und der Kilonova AT2017gfo beobachtet wurden. Diese erste Multimessenger-Beobachtung eines binären Neutronensternsystems markierte den Beginn einer neuen Ära der Multimessenger-Astronomie und ermöglichte beispiellose Einblicke in die Astrophysik, Kernphysik und Kosmologie.

Dennoch bleiben Fragen offen. Einerseits ist der Einfluss systematischer, modellabhängiger Fehler bei der Messung fundamentaler Kenngrößen noch nicht vollständig verstanden. Andererseits bleibt die geringe Anzahl bislang nachgewiesener Gravitationswellenereignisse dieser Art eine Herausforderung. Darüber hinaus sind grundlegende Fragen zur unbekannten Zustandsgleichung dichter Kernmaterie in Neutronensternen und die Natur dunkler Materie nach wie vor ungeklärt. Um astronomische Phänomene mit komplexen Signaturen zu untersuchen, stützt sich diese Arbeit auf Methoden der bayesschen Statistik. Insbesondere wird mithilfe eines bayesschen Kernphysik- und Multimessenger-Astrophysik-Codes gezeigt, dass eine gemeinsame statistische Analyse verschiedener astrophysikalischer Prozesse tiefere Einblicke in die Verschmelzung binärer Neutronensterne ermöglichen kann.

Die zu Beginn vorgelegten Untersuchungen zu systematischen Fehlern in Gravitationswellenmodellen zeigen, dass mehrere Beobachtungen binärer Neutronensternsysteme mit den derzeit verfügbaren Detektoren zu erheblichen systematischen Fehlern bei der Abschätzung des Neutronensternradius führen können. Dies unterstreicht den Bedarf an noch präziseren Wellenformmodellen. Umgekehrt haben sich dieselben systematischen Effekte auf die Bestimmung der kosmologischen Expansionsrate des Universums als vernachlässigbar erwiesen.

Da bisher nur wenige Verschmelzungen von Neutronensternen durch Gravitationswellen beobachtet wurden, hat sich die Untersuchung von Gammablitzen mit Hilfe bayesscher Statistik über mehrere Wellenlängen hinweg als vielversprechende komplementäre Alternative herausgestellt, um solche Ereignisse auch ohne Gravitationswellendaten zu identifizieren und zu charakterisieren. Eine Ausweitung dieser Methode auf weitere astrophysikalische Szenarien könnte wertvolle neue Erkenntnisse über die Ursprünge von Gammablitzen und ihre Verbindung zu kompakten Binärsystemen liefern.

Um grundlegende offene Fragen zur unbekannten Zustandsgleichung von Neutronensternen zu adressieren, zeigen die Ergebnisse, dass zukünftige Gravitationswellenbeobachtungen helfen könnten, verschiedene Modelle dreiteilchenbasierter Kernwechselwirkungen zu unterscheiden. Diese Drei-Nukleon-Wechselwirkungen, die zusätzlich zu den Zweikörperkräften wirken, beeinflussen die Zustandsgleichung von Neutronensternmaterie und sind demnach von großer Bedeutung für die Kernphysik. Aufbauend auf verschiedenen kernphysikalischen Modellen zeigte eine weiterführende Analyse, dass zukünftige Gravitationswellendetektionen verbesserte Einschränkungen auf mikrophysikalische Modellparameter ermöglichen könnten, die das Verhalten von Kernmaterie unter extremen Dichten in Neutronensternen bestimmen.

Ebenso bleibt die Natur der dunklen Materie eine der größten offenen Fragen. Die Analysen simulierter Gravitationswellenbeobachtungen von binären Neutronensternen mit dunkler Materie deuten darauf hin, dass Detektoren der nächsten Generation nur eine begrenzte Empfindlichkeit besitzen, um die Existenz dunkler Materie in solchen Systemen nachzuweisen oder auszuschließen. Entsprechend wird die Anwesenheit dunkler Materie in Neutronensternen, zumindest für das in dieser

Arbeit betrachtete Modell, nicht unterstützt. Somit liefern die Ergebnisse keine richtungsweisenden Erkenntnisse hinsichtlich der Eigenschaften oder der Natur dunkler Materie.

Annotated list of publications

The following section provides a list of selected publications that form the foundation of this dissertation, presented in the order of their appearance. Each entry includes a detailed account of my contributions to the respective article. Further publications, not presented in this work, can be found in my curriculum vitae.

- Peter T. H. Pang, Tim Dietrich, Michael W. Coughlin, Mattia Bulla, Ingo Tews, Mouza Almualla, Tyler Barna, Ramodgwendé Weizmann Kiendrebeogo, **Nina Kunert**, Gargi Mansingh, Brandon Reed, Niharika Sravan, Andrew Toivonen, Sarah Antier, Robert O. VandenBerg, Jack Heinzel, Vsevolod Nedora, Pouyan Salehi, Ritwik Sharma, Rahul Somasundaram, Chris Van Den Broeck. An updated nuclear-physics and multi-messenger astrophysics framework for binary neutron star mergers. Nature Communications, 14(1):8352, 2023. doi: 10.1038/s41467-023-43932-6.

  I contributed to the joint multi-messenger simulations carried out for this article and demonstrated the performance scaling of the code as shown in the manuscript. Additional contributions include image visualizations, software development, and editing the manuscript.

- **Nina Kunert**, Peter T. H. Pang, Ingo Tews, Michael W. Coughlin, and Tim Dietrich. *Quantifying modeling uncertainties when combining multiple gravitational-wave detections from binary neutron star sources.* Phys. Rev. D, 105(6):L061301, 2022. doi: 10.1103/PhysRevD.105.L061301.

  I carried out parameter estimation simulations in collaboration with Dr. Peter Pang, performed data analysis, visualized results, and authored the manuscript. Preliminary findings were presented in my master's thesis, while the final publication provides a refined analysis and extended investigations to evaluate the impact of systematic biases.

- **Nina Kunert**, Jonathan Gair, Peter T. H. Pang, Tim Dietrich. *Impact of gravitational waveform model systematics on the measurement of the Hubble constant.* Phys.Rev.D 110 (2024) 4, 043520.

  The analysis in this study builds upon data from my previous work [Phys. Rev. D, 105(6):L061301, 2022]. I conducted data analysis under guidance of Dr. Jonathan Gair, visualized the results, and authored the manuscript.

- **Nina Kunert**, Sarah Antier, Vsevolod Nedora, Mattia Bulla, Peter T. H. Pang, Shreya Anand, Michael Coughlin, Ingo Tews, Jennifer Barnes, Thomas Hussenot-Desenonges, Brian Healy, Theophile Jegou du Laz, Meili Pilloix, Weizmann Kiendrebeogo, Tim Dietrich, *Bayesian model selection for GRB 211211A through multiwavelength analyses.* Mon. Not. Roy. Astron. Soc., 527(2):3900–3911, 2024. doi: 10.1093/mnras/stad3463.

  I collected and processed the X-ray data, while the remaining observational data were primarily compiled by my colleagues, Dr. Sarah Antier and Prof. Dr. Michael Coughlin. I conducted all parameter estimation simulations, performed data analysis, visualized the results, and authored the manuscript.

- Henrik Rose, **Nina Kunert**, Tim Dietrich, Peter T. H. Pang, Rory Smith, Chris Van Den Broeck, Stefano Gandolfi, and Ingo Tews. *Revealing the strength of three-nucleon interactions with the proposed Einstein Telescope.* Phys. Rev. C, 108(2):025811, 2023. doi: 10.1103/PhysRevC.108.025811.

  My contributions to this article include conducting parameter estimation simulations, providing support for the data analysis presented in this study, and contributing to the manuscript.

- Hauke Koehn, Edoardo Giangrandi, **Nina Kunert**, Rahul Somasundaram, Violetta Sagun, Tim Dietrich. *Impact of dark matter on tidal signatures in neutron star mergers with Einstein Telescope.* Phys.Rev.D, doi: 10.1103/PhysRevD.110.103033.

  My contributions include consultation during data analysis and contributing to the manuscript through review and proofreading.

Contents

List of symbols

This dissertation explores compact binaries across diverse scientific disciplines, including observational astronomy, gravitational-wave astrophysics, nuclear physics, and cosmology. To ensure clarity, notations, symbols, and units used throughout the dissertation are listed below.

Symbol Description

Symbol	Description
$A_\alpha B^\alpha$	denotes a sum over repeated indices according to Einstein summation convention.
$\Box$	refers to the d'Alembert operator or Laplace operator of Minkowski space.
∇	denotes the nabla operator, which is a vector differential operator.
$\Re$	represents the real part of a mathematical quantity.
$\mathbf{x}$	denotes a vector quantity using bold font.
$\mathrm{M}_\odot$	is a weight unit in terms of the solar mass: 1 $\mathrm{M}_\odot = 1.99 \times 10^{30}$ kg.
Mpc	is an astronomical distance scale, whereas 1 Mpc $\simeq 3,09 \cdot 10^{22}$ m.
fm	is a typical length-scale in nuclear physics corresponding to 10^{-15} m.
erg	is a unit of energy corresponding to 10^{-7} J.

Part I

Introduction

Preface

Throughout history, astronomers relied on electromagnetic (EM) waves to explore the cosmos. Initially confined to visible light, early observations provided only a limited window into the universe. However, as scientific and technological progress enabled access to the entire EM spectrum, astronomy transformed into a multi-wavelength science. Observations in the radio, infrared, and optical regime have enabled the detection of distant galaxies, unveiled stellar nurseries, and revealed that the universe expands and is dominated by two dark components, namely dark matter and dark energy, with dark energy driving the accelerated expansion. On the other hand, ultraviolet, X-rays, and gamma-rays carry information about the most violent and energetic processes in the universe including accretion in active galactic nuclei, supernova (SN) explosions, and gamma-ray bursts (GRBs). By harnessing the entire spectrum of EM waves, known as multi-wavelength astronomy, astronomers have expanded our understanding of the cosmos, uncovering its structure, evolution, and fundamental physical laws.

On September 14, 2015, a new era in astronomy began with the first detection of a gravitational-wave (GW) signal, GW150914 [6], originating from the merger of two black holes (BHs). This groundbreaking discovery established GW astronomy as a fundamental observational discipline for exploring the universe from an entirely new perspective. A crucial prerequisite for this discovery was Albert Einstein's theory of general relativity [231], which revolutionized our understanding of gravity. Unlike Isaac Newton's interpretation of gravity as a force acting at a distance [468], Einstein revealed that gravity arises from the curvature of spacetime caused by mass or energy. Based on his theory, Einstein predicted the existence of GWs in 1915 [232], describing them as ripples in spacetime generated by accelerating massive objects, such as BHs and neutron stars (NSs). While strong indirect evidence for GWs came from the Hulse–Taylor binary pulsar [321], it took nearly a century after Einstein's prediction to achieve a direct detection. This required the development of advanced technologies capable of detecting tiny distortions in spacetime, on the order of 1/200th of a proton's radius ($\sim 10^{-13}$ cm) [176], caused by passing GWs. This breakthrough not only validated Einstein's prediction, but also opened an entirely new way of observing the cosmos, allowing scientists to study the most extreme phenomena in the universe.

The detection of compact binaries containing NSs is of particular interest in GW astronomy. The merger of two NSs represents a complex astrophysical event that emits a diverse array of observational signals across multiple messengers, including GWs, neutrinos, and EM radiation spanning the entire spectrum from X-rays to ultraviolet, optical, infrared, and radio waves. The anatomy of binary neutron star (BNS) mergers, as shown in Figure 1, plays a fundamental role in shaping the rich spectrum of astrophysical messengers they generate. Unlike NSs, which consist of ultra-dense nuclear matter and maintain a well-defined surface capable of emitting EM radiation, BHs lack a material surface and do not emit light from within their event horizon.[1] Consequently, these coalescences, along with neutron star–black hole (NSBH) mergers, are prime multi-messenger candidates and are expected to produce a variety of signals, governed by their composition, dynamical evolution, and the distinct emission mechanisms at play. While the GW emission results from the inspiral of accelerated binary masses causing disturbances in the fabric of spacetime, the EM emission arises from different ejecta components expelled during the merger[2], as depicted in Figure 1. The prompt GRB emission in the form of collimated jets releases energy through relativistic outflows, while the afterglow results from the interaction of the jet with the surrounding ambient medium. Additionally, merger ejecta concentrated around the remnant lead to a distinct kilonova emission, powered by the radioactive decay of heavy elements synthesized via r-process nucleosynthesis during the merger. This kilonova signature serves as a crucial probe of neutron-rich ejecta and provides insights into the cosmic origin of heavy elements such as gold and platinum.

A landmark event in this field occurred on August 17, 2017, when a BNS merger was observed simultaneously in GWs and EM radiation for the first time [11] by the Laser Interferometer

[1] However, in gaseous environments, BHs can still produce EM signals through interactions with surrounding matter, such as accretion flows or relativistic jets.

[2] Some studies suggest that EM emission may also occur in the pre-merger phase [488, 507, 453].

Gravitational-wave Observatory (LIGO) and Virgo detectors [1, 34, 10]. This historic multi-messenger observation, shown in Figure 1, included GW170817, the GW signal, the associated short GRB and afterglow termed GRB 170817A, detected by Fermi and INTEGRAL [9, 282], and the kilonova emission AT2017gfo, observed in the optical and infrared bands [186, 342, 58, 398, 648]. This unprecedented opportunity to combine these diverse observed messengers marked a new era in multi-messenger astronomy, driving significant advancements across multiple research fields.

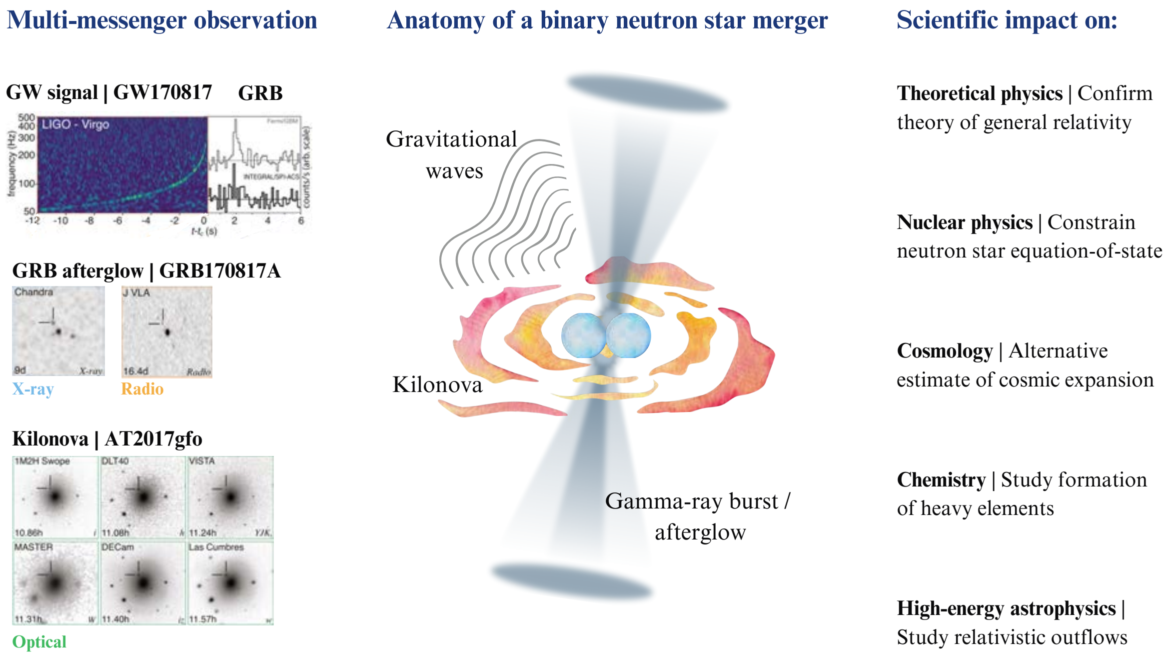

FIGURE 1
Illustration of the anatomy of a BNS merger showing expected emission components and messengers including GWs, GRBs and their afterglows, and kilonovae. Left: The first multi-messenger observation of a BNS merger including the GW signal GW170817, the prompt GRB emission and its afterglow GRB170817A related to the collimated relativistic outflow, and the kilonova AT2017gfo resulting from the radioactive decay of heavy elements synthesized in the merger ejecta. Right: Major scientific implications across astrophysics, nuclear physics, chemistry, and cosmology. Plots are taken from [11].

One of the most significant outcomes of this joint detection was the improved constraint on NS properties, particularly the equation of state (EOS) of supranuclear dense matter [13, 83, 529, 451, 633, 182, 214]. By combining GW and EM data, researchers placed tighter limits on the NS radius [451, 153, 214, 471], offering critical insights into the nature of matter at extreme densities. Additionally, the observation of both gravitational and EM signals allowed for an independent measurement of the Hubble constant, providing an alternative method for determining the expansion rate of the universe [7, 291, 317, 214, 657, 140, 489]. Furthermore, the analysis of the kilonova emission confirmed BNS mergers as a cosmic production site for heavy elements [342, 502, 224, 313, 174]. Moreover, compact binary mergers, including the event associated with GW170817, have enabled tests of general relativity using this new type of sources, providing strong confirmation of its predictions and demonstrating agreement with Einstein's theory of general relativity [17]. Lastly, the combined observation of GRB 170817A/AT2017gfo enabled the study of relativistic outflows and provided constraints on the merger environment as well as the properties of synchrotron emission [672, 293, 294].

This groundbreaking joint observation has made a significant impact across multiple scientific disciplines, exemplifying the immense potential of multi-messenger astronomy. Despite being a single event, it has already led to significant advancements in theoretical physics, nuclear physics, cosmology, chemistry, and high-energy astrophysics, enhancing the understanding of the universe's most extreme phenomena.

Objectives

While this multi-messenger observation has significantly advanced our understanding of the physics guiding the merger of compact binaries, it remains susceptible to various sources of bias, including model-dependent interpretations. Recognizing these limitations and systematically assessing potential biases is essential for ensuring the robustness and accuracy of future research in multi-messenger astronomy. Systematic biases can arise from the use of imperfect or incomplete theoretical models of compact binary coalescences (CBCs), which are cross-correlated with observational data to infer source properties. With regard to gravitational waveform models, systematic uncertainties arise from approximations in modeling the relativistic two-body problem, including Post-Newtonian methods [108, 109], the effective-one-body formalism [142, 191, 143], phenomenological models [46, 297, 322, 349, 213, 511, 635], or numerical relativity simulations [97, 69, 216, 329]. These uncertainties become more significant when combining multiple GW signals or analyzing high signal-to-noise ratio events. Understanding these systematics is crucial for accurately constraining the NS EOS, including properties such as the NS radius [483, 269, 571, 535]. In this context, the present work aims to investigate and quantify the impact of gravitational waveform model systematics on the measurement of astrophysical and cosmological parameters, namely the NS radius and the expansion rate of the universe.

Despite the detection of a likely more massive BNS merger associated with the GW signal GW190425 [19], no further multi-messenger observations of BNS mergers have been reported to date [30]. In the absence of a GW observation, studying compact binaries such as BNS systems remains feasible through the analysis of EM transient observations, namely GRB detections. The duration of GRB signals can serve as a classification metric. Short GRBs, lasting less than $2-3$ s, are typically linked to compact binary mergers, including BNS and NSBH mergers, whereas GRBs with longer durations are generally attributed to core-collapse supernovae (CCSNe) of massive stars. In principle, such a classification could offer a way to infer a compact binary in the absence of a GW observation. However, this classification scheme faces significant challenges, as exemplified by the anomalous GRB signal, GRB 211211A, detected on December 11, 2021 [533, 642]. While its duration is consistent with a core-collapse SN from a massive star, its observed properties are more consistent with a BNS merger origin. This discrepancy highlights the limitations of the duration-based GRB classification and indicates that the classification of astrophysical scenarios associated with GRBs is more complex [684, 554]. Consequently, it underscores the necessity of alternative methodologies to infer compact binaries from GRB progenitors. By examining GRB 211211A, this work illustrates how compact binary mergers, including BNS mergers, can be inferred in the absence of GW detections through Bayesian model selection applied to multi-wavelength EM data.

In NSs, where extreme gravity meets extreme matter, fundamental principles of nuclear physics and general relativity can be tested, making NSs unique laboratories. However, the NS EOS remains one of the unsolved puzzles in astrophysics. It dictates the thermodynamic properties of dense matter, governs its chemical composition, and shapes the macroscopic structure of NSs. Various theoretical models propose different EOS formulations, each offering distinct descriptions of nuclear interactions and compositions of NS matter [418, 419, 401, 312, 223, 348, 160, 645, 646]. Given the uncertainties in the fundamental properties of dense matter, these models explore a range of possible microphysical behaviors. GW signals from BNS mergers encode crucial information about their astrophysical origin and thus can probe their internal structure, composition, and nuclear interactions [83, 529, 451, 633, 214, 553]. Consequently, these signals serve as a powerful probe for nuclear physics, providing a way to constrain the NS EOS by comparing both observational and synthetic data with different theoretical models. Using different EOS models, this work aims to refine our understanding of nuclear interactions at supranuclear densities and to constrain fundamental nuclear parameters.

Beyond the challenge of understanding the behavior of nuclear matter at extreme densities, an additional source of uncertainty stems from our limited knowledge of the broader cosmic environment. Dark matter (DM), despite constituting the dominant mass component in the cosmos, remains one of the most profound mysteries in astrophysics. Its fundamental properties, including its composition, interaction mechanisms, and possible coupling to Standard Model particles, continue to elude direct detection, driving extensive theoretical and observational efforts [4, 116, 354]. NSs, which are modeled as being composed of baryonic nuclear matter, may accrete DM through scattering interactions over cosmic timescales, particularly in dark-matter-rich environments such as galactic halos [478, 688, 689, 560]. If sufficient DM accumulates, it could alter the properties of the NS, including mass, radius, and tidal deformability, thereby affecting the interpretation of BNS observations [99, 328]. Future GW observations of BNSs could reveal deviations from expected nuclear-physics predictions, potentially signaling the presence of DM. This work simulates GW observations of DM-admixed NS mergers to assess their impact on compact binary inferences and explore the feasibility of constraining DM properties.

Outline

Part I introduces the preface and rationale, serving as the foundation for the thesis structure.

Part II establishes the theoretical foundation for studying compact binaries through multi-messenger astronomy. Chapter 1 outlines the overarching theoretical framework on the basis of general relativity and consistently derives the cosmological framework and the existence of GWs. Chapter 2 revisits the formation of compact objects, including BHs and NSs, and discusses BNS and NSBH mergers as ideal candidates for multi-messenger astronomy. Chapter 3 details multi-messenger signatures of compact binary mergers, including GWs, GRBs, their afterglows, and kilonovae.

Part III focuses on the methodological framework for multi-messenger data analysis. Chapter 4 presents the statistical and computational tools, introducing Bayesian inference for multi-messenger data analysis and employing advanced parameter estimation algorithms to infer information from models with high-dimensional parameter spaces. Chapter 5 consistently integrates these methods in a nuclear-physics and multi-messenger astrophysics code, termed NMMA, demonstrating a multi-messenger and multi-physics approach to extracting astrophysical parameters.

Part IV is dedicated to addressing the central research question concerning the impact of model-dependent biases in multi-messenger astronomy, with specific emphasis on systematic uncertainties in gravitational waveform modeling. Chapter 6 investigates the influence of these model-dependent biases on the measurement of the NS radius, while Chapter 7 examines their implications for the determination of the expansion rate of the universe.

Part V presents a Bayesian model selection study of the GRB signal GRB 211211A in Chapter 8, illustrating how multi-wavelength data can be used in Bayesian studies to gain insights into BNS mergers even when no associated GW signal is detected.

Part VI focuses on the use of GW observations from BNS mergers to probe both nuclear and dark matter properties. Chapter 9 investigates whether future GW observations of BNS mergers can provide insight into distinct nuclear particle interactions, focusing on different models of three-nucleon interactions. Chapter 10 examines whether multiple GW detections of DM-admixed BNS mergers with next-generation observatories can help constrain the properties of DM. Building on this, Chapter 11 aims to explore the potential of next-generation GW detectors to constrain both nuclear matter parameters governing the NS EOS and DM properties in BNS mergers.

Part VII concludes with a summary and an outlook on the future of multi-messenger astronomy.

Part II

Multi-messenger studies of compact binaries across the universe

1

Outlining the big picture with general relativity

CONTENTS

Albert Einstein's theory of general relativity (GR) fundamentally transformed our understanding of the cosmos [231], showing that the universe is a dynamic tapestry where space, time, and matter are forever interlinked. His brilliant insight, the equivalence principle, states that, in small enough regions of space and time, the effects of gravity are indistinguishable from the effects of acceleration. In this conception, gravity is no longer seen as a force in the traditional sense acting at a distance to gravitationally bind objects as postulated by Isaac Newton's law of universal gravitation [468]. Instead it is a manifestation of the curvature of spacetime, leading objects to warp the fabric of spacetime itself, guiding everything from light to massive objects along curved paths. These paths, known as geodesics, represent the trajectories of freely falling objects in curved spacetime. In this framework, the Earth's motion around the Sun is not driven by a gravitational force in the Newtonian sense, but rather by the planet following a geodesic in curved spacetime. This geometric interpretation of gravity forms the foundation of GR and has profound implications for modern astrophysics. As explored in the following chapters, GR provides a powerful framework for investigating compact objects, such as BHs and NSs, analyzing their GW signatures, and probing the large-scale dynamics and evolution of the universe.

1.1 General relativity

The Einstein field equations (EFEs) lie at the core of GR, relating the geometric properties of spacetime, encapsulated by the Einstein tensor $G_{\mu\nu}$, to the distribution of matter and energy, given by the stress-energy-momentum tensor $T_{\mu\nu}$. While differential geometry forms the mathematical heart of GR, the EFEs embody its central physical insight. This insight is captured in compact tensorial form and is often intuitively illustrated by the well-known phrase[1]:

$$\underset{\text{how to move, and}}{\text{Spacetime tells matter}} \quad G_{\mu\nu} = \kappa T_{\mu\nu} \quad \underset{\text{how to curve.}}{\text{matter tells spacetime}} \tag{1.1}$$

In GR, gravity is interpreted as the manifestation of spacetime curvature induced by mass and energy. This interpretation means that gravity is not fundamentally a force, but is instead seamlessly woven

[1] In Eq. (1.1), the Einstein gravitational constant $\kappa = 8\pi G/c^4$ is given through the Newtonian constant of gravitation G and the speed of light in vacuum c.

into the architecture of the universe itself. To explore spacetime curvature, the language of tensors is indispensable. Tensors ensure that physical laws remain invariant under changes in coordinates, maintaining covariance under general transformations. For tensor calculus, it is convenient to employ the *Einstein summation convention*, wherein repeated indices in superscript and subscript positions imply a sum:

$$x_\mu y^\mu = \sum_\mu x_\mu y^\mu. \tag{1.2}$$

Henceforth, Greek indices, $\mu, \nu, ... = 0, 1, 2, 3$, will denote spacetime coordinates, while Latin indices $i, j, ... = 1, 2, 3$ will refer to spatial coordinates. In GR, the mathematical fabric of spacetime is a four-dimensional manifold $\mathcal{M}$, whose points represent single events $x^\mu (\mu = 0, 1, 2, 3)$, combining time and three spatial dimensions $x(t, x, y, z)$. Closely related to this is the metric tensor $g_{\mu\nu}$, which is a rank-2 tensor and encapsulates all geometric and causal structures of spacetime itself. As the metric of spacetime, it can be used to describe an infinitesimal spacetime interval

$$ds^2 = g_{\mu\nu} dx^\mu dx^\nu, \tag{1.3}$$

which provides a way to measure the distance between two neighboring events (x^μ, $x^\mu + dx^\mu$) within the manifold. Additionally, it is crucial for index operations such as raising and lowering indices, e.g., $x_\mu = g_{\mu\nu} x^\nu$. In the following, metrics are expressed using the $(-, +, +, +)$ signature. The Riemann curvature tensor $R_{\mu\nu\rho\sigma}$ measures how much spacetime curves under the presence of mass or energy and is given as

$$R_{\mu\nu\rho\sigma} = g_{\rho\lambda}(\partial_\mu \Gamma^\lambda_{\nu\sigma} - \partial_\nu \Gamma^\lambda_{\mu\sigma} + \Gamma^\lambda_{\mu\eta}\Gamma^\eta_{\nu\sigma} - \Gamma^\lambda_{\nu\eta}\Gamma^\eta_{\mu\sigma}). \tag{1.4}$$

It is a function of the metric tensor $g_{\mu\nu}$ and its derivatives and involves calculating the connection coefficients encoded in the Christoffel symbols. These are defined as

$$\Gamma^\sigma_{\mu\nu} = \frac{1}{2} g^{\sigma\alpha}(\partial_\mu g_{\alpha\nu} + \partial_\nu g_{\alpha\mu} - \partial_\alpha g_{\mu\nu}), \tag{1.5}$$

in which $\partial_\mu = \partial/\partial x^\mu$ is the partial derivative acting on the coordinates x^μ. While the Riemann tensor fully describes the curvature of spacetime, it can be contracted into a simpler rank-2 tensor, the Ricci tensor

$$R_{\mu\nu} = g^{\rho\sigma} R_{\mu\nu\rho\sigma}, \tag{1.6}$$

which provides a simplified view of curvature that specifically describes volume-changing curvature effects. Together with the Ricci scalar

$$\mathcal{R} = g^{\mu\nu} R_{\mu\nu}, \tag{1.7}$$

the trace of the Ricci tensor, the Einstein tensor fully encapsulates spacetime curvature

$$G_{\mu\nu} := R_{\mu\nu} - \frac{1}{2}\mathcal{R} g_{\mu\nu}. \tag{1.8}$$

The source of curvature is any distribution of matter, energy, or stress as given by the stress-energy-momentum tensor $T_{\mu\nu}$. The forthcoming chapters will provide a more in-depth exploration of ideal sources of curvature, such as compact objects. To describe the evolution of the universe, the EFEs can be further extended with a cosmological constant, Λ, yielding

$$G_{\mu\nu} + \Lambda g_{\mu\nu} = \frac{8\pi G}{c^4} T_{\mu\nu}. \tag{1.9}$$

This synthesis of geometry and physics in Eq. (1.9) is one of the most important achievements in modern science, enabling the exploration from compact binaries to the evolution of the universe itself.

1.2 Cosmological framework: standard model of cosmology

Applying the EFEs to the universe as a whole allows modeling its large-scale structure and dynamical evolution. This forms the foundation of modern cosmology, providing a framework to describe the expansion, contraction, or equilibrium of the universe based on its underlying constituents.

A central aspect in modern cosmology is the cosmological principle, positing that the universe is homogeneous and isotropic on large scales. This simplifies cosmological models by assuming that the universe appears uniform and isotropic in all directions. A metric that satisfies the cosmological principle is the Friedmann-Lemaître-Robertson-Walker (FLRW) metric given in comoving coordinates (t, r, θ, ϕ)

$$ds^2 = -c^2dt^2 + a^2(t)\Big(\frac{dr^2}{1-kr^2} + r^2d\theta^2 + r^2\sin^2\theta d\phi^2\Big), \tag{1.10}$$

which describes the expansion of the universe over time in terms of a dimensionless cosmic scale factor $a(t)$ and a curvature constant k. Substituting the FLRW metric into the definitions of the Ricci tensor and Ricci scalar yields the Einstein tensor, which governs the dynamics of the universe through the EFEs. The stress-energy-momentum tensor on the right-hand side of Eq. (1.9) is assumed to encapsulate all sources of curvature, such as baryonic matter, DM, radiation, and any other conceivable contributors by modeling them as a perfect fluid. Under this assumption, $T_{\mu\nu}$ is given by

$$T_{\mu\nu} = (\rho + p)u_\mu u_\nu + pg_{\mu\nu}\,, \tag{1.11}$$

whereas ρ is the total energy density of the universe, p is the total pressure, and u_μ is the fluid's four-velocity. Solving the EFEs within the FLRW metric framework for the tt-component and spatial components yields the Friedmann equations,

$$\Big(\frac{\dot{a}}{a}\Big)^2 = H^2 = \frac{8\pi G}{3}\rho - \frac{kc^2}{a^2} + \frac{\Lambda c^2}{3}, \tag{1.12}$$

$$\frac{\ddot{a}}{a} = -\frac{4\pi G}{3}\Big(\rho + \frac{3p}{c^2}\Big) + \frac{\Lambda c^2}{3}, \tag{1.13}$$

governing the evolution and dynamics of an isotropic and homogeneous universe. Grounded in GR, the Friedmann equations form the mathematical cornerstone of the Lambda Cold Dark Matter (ΛCDM) model, the prevailing paradigm in cosmology. In this model, the cosmic history of the universe began approximately 13.8 billion years ago [43], starting with an energetic expansion from an initial hot dense plasma filled with matter and photons, known as the Big Bang. Since then, the universe has undergone rapid expansion, whereas the rate of cosmic expansion can be quantified with the Hubble parameter

$$H \equiv \frac{\dot{a}}{a}. \tag{1.14}$$

As the universe expanded and cooled, protons and electrons combined into neutral atoms approximately 380,000 years after the Big Bang, a process known as recombination. This allowed photons to decouple from matter and propagate freely, forming the cosmic microwave background (CMB) radiation that is observed today. While the expansion of the universe persists, gravity drives matter overdensities to propel the formation of stars and galaxies. Over time, these structures evolve into a vast cosmic web of filaments and voids spanning the observable universe. Eventually, dark energy becomes the dominant influence, a form of energy with negative pressure that drives the accelerated expansion of the universe and is denoted by the cosmological constant Λ in the Friedmann equations. Given different energy densities and curvatures, the universe's evolutionary trajectory can take one of three possible cases:

$$k = \begin{cases} 1, & \text{for a closed universe with spherical geometry,} \\ 0, & \text{for a flat universe,} \\ -1, & \text{for an open universe with hyperbolic geometry.} \end{cases} \tag{1.15}$$

A crossover point is marked for the case when $k = 0$, separating open and closed universes. For a flat universe with $k = 0 = \Lambda$, a critical density

$$\rho_c = \frac{3H^2}{8\pi G}, \tag{1.16}$$

can be derived from Eq. (1.12). This can be used to introduce density parameters for both matter and radiation $\Omega_{m,r}$

$$\Omega_{m,r} \equiv \frac{\rho_{m,r}}{\rho_c} = \frac{8\pi G \rho_{m,r}}{3H^2}, \tag{1.17}$$

which quantifies the universe's density relative to this critical value. Using the expression for the density parameters in Eq. (1.12), the first Friedmann equation can be rewritten as

$$1 = \Omega_r + \Omega_m + \Omega_\Lambda + \Omega_k \,, \tag{1.18}$$

whereas the dark energy density parameter Ω_Λ and the curvature density parameter Ω_k are defined as

$$\Omega_\Lambda \equiv \frac{\Lambda c^2}{3H^2} \quad \text{and} \quad \Omega_k \equiv -\frac{kc^2}{H^2 a^2}. \tag{1.19}$$

Each density parameter in Eq. (1.18) evolves differently with the cosmic scale factor $a(t)$,

$$\Omega_r = \Omega_{0,r} a^{-4}; \quad \Omega_m = \Omega_{0,m} a^{-3}; \quad \Omega_k = \Omega_{0,k} a^{-2}; \quad \Omega_\Lambda = \Omega_{\Lambda,0} \,, \tag{1.20}$$

whereas the subscript $\Omega_{0,i}$ denotes the present-day values of the i-th density parameter. By using these expressions and multiplying by H^2, the first Friedmann equation in Eq. (1.18) can be rewritten as a function of present-day density parameters,

$$H^2 = H_0^2(\Omega_{0,r} a^{-4} + \Omega_{0,m} a^{-3} + \Omega_{0,k} a^{-2} + \Omega_{0,\Lambda}), \tag{1.21}$$

highlighting the importance for the present-day cosmological measurements.[2] The latest observation using the CMB radiation revealed that the universe is composed of 70% dark energy ($\Omega_{0,\Lambda} \sim 0.7$), 30% baryonic and DM ($\Omega_{0,m} \sim 0.3$), and is close to a flat geometry according to $\Omega_{0,k} \sim 0$ [43]. Additionally, the present-day value of the Hubble parameter, known as the Hubble constant H_0, has been a subject of intense scientific investigation, leading to the Hubble tension.

While the ΛCDM model offers remarkable consistency with observations, questions about the nature of DM, dark energy, and the expansion rate of the universe remain unanswered, making it a fertile ground for future research. Nevertheless, given its robust explanatory power and empirical support, the ΛCDM model will be assumed as the fundamental cosmological framework for this work.

1.2.1 Dark matter

The nature of DM remains a mystery. DM, an invisible yet fundamental component of the universe, plays a crucial role in the formation of cosmic structures and influences a wide range of astrophysical phenomena through its gravitational effects. As a non-luminous form of matter, DM neither emits nor absorbs electromagnetic radiation, making it undetectable by conventional observational methods. Its

[2]Note that the radiation density is considered negligible, as matter and dark energy constitute the dominant components of the energy density.

existence is therefore inferred solely from its gravitational influence on cosmological and astrophysical systems. While DM is thought to interact predominantly via gravity, no evidence currently suggests a coupling to the other fundamental forces mediated by gauge bosons. However, such a coupling cannot be ruled out, as it may lie below current detection thresholds. Within the framework of the standard cosmological model, DM is estimated to constitute approximately 25 % of the universe's total energy density, exceeding the roughly 5 % contribution from baryonic matter [43].

Evidence for DM has evolved over decades, beginning with early observational evidence found in the 1930s by Jan Hendrik Oort and Fritz Zwicky. While Oort's studies of stellar motions in the Milky Way hinted at a mass discrepancy within our own galaxy [478], Zwicky was the first to identify DM on a larger cosmic scale. Applying the virial theorem, Zwicky demonstrated that the observed galaxy velocities exceeded those predicted by visible mass alone, implying the presence of a significant unseen mass component [688, 689]. In the 1970s, Vera Rubin and Kent Ford discovered flat rotation curves in spiral galaxies, an observation inconsistent with the expected decline in rotational speeds based on visible matter alone [560]. More recent evidence has emerged from gravitational lensing studies, such as those of the Bullet Cluster, where the spatial separation between the lensing mass and the baryonic mass provides compelling evidence for DM [175, 421]. Additionally, precise measurements of the CMB radiation have revealed anisotropy patterns that require DM to reconcile the observed temperature fluctuations with theoretical models [36, 43].

Despite substantial evidence supporting the existence of DM, its fundamental nature remains highly uncertain and is a topic of active research. Consequently, a wide range of DM candidates, spanning an extensive mass spectrum, has been proposed to account for its properties, as depicted in Figure 1.1.

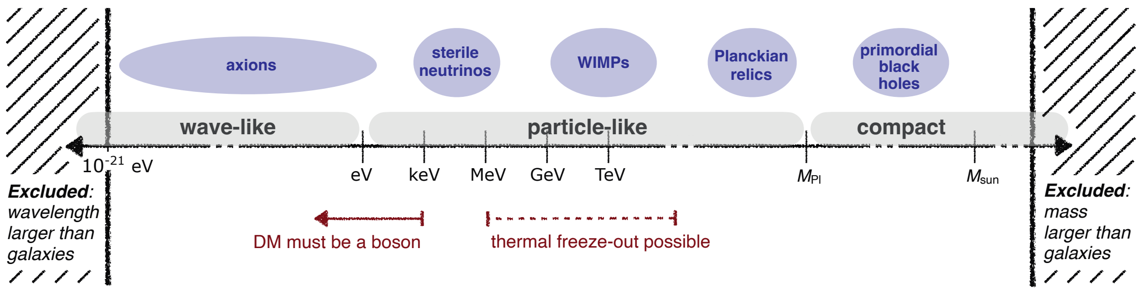

FIGURE 1.1
The possible mass range of DM particles spans a broad spectrum. For masses above the Planck scale ($M_{\mathrm{Pl}} \sim 10^{19}$ GeV), DM manifests as macroscopic, compact objects, while for masses below 1 eV, DM is better described by collective, wave-like phenomena. Image taken from [73].

Within the framework of GR, where the density and flux of energy and momentum act as sources of the gravitational field, DM, primarily interacting through gravity, can influence spacetime in a manner that alters the properties of GWs, potentially leaving detectable imprints in their signatures. Consequently, GW observations could provide indirect constraints on the properties and distribution of DM in the universe. Different GW probes of DM are discussed in Bertone et al. [98] and include direct searches, primordial BHs, phase transitions, non-perturbative DM production, environmental effects, and exotic compact objects. This work specifically examines exotic compact objects, with a particular focus on DM-admixed NS mergers.
In light of observational evidence, it is a widely accepted hypothesis to assume that DM halos encompass galaxies. While one perspective suggests that DM is smoothly distributed throughout the Galactic halo, theoretical models predict that cold DM naturally forms subhalo structures [94, 126]. Consequently, stars and stellar remnants are expected to be embedded within DM halos and may undergo rapid DM accretion via scattering when transiting overdense regions within DM subhalos

[89, 94, 126]. DM capture scales with the product of a star's nucleon count and its escape velocity, making compact objects such as NSs prime targets for detecting DM accretion effects [99]. As a result, NSs can accumulate significant DM [550, 99, 201], with BNS systems possibly retaining more due to their extended lifetimes and enhanced gravitational influence.

DM, whether concentrated in the core or surrounding a NS, can alter its internal structure, affecting key properties such as mass, radius, and tidal deformability [99, 341, 328, 281, 338]. These structural modifications influence the NS EOS and imprint distinct signatures on GW signals, making BNS mergers potential probes of DM. The extent of these imprints is governed by the DM particle mass and the fraction of DM accumulated within NSs. Since the amount of captured DM in BNS mergers depends on the DM particle mass, the interaction cross-section, and the ambient DM density, variations in the fraction of captured DM across different mergers might exist [362] and could provide crucial insights into the properties and distribution of DM. However, the fraction of DM within NSs may be small, such that the resulting change in tidal deformability would be subtle, necessitating the sensitivity of next-generation GW observatories, such as the Einstein Telescope (ET) [307, 519, 577, 128] or Cosmic Explorer (CE) [8, 541, 241], for possible detection.

Beyond their role as potential DM probes, BNS mergers also serve as standard sirens, cosmological distance indicators based solely on GW observations, as outlined in Subsec. 1.3.4. This capability makes them a powerful tool for exploring another key cosmological challenge, the Hubble tension.

1.2.2 The Hubble tension

With the theory of GR being established, Einstein introduced the cosmological constant Λ in his equations in 1917 to support a static universe [230]. However, Einstein's universe needed a perfect balance and was thus inherently unstable. Hence, the view of a static universe shifted radically within the following decade. While Alexander Friedmann theoretically demonstrated dynamic solutions of the EFEs in 1922 [264] and Georges Lemaître derived the linear velocity-distance relationship and connected his solutions to observations in 1927 [390], at the latest, with Edwin Hubble's observational evidence revealing the relationship between the distance of galaxies and their recessional velocity in 1929 [320], the idea of an expanding universe began to gain traction.

A fundamental aspect of this discovery is the Hubble law, more recently also referred to as Hubble-Lemaître law,[3]

$$v = H_0 d, \tag{1.22}$$

which is a linear relationship between the recession velocity v and the distance d of an astrophysical object, valid at small distances. While H_0 denotes the present-day value of the expansion rate as outlined in Section 1.2, the evolution of the expansion rate over cosmic time is described by the Hubble parameter, or Hubble-Lemaître parameter, $H(t)$.

As one of the most significant cosmological discoveries, the measurement of the universe's expansion rate has continually captivated the attention of scientists. However, determining its precise value has proven challenging, leading to a variety of measurement techniques. In recent years, measuring H_0 has emerged as a major frontier in cosmology, with a key challenge being the reconciliation of measurements from the early and late universe.[4]

Probing the early universe, the CMB radiation represents a snapshot of the universe when photons decoupled from matter, leaving behind a faint glow that has since redshifted into the microwave range due to cosmic expansion. It exhibits faint temperature anisotropies across the sky that formed due to the complex interplay between matter and radiation in the early universe prior to the epoch of recombination. The angular distribution of these anisotropies reveals a characteristic pattern, which

[3] Although the discovery involved multiple contributors, the credit is nowadays distributed to honor both Hubble's observational evidence and Lemaître's theoretical derivation.

[4] Among the various measurement techniques for H_0, the main focus in this work will be on values inferred from the SH0ES and Planck collaboration.

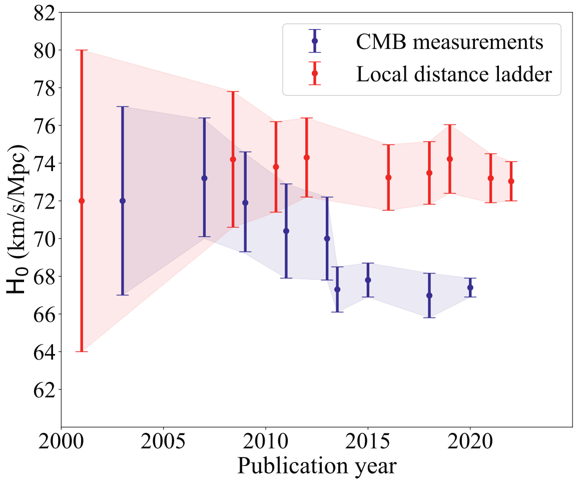

FIGURE 1.2
Illustration of the H_0-tension between early- and late-time measurements using the CMB radiation and the local distance ladder, respectively. Figure taken from [318], original data compilation in [499].

can be analyzed in terms of its frequency components. This analysis yields a power spectrum displaying a series of peaks, providing valuable insights into the physical properties of the early universe. The first peak primarily constrains the overall curvature of the universe, while the second and third peaks provide crucial information about the densities of baryonic and DM, respectively. By assuming the ΛCDM model as the underlying cosmological model and fitting it to the CMB's power spectrum, the cosmological expansion rate can be inferred. The Planck satellite's observations of the CMB have provided a highly precise estimate of $H_0 = 67.36 \pm 0.54$ km s^{-1}Mpc^{-1} at 68% credibility [43].

In the late universe, the cosmic distance ladder method offers an independent determination of the universe's current expansion rate. The SH0ES (Supernovae, H_0, for the Equation of State of Dark Energy) collaboration employs this approach to build a hierarchical chain of distance measurements to progressively greater cosmic scales, ultimately calibrating the relationship between distances and redshifts. The key building blocks are so-called *standard candles* that are astronomical objects with well-understood intrinsic luminosities that enable precise distance measurements. The SH0ES methodology involves three main rungs of the cosmic distance ladder. These include geometric anchors (e.g. parallaxes) to measure nearby distances, Cepheid variable stars to extend distance measurements to galaxies, and Type Ia SNe to reach far greater cosmic scales. Using this method, the SH0ES Collaboration determined an estimate of $H_0 = 74.03 \pm 1.42$ km s^{-1}Mpc^{-1} [546].

This discrepancy, referred to as the Hubble tension, also known as the Hubble-Lemaître tension, highlights a significant divergence between the two state-of-the-art measurements of the Hubble constant. Figure 1.2 not only illustrates the significant improvements in the precision of H_0 measurements but also highlights the persistent discrepancy between different methods, raising fundamental questions about its underlying cause. To date, the origin of this discrepancy remains unresolved, and explanations for the prevailing tension are as diverse as the methods employed to measure H_0. The tension has been attributed either to systematic uncertainties in one or more measurements or to potential shortcomings in the standard ΛCDM model, requiring modifications or entirely new theoretical frameworks [93, 115, 412, 510]. A promising alternative for inferring H_0 involves the use of GW signals as will be detailed in Subsec. 1.3.4. This approach, however, necessitates an introduction to the linearized theory of gravity.

1.3 Linearized theory of gravity

Within the established cosmological framework, compact objects such as BHs, NSs, and white dwarfs serve as cosmic laboratories of extreme gravity due to their extreme densities and spacetime curvatures. While gravity in the vicinity of compact objects is strong, most regions in the universe, when considered at a sufficient distance from the source, exhibit weak gravitational fields.

This *weak-field approximation* leads to the linearized theory of gravity in which the spacetime geometry is nearly flat and the EFEs in Eq. (1.1) can be solved analytically. This approximation, fundamental to Einstein's prediction of GWs [232], implies that the spacetime metric $g_{\mu\nu}$ is considered to be

$$g_{\mu\nu} = \eta_{\mu\nu} + h_{\mu\nu}, \tag{1.23}$$

the Minkowski metric $\eta_{\mu\nu}$ altered with small metric perturbations $h_{\mu\nu}$. In this sense, GWs can be considered as small perturbations in the metric deviating from flat Minkowski metric. The line element of the Minkowski spacetime in Cartesian coordinates reads

$$ds^2 = \eta_{\mu\nu} dx^\mu dx^\nu = -c^2 dt^2 + dx^2 + dy^2 + dz^2. \tag{1.24}$$

The perturbations of $h_{\mu\nu}$ are required to be

$$|h_{\mu\nu}| \ll 1, \quad \text{with} \quad |\partial_\sigma h_{\mu\nu}| \ll 1. \tag{1.25}$$

Under this assumption, any higher-order terms, such as $h_{\alpha\beta} h_{\mu\nu} \approx 0$, can be neglected and indices of $h_{\mu\nu}$ can be raised or lowered with the help of the flat Minkowski metric $\eta_{\mu\nu}$.

Linearizing the Einstein tensor $G_{\mu\nu}$ in Eq. (1.8) requires calculating the inverse spacetime metric $g^{\mu\nu}$, the Christoffel symbols $\Gamma^\sigma_{\mu\nu}$, and the Riemann tensor $R^\alpha_{\beta\mu\nu}$ under small perturbations $h_{\mu\nu}$. The inverse spacetime metric is then given by $g^{\mu\nu} = \eta^{\mu\nu} - h^{\mu\nu}$ and can be used to calculate the Christoffel symbols that take the form

$$\Gamma^\sigma_{\mu\nu} = \frac{1}{2} \eta^{\sigma\alpha} (\partial_\nu h_{\alpha\mu} + \partial_\mu h_{\alpha\nu} - \partial_\alpha h_{\mu\nu}), \tag{1.26}$$

while neglecting higher-order terms $\mathcal{O}(h^2)$. As Christoffel symbols are first-order quantities, only their derivatives contribute to the linearized Riemann tensor and terms involving products of Christoffel symbols in Eq. (1.4) can be neglected so that the linearized Riemann tensor,

$$R_{\mu\nu\sigma\rho} = \frac{1}{2} (\partial_\rho \partial_\nu h_{\mu\sigma} + \partial_\sigma \partial_\mu h_{\nu\rho} - \partial_\sigma \partial_\nu h_{\mu\rho} - \partial_\rho \partial_\mu h_{\nu\sigma}), \tag{1.27}$$

can be obtained by using Eq. (1.26) in Eq. (1.4). The linearized Ricci tensor can be retrieved by using the linearized Riemann tensor in Eq. (1.6) and is given as,

$$R_{\mu\nu} = \frac{1}{2} (\partial_\alpha \partial_\mu h^\alpha{}_\nu + \partial_\alpha \partial_\nu h^\alpha{}_\mu - \partial_\mu \partial_\nu h - \Box h_{\mu\nu}), \tag{1.28}$$

in which the scalar $h := \eta^{\mu\alpha} h_{\mu\alpha}$ is defined as the trace of the perturbation $h_{\mu\nu}$ and $\Box$ refers to the d'Alembertian

$$\Box := \partial_\mu \partial^\mu = \eta^{\mu\alpha} \partial_\mu \partial_\alpha = -\frac{1}{c^2} \frac{\partial^2}{\partial t^2} + \nabla^2. \tag{1.29}$$

The Ricci scalar in its linearized form is given as

$$R = \partial_\mu \partial_\nu h^{\mu\nu} - \Box h. \tag{1.30}$$

The linearized Einstein tensor is then obtained by using the linearized Ricci tensor and Ricci scalar in Eq. (1.8)

$$G_{\mu\nu} = \frac{1}{2}\Big(\partial_\mu \partial_\alpha h^\alpha{}_\nu + \partial_\nu \partial_\alpha h^\alpha{}_\mu - \partial_\mu \partial_\nu h - \Box h_{\mu\nu} + \eta_{\mu\nu}(\Box h - \partial_\alpha \partial_\beta h^{\alpha\beta})\Big). \tag{1.31}$$

It proves advantageous to introduce a trace-reversed metric perturbation

$$\bar{h}_{\mu\nu} := h_{\mu\nu} - \frac{1}{2}\eta_{\mu\nu} h\,, \tag{1.32}$$

which can be in Eq. (1.31) to simplify the linearized Einstein tensor to

$$G_{\mu\nu} = \frac{1}{2}\Big(\partial_\mu \partial_\alpha \bar{h}^\alpha{}_\nu + \partial_\nu \partial_\alpha \bar{h}^\alpha{}_\mu - \eta_{\mu\nu}\partial_\alpha \partial_\beta \bar{h}^{\alpha\beta} - \Box \bar{h}_{\mu\nu}\Big). \tag{1.33}$$

While the linearized Einstein tensor as given in Eq. (1.33) governs the dynamics of the metric perturbation, it contains redundant degrees of freedom due to coordinate invariance. By utilizing the gauge freedom to perform infinitesimal coordinate transformations $x^\mu \to x^{'\mu} = x^\mu + \xi^\mu(x^\nu)$, for which $|\partial_\mu \xi_\nu| \lesssim |h_{\mu\nu}|$, and imposing the Lorenz gauge condition

$$\partial^\nu \bar{h}_{\mu\nu} = 0, \tag{1.34}$$

the first three terms in Eq. (1.33) can be eliminated so that the Einstein tensor reads

$$G_{\mu\nu} = -\frac{1}{2}\Box \bar{h}_{\mu\nu}. \tag{1.35}$$

Using this expression in Eq. (1.1), the linearized EFEs are finally given as

$$\Box \bar{h}_{\mu\nu} = -\frac{16\pi G}{c^4} T_{\mu\nu}. \tag{1.36}$$

1.3.1 Propagation of gravitational waves in vacuum

In the absence of matter and energy sources, the stress-energy-momentum tensor vanishes so that $T_{\mu\nu} = 0$ and Eq. (1.36) reduces to

$$\Box \bar{h}_{\mu\nu} = \Big(-\frac{1}{c^2}\frac{\partial^2}{\partial t^2} + \nabla^2\Big)\bar{h}_{\mu\nu} = 0, \tag{1.37}$$

thereby exposing the underlying wave-equation structure of the linearized EFEs. A general solution of Eq. (1.37) is a linear combination of plane waves

$$\bar{h}_{\mu\nu} = \Re\Big[A_{\mu\nu} e^{ik_\sigma x^\sigma}\Big] = A_{\mu\nu}\cos(k_\sigma x^\sigma), \tag{1.38}$$

where $\Re$ denotes the real part which is important for physical applications. The polarization tensor $A_{\mu\nu}$ encodes information about the amplitude and polarization of the wave, while k_σ determines its propagation direction and frequency. There exists a hypersurface on which the value of $k_\sigma x^\sigma$ is constant and can be decomposed as

$$k_\sigma x^\sigma = k_0 x^0 + k_i x^i = -\omega t + \mathbf{k}\cdot\mathbf{x} = \text{const.}, \tag{1.39}$$

where $x^0 = ct$ is the time component of the spacetime vector, $k_0 = -\omega/c$ is the temporal component of the wave four-vector, $\mathbf{k} = k_i = (k_1, k_2, k_3)$ denotes the spatial components of the wave vector, and $\mathbf{x} = x^i = (x^1, x^2, x^3)$ refers ot the spatial coordinates. Consequently, by symmetry of the cosine function, the wave equation in Eq. (1.38) can also be written as

$$\bar{h}_{\mu\nu} = A_{\mu\nu}\cos(\omega t - \mathbf{k}\cdot\mathbf{x}). \tag{1.40}$$

By choosing a coordinate system in which the GW propagates along the z-axis, the wave phase simplifies to $\omega t - \mathbf{k} \cdot \mathbf{x} = \omega(t - z)$. For the wave equation to be satisfied, the wave vector k_σ must fulfill the condition

$$|k|^2 = \eta^{\mu\sigma} k_\mu k_\sigma = k^\sigma k_\sigma = 0, \tag{1.41}$$

indicating that it is a *light-like* or *null-vector*. This implies that $\omega = c|\mathbf{k}|$, indicating that GWs propagate at the speed of light without dispersion. In order to identify the two characteristic polarization states of GWs, the 16 components of the polarization tensor $A_{\mu\nu}$ must be systematically reduced to two independent degrees of freedom. By taking advantage of the symmetry of $A_{\mu\nu} = A_{\nu\mu}$ (6 constraints), focusing on the Lorenz gauge class of coordinate systems (4 constraints)

$$A_{\mu\nu} k^\mu = 0, \tag{1.42}$$

and further refining to the transverse-traceless (TT) gauge (4 constraints)

$$A_{\mu\nu} u^\mu = 0 = A^\mu{}_\mu, \tag{1.43}$$

where u^μ is the four-velocity vector, one can show that the polarization tensor $A_{\mu\nu}$ possesses only two independent components

$$A_{\mu\nu}^{\mathrm{TT}} = \begin{pmatrix} 0 & 0 & 0 & 0 \\ 0 & A_{xx} & A_{xy} & 0 \\ 0 & A_{xy} & -A_{xx} & 0 \\ 0 & 0 & 0 & 0 \end{pmatrix} = \begin{pmatrix} 0 & 0 & 0 & 0 \\ 0 & A_+ & A_\times & 0 \\ 0 & A_\times & -A_+ & 0 \\ 0 & 0 & 0 & 0 \end{pmatrix}. \tag{1.44}$$

In a coordinate system in which the z-axis coincides with the direction of wave propagation, the metric perturbation in TT-gauge

$$\bar{h}_{\mu\nu}^{TT} = \begin{pmatrix} 0 & 0 & 0 & 0 \\ 0 & h_+ & h_\times & 0 \\ 0 & h_\times & -h_+ & 0 \\ 0 & 0 & 0 & 0 \end{pmatrix} = \begin{pmatrix} 0 & 0 & 0 & 0 \\ 0 & A_+ & A_\times & 0 \\ 0 & A_\times & -A_+ & 0 \\ 0 & 0 & 0 & 0 \end{pmatrix} \cos[\omega(t - z)], \tag{1.45}$$

can be written in terms of the *plus* polarization h_+ and the *cross* polarization $h_\times$, respectively. These polarizations are fundamental to both the theoretical framework and the observational detection of GWs.

A well-known example that helps to illustrate the effect of the two GW polarization states is to consider a GW that passes in perpendicular direction through a ring of test particles located in the $x - y$ plane. The presence of a GW induces periodic perturbations in the spatial coordinates of the particles as shown in Figure 1.3.

As a GW propagates through an initially circular ring of material particles, the plus polarization induces vertical and horizontal stretching and squeezing along the principal axes, while the cross polarization causes stretching and compression along diagonal axes rotated by 45°. The interplay of these effects leads to the characteristic oscillatory deformation patterns observed in GW detections. In this setup, the separation between the test particles plays a crucial role in determining the amplitude of the induced deformations. Specifically, larger separations amplify the relative displacements caused by the GW, thereby enhancing the strain signal and improving the detectability of the GW.

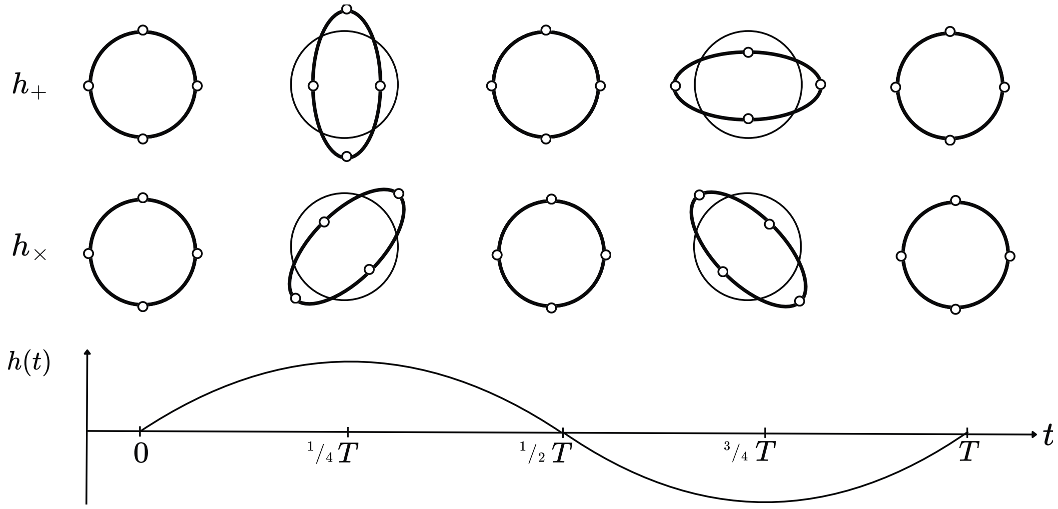

FIGURE 1.3
Illustration of the effect of a GW passing through a ring of test particles located in the $x - y$ plane, shown for the plus polarization h_+ and cross polarization $h_\times$.

1.3.2 Generation of gravitational waves

Binary systems composed of compact objects are primary sources of GWs. A compact source introduces a non-vanishing stress-energy-momentum tensor $T_{\mu\nu}$, necessitating the treatment of

$$\Box\bar{h}_{\mu\nu} = -16\pi G T_{\mu\nu}\,, \tag{1.46}$$

in which the speed of light c has been set to unity ($c = 1$). A solution of Eq. (1.46) is given through Green's function[5]

$$\bar{h}_{\mu\nu}(x^\sigma) = -16\pi G \int \tilde{G}(x^\sigma - y^\sigma) T_{\mu\nu}(y^\sigma) d^4y\,, \tag{1.47}$$

satisfying the wave equation in the presence of a Dirac delta-function source

$$\Box_{(x)}\tilde{G}(x^\sigma - y^\sigma) = \delta^{(4)}(x^\sigma - y^\sigma), \tag{1.48}$$

where $\Box_{(x)}$ refers to the d'Alembert operator with respect to the coordinates x^σ. Following the approach in [157], the retarded Green function can be written as

$$\tilde{G}(x^\sigma - y^\sigma) = -\frac{1}{4\pi|\mathbf{x}-\mathbf{y}|}\delta[|\mathbf{x}-\mathbf{y}| - (x^0 - y^0)]\Theta(x^0 - y^0)\,, \tag{1.49}$$

in which $\mathbf{x}$ and $\mathbf{y}$ refer to spatial vectors, $|\mathbf{x}-\mathbf{y}|$ symbolizes their norm, and the theta function $\Theta(x^0 - y^0)$ equals 1 when $x^0 > y^0$, and zero otherwise. The retarded time refers to the time delay associated with the propagation of GWs from a source to an observer and can be related to time t as

$$t_r = t - |\mathbf{x}-\mathbf{y}|, \tag{1.50}$$

ensuring the adherence to causality. Using Eq. (1.49) in Eq. (1.47) yields

$$\bar{h}_{\mu\nu}(t,\mathbf{x}) = 4G\int \frac{1}{|\mathbf{x}-\mathbf{y}|} T_{\mu\nu}(t - |\mathbf{x}-\mathbf{y}|, \mathbf{y}) d^3y, \tag{1.51}$$

[5]The notation for the Green's function $\tilde{G}(x^\sigma - y^\sigma)$ is deliberately chosen to differ from that of the gravitational constant G to minimize potential ambiguities.

where the delta function was utilized to perform the integral over y^0. To analyze oscillatory phenomena like spacetime perturbations, it is convenient to work in Fourier space. Reviewing the equations for the Fourier transform and its inverse for a spacetime function $\phi(t, \mathbf{x})$

$$\begin{aligned} \tilde{\phi}(\omega, \mathbf{x}) &= \frac{1}{\sqrt{2\pi}} \int dt\, e^{i\omega t} \phi(t, \mathbf{x}), \\ \phi(t, \mathbf{x}) &= \frac{1}{\sqrt{2\pi}} \int d\omega\, e^{-i\omega t} \tilde{\phi}(\omega, \mathbf{x}), \end{aligned} \tag{1.52}$$

helps to write down the Fourier-transformed metric perturbation as

$$\tilde{\bar{h}}_{\mu\nu}(\omega, \mathbf{x}) = \frac{1}{\sqrt{2\pi}} \int dt\, e^{i\omega t} \bar{h}_{\mu\nu}(t, \mathbf{x}). \tag{1.53}$$

By inserting Eq. (1.51) in Eq. (1.53), performing a change of variables from t to t_r, and further reformulations using Eq. (1.52), the Fourier-transformed metric perturbation can be rewritten as

$$\tilde{\bar{h}}_{\mu\nu}(\omega, \mathbf{x}) = 4G \int d^3y\, e^{i\omega|\mathbf{x}-\mathbf{y}|} \frac{\tilde{T}_{\mu\nu}(\omega, \mathbf{y})}{|\mathbf{x}-\mathbf{y}|}. \tag{1.54}$$

In the specific case of an isolated source, where the spatial extent δr is significantly smaller than the distance to the observer r and the radiation frequencies ω are sufficiently low ($\delta r \ll \omega^{-1}$), the term $e^{i\omega|\mathbf{x}-\mathbf{y}|}/|\mathbf{x}-\mathbf{y}|$ can be replaced by $e^{i\omega r}/r$. By factoring this term out of the integral, Eq. (1.54) can be expressed as

$$\tilde{\bar{h}}_{\mu\nu}(\omega, \mathbf{x}) = 4G \frac{e^{i\omega r}}{r} \int d^3y\, \tilde{T}_{\mu\nu}(\omega, \mathbf{y}). \tag{1.55}$$

Since the Lorenz gauge condition in Fourier space implies

$$\tilde{\bar{h}}^{0\nu} = -\frac{i}{\omega} \partial_i \tilde{\bar{h}}^{i\nu}, \tag{1.56}$$

only spatial components $\tilde{T}^{ij}$ need to be considered in Eq. (1.55). This integral can be calculated by making use of the Fourier-space version of $\partial_\mu T^{\mu\nu} = 0$, which is $-\partial_k \tilde{T}_{k\mu} = i\omega \tilde{T}^{0\mu}$, so that one finds

$$\int d^3y\, \tilde{T}^{ij}(\omega, \mathbf{y}) = -\frac{\omega^2}{2} \int y^i y^j \tilde{T}^{00} d^3y. \tag{1.57}$$

Introducing a definition of the quadrupole moment tensor of the energy density of the source

$$I_{ij}(t) = \int y^i y^j T^{00}(t, \mathbf{y}) d^3y, \tag{1.58}$$

and using its Fourier transform, one finally obtains the *quadrupole formula*[6]

$$\bar{h}_{ij}(t, \mathbf{x}) = \frac{1}{r} \frac{2G}{c^4} \ddot{I}_{ij}(t_r), \tag{1.59}$$

in which the speed of light constant has been restored. This formula reveals that GW emission from an isolated, non-relativistic source arises from the second time derivative of its energy-density quadrupole moment, highlighting that accelerating mass distributions, characterized by quadrupole and higher-order multipole moments, emit GWs.[7] These waves, described by the GW strain signal h_{ij}, can be detected by GW observatories, providing valuable insights into the nature of their astrophysical sources.

[6] Note that this derivation provides insight into the physical origin of the metric perturbation. To obtain the observable gravitational wave strain, $\bar{h}_{ij}$ must be projected onto the TT gauge.

[7] This contrasts with EM radiation, which arises from the time-dependent dipole moment of the charge density.

1.3.3 Gravitational-wave emission from the inspiral of compact binaries

The quadrupole formalism is essential for understanding GW emission from binary-star systems, where orbiting massive objects produce quadrupole moments that make them ideal sources for GW astronomy. Following the approach in [409], one can consider a Newtonian binary system comprising two point-like objects with masses m_1 and m_2, spatially related through a relative coordinate $\mathbf{x_0} = \mathbf{x_1} - \mathbf{x_2}$. The total mass can be defined as $M_{\text{tot}} = m_1 + m_2$ and the reduced mass as $\mu = m_1\, m_2/M_{\text{tot}}$. In the center-of-mass frame, the mass density for a non-relativistic system is then given as

$$\rho(t, \mathbf{x}) = \mu\delta^{(3)}(\mathbf{x} - \mathbf{x_0}(t)). \tag{1.60}$$

For the simple case of circular orbits in the x-y plane, one can write

$$\begin{aligned} x_0(t) &= R\cos(\omega_s t + \pi/2), \\ y_0(t) &= R\sin(\omega_s t + \pi/2), \\ z_0(t) &= 0, \end{aligned} \tag{1.61}$$

where ω_s is the orbital frequency, R is the orbital radius, and the phase $\pi/2$ is a helpful choice for the origin in time to calculate the nonzero components of quadrupole moment tensor that will then take the form

$$\begin{aligned} I_{11} &= \mu R^2 \tfrac{1-\cos(2\omega_s t)}{2}, \\ I_{22} &= \mu R^2 \tfrac{1+\cos(2\omega_s t)}{2}, \\ I_{12} &= -\tfrac{1}{2}\mu R^2 \sin(2\omega_s t). \end{aligned} \tag{1.62}$$

Calculating the second time derivatives for each component and evaluating Eq. (1.59), one can show that the two GW polarizations can be written as

$$h_+ = \frac{1}{r}\frac{4G\mu\omega_s^2 R^2}{c^4}\left(\frac{1+\cos^2\iota}{2}\right)\cos(2\omega_s t_r), \tag{1.63a}$$

$$h_\times = \frac{1}{r}\frac{4G\mu\omega_s^2 R^2}{c^4}\cos\iota\sin(2\omega_s t_r), \tag{1.63b}$$

in which r corresponds to the observer's distance to the binary source and ι refers to the angle between the normal to the orbit and the line of sight. Using Kepler's third law to express the orbital frequency as

$$\omega_s = \sqrt{\frac{GM_{\text{tot}}}{R^3}}, \tag{1.64}$$

and introducing the chirp mass

$$\mathcal{M} = \mu^{3/5} M_{\text{tot}}^{2/5} = \frac{(m_1 m_2)^{3/5}}{(m_1+m_2)^{1/5}}, \tag{1.65}$$

one can rewrite Eqs. (1.63a - 1.63b) as

$$h_+ = \frac{4}{r}\left(\frac{G\mathcal{M}}{c^2}\right)^{5/3}\left(\frac{\pi f_{\text{gw}}}{c}\right)^{2/3}\frac{1+\cos^2(\iota)}{2}\cos(2\pi f_{\text{gw}} t_r), \tag{1.66a}$$

$$h_\times = \frac{4}{r}\left(\frac{G\mathcal{M}}{c^2}\right)^{5/3}\left(\frac{\pi f_{\text{gw}}}{c}\right)^{2/3}\cos(\iota)\sin(2\pi f_{\text{gw}} t_r). \tag{1.66b}$$

in which $f_{\text{gw}} = \omega_{\text{gw}}/2\pi$ with $\omega_{\text{gw}} = 2\omega_s$. The above equation yields several key insights for a self-gravitating, non-relativistic binary system on circular orbits:

1. Binary systems emit GWs at a frequency twice their orbital frequency to leading order.
2. The masses of the binary system enter the GW amplitude only through the chirp mass, meaning that this combination of masses is best measured when GWs are observed.
3. GW amplitudes are highest when viewed face-on at $\iota = 0°$ or $\iota = 180°$, whereas $h_\times$ vanishes and h_+ reaches half of its maximum when viewed edge-on at $\iota = 90°$.

While the consideration of a binary system on circular orbits represents an idealized scenario, it highlights fundamental physical mechanisms underlying the inspiral of compact binary systems. The previous considerations did not yet include the backreaction, meaning that the emission of gravitational radiation removes energy and angular momentum from the system, causing the orbit to shrink.
The radiated energy budget is the sum

$$E = E_{\text{pot}} + E_{\text{kin}} = -\frac{Gm_1m_2}{2R}, \tag{1.67}$$

of the potential energy E_{pot} and kinetic energy E_{kin}. This implies that as the binary emits GWs, its orbital energy becomes increasingly negative. To compensate for this loss, the orbital separation R must decrease over time, while the orbital frequency ω_s increases in accordance with Eq. (1.64). The total radiated power over a solid angle Ω in the quadrupole approximation

$$P_{\text{quad}} = \frac{dE_{\text{quad}}}{dt} = \frac{r^2c^3}{16\pi G}\int d\Omega\langle \dot{h}_+^2 + \dot{h}_\times^2\rangle = \frac{32}{5}\frac{c^5}{G}\Big(\frac{G\mathcal{M}\omega_{gw}}{2c^3}\Big)^{10/3}, \tag{1.68}$$

grows with rising ω_{gw}, further enhancing the energy loss and driving the system into a self-reinforcing inspiral. Ultimately, this emission process will lead to the merger of the two compact objects. Throughout the inspiral, the assumption of quasi-circular orbital motion remains valid as long as the orbital frequency evolves slowly, i.e., as long as

$$\dot{\omega}_s \ll \omega_s^2. \tag{1.69}$$

In this regime, one can obtain an expression for the GW frequency

$$f_{\text{gw}}(\tau) = \frac{1}{\pi}\Big(\frac{5}{256}\frac{1}{\tau}\Big)^{3/8}\Big(\frac{G\mathcal{M}}{c^3}\Big)^{-5/8}, \tag{1.70}$$

as a function of time to coalescence $\tau \equiv t_{\text{coal}} - t$, when equating Eq. (1.68) to the time derivative of Eq. (1.67) and using the relation $f_{\text{gw}} = \omega_{\text{gw}}/(2\pi)$. Equation (1.70) demonstrates that GWs emitted by coalescing compact binaries exhibit a characteristic time-dependent frequency increase, commonly referred to as the *chirp signal.* This behavior is shown in Figure 1, which depicts the GW signal GW170817, observed as part of the multi-messenger detection of a BNS merger.

1.3.4 Gravitational-waves as cosmological probes

Traditionally, the expansion rate of the Universe has been inferred from EM observations, as detailed in Subsec. 1.2.2. More recently, GW astronomy has emerged as a powerful tool in cosmology, offering an independent avenue to measure the Hubble constant. Central to this approach are *standard sirens*, the GW analogues of standard candles, whose theoretically well-understood, model-predictable properties enable direct luminosity distance measurements, thereby circumventing the need for traditional EM distance measurement techniques. This concept was originally introduced by Bernard Schutz in 1986, when he proposed using GW signals from compact binary systems as cosmological probes [583].
To study the evolution of the universe, it is worthwhile to introduce the redshift. In the cosmological context, the redshift can be related to the cosmic scale factor

$$z = \frac{a(t_0)}{a(t_e)} - 1, \tag{1.71}$$

where $a(t_e)$ refers to the size of the universe when the light was emitted and $a(t_0) = 1$ is the universe's size when the light was observed. For present-day astrophysical observations, this equation simplifies to $a(t) = 1/(1+z)$. Using this expression in Eq. (1.21), one can define the dimensionless Hubble parameter $E(z)$ as a function of cosmological redshift

$$E(z) \equiv \frac{H(z)}{H_0} = \sqrt{\Omega_{m,0}(1+z)^3 + \Omega_{k,0}(1+z)^2 + \Omega_{\Lambda,0}}\,, \tag{1.72}$$

thereby providing a framework that facilitates the formulation of consistent distance measures. In a flat ΛCDM universe, the luminosity distance D_L is equivalent to the redshifted comoving transverse distance[8], D_M, and is given as

$$D_L = (1+z)D_M = (1+z)\frac{c}{H_0}\int_0^z \frac{dz'}{E(z')}. \tag{1.73}$$

In the regime of low redshifts ($z \ll 1$), this equation simplifies to the linear relation with redshift

$$cz \approx H_0 D_L, \tag{1.74}$$

already introduced in Eq. (1.22). Within this framework, obtaining measurements of both the redshift and the luminosity distance for a given compact binary is essential to determine the value of H_0. The luminosity distance is encoded within the GW strain signal produced by a CBC. The evolution of a gravitational waveform $\tilde{h}(f)$ over frequency can be written in terms of an amplitude $\tilde{A}$ and the phase ϕ as

$$\tilde{h}(f) = \tilde{A}(f)\exp(-i\phi(f)). \tag{1.75}$$

At leading order, the two GW polarizations can be written as [409]

$$\tilde{h}_+(f) \propto \frac{\mathcal{M}_z^{5/6}}{D_L}\frac{1+\cos^2(\iota)}{2}f^{-7/6}\exp(i\phi(\mathcal{M}_z, f)), \tag{1.76}$$

$$\tilde{h}_\times(f) \propto \frac{\mathcal{M}_z^{5/6}}{D_L}\cos\iota f^{-7/6}\exp(i\phi(\mathcal{M}_z, f) + i\pi/2), \tag{1.77}$$

where $\mathcal{M}_z \equiv \mathcal{M}(1+z)$ denotes the detector-frame (or redshifted) chirp mass and the previously defined observer-source separation r is now expressed in terms of the luminosity distance D_L. These equations demonstrate that the amplitude of the GW strain is inversely proportional to the source's luminosity distance. By comparing the observed GW strain with theoretically derived waveform templates derived from GR, one can infer both intrinsic and extrinsic parameters of an astrophysical source, including the luminosity distance. The redshift as a key observational parameter in astronomy stems from the relativistic Doppler effect and reflects

$$z = \frac{\lambda_{\text{obs}} - \lambda_{\text{emit}}}{\lambda_{\text{emit}}}, \tag{1.78}$$

how much an observed wavelength λ_{obs} of an astrophysical source is shifted relative to the wavelength at the time of emission λ_{emit}. When determining the Hubble constant using compact CBCs, the redshift can be obtained by identifying the host galaxy associated with the GW signal and measuring the redshift using spectroscopy or photometry.

This approach, termed the *bright siren* methodology, involves GW events with detectable EM counterparts. Primary sources are BNS and NSBH mergers, which are expected to emit observable EM signals during and after the merger. The first multi-messenger observation of a BNS merger [7, 16, 11] by the LIGO and Virgo detectors [1, 34] is a prime example for inferring H_0 [7, 23]. This

[8] The comoving transverse distance is a measure of distance between two points, perpendicular to the line of sight to a distant source, in an expanding universe that remains constant over time.

achievement utilizes the luminosity distance information encoded within the GW signal, combined with the measured redshift of the identified host galaxy. While current GW observations have not yet resolved the Hubble tension [170, 247, 245, 248], future observations hold promise for further constraining this cosmological parameter. In particular, multi-messenger observations offer significant potential to enhance the accuracy of H_0 measurements by combining GW derived luminosity distances with EM redshift data [7, 291, 317, 657, 214, 140, 489].

In contrast, the *dark siren* approach applies to cases in which no EM counterpart can be identified, and the redshift information must be inferred using statistical methods. Notable examples of these techniques include the galaxy catalog method [203, 170, 252, 287, 29, 289, 288, 425, 122], the cross correlation method [477, 455, 92], the spectral siren technique [245, 424, 454, 243], and the Love siren method [431, 164, 334].

Together, both bright and dark siren methodologies underscore the potential of GW observations as independent tools for cosmological inference. By enabling direct measurements of the luminosity distance from the GW signal, without reliance on the cosmic distance ladder or on observations of the CMB radiation, these approaches provide a novel avenue for constraining key cosmological parameters, most notably the Hubble constant.

2

From relics: compact binaries

CONTENTS

Compact objects such as BHs, NSs, and white dwarfs are evolutionary endpoints of stars. Once nuclear fusion ceases, they form as relics of stellar evolution through gravitational collapse, as illustrated in Figure 2.1. The final outcome depends on the progenitor star's mass, composition, and evolutionary history [671].

In contrast to normal stars, which rely on outward thermal pressure from nuclear fusion to balance inward gravitational attraction, compact objects lack the nuclear fuel necessary for fusion and thus cannot generate the heat required for stability [353]. Consequently, the pressure supporting compact stars in hydrostatic equilibrium arises from different mechanisms.

Low- and intermediate-mass stars (up to $\sim 8\ M_\odot$) evolve into white dwarfs and are supported by electron degeneracy pressure.[1] High-mass stars (roughly 8–20 $M_\odot$) undergo gravitational collapse after a SN explosion during which protons and electrons can combine to form neutrons via inverse beta decay, thereby creating neutron-rich objects denoted as NSs. The remnant core is stabilized by neutron degeneracy pressure. However, there is a theoretical upper mass limit commonly referred to as the Tolman-Oppenheimer-Volkoff limit [638], beyond which even the neutron degeneracy pressure cannot prevent gravitational collapse. In these cases, no known form of degeneracy or internal pressure can resist a gravitational collapse, resulting in the formation of a singularity within an event horizon [479, 588]. Hence, compact objects surpassing this upper-mass bound collapse into BHs.[2]

All compact objects exhibit substantially larger mass-to-radius ratios than ordinary stars, resulting in densities that far exceed those of conventional atomic matter. The concept of compactness is often expressed as a dimensionless ratio,

$$C = \frac{GM}{Rc^2}, \tag{2.1}$$

in which M and R represent the mass and radius of the compact object. The compactness parameter C exhibits a broad spectrum of values depending upon the type of compact object. For non-rotating (Schwarzschild) BHs, the compactness of a non-rotating (Schwarzschild) BH is exactly $C = 0.5$.[3] In the case of rotating (Kerr) BHs, the horizon radius decreases with increasing spin, reaching $R = GM/c^2$ in the extremal limit, where the compactness would attain its maximum value of $C = 1$ [157]. In contrast, NSs exhibit compactnesses of roughly $0.1 - 0.2$, and white dwarfs are characterized by significantly lower compactness parameters, approximately $\sim 10^{-4}$ [588, 166].

[1] In 1931, Chandrasekhar established the Chandrasekhar limit of approximately 1.4 solar masses for white dwarfs, beyond which electron degeneracy pressure cannot prevent gravitational collapse [163].

[2] For more detailed explanations, the reader may consult additional literature such as [588, 302].

[3] cf. Eq (2.2) in Subsec. 2.1.

Although all three types of stellar remnants are of considerable interest, this work focuses on BHs and NSs and will elaborate on these compact objects and their related compact binaries in more detail.

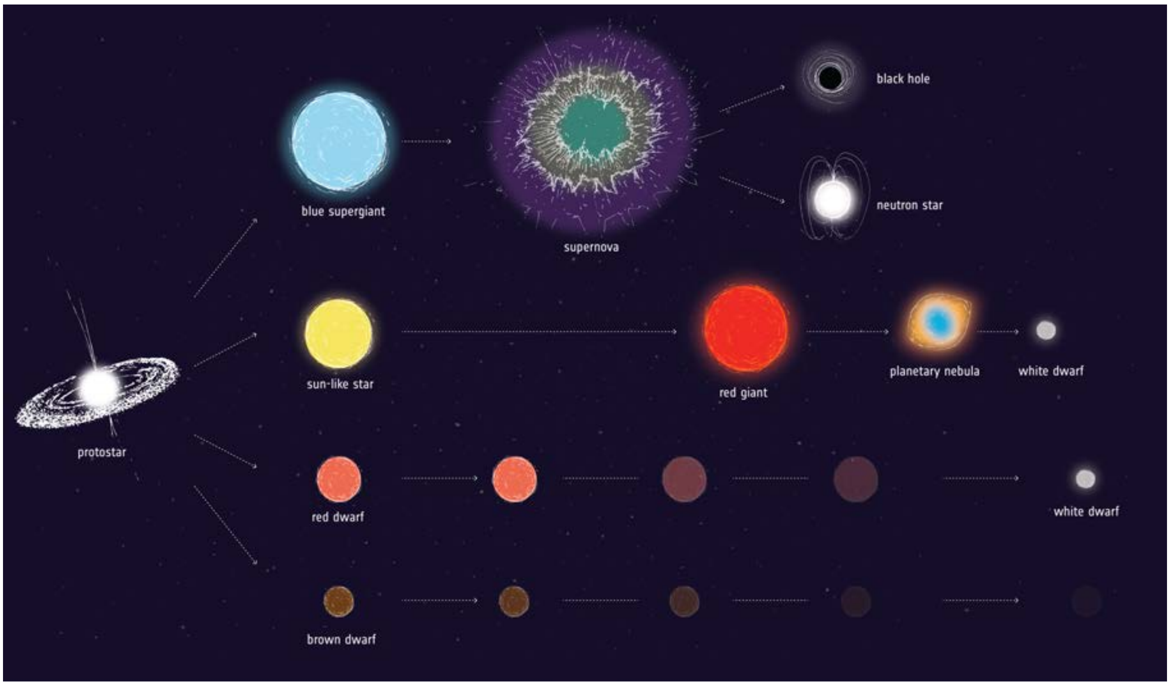

FIGURE 2.1
Possible stellar evolutionary tracks for stars of different initial masses and resulting stellar relics such as BHs, NSs, and white dwarfs. Image taken from [42].

2.1 Black holes

BHs are solutions to the EFEs that define regions of spacetime with gravitational fields so strong that nothing, neither light nor particles, can escape from it. Although BH spacetimes were theoretically predicted shortly after the formulation of GR[4], their astrophysical significance was not fully appreciated until the seminal work of Oppenheimer and Snyder [479], which explored the possibility of stellar collapse into these objects.

According to the *no-hair theorem*, BHs are characterized exclusively by three fundamental physical properties: mass, angular momentum (spin), and electric charge, rendering them relatively featureless objects. The mass is the most straightforward property of a BH, determining the strength of its gravitational field. The size of a non-rotating BH, as determined by the radius of the event horizon, or Schwarzschild radius,

$$R_s = \frac{2GM}{c^2}, \tag{2.2}$$

[4]Karl Schwarzschild derived exact solution to EFEs for the gravitational field of a non-rotating, spherically symmetric body in 1916, yielding the well-known Schwarzschild metric [585, 584]. Other important works include those by [540, 473, 663, 330].

is proportional to the mass M of the BH. Based on the mass, BHs can be further classified into three main categories[5]:

- **Supermassive BHs**: with masses ranging roughly from 10^6 to 10^9 $M_\odot$,
- **Intermediate-mass BHs:** with masses ranging roughly from 10^2 to 10^6 $M_\odot$, and
- **Stellar-mass BHs:** possessing masses roughly between $\sim 5 - 10^2$ $M_\odot$.

An interesting aspect is that stellar evolution models predict that stellar-mass BHs with masses in the so-called *lower-mass gap* (from roughly $2-3$ to 5 $M_\odot$) and in the *higher-mass gap* (from roughly 50 to 150 $M_\odot$) cannot be directly formed by the gravitational collapse of a star [14].[6] While the upper-mass gap is thought to result from extremely massive stars undergoing pair-instability SNe resulting in a disruption of a star leaving no remnant, the existence and theoretical foundation for a lower-mass gap are not fully established [363].

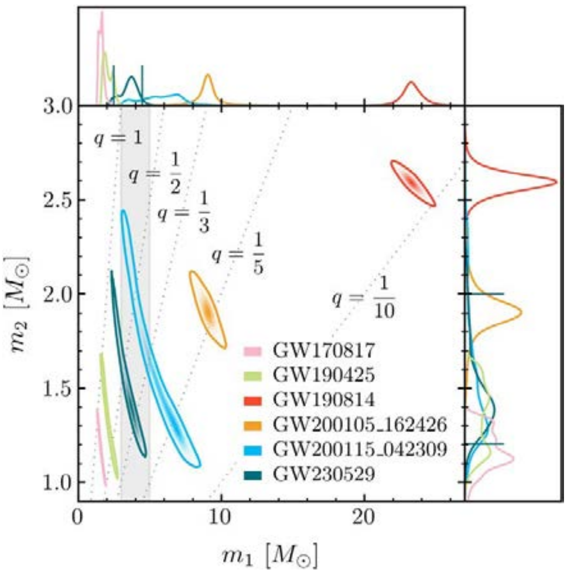

FIGURE 2.2
The one- and two-dimensional posterior probability distributions for the component masses of GW230529 (teal), two NSBH events GW200105_162426 and GW200115_042309 (orange and blue), the two confident BNS events GW170817 and GW190425 (pink and green), and GW190814 (red), where the secondary component may be a BH or a NS. Lines of constant mass ratio are indicated by dotted gray lines and the gray-shaded region marks the $3-5$ $M_\odot$ range of primary masses. Contours in the main panel denote the 90% credible regions, with vertical and horizontal lines in the side panels denoting the 90% credible interval for the marginalized one-dimensional posterior distributions. Image taken from [3].

The lower-mass gap is thought to exist between the upper-mass range of NSs, spanning approximately 2.1 to 2.5 $M_\odot$ [691, 416], and the lightest BHs with masses of roughly ~ 5 $M_\odot$. GW observations of compact binary systems offer a promising avenue to further investigate the nature of this mass

[5]The mass ranges associated with the listed classes of BHs should be considered approximate, as variations exist in the literature.

[6]Estimates for the lower and upper-mass gap may exhibit variability depending on the methodology and data used in their determination. However, the study of [250] indicated an upper limit for stars with a maximum mass of 150 $M_\odot$.

gap, as they enable to retrieve information on the masses, spins, and tidal properties, thereby enabling the characterization of compact objects in this mass region. In particular, tidal deformability measurements can help to distinguish NSs from BHs [10, 11], while spins can offer clues to formation mechanisms [131, 35, 505]. With a growing catalog of GW detections [31, 30], hierarchical population-level analyses can assess the statistical significance of this mass gap, clarifying whether it constitutes a genuine astrophysical feature. Figure 2.2 shows recent GW observations of CBCs, with component masses located within or near the lower-mass gap (gray-shaded region for primary mass).
GW230529 was observed during the fourth observing run of the LIGO–Virgo–KAGRA (LVK) detector network on 2023 May 29 by the LIGO Livingston observatory. The signal originated from a coalescing compact binary with component masses $2.5 - 4.5\ M_{\odot}$ and $1.2 - 2.0\ M_{\odot}$ reported at the 90% credible level and was most likely an NSBH merger [3] (shown in teal in Figure 2.2). GW observations of compact binaries, such as GW230529, provide crucial observational evidence for the existence of lower-mass gap objects and serve as sources for multi-messenger astronomy, as detailed in Section 2.3.

2.2 Neutron stars

As dense relics of stellar evolution, NSs constitute the most compact form of matter known to exist in the universe. A typical NS with a mass of $1.4\ M_{\odot}$ has a radius constrained to 11 km to 13 km [214, 324, 492] and reaches densities as high as 10^{15} g cm^{-3} [384]. These conditions make NSs unique natural laboratories for exploring both extreme matter and gravity conditions unattainable on Earth, which are important for nuclear physics and GR. A fundamental open question regarding NSs is their EOS, which describes the thermodynamic properties of dense matter and governs their chemical composition and macroscopic structure. Constraining the NS EOS is thus crucial to understand the properties of strongly interacting matter.

2.2.1 Interior and structure

In theoretical modeling of NS interiors, the relativistic equations of stellar structure, the Tolman–Oppenheimer–Volkoff (TOV) equations [480, 637], provide the relativistic version of the hydrostatic equilibrium condition for spherically symmetric, non-rotating stellar objects composed of a perfect fluid. By analogy to its cosmological application, as defined in Eq. (1.11) in Chapter 1, the idealized fluid model can be used to study the structure of spherically symmetric, non-rotating objects. In this framework, the stress–energy–momentum tensor

$$T_{\mu\nu} = (\epsilon + p)u_\mu u_\nu + p g_{\mu\nu}, \tag{2.3}$$

is expressed as a function of the total energy density ϵ which is given by

$$\epsilon = \rho c^2 + \varepsilon, \tag{2.4}$$

where the total energy density, ϵ, comprises the rest-mass density of the fluid, ρ, and the internal energy density, ε, which represents the thermal motion of the fluid particles [604]. According to Birkhoff's theorem, any spherically symmetric solution to the vacuum field equations must be static and asymptotically flat, implying that the exterior region around a spherical, non-rotating mass follows the Schwarzschild metric [585, 584]. In contrast to the exterior solution, the interior of these objects necessitates a more general metric in form of [604]

$$ds^2 = -e^{2\Phi(r)}dt^2 + \Big(1 - \frac{2m(r)}{r}\Big)^{-1} dr^2 + r^2(d\theta^2 + \sin^2(\theta)d\phi^2), \tag{2.5}$$

to describe a static density and pressure profile for a spherically symmetric, self-gravitating perfect fluid configuration.[7] Inserting the metric in Eq. (2.5) and the stress-energy-tensor given in Eq. (2.3) into the EFEs in Eq. (1.1) yield the TOV equations:

$$\frac{dm}{dr} = 4\pi r^2 \epsilon, \tag{2.6a}$$

$$\frac{dp}{dr} = -(\epsilon + p)\frac{m + 4\pi r^3 p}{r(r-2m)}, \tag{2.6b}$$

$$\frac{d\Phi}{dr} = -\frac{1}{\epsilon + p}\frac{dp}{dr}. \tag{2.6c}$$

The tt-component of the Einstein tensor yields Eq. (2.6a), which describes the mass m enclosed along the radial coordinate r. Matching this interior solution to the exterior Schwarzschild solution determines the NS mass $M = m(R)$. The rr-component of the Einstein tensor and the use of conservation of energy ($\nabla_\nu T^{\mu\nu} = 0$) lead to the derivation of Eqs. (2.6b) and (2.6c). For the limit, when $m(r) \ll r$ and $p(r) \ll \epsilon$, Eq. (2.6b) reduces to the Newtonian equation of hydrostatic equilibrium and Φ is the Newtonian gravitational potential in such a case. Furthermore, Eq. (2.6b) reveals that pressure not only provides the outward force necessary for hydrostatic equilibrium, but also acts a source of gravity within the framework of GR, thereby imposing a limit on the maximum mass attainable by a NS.

When supplemented with an EOS, $p = p(\epsilon)$, which relates pressure to the total energy density, the TOV equations completely determine the structure of a spherically symmetric body of isotropic material in equilibrium. Determining the NS EOS remains an area of active research, as it provides crucial insights into the nature of nuclear matter at densities far exceeding those achievable in terrestrial laboratories.

The NS EOS encapsulates how pressure relates to energy density (or density) within the star. Because NSs exhibit vastly different densities at different radii, the star is typically modeled as a layered structure [385, 386] with an outer/inner crust and outer/inner core, each governed by distinct microphysics and, hence, by specific EOS regimes. Figure 2.3 depicts the layered structure of a NS, revealing a thin outer atmosphere (with a radial width of $R_W = 10^{-4}$ km) composed of hydrogen, helium, and carbon, with a baryon density, n_B, of $n_B < 10^{-7}$ $\mathrm{n_{sat}}$, overlying a more complex interior.[8]

2.2.2 Tidal deformability

The tidal deformation of an object arises from variations in the gravitational field exerted by its binary companion. While BHs are tidally rigid [104, 173], NSs exhibit a measurable tidal response. This response results from the presence of an external gravitational field or, in essence, from the curvature of spacetime from the companion. The resulting deformations manifest as changes in the multipole structure of the NS's exterior spacetime, $\mathcal{Q}_l$. The extent of tidal deformation,

$$\lambda_l = -\frac{\mathcal{Q}_l}{\varepsilon_l}, \tag{2.7}$$

is given as the ratio of induced multipole deformation in the NS's exterior spacetime and the strength of the multipolar tidal field, ε_l, exerted by the companion [216]. In circular binaries, the fundamental modes exhibit the strongest tidal coupling [590, 358, 377], with the quadrupole mode ($l = 2$) being the dominant contributor [216]. While the quadrupole tidal deformability is the leading-order effect, higher-order terms such as dynamical tides [268, 513, 582, 615] or spin-tidal couplings to the NS

[7] The metric is expressed geometric units with $G = c = 1$.

[8] The saturation density, or nuclear saturation density, $\mathrm{n_{sat}}$, is the characteristic density at which the strong nuclear force saturates. The saturation density is typically around 0.16 fm^{-3} corresponding to approximately 2.7×10^{17} $\mathrm{kg/m^3}$.

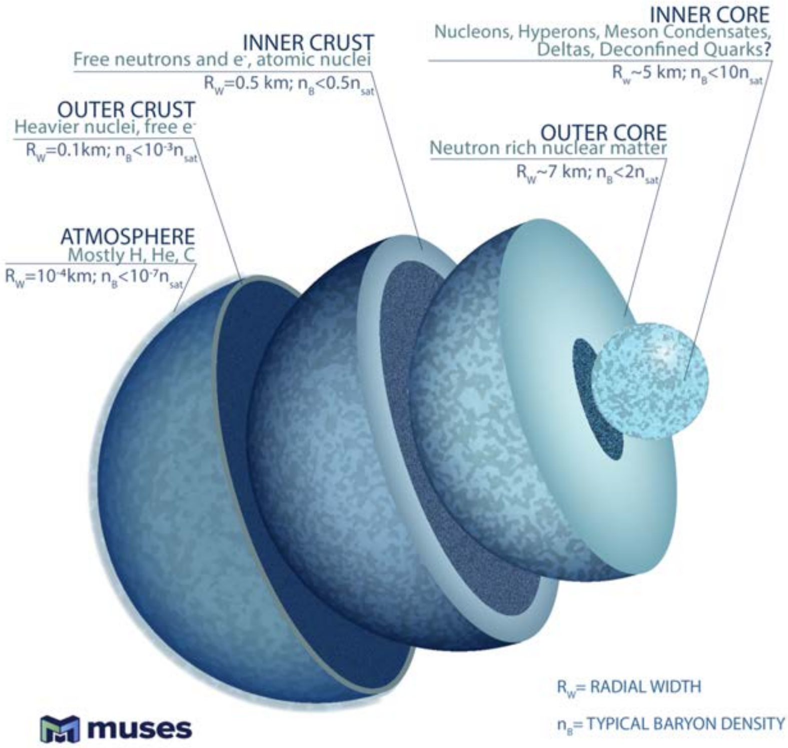

FIGURE 2.3
Structure of the interior of a NS composed of outer crust, inner crust, outer core, and inner core with typical radial widths, R_W, baryon densities, n_B, and assumed particle species shown from the left to the right. The image is taken from [177]; image credit: Muses collaboration.

rotation [33, 493, 381] introduce further corrections. Although these corrections are essential for accurately modeling GW signals, their influence is expected to be subdominant for current-generation detectors [166].

The tidal response of a NS to an external quadrupolar gravitational field, and thereby its tidal deformability Λ, can be determined by solving the TOV equations in conjunction with a perturbative equation describing the star's linear response to external curvature. A quadrupolar ($l = 2$) linear perturbation applied to a spherically symmetric star leads to a static, even-parity deformation of the spacetime metric [308, 309]. The key quantity describing this tidal perturbation is the function $H(r)$, which satisfies a second-order differential equation [509]

$$H''(r) + H'(r)\left[\frac{2}{r} + e^{\lambda(r)}\left(\frac{2m(r)}{r^2} + 4\pi r\left(p(r) - \rho(r)\right)\right)\right] + H(r)Q(r) = 0, \tag{2.8}$$

where the primes denote derivatives with respect to r, and $Q(r)$ encodes matter and metric contributions, given by

$$Q(r) = 4\pi e^{\lambda(r)}\left(5\rho(r) + 9p(r) + \frac{\rho(r) + p(r)}{c_s^2(r)}\right) - \frac{6e^{\lambda(r)}}{r^2} - \left(\nu'(r)\right)^2. \tag{2.9}$$

Here, $\rho(r)$ and $p(r)$ are the energy density and pressure, respectively, $c_s^2(r)$ is the speed of sound squared, and the metric functions $\lambda(r)$ and $\nu(r)$ are defined as

$$e^{\lambda(r)} = \left[1 - \frac{2m(r)}{r}\right]^{-1}, \qquad \nu'(r) = 2e^{\lambda(r)} \frac{m(r) + 4\pi p(r) r^3}{r^2}. \tag{2.10}$$

This second-order differential equation for the metric perturbation $H(r)$ in Eq. (2.8) can be reformulated as a first-order equation by introducing the dimensionless function $y(r) \equiv rH'(r)/H(r)$. This yields [509]

$$ry'(r) + y(r)^2 + y(r)e^{\lambda(r)} \left[1 + 4\pi r^2 \left(p(r) - \rho(r)\right)\right] + r^2 Q(r) = 0, \tag{2.11}$$

which is integrated outward from the stellar center to the surface. The value of y at the surface with stellar radius R, $y_R \equiv y(R)$, along with the compactness in geometric units $C = M/R$, fully determines the tidal Love number[9]

$$\begin{aligned} k_2(C, y_R) = {} & \frac{8}{5} C^5 (1 - 2C)^2 \left[2 - y_R + 2C(y_R - 1)\right] \times \\ & \left\{2C\left(6 - 3y_R + 3C(5y_R - 8) + 2C^2\left[13 - 11y_R + C(3y_R - 2) + 2C^2(1 + y_R)\right]\right)\right. \\ & \left. + 3(1 - 2C)^2 \left[2 - y_R + 2C(y_R - 1)\right\} \log(1 - 2C)\right]^{-1}. \end{aligned} \tag{2.12}$$

This Love number quantifies the star's quadrupolar deformation in response to an external tidal field. In GW observations, the imprint of these tidal interactions enters the waveform phase evolution through the *dimensionless tidal deformability*,

$$\Lambda \equiv \frac{\lambda}{M^5} = \frac{2}{3} k_2 \left(\frac{R}{M}\right)^5 = \frac{2}{3} k_2 C^{-5}, \tag{2.13}$$

in which M denotes the star's mass and R refers to the star's radius. Eq. (2.13) reveals that the amount of tidal deformation depends on the internal structure of the NS, in other words, the NS EOS. Consequently, GW observations of BNS mergers provide a unique opportunity to constrain the EOS of dense matter.[10] In fact, GW detectors effectively measure a combination of tidal deformabilities,

$$\tilde{\Lambda} = \frac{8}{13}\Big[(1 + 7\eta - 31\eta^2)(\Lambda_1 + \Lambda_2) + \sqrt{1 - 4\eta}(1 + 9\eta - 11\eta^2)(\Lambda_1 - \Lambda_2)\Big], \tag{2.14}$$

which is more tightly constrained by observational data than individual tidal deformabilities, as given in Eq. (2.13) due to their strong correlation [253, 655].[11] The significance of this property originates from the tidal deformation of NSs within binary systems, which accelerates the inspiral rate and imprints a distinctive tidal signature on the GW signal [309, 194, 193] as shown in Figure 2.4 for different tidal deformability values for the case of a BNS and NSBH coalescence. Figure 2.4 demonstrates that increasing tidal deformability accelerates the inspiral and advances the coalescence time of the binary. This behavior is consistently observed in both BNS and NSBH mergers and affects the GW phase evolution only during the late inspiral stage around a few hundred Hertz [166, 216, 298]. In contrast, the chirp mass affects the waveform at lower frequencies, approximately around ~ 100 Hz, where current GW detectors exhibit greater sensitivity compared to higher frequencies (cf. Figure 2 in [216]).

Tidal interactions play a crucial role in binary systems such as BNS and NSBH mergers, as they enable constraints on the NS EOS and significantly influence the emission of EM signatures essential for multi-messenger astronomy. Consequently, subsequent sections offer an examination of these two binary configurations, focusing on their fundamental properties.

[9] Love numbers are dimensionless parameters providing a measure of rigidity and deformability of an object in the presence of an external tidal field. For NSs, typical values between $k_2 \sim 0.05 - 0.1$ [309].

[10] For example, GW170817 ruled out very large tidal deformabilities [10, 13].

[11] The symmetric mass ratio, η, is defined as $\eta = m_1 m_2 / M_{\rm tot}^2$ and $M_{\rm tot}$ refers to the total mass of the binary system.

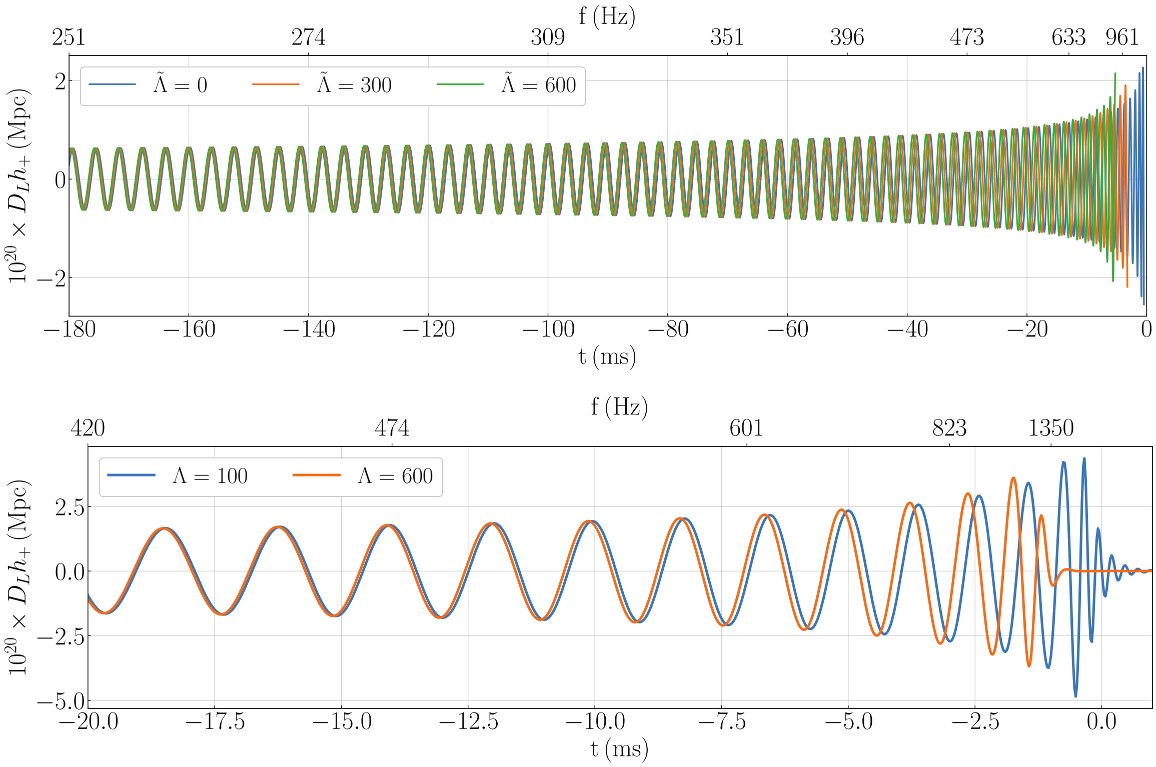

FIGURE 2.4
Imprint of different tidal deformabilities on the GW signal for an equal-mass, nonspinning BNS system (upper panel) and for a binary consisting of a nonspinning 1.4 $M_\odot$ NS and a nonspinning 5 $M_\odot$ BH (lower panel) during the inspiral and merger stage. In the upper subplot, the BNS waveform was generated with `IMRPhenomD_NRTidalv2` [322, 349, 626, 210, 213, 212] and the x-axis denotes the corresponding frequency (top) and time (bottom) for the $\tilde{\Lambda} = 0$ binary. In the lower subplot, the waveform was generated with `IMRPhenomNSBH` [635] and the upper x-axis denotes the corresponding frequency for the $\tilde{\Lambda} = 100$ binary. Both plots were taken from [166].

2.3 Compact binaries

The primary objective of this study is to investigate the coalescence of compact binaries, which provides valuable insights into associated multi-messenger signals, strong-field gravitational regimes, the behavior of matter at supranuclear densities, and stellar formation processes. Generally, double compact objects in binary systems, such as BNS, NSBH, and binary black hole (BBH) coalescences, are believed to form through two principal formation channels [88]: *isolated binary evolution in galactic fields* [397, 87, 617] and *dynamical evolution of stars in dense clusters* [508, 66].
In the context of multi-messenger astronomy, this work will focus on compact binaries, specifically BNS and NSBH systems, which are prime candidates for joint detections of GW and EM signals. Unlike BBH mergers, BNS and NSBH mergers can produce a diverse array of EM counterparts, including for example GRBs, synchrotron afterglows [485, 229, 460], and kilonovae [622, 435]. To date, comparatively few GW detections of BNS and NSBH binaries have been made, while BBH mergers have been observed in greater numbers [30].

2.3.1 Binary neutron star mergers

Although the first BNS system, the Hulse-Taylor binary pulsar, was identified exclusively through EM observations in 1974 [321], it was subsequently recognized that binary relativistic stars are significant sources of GWs[12].

GW observations: To date, two GW observations have provided evidence suggesting the coalescence of BNS mergers. The first detection of a BNS system in GWs, GW170817, occurred in 2017 and revealed a total binary mass of $2.77^{+0.22}_{-0.05}\ M_\odot$ [10], consistent with the galactic NS binary population [627]. This event marked the first observation with both derived tidal constraints and multi-messenger signatures across the EM spectrum [11]. GW190425, the second candidate with a total mass of $3.4^{+0.3}_{-0.1}\ M_\odot$, is likely a BNS merger despite being more massive than galactic NS binaries [19], suggesting the formation of more massive NSs in compact binary systems. However, the absence of an EM counterpart and the limited tidal information in the GW signal complicate efforts to unambiguously identify the nature of the components in GW190425 [149]. While the GW signal of the inspiral phase reveals information about the properties of the progenitor NSs, the GW signal of the post-merger phase encodes valuable insights on the fate of BNS mergers. For both GW170817 and GW190425, GW signals from the post-merger remnants were not detected [12, 284]. This non-detection is primarily attributed to the limitations of current detector sensitivities [576].

Post-merger evolution: The fate of BNS mergers is determined by intrinsic system properties, which influence four distinct post-merger evolutionary pathways and consequently impact the prospect of EM detectability. These remnant scenarios are primarily governed by the remnant mass, M_{rem}, and the NS EOS, determining the TOV mass[13], M_{TOV}.[14] Figure 2.5 illustrates four different outcomes after two NSs merged (panels A $\rightarrow$ B) depending on the remnant mass [576]:

- $M_{\mathrm{rem}} \gtrsim \chi M_{\mathrm{TOV}}$: a *prompt BH formation* occurs (panels B $\rightarrow$ C) accompanied with an accretion torus and jet. χ is the threshold for prompt collapse depending on NS EOS and ranges in $1.3 \lesssim \chi \lesssim 1.6$ (cf. [576] and references therein).
- $1.2\ M_{\mathrm{TOV}} \lesssim M_{\mathrm{rem}} \lesssim \chi M_{\mathrm{TOV}}$: a *hypermassive* NS forms (panels B $\rightarrow$ D) which will collapse to form a BH on dynamical time scales of $\mathcal{O}(1\mathrm{s})$ (panels D $\rightarrow$ E).
- $M_{\mathrm{TOV}} < M_{\mathrm{rem}} \lesssim 1.2\ M_{\mathrm{TOV}}$: a *supramassive* NS forms after the merger (panels A $\rightarrow$ B $\rightarrow$ D $\rightarrow$ F) and will form a BH on time scales of $\lesssim 10^5$ s (panels F $\rightarrow$ G).
- $M_{\mathrm{rem}} < M_{\mathrm{TOV}}$: a massive, stable NS survives the merger (panels F $\rightarrow$ H).

EM counterpart detection: While for GW190425 no EM counterpart was detected after the GW trigger, the detection of GW170817 was accompanied by a range of EM signals including a burst of gamma rays [9, 282] and emission ranging from X-rays to radio spectral regime [11]. In the absence of a direct detection of GWs from the post-merger, EM observations of ejected and stripped material can provide complementary insights into the hot nuclear EOS, their remnant fate, short GRBs, and kilonovae. As indicated, several factors determine whether and how prominently BNS mergers will produce observable EM signals following the coalescence. Apart from the remnant mass and NS EOS primarily determining the fate of the BNS merger remnant (BH or NS), other factors such as the mass ratio [314, 211, 592], the NS spin [211], the composition of ejected material [342], the viewing angle and the ambient environment can influence the detectability of EM signals. Notably, comprehensive investigations into the interplay of these factors, as outlined above, remain an active area of research, with the outcomes of these variations not yet fully elucidated.

---

[12] Since then, additional BNS systems have been identified through EM observations (cf. Table 2 in [627]).

[13] The TOV mass, M_{TOV}, represents the maximum mass that a non-rotating NS can sustain.

[14] Other factors influencing the post-merger outcome include the mass ratio and spin [216].

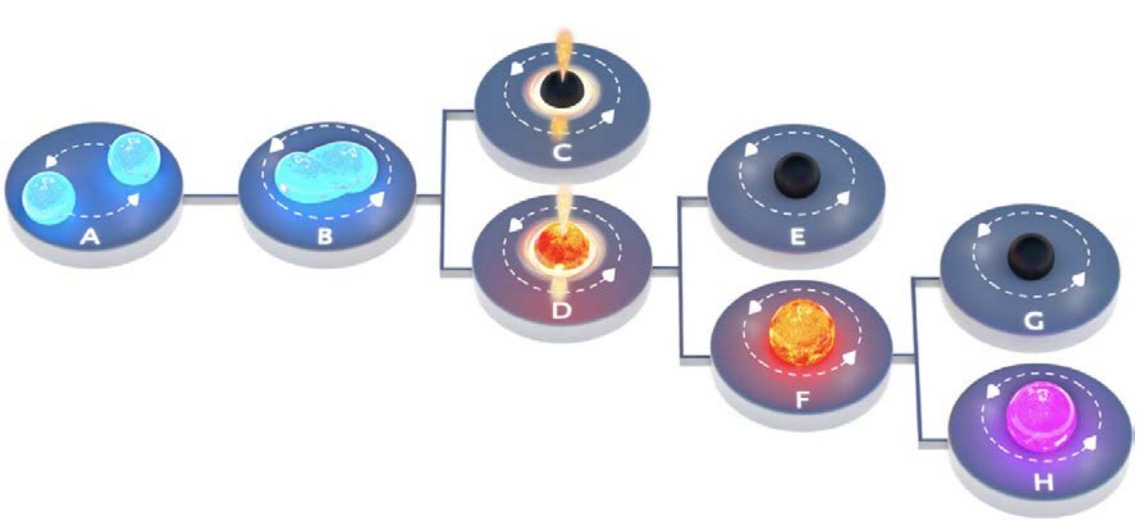

FIGURE 2.5
The fate of BNS merger remnants. Two NSs coalesce until they merge (panels A $\rightarrow$ B). Depending on the mass of the remnant, it will either promptly collapse to form a BH with an accretion torus and jet (panels B $\rightarrow$ C), or form a rapidly, differentially rotating NS (panels B $\rightarrow$ D). Depending on the mass of this NS, it will either be hypermassive, in which case it will collapse to form a BH in $\mathcal{O}(1\text{s})$ (panels D $\rightarrow$ E), it will be supramassive, collapsing to form a BH in 10^5 s (panels F $\rightarrow$ G), or it will form an infinitely stable NS (panels F $\rightarrow$ H). Image taken from [576].

2.3.2 Neutron star-black hole mergers

Merger scenarios: Two distinct merger scenarios are possible for NSBH systems, depending upon their intrinsic properties. For a NS of mass $M_{\rm NS}$ orbiting a BH of mass $M_{\rm BH}$, tidal disruption occurs when the tidal gravity gradient across the stellar radius, $R_{\rm NS}$, exceeds the self-gravity of the NS. This critical separation distance, $d_{\rm tidal}$, scales as $d_{\rm tidal} \sim (M_{\rm BH}/M_{\rm NS})^{1/3} R_{\rm NS}$ [77]. When the separation distance exceeds the innermost stable circular orbit[15] (ISCO), $d_{\rm tidal} > R_{\rm ISCO}$, the NS is disrupted, dispersing neutron-rich material into its vicinity. This disruption is expected to produce an EM counterpart, while the GW signal rapidly diminishes [374, 426, 635], as illustrated by the orange GW signal in Figure 2.4. When $d_{\rm tidal} < R_{\rm ISCO}$, the NS is mildly deformed [166], or undergoes tidal disturbance in the vicinity of the BH [77], resulting in the NS plunging into the BH. Consequently, no EM counterpart is produced and the GW signal resembles that of a BBH merger, exhibiting a characteristic ringdown to a steady state [257]. This is illustrated by the blue GW signal in Figure 2.4.

GW observations: Four candidate NSBH mergers (GW190426, GW190917, GW200105, GW200115) exhibit primary masses consistent with BHs and secondary masses consistent with NSs, indicating at least four potential detections of such systems [25, 27]. However, the absence of tidal signatures and EM counterparts prevents their definitive identification [149]. Furthermore, BHs involved in NSBH mergers have systematically smaller spin magnitudes [106] and are less massive ($\lesssim 15 M_\odot$) than those in BBH systems [687, 679, 106, 3]. In addition to the identified NSBH candidates, events such as GW230529 and GW190814 warrant particular attention due to their unusual mass configurations. GW230529 likely represents a NSBH merger, involving a $2.5 - 4.5\ M_\odot$ object and a lower-mass companion consistent with a NS. The presence of a higher-mass object in the merger suggests that compact objects within the lower mass gap can form and participate in binary coalescences [3]. GW190814 featured a secondary object with a mass of approximately $2.6\ M_\odot$, placing it lower mass gap between the heaviest known NSs and the lightest BHs. Despite its high SNR, no tidal signatures

[15] For a non-spinning massive object, the radius of the innermost stable circular orbit, $R_{\rm ISCO}$, is defined as $R_{\rm ISCO} = 3R_S$.

or EM counterparts were observed. GW190814's unusual combination of component masses, extreme mass ratio, and inferred merger rate remains unexplained by existing binary evolution models in both galactic and dense stellar environments. Its discovery poses a significant challenge to current theories of compact-object formation and may point to new pathways for producing the lightest BHs or the most massive NSs [24].

EM counterpart detection: Given these insights through GW observations, only a small fraction ($\lesssim 20$ %) of NSBH mergers may have observable EM emission [19, 27, 260, 106, 3]. In fact, no EM counterpart was observed for the mentioned NSBH candidates. The detectability of EM signals from NSBH mergers depends on the system's intrinsic properties. More unequal mass ratios disfavor NS disruption, whereas more equal mass ratios lead to more significant NS tidal disruption and a larger remnant mass. Such disruption is more likely in systems featuring low BH masses, substantial BH spins aligned with the orbital angular momentum (as higher BH spins reduce the horizon radius, enabling the NS to orbit closer before merger), and NSs with lower compactness, which enhances their deformability [166]. In general, the latter is expected to be small for NSBH binaries as $\tilde{\Lambda} \sim q^4$, where q refers to the mass ratio [166, 368].

3

To ripples: multi-messenger signatures

CONTENTS

Both BNS and NSBH mergers are among the most energetically extreme events in the universe, serving as prime multi-messenger laboratories. These coalescences generate GWs detectable by advanced ground-based observatories and can emit a diverse array of EM counterparts, including short GRBs, afterglow emission, and kilonovae. In addition, these events may produce neutrinos, offering further insight into the merger dynamics. Figure 3.1 illustrates distinct stages of a BNS merger event and underlying physical processes, highlighting corresponding observational signatures emitted over time.[1] The subsequent sections will explore these multi-messenger signatures and their physical processes, with a focus on GW emission, GRB bursts, afterglows, and kilonovae.

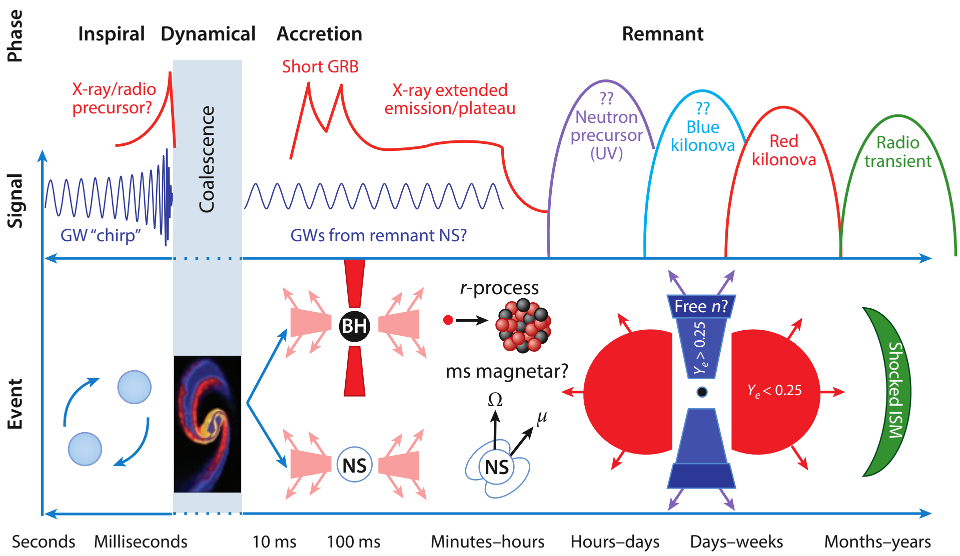

FIGURE 3.1
Phases of a BNS merger as a function of time, showing the associated observational signatures and underlying physical phenomena. Abbreviations: black hole (BH); γ-ray burst (GRB); gravitational wave (GW); interstellar medium (ISM); neutron (n); ultraviolet (UV); electron fraction (Y_e). Image taken from [249] and coalescence inset courtesy from [516].

[1]Note that the indicated GW signal duration is detector-dependent and increases with lower frequency cutoffs.

3.1 Gravitational waves

GW detection and the development of waveform models are both fundamental to GW astronomy, as detections provide the observational data necessary to identify astrophysical events, while waveform models enable the accurate extraction of source properties. Subsec. 3.1.1 provides an overview of GW detection, highlighting interferometric GW detectors and essential data analysis techniques used to extract GW signals from noisy data. Subsec. 3.1.2 presents an overview of gravitational waveform models used to infer astrophysical properties from observed GW sources.

3.1.1 Detection

Almost a century passed between Albert Einstein's theoretical prediction of GWs in 1915 [232] and the first direct GW detection of a BBH merger (GW150914) [6] on September 14, 2015, by the LIGO and Virgo collaborations, enabled by significant advancements in GW detector technology [1, 34] and data analysis techniques [18].

Interferometer

The detection of GW signals relies on the interferometric design of GW detectors, which measures the periodic stretching and compression effects on test masses induced by a GW (cf. Figure 1.3). A schematic illustration of an interferometer is shown in Figure 3.2.

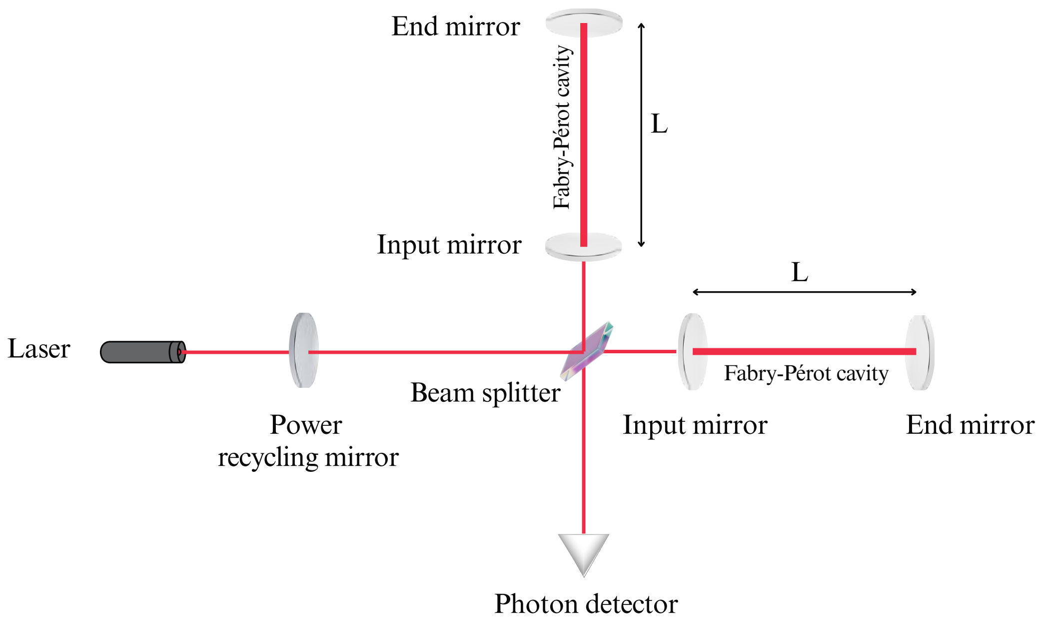

FIGURE 3.2
Schematic layout of a GW laser interferometer. The system employs power recycling mirrors and Fabry-Pérot cavities to enhance laser power and sensitivity. The photon detector measures the phase difference and thus the length difference of both interferometer arms.

Figure 3.2 illustrates the operational principles of an interferometric GW detector. A laser beam is introduced into the interferometer to precisely measure differential changes in the lengths of its two orthogonal arms. The beam splitter divides the laser light into two coherent beams, which propagate along the orthogonal arms. At the end of each arm, mirrors reflect the beams back toward the beam splitter. When a GW traverses the interferometer, it induces differential changes in the arms, causing one arm to elongate while the perpendicular arm contracts as the GW oscillates through its peaks and troughs. In the absence of a GW, the reflected laser beams recombine at the output photodiode and undergo destructive interference, resulting in no detectable signal. However, the passage of a GW introduces slight variations in the arm lengths, leading to a characteristic interference pattern in the recombined laser light. The change in arm length, δL, relative to the original arm length, L, produces a GW strain,

$$h(t) = \frac{\delta L}{L}, \tag{3.1}$$

enabling the detection of GWs. The first directly measured GW strain, GW150914, had a maximum (dimensionless) amplitude of 10^{-21}, which means that the 4 km LIGO arms changed in length by $10^{-21} \times 4 \times 10^5$ cm $= 4 \times 10^{-16}$ cm. Contrasting this length with the proton radius of 10^{-13} cm, GW detectors aim to detect length changes of the order of 1/200 of the proton radius with a typical laser wavelength of the order of 10^{-4} cm [176].

To achieve such extraordinary sensitivity, GW interferometers incorporate Fabry–Pérot cavities within their arms. These cavities effectively amplify the optical path length without necessitating physically longer arms by enabling the laser light to undergo multiple round trips between highly reflective mirrors. Consequently, a vast number of coherent photons are repeatedly traversed along the interferometer arms before recombining at the output photodiode [176].

The response of a GW detector to the two fundamental polarization states, h_+ and $h_\times$, varies as a function of the source's sky location and the detector's orientation. This directional sensitivity is characterized by the detector's antenna pattern functions, denoted as F_+ and $F_\times$. The measured strain $h(t)$ in an interferometric detector due to an incoming GW signal is given by

$$h(t) = F_+(\theta, \phi, \psi) h_+(t) + F_\times(\theta, \phi, \psi) h_\times(t), \tag{3.2}$$

where θ, ϕ represent the polar and azimuthal angles, respectively, specifying the direction of the incoming wave relative to the detector, while ψ denotes the polarization angle of the wave.

From detection to the GW signal

Extracting GW signals from detector data involves a series of sophisticated data analysis techniques[2] designed to identify, isolate, and characterize extremely subtle spacetime distortions caused by astrophysical events. During the *calibration* procedure, the raw detector photodiode output is converted to GW strain data as a time series,

$$d(t) = h(t) + n(t), \tag{3.3}$$

containing the actual GW signal, $h(t)$, concealed by noise, $n(t)$. *Noise mitigation* procedures aim to identify various noise sources, such as seismic noise, thermal noise, or quantum noise (shot noise and radiation pressure noise)[3]. Effective noise modeling, such as glitches, enables the removal of noise artifacts from the data stream.

The calibrated strain data undergoes a sequence of processing steps, including windowing, whitening, and bandpassing (cf. Figure 3 in [18]), prior to the application of *matched filtering*. In this process, detector data is compared with a bank of theoretical waveform templates representing possible GW signals. This method maximizes the signal-to-noise ratio (SNR)

$$\rho_{\mathrm{GW}} = \frac{\langle d(t) | h(t) \rangle}{\sqrt{\langle h(t) | h(t) \rangle}}, \tag{3.4}$$

[2] A simple schematic illustration of required data processing steps in LIGO-Virgo from raw data to the results in presented in GW catalogs is shown in Figure 1 in [18].

[3] A more detailed discussion of different noise sources can be found in [137, 18].

by correlating the data with each waveform template and requires evaluating the noise-weighted inner product

$$\langle a|b\rangle = 4\Re \int_0^\infty df \frac{\tilde{a}^*(f)\tilde{b}(f)}{S_n(f)}, \tag{3.5}$$

in which $\tilde{a}$ and $\tilde{b}$ are the Fourier transforms of the time series $a(t)$ and $b(t)$, respectively, $\tilde{a}^*$ is its complex conjugate, and $S_n(f)$ refers to the power spectral density (PSD) of the noise. The optimal matched-filtering SNR associated with a given GW signal, $h(t)$, is given through

$$\rho_{\rm opt} = \sqrt{\langle h|h\rangle}. \tag{3.6}$$

Once a GW event has been identified, *parameter estimation* can be carried out to infer the astrophysical characteristics and properties of the GW source.[4]

Current and future GW detectors

GW astronomy spans a vast frequency spectrum, each band requiring specialized detection techniques. Ground-based interferometers are more sensitive in the high-frequency regime (Hz to kHz), in which GW signals are expected from compact binary inspirals, CCSNe, and pulsars. At the time of writing, there are several ground-based GW detectors: two Advanced LIGO interferometers located in Hanford and Livingston in the United States [1], Advanced Virgo in Italy [34], KAGRA in Japan [48, 610, 67], and GEO600 located in Germany.[5] An additional ground-based GW detector, expected to become operational in the latter half of this decade, is currently under construction in India, thus extending the LIGO Collaboration observational network [570]. The next (third) generation of GW detectors includes ET [519, 263, 306, 307] in Europe and CE [8, 541, 241] in the United States, further increasing sensitivity.

While ground-based detectors are sensitive and optimized for higher frequencies due to seismic and thermal noise limitations, space-based GW detectors such as the Laser Interferometer Space Antenna (LISA) [71, 180, 62, 50, 587] will probe the low-frequency (mHz) regime, unveiling mergers of massive binaries, extreme mass ratio inspirals, and galactic binaries. In addition, Pulsar timing arrays enable the exploration of ultra-low frequency regimes (in the nanohertz), probing supermassive BH binaries and stochastic GW backgrounds [208, 41]. The combination of observations across diverse GW frequency bands, analogous to multi-wavelength EM astronomy, provides a comprehensive view of the universe.

3.1.2 Waveform models

Gravitational waveform modeling is indispensable for detecting and interpreting GW signals. GWs convey comprehensive information about their originating astrophysical sources. To determine the astrophysical parameters of a GW source, it is necessary to compare observational data with theoretical gravitational waveform templates. These templates are constructed within the framework of GR under different approximations, enabling the characterization of a GW signal in terms of a set of intrinsic and extrinsic parameters. While BBH mergers are described by 15 parameters, additional physics must be included to model BNS systems due to the finite-size effects of NSs. In particular, the leading-order tidal deformabilities (Λ_1, Λ_2) account for how each star deforms in its companion's gravitational field. More advanced models may also include higher-order tidal deformabilities or quantities like f-mode oscillation frequencies, which encode additional information about the NS EOS. For quasi-circular binaries with tidal effects at leading order, the set of BNS parameters is given as [534]:

[4] A more detailed explanation of required statistical and computational methodologies will be provided in Chapter 4.
[5] The GEO600 detector primarily serves as a testbed for fundamental research and the development of advanced technologies for GW detection.

$$\boldsymbol{\theta}_{\mathrm{BNS}} = \{\underbrace{m_1, m_2, a_{\mathrm{spin1}}, \phi_{\mathrm{spin1}}, \theta_{\mathrm{spin1}}, a_{\mathrm{spin2}}, \phi_{\mathrm{spin2}}, \theta_{\mathrm{spin2}}, \Lambda_1, \Lambda_2}_{\text{intrinsic}}, \underbrace{D_L, t_c, \phi_c, \alpha, \delta, \iota, \psi}_{\text{extrinsic}}\}. \tag{3.7}$$

Intrinsic parameters, such as the masses (m_1, m_2), spins[6] $(a_{\mathrm{spin1,2}}, \phi_{\mathrm{spin1,2}}, \theta_{\mathrm{spin1,2}})$, and leading-order tidal deformabilities (Λ_1, Λ_2) affect the physical dynamics of the system, while extrinsic parameters describe observer-dependent aspects, including the source's luminosity distance D_L, sky location (right ascension α; declination δ), inclination angle ι, polarization angle ψ, and time and phase of coalescence (t_c, ϕ_c).
Given the complexity of GW dynamics and the need for accurate waveform modeling, different theoretical approaches have been developed to predict gravitational waveforms. These approaches vary in terms of their accuracy, applicability range, and computational feasibility, giving rise to four distinct approaches:

- Numerical relativity (NR) waveforms,
- Post-Newtonian (PN) waveforms,
- Effective-One-Body (EOB) waveforms, and
- Phenomenological waveforms.

Figure 3.3 depicts three distinct stages of a CBC, namely, inspiral, merger, and ringdown (IMR), for the case of a NSBH coalescence. Additionally, the figure outlines different gravitational waveform modeling approximation schemes and their respective domains of applicability.

Inspiral: The two bodies orbit each other with decreasing separation due to the emission of gravitational radiation. Throughout most of the binary evolution, orbital velocities remain relatively low compared to the final merger stage[7], allowing for approximation through analytical expansions. EOB [190, 142, 143, 191] and PN frameworks [108] provide successful descriptions of this phase.

Merger: Analytical schemes break down in the late inspiral phase around the time of merger until the two bodies plunge together to form a single, highly dynamical object. In this regime, NR simulations model highly relativistic effects that dominate this brief but strongly non-linear stage.

Ringdown: The GW signal following the merger is shaped by the nature of the remnant and exhibits characteristic spectral signatures. In the case of a direct plunge of the NS into the BH, the remnant rapidly collapses, leaving minimal GW emission. The newly formed BH stabilizes by radiating residual perturbations as quasi-normal modes, described by perturbation theory. For the case in which the tidal separation distance exceeds the ISCO, the NS is tidally disrupted. This leads to characteristic modifications in the gravitational waveform and may result in detectable EM counterparts due to the formation of an accretion disk and potential mass ejection (cf. Figure 3.3). In contrast, post-merger GW signals from certain BNS mergers could provide insight into the hot nuclear EOS under conditions inaccessible in terrestrial experiments [85, 340].

NR waveforms: Solving the complete set of the EFEs analytically[8] is generally unattainable due to their inherent nonlinearity and complexity. NR addresses this challenge by utilizing computational methods and algorithms to accurately model the fully nonlinear relativistic dynamics of merging compact objects in late inspiral, merger, and ringdown (cf. Figure 3.3). A necessary precursor was the

[6] The dimensionless spin magnitudes are defined as $0 \leq a_{\mathrm{spin1,2}} \equiv S_{1,2}/M_{1,2}^2 \leq 1$, where $S_{1,2}$ and $M_{1,2}$ denote binary spins and masses, respectively. Spin orientations are given by the polar and azimuthal angles $\theta_{\mathrm{spin1,2}}, \phi_{\mathrm{spin1,2}}$, relative to the line of sight.

[7] For example, the two BHs involved in the first GW detection, GW150914, reached a relative velocity of $v/c \sim 0.6$ at merger [6].

[8] Known analytic solutions of the EFEs include the flat Minkowski spacetime in special relativity, the Schwarzschild and Kerr spacetimes describing single BHs, and the FLRW spacetime used for the standard model of cosmology.

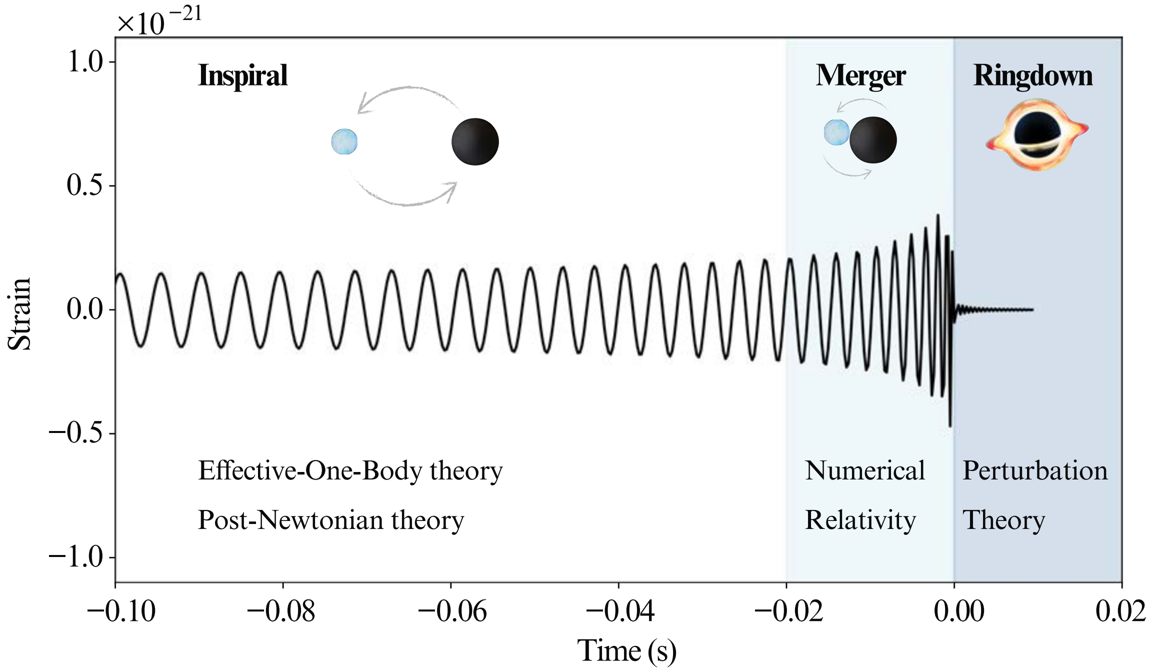

FIGURE 3.3
Schematic illustration of gravitational waveform as a function of time for a non-spinning 1.4 $M_\odot$ NS merging with a non-spinning 5 $M_\odot$ BH at a distance of 100 Mpc, generated with `IMRPhenomNSBH` [635], similar to [166]. Different merger stages such as inspiral, merger, and ringdown are illustrated at the top, while gravitational waveform-model approximation schemes and their range of applicability are indicated on the bottom. In this configuration, the NS undergoes tidal disruption prior to merger, imprinting characteristic signatures on the GW signal and giving rise to EM counterparts, thereby potentially enabling multi-messenger observations.

decomposition of spacetime into separate spatial and temporal components, known as *3+1 decomposition* [60].[9] By foliating the four-dimensional manifold into a sequence of three-dimensional spacelike hypersurfaces at constant time, the EFEs can be recast into a form suitable for numerical integration. While the ADM formalism developed by Richard Arnowitt, Stanley Deser, and Charles W. Misner was groundbreaking, subsequent developments have refined and extended the 3+1 decomposition to improve numerical stability and accuracy.[10] Another significant milestone in NR was the successful simulation of BBH mergers [515, 152, 72]. These simulations proved exceptionally challenging due to problems such as singularities and the need for stable numerical algorithms. Nowadays, various NR codes are available that model the nonlinear relativistic dynamics of compact binary systems, enabling the extraction of highly accurate gravitational waveforms throughout the late inspiral, merger, and post-merger phases: BAM [634, 134, 133, 132], THC [530], SACRA [676], WHISKY [68, 280], or SPEC [350] and SPECTRE [351].

Although NR waveforms provide the most accurate representation of the highly nonlinear dynamics in the late inspiral and merger phases, the computational expense of running full NR simulations makes them impractical for GW data analysis. Consequently, waveform models incorporate NR results to capture the merger and ringdown regimes and calibrate their waveforms against NR waveforms to

[9]The 3+1 decomposition, introduced by Richard Arnowitt, Stanley Deser, and Charles W. Misner in their ADM formalism, has been crucial for understanding spacetime dynamics in GR and has become foundational in the field of NR.

[10]Notable examples include BSSN Formalism [459, 593, 594, 82] or the Z4 formulation [120, 121].

enhance accuracy during these stages. As a result, NR simulations serve as important prerequisite and testbed for GW modeling.

PN waveforms: At low velocities ($v \ll c$) and relatively wide separations, the PN formalism can accurately describe the inspiral phase (cf. Figure 3.3). As the system approaches the last orbits before merger, fully nonlinear effects become dominant, and purely PN treatments lose accuracy. Moreover, GWs are not generated only by the quadrupole moment as derived in Subsec. 1.3.2, but exhibit a multipolar structure that represents an expansion in powers of (v/c). Furthermore, the influence of the source's self-gravity, arising from its gravitational binding, cannot be neglected. Incorporating these effects leads to an expansion of order $\mathcal{O}(v^2/c^2)$. Hence, the PN expansion at n-th order will contribute to $\mathcal{O}(v^{2n}/c^{2n})$ term, yielding higher-order curvature corrections for both the orbital dynamics and the gravitational waveform.
In Subsec. 1.3.3, the consideration of a binary inspiral under adiabatic approximation[11] showed that the GW luminosity,

$$\mathcal{F} = -\frac{d\mathcal{E}}{dt}, \tag{3.8}$$

originates from the change in orbital energy, E, averaged over a period, where $\mathcal{E} = EM_{\rm tot}$. The idea of the PN formalism is to compute the orbital phase, $\Phi_{\rm orb}$, of a binary as a perturbative expansion in a small parameter $v = \pi M_{\rm tot} f_{gw}$. In the case of circular orbits, one can use the energy balance equation, Eq (3.8), and Kepler's third law to obtain a description of the evolution of the orbital phase [144]

$$\frac{d\Phi_{\rm orb}}{dt} = \frac{v^3}{M_{\rm tot}}, \tag{3.9}$$

$$\frac{dv}{dt} = -\frac{\mathcal{F}(v)}{E'(v)M_{\rm tot}}, \tag{3.10}$$

or equivalently,

$$\Phi_{\rm orb}(v) = \Phi_{\rm ref} + \int_v^{v_{\rm ref}} dv v^3 \frac{E'(v)}{\mathcal{F}(v)}, \tag{3.11}$$

$$t(v) = t_{\rm ref} + M_{\rm tot} \int_v^{v_{\rm ref}} dv \frac{E'(v)}{\mathcal{F}(v)}, \tag{3.12}$$

in which E' corresponds to the derivative of the binding energy, $t_{\rm ref}$ and $\Phi_{\rm ref}$ are integration constants, and $v_{\rm ref}$ is an arbitrary reference velocity. Different PN treatments emerge from the freedom to handle the right-hand side of Eq. (3.9) via distinct approaches, provided that the correct order of the expansion is maintained. However, the expressions $\mathcal{F}$ and E are indispensable for any PN calculation. Recent advances have yielded energy up to fourth-PN (4PN) order and gravitational waveform and flux expressions up to 4.5PN order [109]. Substituting these refined energy and flux expressions into Eqs. (3.9) and (3.10) yields a rigorous formulation for the phase's time evolution. Waveforms developed through this approach belong to the so-called TAYLOR family [144]. These time-domain PN models can accurately describe early inspiral dynamics but are impractical for large-scale GW searches in noisy data and for parameter estimation.

The stationary phase approximation[12] (SPA) provides an approach to convert slowly evolving PN

[11]The adiabatic approximation assumes that the fractional change in orbital velocity per orbital period is negligibly small, implying a slow and gradual evolution of the orbit, cf. Eq.(1.69).

[12]The SPA approximates the Fourier transform of a slowly evolving inspiral waveform by assuming that the dominant contribution arises from stationary points where the phase varies least rapidly. This is valid under the assumption of a slowly moving binary during the inspiral phase where $v^2/c^2 \ll 1$.

time-domain signals into closed-form frequency-domain expressions. These frequency-domain expressions facilitate GW searches and data analysis. Under this approximation, Eqs. (3.9) and (3.10) can be equivalently written as [144]

$$\frac{d\Psi}{df} = 2\pi t, \tag{3.13}$$

$$\frac{dt}{df} = -\frac{\pi M_{\rm tot}^2}{3v^2}\frac{E'(f)}{\mathcal{F}(f)}, \tag{3.14}$$

enabling the computation of Fourier-transformed PN waveforms. One of the most commonly used frequency-domain models is the TaylorF2 model which is given in the SPA approximation as

$$\tilde{h}_{\rm SPA}(f) = \mathcal{A} f^{-7/6} \exp^{-i\Psi(f)}, \tag{3.15}$$

where $\mathcal{A}$ corresponds to the amplitude and Ψ is the GW phase in the frequency domain [144]. This waveform is characterized by a fully analytical frequency-domain representation, which enables exceptionally efficient computation. Nevertheless, as the binary system nears the last stable orbit before the merger, nonlinear effects start to dominate, thereby diminishing the accuracy and applicability of PN treatments.

EOB waveforms: To address the limitations of the PN approach, the EOB formalism was developed [142, 191, 143]. Central to this approach is the idea to transform the relativistic two-body problem, up to the highest available PN order, into an equivalent one-body problem with a reduced mass μ in an effective background metric, $g^{\rm eff}_{\mu\nu}$. In polar coordinates (r, ϕ), the EOB metric takes the form [144]

$$ds^2_{\rm eff} = g^{\rm eff}_{\mu\nu} dx^\mu dx^\nu = -A(r)dt^2 + \frac{D(r)}{A(r)}dr^2 + r^2(d\theta^2 + \sin^2\theta d\phi^2), \tag{3.16}$$

in which the coefficients $A(r)$ and $D(r)$ can be written as a Taylor expansion. The system's dynamics can be described with the Hamiltonian

$$H^{\rm real}(r, p_r, p_\phi) = \mu \hat{H}^{\rm real} = M_{\rm tot}\sqrt{1 + 2\eta\Big(\frac{H^{\rm eff} - \mu}{\mu}\Big)}, \tag{3.17}$$

in which p_r and p_ϕ represent the conjugate momenta, μ is the reduced mass as introduced in Subsec. 1.3.3, η refers to the symmetric mass ratio and is related to the effective Hamiltonian given as [142, 191]

$$H^{\rm eff}(r, p_r, p_\phi) \equiv \mu\sqrt{A(r)\left[1 + \frac{A(r)}{D(r)}p_r^2 + \frac{p_\phi^2}{r^2} + 2(4-3\eta)\eta\frac{p_r^4}{r^2}\right]}. \tag{3.18}$$

Solving the Hamiltonian system

$$\frac{dr}{d\hat{t}} = \frac{\partial \hat{H}^{\rm real}}{\partial p_r}(r, p_r, p_\phi), \tag{3.19a}$$

$$\frac{d\phi}{d\hat{t}} = \frac{\partial \hat{H}^{\rm real}}{\partial p_\phi}(r, p_r, p_\phi), \tag{3.19b}$$

$$\frac{dp_r}{d\hat{t}} = -\frac{\partial \hat{H}^{\rm real}}{dr}(r, p_r, p_\phi), \tag{3.19c}$$

$$\frac{dp_\phi}{d\hat{t}} = \hat{\mathcal{F}}_\phi(r, p_r, p_\phi), \tag{3.19d}$$

in which $\hat{H}^{\text{real}}$ refers to the dimensionless Hamiltonian introduced in Eq. (3.17), $\hat{t} = t/M_{\text{tot}}$, and $\hat{\omega} \equiv d\phi/d\hat{t}$, yields the orbital motion of the binary constituents. To derive the EOB waveform, it is essential to incorporate the dissipative effects associated with gravitational radiation when mapping the orbital dynamics to the emitted multipolar waveform. These effects are encoded in the radiation reaction force $\hat{\mathcal{F}}_\phi$, which drives the loss of angular momentum due to GW emission. The radiation reaction provides a self-consistent coupling between the conservative dynamics, governed by the effective Hamiltonian, and the emitted radiation, enabling the binary to inspiral and merge. To enhance the physical accuracy of the resulting waveforms, the EOB formalism can be further refined by calibrating its parameters to NR waveforms. Depending on the approach taken to compute the Hamiltonian H^{eff} and the coefficients in Eq. (3.16), there are two types of EOB waveforms: TEOBResum and SEOBNR.

A key model for the studies presented in this work is SEOBNRv4_ROM_NRTidalv2. SEOBNRv4 is a calibrated waveform model for spinning, non-precessing BBHs, developed using perturbation theory waveforms and NR simulations [118]. This model extends to higher positive aligned spins and more spin-asymmetric configurations compared to previous versions. By incorporating an NRTidal description, as detailed below, the BBH model is extended to a BNS model. For fast and efficient waveform generation, a reduced order model (ROM) was constructed for this model [522].

Phenomenological waveforms: While EOB models are more physically grounded, their computational cost makes them inefficient for GW data analysis, which requires generating millions of waveforms. Phenomenological models address this limitation by utilizing analytically motivated approaches, calibrated to NR waveforms, enabling significantly faster waveform generation. Central to this approach is the decomposition of the gravitational waveform[13]

$$\tilde{h} = \tilde{A}(f)e^{-i\psi(f)}, \tag{3.20}$$

into the amplitude $\tilde{A}(f)$ and the phase $\psi(f)$ and to construct different approaches for the inspiral (insp), intermediate (int), and merger-ringdown (MR) regime in respective frequency domains[14]:

$$\tilde{h}(f) = \begin{cases} \tilde{A}_{\text{insp}}(f)\, \exp[-i\psi_{\text{insp}}(f)] & f < f_1, \\ \tilde{A}_{\text{int}}(f)\, \exp[-i\psi_{\text{int}}(f)] & f_1 \leq f \leq f_2, \\ \tilde{A}_{\text{MR}}(f)\, \exp[-i\psi_{\text{MR}}(f)] & f > f_2. \end{cases} \tag{3.21}$$

Whereas $\tilde{A}_{\text{insp}}$ and ψ_{insp} are modeled on PN/EOB expansions at low frequencies in the early inspiral, $\tilde{A}_{\text{MR}}$ and ψ_{MR} are fitted to NR waveforms at high frequencies in the late inspiral, merger, and ringdown stages. An intermediate or transition segment of $\tilde{A}_{\text{int}}$ and ψ_{int} ensures continuity and smoothness in amplitude and phase at the matching frequencies. Similarly, the phase is modeled using a decomposition motivated by the PN expansion of the GW phase for quasi-circular binaries in the frequency domain. This decomposition of the phase

$$\psi(f) = \psi_{\text{PP}}(f) + \psi_{\text{SO}}(f) + \psi_{\text{SS}}(f) + \psi_{\text{T}}(f) + \ldots, \tag{3.22}$$

captures distinct physical contributions such as the non-spinning point-particle dynamics ψ_{pp}, spin effects such spin-orbit ψ_{SO} and spin-spin ψ_{SS} contributions, and tidal interactions ψ_{T}.[15] Higher-order spin contributions, including cubic-in-spin terms, as well as spin–tidal coupling effects, are not incorporated in this decomposition, but may be incorporated in extended PN frameworks to improve the accuracy of the phase model.

This piecewise construction is the foundation of phenomenological IMR waveform models, or so-called IMRPhenom models, which have the advantage that these templates are computationally

[13] Note that this thesis focuses on frequency-domain phenomenological models.

[14] cf. Figure 4 in [349].

[15] For BBH coalescences, tidal effects are zero and do not necessitate the inclusion of tidal phase contributions. In contrast, tidal contributions become significant when at least one NS is present in a CBC.

fast to generate, thus ideal for large-scale data analysis and parameter-estimation studies. Different phenomenological models have been developed including IMRPhenomB [46], IMRPhenomC [574], IMRPhenomD [322, 349], IMRPhenomP [297], IMRPhenomXAS [511], IMRPhenomXHM [273], and IMRPhenomXP [512]. For the purpose of this work, more focus will be given to the model IMRPhenomD.

IMRPhenomD describes non-precessing BBH coalescences throughout the different stages mentioned above [322, 349]. The amplitude is constructed by deriving the inspiral amplitude from a re-expanded SPA amplitude, the MR amplitude is modeled as a Lorentzian around the main ringdown frequency, and the intermediate amplitude is modeled as a four-degree polynomial function [322]. The PP phase, $\psi_{\rm pp}$, in IMRPhenomD is based on the TaylorF2 phase, whereas spin-orbit contributions are included up to 3.5 PN order [119] and spin-spin contributions up to 2PN order [61, 444]. Furthermore, IMRPhenomD includes information obtained from the SEOBNRv2 model [626] in the early inspiral stage, while the intermediate and merger-ringdown regime is informed through NR simulations.

NRTidal models: BBH systems do not require the incorporation of matter effects. However, when a NS is involved, these effects impart additional signatures in GW signals as illustrated in Figure 2.4 in Subsec. 2.2.2. Consequently, phenomenological waveform models for BBHs can be enhanced by incorporating tidal contributions. This augmentation is expressed as

$$\tilde{h}^{\rm Tidal} = \tilde{h}^{\rm PP} \cdot (\tilde{A}^{\rm NRTidal} e^{-i\psi^{\rm NRTidal}}), \tag{3.23}$$

and facilitates the modeling of gravitational waveforms from BNS and NSBH mergers through the NRTidal framework introduced in [213]. The main idea is to derive a closed-form approximation for the tidal phase contribution $\psi_{\rm T}$ in Eq. (3.22), calibrated to NR simulations obtained with different EOSs.[16] The non-spinning tidal effects appear in the GW phase at 5PN order. Beyond this, analytical progress has led to partial results extending to 7.5PN [195] and beyond, especially in the context of dynamical tides [615]. For the example of IMRPhenomD_NRTidalv2 [322, 349, 626, 210, 213, 212], the tidal phase contribution can be obtained through

$$\psi_T(x) = -\kappa^T_{\rm eff} \frac{39}{16\eta} x^{5/2} \tilde{P}_{\rm NRTidalv2}(x), \tag{3.24}$$

in which $\kappa^T_{\rm eff}$ refers to the effective tidal coupling constant and describes the dominant tidal and mass ratio effects, $x = \hat{\omega}^{2/3}$, whereas $\hat{\omega} = M_{\rm tot}\omega$ is the dimensionless GW frequency with $M_{\rm tot}$ being the total mass , and $\tilde{P}_{\rm NRTidalv2}$ is the Padé approximant. The effective tidal coupling constant is related to the mass-weighted tidal deformability through $\tilde{\Lambda} = 16/3 \cdot \kappa^T_{\rm eff}$ [212]. While the GW phase is crucial for extracting binary properties, accurate amplitude modeling is important and requires a correction, which for NRTidalv2 takes the form [212]

$$\tilde{A}_T^{\rm NRTidalv2} = -\sqrt{\frac{5\pi\eta}{24}} \frac{9M_{\rm tot}^2}{D_L} \kappa^T_{\rm eff} x^{13/4} \frac{1 + \frac{449}{108}x + \frac{22672}{9}x^{2.89}}{1 + d\,x^4}, \tag{3.25}$$

in which d is obtained by fitting. The recent NRTidalv3 model is based on a larger set of NR BNS waveforms including various total masses, EoSs, and mass ratios, includes a mass-ratio dependence of the fitting parameters in the calibrated model, and incorporates dynamical tides (cf. [2] and references therein).

[16] In addition to the tidal phase contribution, also spin effects entail information about the EOS because that part of the phase depends on the spin-induced quadrupole and, hence, need to be considered for an accurate description [298]. However, the NS's spin is small enough that the tidal deformability often provides the dominant EOS imprint.

3.2 Electromagnetic signatures

Compact binary mergers involving at least one NS can generate a range of EM signals due to the extreme energies and matter dynamics involved. The formation of ultra-relativistic jets can produce GRBs, while the interaction of these jets with the ambient medium gives rise to broadband afterglow emission. Furthermore, the ejection of neutron-rich material during the merger powers an EM transient known as a kilonova. The physical mechanisms underlying these transients will be discussed in detail in the following subsections.

3.2.1 Gamma-ray bursts and afterglows

GRBs are among the most energetic astrophysical phenomena, characterized by intense EM emission spanning energy ranges from tens of keV to several MeV [680]. The initial release of energy, predominantly in hard X-rays and soft γ-rays, is commonly termed as *prompt emission*. This phase is followed by a prolonged, gradually decaying *afterglow emission*, which extends across the entire EM spectrum and persists over timescales ranging from days to years.
GRBs are broadly categorized into two classes based on their observed duration[17] of the prompt emission: *short-duration GRBs* (≤ 2 seconds) are thought to originate from compact binary mergers (BNS or NSBH), whereas *long-duration GRBs* (≥ 2 seconds) are typically associated with core-collapse of massive stars [669, 487, 10].[18] In both scenarios, a compact object surrounded by a massive accretion disk launches a GRB jet through the Blandford–Znajek mechanism [114], extracting rotational energy from a magnetized BH to power the prompt and afterglow emission. This energy extraction mechanism is considered to be an important component of central engine models that power GRBs and provides the energy reservoir for the relativistic outflows described by the so-called *fireball model*[19], which is illustrated in Figure 3.4. In this broad conceptual framework, a GRB is described as an ultra-relativistic outflow or blastwave, regardless of the progenitor system (compact binary merger or massive star collapse) or GRB classification (short or long) as indicated in Figure 3.4. Central to this idea is the formation of a compact object as central engine (in most cases a newly formed BH or a rapidly spinning magnetar) surrounded by an accretion disk, which launches an ultra-relativistic jet into the surrounding ambient medium giving rise to the prompt emission and afterglow. From a theoretical perspective, GRB prompt emission and afterglow are distinguished based on the physical regions where radiation is produced. However, in practice, differentiating between internal and external emission is difficult [680]. The fireball model continues to serve as a general theoretical framework for understanding key features of GRBs[20], including both the prompt emission and the extended afterglow. However, over time, it has been progressively refined through additional theoretical developments.

Prompt emission: Following the formation of a central engine after a compact binary merger or the collapse of a massive star, a portion of the released energy is emitted as GWs and neutrinos, while another fraction is converted through accretion onto the central engine into an ultra-relativistic outflow of photons and baryons, forming a collimated jet. As relativistic outflows are launched with variability in their Lorentz factors, faster ejecta shells will catch up with slower ones, creating collisions or internal shocks within the outflow. Internal shocks convert kinetic energy into high-energy

[17]The duration or T_{90} statistic is defined as the time interval between the epochs when 5% and 95% of the total fluence is detected, with main limitations being due to detector energy bandpass and sensitivity.

[18]For short GRBs, $T_{90} < 2$ s, with an average $T_{90} \sim 0.5$ s, while for long GRBs $T_{90} > 2 - 3$ s with an average of $T_{90} \sim 30$ s. However, the origins of sGRBs and lGRBs remain uncertain, with observations like GRB 211211A challenging this classification, cf. Chapter 8.

[19]The *fireball* paradigm was first proposed by Mészáros & Rees [433] and Waxman & Piran [659] in the early 1990s to account for the extremely high-energy and non-thermal spectra observed in GRBs.

[20]cf. [276] for a recent review.

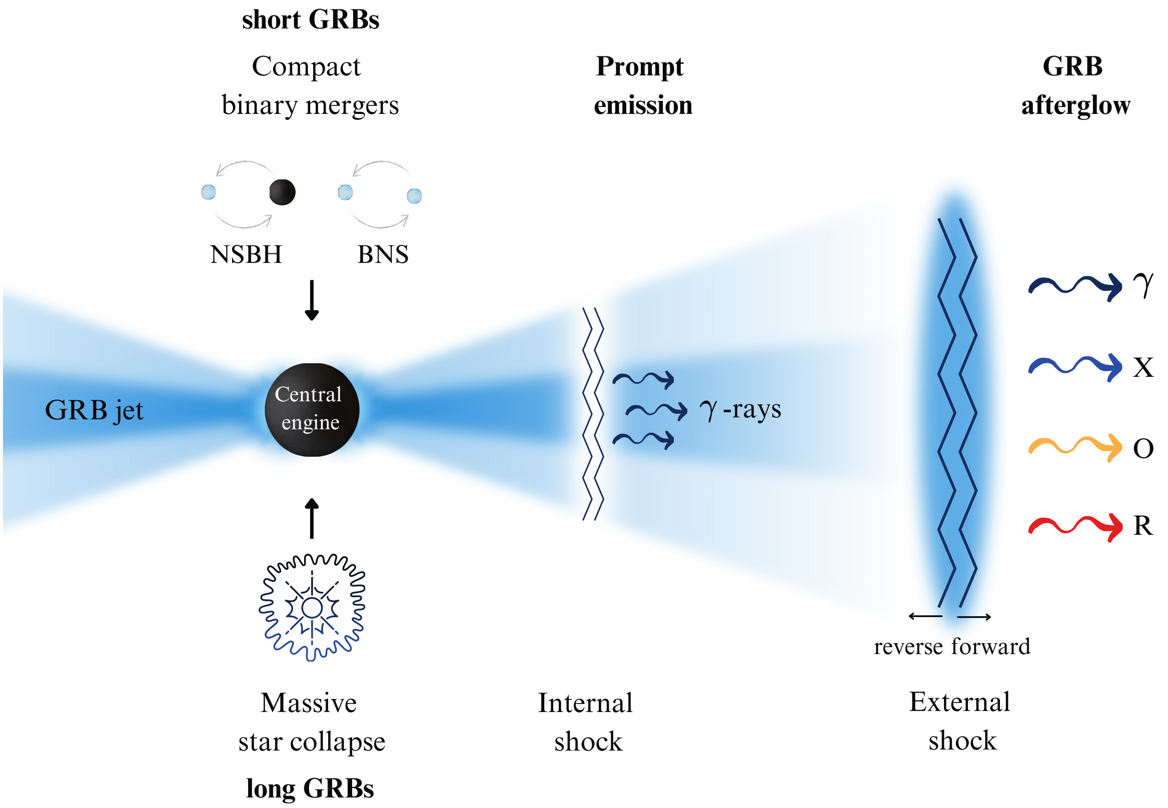

FIGURE 3.4
Illustration of the two main GRB classes and hypothesized progenitors in the framework of the *fireball model*. Short GRBs are typically associated with compact binary mergers, while long GRBs are connected to massive star collapses. In both cases, the accretion of matter onto a newly formed central engine powers the GRB jet released into the surrounding ambient medium. The internal shock produces γ-rays as part of the prompt emission, and the external shock produces the GRB afterglow ranging from γ-rays and X-rays to optical (O) and radio (R) waves. Own illustration oriented towards [433, 275].

photons, producing high-energy photons that manifest as the initial spikes in the prompt emission. Consequently, prompt-emission light curves exhibit highly irregular temporal structures with complex observational features [680]. To this day, the driving mechanisms that produce the highly variable prompt emission remains poorly understood and an active research area. A number of alternative models have been proposed to explain the prompt emission [220, 339, 227, 91, 147], indicating that the prompt emission could be multi-component or dominated by different physical processes.

After the prompt gamma-ray emission, many GRBs exhibit a prolonged plateau phase in their X-ray afterglow (cf. Figure 3.1). Two leading explanations for this plateau involve either (i) extended energy injection from the central engine [474, 681] or (ii) spin-down of a newly formed magnetar that transfers rotational energy to the expanding shock [189, 683, 439]. Once the plateau phase ends, the afterglow light curve typically transitions to a steeper decay consistent with standard GRB afterglow modeling.

GRB afterglow: Unlike the prompt emission, the GRB afterglow is more comprehensively understood and can be modeled by describing the dynamics of a relativistic blast wave interacting with the circumburst medium. As it decelerates, the blast wave shocks the surrounding matter, requiring a treatment based on relativistic shock physics. Across the non-magnetized shock front, three conservation laws govern the physical condition of the shocked plasma: baryon number, energy, and momentum fluxes. These conservation equations can be reduced into a system of equations (cf. Eqs. (35-37) in [369], see also [113, 543]), which can be solved to describe relativistic shocks propagating into the upstream medium. During the deceleration phase, two shocks form: a *forward shock* (FS) propagating into the external medium and a *reverse shock* (RS) propagating backward into the ejecta (cf. Figure 3.4). Multi-wavelength observations of GRB afterglows suggest that their dominant emission component arises from the external forward shock, exhibiting a broadband spectrum described by a broken power law [680].[21] Particles, primarily electrons and protons, that are accelerated within these shock fronts, produce intense, broadband, non-thermal radiation via synchrotron emission at the shock front. The flux at the peak of the spectrum is given as [369]

$$f_{\nu,\max} = \frac{(1+z)L'_\nu \Gamma}{4\pi D_L^2} \approx \frac{N_{\rm tot} P'_{\nu,\max}\Gamma}{4\pi D_L^2}, \tag{3.26}$$

in which L'_ν is the luminosity in the jet comoving frame, Γ is the Lorentz factor, $N_{\rm tot}$ is the total number of electrons contributing to radiation at frequency ν, and the power radiated per unit frequency for one electron at the peak of the spectrum is given as

$$P'_{\nu,\max} \approx \frac{\sqrt{3}q^3 B'}{m_e c^2}, \tag{3.27}$$

in which B' refers to the magnetic field strength, and q denotes the particle charge, and m_e denotes the electron mass. The synchrotron-emitting electrons produce a broadband (radio to X-ray) spectrum characterized by a multi-segment broken power law. The deceleration of the relativistic outflow causes temporal softening and fading, resulting in an afterglow with power-law decay across wavelengths. The flux density can be characterized as

$$F_\nu(t,\nu) \propto t^{-\alpha}\nu^{\beta}, \tag{3.28}$$

in which α denotes the temporal decay index and β refers to the spectral index. A comprehensive GRB afterglow model necessitates a detailed description of the blast wave, including the FS, RS, and the contact discontinuity separating them. Emission from the RS is calculated similarly to the FS, with their relative contributions depending on the microphysical parameter ratios and the Lorentz factors of both shock fronts [355, 682, 461]. In addition, synchrotron self-Compton (SSC) processes can be significant in modeling GRB afterglows, as synchrotron photons generated by a population of electrons may be scattered to higher energies by the same electrons. This mechanism can produce an additional high-energy bump in the GRB flux. More generally, inverse Compton scattering, including SSC and external Compton contributions, plays an important role in shaping the high-energy afterglow emission.

GRB jet breaks and structures: Observational evidence indicates that GRB outflows are collimated, as initially proposed by Rhoads [544], based on the detection of *jet break* in numerous afterglow light curves. The subsequent steepening of the light curve following a jet break is generally attributed to two principal effects: the edge effect and the sideways expansion effect [545, 506]. For a tightly collimated outflow, the bulk Lorentz factor Γ initially satisfies $\Gamma \gg 1/\theta_j$, where θ_j is the half-opening angle, so that the emission is beamed. As the jet decelerates over time, Γ drops to $\sim 1/\theta_j$ at the so-called jet break time. When $\Gamma < 1/\theta_j$, the observer will be able to see the jet's lateral extent. This transition alters the radiation emission, leading to a noticeable change in the afterglow's decay rate, characterized by a steeper temporal index in Eq. (3.28) with $\alpha_2 > \alpha_1$. Additionally, as the jet undergoes lateral expansion, varying in degree across models, the energy per solid angle directed toward the observer decreases. Combined with changes in relativistic beaming, this results in a sharp

[21] Note that in the early afterglow phase, the afterglow is not only the external shock emission, but a superposition of multiple emission components. These include the external forward shock, the external reverse shock and an internal dissipation site launched due to late central engine activities [680].

drop in observed flux, known as a *jet break* in the afterglow light curve observed across multiple wavelengths.

The jet break is sensitive to the jet structure. If the jet has a structured energy or angular profile (i.e., a "structured jet"), the jet break transition can manifest differently, possibly leading to multiple breaks or a smoother light-curve evolution. Previous numerical simulations indicate that jet angular energy distributions often exhibit a structured profile, characterized by a highly energetic core surrounded by power-law wings (cf. Figure 1 in [566]). In this context, the structured jet is a GRB jet model in which the isotropic equivalent energy of the blast wave, $E_{\rm iso}$, is a function of the angle from the jet axis: $E_{\rm iso} = 4\pi dE/d\Omega \equiv E(\theta)$ [566]. GRB jet structures are commonly approximated using uniform Top-Hat jets, Gaussian jets and power-law distributions, characterized by a smoothly varying core, expressed as [566]

$$E(\theta) = E_0 \exp\Big(-\frac{\theta^2}{2\theta_c^2}\Big) \qquad \text{Gaussian,} \tag{3.29a}$$

$$E(\theta) = E_0 \Big(1 + \frac{\theta^2}{b\theta_c^2}\Big)^{-\frac{b}{2}} \qquad \text{Power law,} \tag{3.29b}$$

in which each model is parametrized by a normalization E_0, a width θ_c, and a power law index b.[22] The structure of the GRB jet is still an active field of research, but is thought to depend on the jet-launching mechanism and on modifications by the sculpting that occurs as the jet burrows out of the surrounding ejecta debris. Overall, extensive examinations of GRB afterglows and jet structures provide insights into the progenitor and its environment, jet properties and the microphysics of collisionless shocks.

3.2.2 Kilonovae

Kilonovae or macronovae are rapidly evolving, luminous astronomical transients powered by the radioactive decay of heavy elements synthesized in BNS or NSBH mergers. The existence of these thermal transient events was first introduced by Li and Paczynski [394], who proposed that rapid neutron capture in the merger ejecta [387, 229, 262] would lead to radioactive decay, producing a detectable EM transient [366, 436, 549]. In 2017, the first multi-messenger observation of a BNS merger including a kilonova, AT2017gfo [11, 185], provided compelling evidence that BNS mergers are key sites of the rapid neutron-capture process (r-process) nucleosynthesis.[23]

Kilonova modeling: Kilonova modeling necessitates a comprehensive multiphysics approach, integrating (i) hydrodynamics to track the evolution and expansion of merger ejecta, (ii) nuclear heating from r-process radioactive decay, and (iii) radiative transfer to predict emergent light curves and spectra. However, the fundamental physics underlying kilonovae can be derived from first principles and analytical astrophysical considerations, as demonstrated in [436, 435].

Consider ejecta with mass $M_{\rm ej}$ expanding spherically[24] at a constant mean velocity v following a merger. The ejecta propagate into the surrounding medium, reaching a radial extent of $R \approx vt$. In the immediate vicinity of the merger, the ejecta remains extremely hot, with a high optical depth inhibiting the escape of thermal radiation. Consequently, repeated photon interactions thermalize the spectrum, resulting in an emission profile that approximates a blackbody. The optical depth and

[22] This notation is adopted in the GRB afterglow model `afterglowpy` [651, 566], which is utilized for the multi-wavelength analysis presented in Chapter 8.

[23] First kilonova detections associated with GRB observations include. for instance, GRB 060614 [677], GRB 080503 [500], and GRB 130603B [624, 95].

[24] Spherical symmetry provides a reasonable first-order approximation, as the ejecta undergo substantial lateral expansion from the merger scale to the kilonova emission peak. Observational studies of the kilonova transient AT2017gfo support this assumption, revealing a high degree of sphericity based on the blackbody-like nature of its spectrum [608, 607].

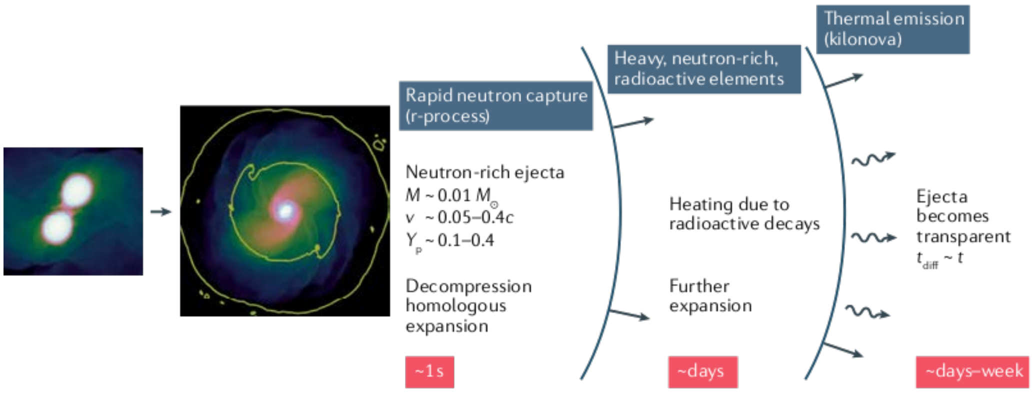

FIGURE 3.5
The kilonova scenario [436]: Neutron-rich, ultra-dense merger ejecta ($M_{\rm ej} \sim 0.01\ M_\odot$), initially dissociated into individual neutrons and protons (proton fraction $Y_p \sim 0.1 - 0.4$), undergo rapid expansion ($v \sim 0.05 - 0.4c$) upon ejection from the merger site. Rapid neutron capture onto newly formed light seed particles proceeds during the first second of expansion, while the ejecta quickly lose internal energy owing to adiabatic expansion. Radioactive decay of neutron-rich nuclei created by the r-process heats material at late times and leads to thermal emission once the photon-diffusion timescale becomes comparable to the expansion timescale ($t_{\rm diff} \sim t$), on a timescale of days to a week. Simulation snapshots show a BNS merger with dynamical ejecta indicated by yellow contours. Image from [597].

photon diffusion timescale in this regime are given by [435]

$$\tau \simeq \rho\kappa R = \frac{3M_{\rm ej}\kappa}{4\pi R^2}, \tag{3.30a}$$

$$t_{\rm diff} \simeq \frac{R}{c}\tau = \frac{3M_{\rm ej}\kappa}{4\pi c R} = \frac{3M_{\rm ej}\kappa}{4\pi c v t}, \tag{3.30b}$$

in which $\rho = 3M_{\rm ej}/(4\pi R^3)$ is the mean density and κ is the opacity. As the ejecta expand, the time required for photons to diffuse out decreases over time, following $t_{\rm diff} \propto t^{-1}$. Eventually, radiation can escape on the same timescale as the expansion, when $t_{\rm diff} = t$ [59].[25] This marks the characteristic time, $t_{\rm peak}$ at which the kilonova light curve reaches its peak defined as

$$t_{\rm peak} = \sqrt{\frac{3M_{\rm ej}\kappa}{4\pi\beta v c}}, \tag{3.31}$$

Assuming ideal blackbody radiation, the temperature of the thermal emission is expressed as

$$T_{\rm eff} = \left(\frac{L_{\rm tot}}{4\pi\sigma R_{\rm ph}^2}\right)^{1/4}, \tag{3.32}$$

in which $L_{\rm tot}$ is the total luminosity summed over all mass shells and $R_{\rm ph}$ is the radius of the photosphere. The source's flux density at a photon frequency ν is then given as

$$F_\nu(t) = \frac{2\pi h\nu^3}{c^2}\frac{1}{\exp[h\nu/kT_{\rm eff}(t)] - 1}\frac{R_{\rm ph}^2(t)}{D_L^2}, \tag{3.33}$$

in which D_L is the luminosity distance. Given that the ejecta are at least heated by the radioactive decay of heavy r-process nuclei, the peak luminosity can be expressed as

[25] The transparency timescale, governed by the diffusion timescale, is critically dependent on the opacity of the ejecta to its radiation, a quantity which comes along with great uncertainty [555, 130].

$$L_{\rm peak} \approx M_{\rm ej}\dot{e}(t_{\rm peak}) \approx 10^{41}{\rm erg\ s}^{-1}\left(\frac{\epsilon_{\rm th,v}}{0.5}\right)\left(\frac{M_{\rm ej}}{10^{-2}M_\odot}\right)^{0.35}\left(\frac{v}{0.1c}\right)^{0.05}\left(\frac{\kappa}{1{\rm cm}^2{\rm g}^{-1}}\right)^{-0.65}, \tag{3.34}$$

in which $\dot{e}$ is the specific heating rate and $\epsilon_{\rm th}$ is the thermalization efficiency. Considering the broad range of parameter values in BNS and NSBH mergers with ejecta masses ranging from $M_{\rm ej} \sim 10^{-3} - 0.1M_\odot$, opacities of $\kappa \sim 0.5 - 30$ cm^{2}g^{-1}, and velocities of $v \sim 0.1 - 0,3c$, the peak luminosities from r-process heating can vary within $L_{\rm peak} \approx 10^{39} - 10^{42}$erg s^{-1} [435].

r-process nucleosynthesis: The emission observed from kilonovae is fundamentally linked to r-process nucleosynthesis, which plays a crucial role in the formation of heavy elements such as gold, platinum, and uranium. While elements up to iron originate in stellar cores and SNe, heavier elements are primarily synthesized through the r-process. Acting as a cosmic factory for the heaviest elements, this process occurs in extreme neutron-rich environments, where rapid neutron capture exceeds β-decay timescales. Burbidge et al. [145] and Cameron [150] proposed that nearly half of these heavy elements form under such conditions, producing neutron-rich isotopes essential to cosmic abundances. The feasibility of r-process nucleosynthesis is governed by the electron fraction, Y_e, a key parameter defined as

$$Y_e \equiv \frac{n_p}{n_n + n_p}, \tag{3.35}$$

in which n_p and n_n denote the number densities of protons and neutrons, respectively. In typical stellar environments, ordinary matter has more protons than neutrons ($Y_e \geq 0.5$), whereas neutron-rich conditions ($Y_e < 0.5$) are generally necessary for the r-process to occur [435]. The proton fraction is highly sensitive to neutrino interactions, which are governed by neutrino radiation transport dynamics within the astrophysical environment where r-process nucleosynthesis occurs.[26] Neutron capture terminates once free neutrons are depleted, leaving behind neutron-rich nuclei that undergo radioactive decay into stable isotopes, depositing energy into the expanding ejecta.[27] The resulting release of nuclear binding energy, occurring across a broad range of decay timescales, follows a power-law heating rate scaling with $t^{-1.3}$. This energy deposition drives kilonova emission and becomes directly observable at the peak luminosity time, $L(t_{\rm peak}) = L_{\rm peak}$. Therefore, kilonova emission depends on the composition of synthesized r-process nuclei, making it a diagnostic of the merger's initial conditions including outflow velocity, ejected mass, and proton fraction.

Sources of neutron-rich ejecta: In both BNS and NSBH mergers, kilonova emission is primarily powered by two distinct ejecta components: the dynamical tidal ejecta and the post-merger outflows from the remnant accretion disk [249, 592]. Unlike NSBH mergers, BNS mergers are also expected to generate shock-driven ejecta in the polar region and winds from the disk can contribute the ejecta mass budget (cf. Table 2 in [435]). Figure 3.6 illustrates the various ejecta components in a BNS merger and presents the associated kilonova emission across different timescales.
The tidal ejecta are expelled dynamically into the orbital plane on millisecond timescales, driven by tidal forces [84, 389] or compression-induced heating at the interface of the merging bodies [314, 84]. The amount of tidal tail ejecta is sensitive to the total binary mass, mass ratio, EOS, and NS spin[28] and ranges for BNS mergers between 10^{-4}–10^{-2} $M_\odot$ with velocities of 0.1–$0.3c$ [314, 527, 125].[29] The expelled neutron-rich ejecta ($Y_e \lesssim 0.25$) undergo r-process nucleosynthesis, producing lanthanide-rich material with high opacities in optical and UV wavelengths. This leads to (near-)infrared-dominated

[26] Neutrino radiation transport schemes are part of sophisticated NR codes [561, 557, 265, 579] and hence provide important information for kilonova modeling.
[27] Radioactive heating is driven by a combination of β-decays, α-decays, and fission processes, as described in [436, 78, 316].
[28] Studies of [211, 228, 452] have shown that NSs with high-spins can also enhance the amount of dynamical tidal ejecta.
[29] For NSBH mergers, the dynamical ejecta mass can range up to ~ 0.1 $M_\odot$ for similar velocities [373, 258].

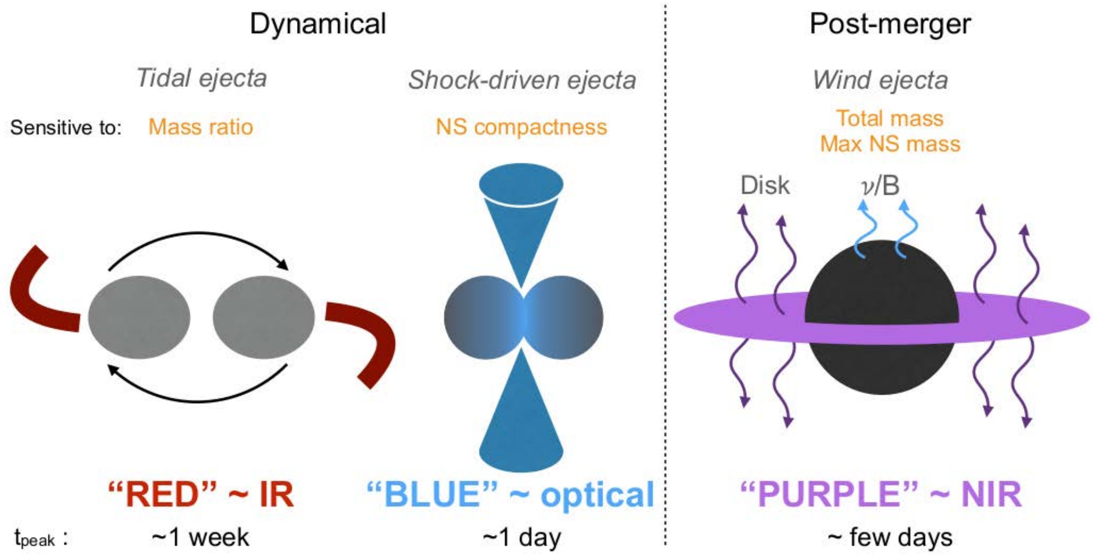

FIGURE 3.6
A schematic representation of ejecta sources in BNS mergers, occurring during or after the merger, along with the corresponding kilonova emission components observed across different timescales. Image taken from [470].

emission, corresponding to the red component of the kilonova light curve peaking on a timescale of a week. A higher mass asymmetry in the binary system ($q \ll 1$) results in an increased production of lanthanide-rich, red kilonova ejecta [556, 84, 389].

Following the merger, an accretion disk forms around the remnant, occurring in all BNS mergers and in NSBH mergers when tidal disruption takes place outside the BH horizon. The amount of disk mass depends on the total mass, the mass ratio, the EOS, and the spins of the binary components [476] and can range between $\sim 0.01 - 0.3\ M_\odot$. At early times, the accretion rate of the disk is high and mass loss is driven by neutrino heating. If the NS remnant lasts longer than ~ 50 ms, enhanced neutrino emission can eject $\sim 10^{-3}\ M_\odot$, with stronger magnetic fields potentially increasing this ejecta [207, 498, 441]. On timescales of days, accretion disk winds can become the dominant contributor to the ejecta mass budget, provided the remnant mass remains sufficiently low. These winds can exhibit a broad range of opacities, from high to low, with intermediate values sometimes referred to as 'purple' opacity [470].

The "blue" kilonova emission in Figure 3.6 is associated with less neutron-rich, high-Y_e, lanthanide-poor shock-heated ejecta, characterized by lower neutron abundances ($Y_e \gtrsim 0.30$) [438, 498]. Low-opacity outflows, typically concentrated in the polar regions due to dynamical ejection or disk-driven winds [445], likely correspond to the blue kilonova component, originating from hot, fast dynamical ejecta and winds driven by neutrino radiation and magnetic fields from a short-lived hypermassive NS [342, 653, 174]. The quantity of high-Y_e ejecta increases when BH formation is substantially delayed, as the prolonged NS lifetime sustains a high neutrino luminosity, enhancing proton-rich material ejection. Hence, in polar regions light r-process elements are produced, which are related to shock-heated dynamical ejecta and winds from a post-merger remnant, as well as from the accretion disk. For the case of AT2017gfo, the early blue emission is mainly attributed to shock-driven ejecta, while the long-lived redder emission to the disk wind ejecta [471].

Overall, the total kilonova emission can be thought of as a combination of the distinct blue and red components, since both high- and low-Y_e components can be visible after merger, while the ratio of the observed fluxes for both components depends on the observer's viewing angle. While it is also common practice to model these components separately, this will propagate quantitative errors onto the inferred ejecta properties [342, 668].

Astrophysical sites of r-process nucleosynthesis: The astrophysical environments responsible for the r-process nucleosynthesis remain one of the most enduring mysteries in nuclear astrophysics. Apart from BNS mergers and NSBH mergers, CCSNe have long been considered a potential site for r-process nucleosynthesis. More specifically, *collapsars*, resulting from the collapse of rapidly rotating massive stars, are associated with long GRBs and broad-lined type Ic (SN Ic BL) SNe, characterized by hydrogen and helium deficiency and broad spectral lines [405]. These systems may synthesize r-process elements through accretion disk processes analogous to those observed in post-merger environments [598]. Unlike post-merger disks, collapsar disks originate from neutron–proton balanced material. At high accretion rates, electron degeneracy induces proton-to-neutron conversion via electron capture [90], maintaining a low proton fraction ($Y_p \sim 0.1$) [599, 172]. This process drives neutron-rich outflows capable of synthesizing the full range of r-process elements, with abundances dependent on the progenitor's structure and rotational profile [172, 440].

An alternative scenario involves magnetorotational or jet-driven CCSNe, where a magnetic jet accelerates neutron-rich material from the proto-NS, a process often associated with hyper-energetic broad-lined Type Ic SNe [151, 666]. This process requires magnetar-strength magnetic fields and millisecond rotation periods [472, 295], while jet instabilities [372, 475], especially with weaker fields, may limit nucleosynthesis to lighter r-process elements [295, 539].

In addition, recent studies [159, 496, 495] provide evidence that magnetar giant flares can produce r-process elements by shock-heating and ejecting NS crustal material. In particular, observations of a hard gamma-ray signal following the giant flare SGR 1806-20 match predictions of r-process nucleosynthesis, indicating the synthesis of $\sim 10^{-6}\ M_\odot$ of heavy elements [495]. This confirms magnetar flares as an r-process site, potentially contributing 1–10% of the Galactic r-process element abundance, with significant implications for early Galactic chemical evolution [495].

3.2.3 Associations of gamma-ray bursts with supernovae and kilonovae

Although GRB duration serves as a preliminary classifier, certain cases remain ambiguous, with some long GRBs possibly originating from compact-object mergers and some short GRBs potentially linked to core-collapse events. Therefore, a definitive progenitor identification relies on establishing the presence of an associated SN or kilonova and ideally an associated GW signal.

Within the broader SN taxonomy, events arise either from core collapse in massive stars or from thermonuclear explosions of accreting white dwarfs. These subtypes are typically distinguished by spectroscopic signatures that reveal ejecta composition and kinematics. A definitive indicator of a GRB-associated SN is the appearance of characteristic SN features in the optical spectrum. So far, spectroscopically identified SNe associated with GRBs belong to broad-lined H/He-deficient SNe (Type Ic-BL SNe) (e.g. 1998bw (GRB 980425), 2003lw (GRB 031203), 2006aj (GRB 060218)) indicating high kinetic energies, although not all Type Ic SNs are linked to a GRB (e.g. 1994l, 1997ef, 2002ap) [680]. GRB-associated SNe exhibit significant diversity in peak luminosity, rise times, light-curve duration, and spectral line widths. A widely supported model attributing the emergence of both a GRB and a SN signature involves the formation of a millisecond magnetar during the collapse of a massive star [664, 670, 437, 367]. Extensive searches for SN emission associated with nearby short GRBs have been conducted, yet no confirmed detections have been reported to date [680]. GW observations of CCSNe could help to reveal or distinguish between the various explosion mechanisms, but their complexity makes parameter estimation challenging. Moreover, LIGO and Virgo have yet to detect such signals [21].

The multi-messenger observation of a BNS merger accompanied by a short GRB signal, GRB 170817A, and a kilonova, AT2017gfo, confirmed that short GRBs can be associated with compact binary mergers. Apart from AT2017gfo, further evidence for a kilonova was also claimed for GRB 060614 [677], GRB 080503 [500], and GRB 130603B [624, 95]. Kilonova transients fade over a few days, peaking in the optical/infrared on similar timescales, whereas SNe often require about a week or more to reach peak brightness. Kilonovae are also intrinsically fainter than GRB-associated SNe and exhibit a distinct redder color evolution due to the presence of heavy, lanthanide-rich r-process elements in the ejecta. Hence, systematic photometric and color evolution measurements over days to weeks allow for the distinction between the slower, brighter SN component and the more rapidly evolving, redder kilonova component.

Part III

Multi-messenger data analysis

4

Statistical and computational methods

CONTENTS

In probability theory, two fundamental paradigms shape statistical inference: the *Frequentist* and *Bayesian* approaches. Frequentist methods treat unknown parameters as fixed values, relying on repeated sampling to draw conclusions, whereas Bayesian inference represents uncertainty through probability distributions, treating parameters as random variables. This distinction is particularly significant in astrophysics, where many phenomena, such as BNS mergers, are rare and nonrepeatable. Bayesian methods naturally address this challenge by combining prior knowledge with data from new observations.

The rapid advancement of observational astrophysics, driven by GW detectors, satellites measuring high-energy radiation, and large-scale optical and radio surveys, has further underscored the necessity of Bayesian techniques. As data volume and complexity continue to grow, modern astrophysics increasingly relies on Bayesian statistical frameworks and advanced computational algorithms to extract meaningful insights. These methods facilitate the incorporation of prior knowledge, the exploration of high-dimensional parameter spaces, uncertainty quantification, and systematic model comparison, making them indispensable for interpreting the universe's most complex and transient phenomena.

At the core of Bayesian statistics lies Bayes' theorem, which establishes a formal framework for updating beliefs about a hypothesis in light of new information. Bayes' theorem serves as the foundation for two primary applications in statistical inference:

- hypothesis testing, and
- parameter estimation.

This chapter presents the fundamental principles of Bayesian statistics, including priors, likelihoods, and posteriors, which are essential for parameter estimation. It further examines their application in statistical model comparison and the computational techniques employed for parameter inference. These fundamental concepts are employed for Bayesian multi-messenger data analysis as demonstrated through the nuclear-physics and multi-messenger astrophysics framework `NMMA` presented in Chapter 5.

4.1 Bayes' theorem: likelihoods, priors, and posteriors

Attributed to Thomas Bayes, the Bayes' theorem follows directly from two fundamental building blocks: the definition of conditional probability and the mathematical relationship for determining the probability of a cause given an observed effect. For two events A and B in a probability space, the *conditional probabilities* of

$$A\,\text{given}\,B: \quad P(A|B) = \frac{P(A\cap B)}{P(B)} \quad \text{where } P(B) \neq 0, \text{ and} \tag{4.1a}$$

$$B\,\text{given}\,A: \quad P(B|A) = \frac{P(B\cap A)}{P(A)} \quad \text{where } P(A) \neq 0, \tag{4.1b}$$

allow to establish the relationship $P(A \cap B) = P(A|B)P(B) = P(B|A)P(A)$ from which Bayes' theorem can be derived as

$$P(A|B) = \frac{P(B|A)P(A)}{P(B)}. \tag{4.2}$$

In scientific applications, the primary objective is to infer the posterior probability distribution of parameters $\boldsymbol{\theta}$ under a given hypothesis $\mathcal{H}$ in order to describe the observed data d. In this setting, Bayes' theorem is often written as

$$p(\boldsymbol{\theta}|d,\mathcal{H}) = \frac{p(d|\boldsymbol{\theta},\mathcal{H})p(\boldsymbol{\theta}|\mathcal{H})}{p(d|\mathcal{H})} \equiv \frac{\mathcal{L}(d|\boldsymbol{\theta})\pi(\boldsymbol{\theta})}{\mathcal{Z}}, \tag{4.3}$$

where $\mathcal{L}(d|\boldsymbol{\theta})$, $\pi(\boldsymbol{\theta})$, and $\mathcal{Z}$ refer to the likelihood, prior, and evidence, respectively. Here, $\boldsymbol{\theta} = (\theta_1, ..., \theta_n)$ represents a vector encapsulating multiple parameters, which is particularly relevant for multiparametric models, e.g. gravitational waveform models.

The *likelihood* function denoted as, $\mathcal{L}(d|\boldsymbol{\theta}) = p(d|\boldsymbol{\theta},\mathcal{H})$, represents the conditional probability density of the observed data d given a specific choice of model parameters $\boldsymbol{\theta}$ under the hypothesis $\mathcal{H}$. The *prior*, $p(\boldsymbol{\theta}|\mathcal{H}) = \pi(\boldsymbol{\theta})$, encodes prior knowledge about model parameters. It can be informative, incorporating specific knowledge, or uninformative, expressing minimal prior assumptions to let the data primarily drive the inference. The product of the likelihood and the prior is normalized with the *evidence*, also known as the marginal likelihood, given as

$$\mathcal{Z} = p(d|\mathcal{H}) = \int_{\Omega_{\boldsymbol{\theta}}} \mathcal{L}(d|\boldsymbol{\theta})\pi(\boldsymbol{\theta})d\boldsymbol{\theta}, \tag{4.4}$$

in which the integral is taken over the entire parameter space $\Omega_{\boldsymbol{\theta}}$, which includes all possible values of the parameter vector $\boldsymbol{\theta}$. The evidence represents the probability of observing the data under the hypothesis, serving as a normalization constant that ensures the posterior distribution integrates to unity.

In the framework of Bayesian inference, the *posterior* probability $p(\boldsymbol{\theta}|d,\mathcal{H})$ encapsulates the probability density function (PDF) of the continuous parameter vector $\boldsymbol{\theta}$ given the observed data d and the underlying hypothesis $\mathcal{H}$. When dealing with a multidimensional parameter space, where $\boldsymbol{\theta} = (\theta_1, ..., \theta_n)$, it is often of interest to examine the posterior distribution of a single parameter while marginalizing over the remaining parameters. This process yields the marginalized posterior distribution, expressed as [636]

$$p(\theta_i|d) = \int \Big(\prod_{k\neq i} d\theta_k\Big) p(\boldsymbol{\theta}|d) = \frac{\mathcal{L}(d|\theta_i)\pi(\theta_i)}{\mathcal{Z}}, \tag{4.5}$$

where the integral is performed over the nuisance parameters, i.e., those not of primary interest. Here, $\mathcal{L}(d|\theta_i)$ represents the likelihood function marginalized over the nuisance parameters.

4.2 Joint probabilities and distributions

In the realm of multi-messenger astronomy, it is of interest to infer the joint posterior probability distribution of model parameters describing an astrophysical event described by distinct physical processes. When dealing with multiple independent observations of one event, Bayes' theorem naturally extends to joint distributions, allowing for the integration of information from separate data sources. Consider two independent sets of observations, d_1 and d_2, which can be modeled with corresponding models comprising two sets of parameters, $\boldsymbol{\theta}_1$ and $\boldsymbol{\theta}_2$. If the two observations of one event are independent, then the joint posterior distribution can be written as

$$p(\boldsymbol{\theta}_1, \boldsymbol{\theta}_2 | d_1, d_2, \mathcal{H}) = \frac{p(d_1, d_2 | \boldsymbol{\theta}_1, \boldsymbol{\theta}_2, \mathcal{H}) p(\boldsymbol{\theta}_1, \boldsymbol{\theta}_2 | \mathcal{H})}{p(d_1, d_2 | \mathcal{H})} = \frac{p(d_1 | \boldsymbol{\theta}_1, \mathcal{H})\, p(d_2 | \boldsymbol{\theta}_2, \mathcal{H})\, p(\boldsymbol{\theta}_1, \boldsymbol{\theta}_2 | \mathcal{H})}{p(d_1, d_2 | \mathcal{H})}, \tag{4.6}$$

in which $p(d_1, d_2 | \boldsymbol{\theta}_1, \boldsymbol{\theta}_2, \mathcal{H})$ is the joint likelihood function, $p(\boldsymbol{\theta}_1, \boldsymbol{\theta}_2 | \mathcal{H})$ refers to the joint prior distribution, and $p(d_1 | \boldsymbol{\theta}_1, \mathcal{H}) p(d_2 | \boldsymbol{\theta}_2, \mathcal{H})$ is the product of two likelihoods given the two independent measurements associated with data sets d_1 and d_2.

A prime example of an astrophysical event described by distinct physical processes is a multi-messenger observation of a BNS merger, observed through GW and EM radiation, associated with data sets d_{GW} and d_{EM}, respectively. For this example, the joint likelihood function can be written as

$$\mathcal{L}_{\mathrm{GW-EM}} = p(d_{\mathrm{GW}}, d_{\mathrm{EM}} | \boldsymbol{\theta}_{\mathrm{GW}}, \boldsymbol{\theta}_{\mathrm{EM}}, \mathcal{H}) = \mathcal{L}_{\mathrm{GW}}(d_{\mathrm{GW}} | \boldsymbol{\theta}_{\mathrm{GW}}, \mathcal{H}) \times \mathcal{L}_{\mathrm{EM}}(d_{\mathrm{EM}} | \boldsymbol{\theta}_{\mathrm{EM}}, \mathcal{H}). \tag{4.7}$$

A direct implementation of a Bayesian multi-messenger data analysis is described in Chapter 5, while also outlining the choice of the GW likelihood (cf. Eq. (5.14)) and the likelihood assumed for the EM observation (cf. (Eq. 5.16)) including the GRB and kilonova emissions.

The principle of joint probability distributions extends naturally to the case of multiple independent observations. Specifically, considering the scenario described above, let N_{obs} represent the number of observed multi-messenger events, each associated with measurements $d_1, ..., d_{N_{\mathrm{obs}}}$. Under the assumption that these events are statistically independent, the joint posterior distribution is formulated as

$$\begin{aligned} p(\boldsymbol{\theta} | d_1, ..., d_{N_{\mathrm{obs}}}, \mathcal{H}) &= \frac{p(d_1, ..., d_{N_{\mathrm{obs}}} | \boldsymbol{\theta}, \mathcal{H}) p(\boldsymbol{\theta} | \mathcal{H})}{p(d_1, ..., d_{N_{\mathrm{obs}}} | \mathcal{H})} \\ &= p(\boldsymbol{\theta} | \mathcal{H}) \prod_{i=1}^{N_{\mathrm{obs}}} \frac{p(d_i | \boldsymbol{\theta}, \mathcal{H})}{p(d_i | \mathcal{H})} \\ &= p(\boldsymbol{\theta} | \mathcal{H})^{1 - N_{\mathrm{obs}}} \prod_{i=1}^{N_{\mathrm{obs}}} p(\boldsymbol{\theta} | d_i, \mathcal{H}) \end{aligned} \tag{4.8}$$

where $\boldsymbol{\theta}$ represents the set of parameters governing both the GW and EM signals, such that $\boldsymbol{\theta} = \{\boldsymbol{\theta}_{\mathrm{GW}}, \boldsymbol{\theta}_{\mathrm{EM}}\}$. The joint probabilities of the likelihood and evidence are determined by their respective product forms, consistent with the assumption of statistical independence across observed events.

4.3 Hypothesis testing

While the evidence in Eq. (4.3) primarily functions as a normalization constant in Bayesian inference, it also plays a crucial role in hypothesis testing and statistical model comparison. Specifically, model selection aims to determine which model is most statistically supported by the observed data and to quantify the relative preference for competing models based on their evidence.

For hypothesis testing, consider two competing hypotheses (represented by models), $\mathcal{H}_1$ and $\mathcal{H}_2$. Evaluating the Bayes' theorem for each of the hypotheses yields corresponding posterior distributions. The ratio of the posterior probabilities of the competing hypotheses defines the *posterior odds*, $\mathcal{O}_2^1$, given as

$$\mathcal{O}_2^1 = \frac{p(\mathcal{H}_1|d)}{p(\mathcal{H}_2|d)} = \frac{p(d|\mathcal{H}_1)}{p(d|\mathcal{H}_2)} \cdot \frac{p(\mathcal{H}_1)}{p(\mathcal{H}_2)} = \underbrace{\mathcal{B}_2^1}_{\text{Bayes factor}} \cdot \underbrace{\Pi_2^1}_{\text{Prior odds}} , \tag{4.9}$$

in which the *prior odds* quantify the relative belief in two competing hypotheses before observing any data. If both hypotheses are equally likely a priori, meaning $\pi(\mathcal{H}_1) = \pi(\mathcal{H}_2) \Rightarrow \pi(\mathcal{H}_1)/\pi(\mathcal{H}_2) = 1$, the *posterior odds* reduces to the *Bayes factor*, which is given as the evidence ratio

$$\mathcal{B}_2^1 = \frac{\mathcal{Z}_1}{\mathcal{Z}_2} = \frac{p(d|\mathcal{H}_1)}{p(d|\mathcal{H}_2)} = \frac{\int d\boldsymbol{\theta}_1 p(d|\boldsymbol{\theta}_1, \mathcal{H}_1) p(\boldsymbol{\theta}_1|\mathcal{H}_1)}{\int d\boldsymbol{\theta}_2 p(d|\boldsymbol{\theta}_2, \mathcal{H}_2) p(\boldsymbol{\theta}_2|\mathcal{H}_2)}. \tag{4.10}$$

A common approach in Bayesian model comparison is to express the Bayes factor in logarithmic form,

$$\log \mathcal{B}_2^1 \equiv \log(\mathcal{Z}_1) - \log(\mathcal{Z}_2), \tag{4.11}$$

which facilitates interpretation and enhances numerical stability. The magnitude of the Bayes factor quantifies the strength of evidence favoring one model over the other, while the sign determines the direction of preference, with positive values indicating support for hypothesis $\mathcal{H}_1$ and negative values favoring hypothesis $\mathcal{H}_2$.

In this context, Bayesian model comparison considers both how well a model fits the data (likelihood) and how complex it is (prior information). Models with more parameters can fit data better simply because they are more flexible, but this can lead to overfitting rather than true explanatory power. The Bayes factor, which compares models by integrating their likelihoods with prior probabilities, naturally penalizes those with more parameters. This follows Occam's razor[1], ensuring that a more complex model is only preferred if it provides a significantly better explanation of the data.

Therefore, the Bayes factor is a fundamental tool in Bayesian model selection, providing a quantitative measure for comparing hypotheses while accounting for both model fit and complexity. Its applicability extends to N_{obs} independent observations $d_1, ..., d_{N_{\text{obs}}}$, enabling the computation of the combined Bayes factor $\hat{\mathcal{B}}_2^1$, expressed as

$$\hat{\mathcal{B}}_2^1 = \frac{p(d_1, ..., d_{N_{\text{obs}}}|\mathcal{H}_1)}{p(d_1, ..., d_{N_{\text{obs}}}|\mathcal{H}_2)} = \frac{\prod_{i=1}^{N_{\text{obs}}} p(d_i|\mathcal{H}_1)}{\prod_{i=1}^{N_{\text{obs}}} p(d_i|\mathcal{H}_2)} = \prod_{i=1}^{N_{\text{obs}}} \mathcal{B}_{2,i}^1 , \tag{4.12}$$

in which $\mathcal{B}_{2,i}^1$ refers to the Bayes factor from the i-th observation.

[1] Occam's razor states that among competing hypotheses that explain the data equally well, the one with the fewest assumptions should be preferred.

4.4 Parameter estimation: computational methods in Bayesian inference

The primary objective of Bayesian inference is to obtain a posterior probability distribution for the model parameters. For the case of models describing a multidimensional parameter space[2], the computation of the posterior can be very challenging and requires sophisticated computational methods. This section presents computational methods for estimating posterior distributions, beginning with the Fisher matrix formalism as an approximation technique, followed by a discussion of sampling algorithms, with a particular focus on nested sampling for efficient parameter inference.

4.4.1 Fisher information formalism

Central to the Fisher information formalism is the Fisher information matrix (FIM), which quantifies the amount of information a sample carries about unknown parameters in a probabilistic model. Consider a gravitational waveform model with parameter vector $\boldsymbol{\theta}$ and a likelihood function $\mathcal{L}(d_{\mathrm{GW}}|\boldsymbol{\theta})$ under stationary Gaussian noise (cf. Eq. (5.14)), the elements of the FIM can be computed as

$$F_{ij} = \mathbb{E}\left(\frac{\partial \ln \mathcal{L}(d_{\mathrm{GW}}|\boldsymbol{\theta})}{\partial \theta_i} \frac{\partial \ln \mathcal{L}(d_{\mathrm{GW}}|\boldsymbol{\theta})}{\partial \theta_j}\right), \tag{4.13}$$

where the expectation $\mathbb{E}(\cdot)$ denotes averaging over the noise realizations in the data d_{GW}. While the off-diagonal elements convey information on the correlation between different parameters θ_i and θ_j, the diagonal elements F_{ii} represent the amount of information available about each parameter θ_i. The larger F_{ii}, the better the parameter θ_i can be estimated, meaning higher Fisher information leads to smaller estimation uncertainties.

The inverse of the FIM serves as an approximation of the covariance matrix associated with the estimates of model parameters. The diagonal elements of this covariance matrix correspond to the variances of the individual parameter estimates. Consequently, the lower bound (Cramér-Rao bound) on parameter uncertainties σ_{θ_i} for each individual parameter θ_i is given as

$$\sigma_{\theta_i} \geq \sqrt{(\mathbf{F}^{-1})_{ii}}. \tag{4.14}$$

These parameter uncertainties can be utilized to approximate the posterior distributions of individual model parameters by assuming a Gaussian distribution centered at a selected simulated value. This approach significantly reduces computational complexity.

However, the Fisher information formalism is valid in the limit of high SNR. At low SNRs, the linear approximations used to compute the FIM become unreliable[3], leading to an underestimation of parameter uncertainties. Moreover, the FIM assumes that the posterior distribution of parameters is Gaussian, which is often not true in GW parameter estimation as GW signals often involve highly correlated parameters. The FIM approach does not account well for such strong degeneracies, leading to poorly constrained parameter estimates. Consequently, while the FIM provides a computationally efficient approximation, more sophisticated sampling algorithms are required for accurate parameter estimation.

4.4.2 Sampling algorithms

Sampling algorithms used in Bayesian inference generally fall into two primary categories: Markov Chain Monte Carlo (MCMC) methods [434, 299] and nested sampling [602]. These approaches are designed to efficiently explore the posterior distribution by generating representative parameter samples.

[2] As discussed in Subsec. 3.1.2, GW signals from BBH mergers are characterized by 15 parameters, while BNS mergers include two additional tidal deformability parameters, resulting in 17 parameters.

[3] The *linear signal approximation* assumes that the template waveform can be expanded linearly around the true parameters $\boldsymbol{\theta}_0$, keeping only the first-order terms: $h(\boldsymbol{\theta}) = h_0 + h_i \delta\theta^i + \ldots$, where $\delta\theta^i \equiv \theta^i - \theta^i_0$ [325].

Specifically, both techniques produce a collection of samples such that the number of samples within a given interval is proportional to the posterior probability distribution, such that $(\boldsymbol{\theta}, \boldsymbol{\theta} + d\boldsymbol{\theta}) \propto p(\boldsymbol{\theta})$ [652]. In the following, more focus is given to nested sampling, as it plays a key role in the sampling methods used for the studies presented in this work. For dedicated reviews the reader is directed to relevant literature, e.g. [407].

Nested sampling: The nested sampling algorithm, introduced by John Skilling in 2004 [602], is a Monte Carlo technique designed to efficiently estimate Bayesian evidence and explore complex, high-dimensional posterior distributions. Nested sampling estimates how the likelihood function $\mathcal{L}(\boldsymbol{\theta})$ relates to the prior mass element $dX = \pi(\boldsymbol{\theta})d\boldsymbol{\theta}$ [603],

$$\underbrace{\mathcal{L}(\boldsymbol{\theta})}_{\text{Likelihood}} \times \underbrace{\pi(\boldsymbol{\theta})d\boldsymbol{\theta}}_{\text{Prior mass}} = \underbrace{\mathcal{Z}}_{\text{Evidence}} \times \underbrace{p(\boldsymbol{\theta})d\boldsymbol{\theta}}_{\text{Posterior}}, \tag{4.15}$$

yielding primarily an estimate for the evidence $\mathcal{Z} = \int \mathcal{L}\, dX = \mathcal{L}(d|\boldsymbol{\theta})\pi(\boldsymbol{\theta})d\boldsymbol{\theta}$ and the posterior $dP = p(\boldsymbol{\theta})d\boldsymbol{\theta}$ as a by-product. A simple approach could be to grid the parameter space, evaluate $\int \mathcal{L}(\boldsymbol{\theta})\pi(\boldsymbol{\theta})d\boldsymbol{\theta}$, and sum the values to approximate the evidence $\mathcal{Z}$. However, in most cases, the Bayesian evidence involves a multidimensional likelihood function, so that the evaluation quickly becomes infeasible due to the curse of dimensionality. To mitigate this issue, the problem is reparametrized in terms of the prior mass X. More specifically, one defines the cumulative prior mass $X(\lambda)$ [603],

$$X(\lambda) = \int_{\{\boldsymbol{\theta}:\mathcal{L}(\boldsymbol{\theta})>\lambda\}} \pi(\boldsymbol{\theta})d\boldsymbol{\theta}, \tag{4.16}$$

which measures how much of the prior distribution falls above a certain likelihood threshold λ. This can be imagined as sorting all possible parameter values $\boldsymbol{\theta}$ based on how likely they are $\mathcal{L}(\boldsymbol{\theta})$.[4] As λ increases, the enclosed prior mass X decreases from 1 to 0. Because $X(\lambda)$ is a smooth, decreasing function, this property enables its inversion to express the likelihood in terms of the prior mass: $\mathcal{L}(X(\lambda)) \equiv \lambda$. This reformulation transforms the original multi-dimensional integral in Eq. (4.4) into a simpler one-dimensional integral [603]

$$\mathcal{Z} = \int_0^1 \mathcal{L}(X)dX. \tag{4.17}$$

This implies that nested sampling systematically explores the parameter space, defined by the prior points $\boldsymbol{\theta}_i$, identifying regions with progressively higher likelihood values $\mathcal{L}_i$ while simultaneously reducing the prior mass. This process is illustrated in Figure 4.1, in which the parameter space is further refined as higher-likelihood regions are explored via the cumulative prior mass function.
In principle, the Bayesian evidence could be approximated numerically, Z, using only standard quadrature methods such as

$$\mathcal{Z} \approx Z = \sum_{i=1}^{N} \mathcal{L}_i w_i, \tag{4.18}$$

in which $\mathcal{L}_i$ refers to the likelihood at a given point i, and w_i is a weight that depends on how the prior mass is distributed and could be evaluated with the trapezoidal rule as $w_i = \frac{1}{2}(X_{i-1} - X_{i+1})$ [603]. However, this approach is only feasible, if the likelihood function $\mathcal{L}(X)$ was known. Since the distribution of likelihood values over the prior mass is generally unknown, Monte Carlo methods must be employed. The procedure for estimating the evidence as well as the generation of posterior samples is outlined below:

[4] Essentially, this means that if λ is small, allowing for low likelihood values, most of the prior is included, so $X(\lambda)$ is close to 1. Conversely, if λ is very large, allowing for high likely values, only a few parameter values are included, so $X(\lambda)$ is close to 0.

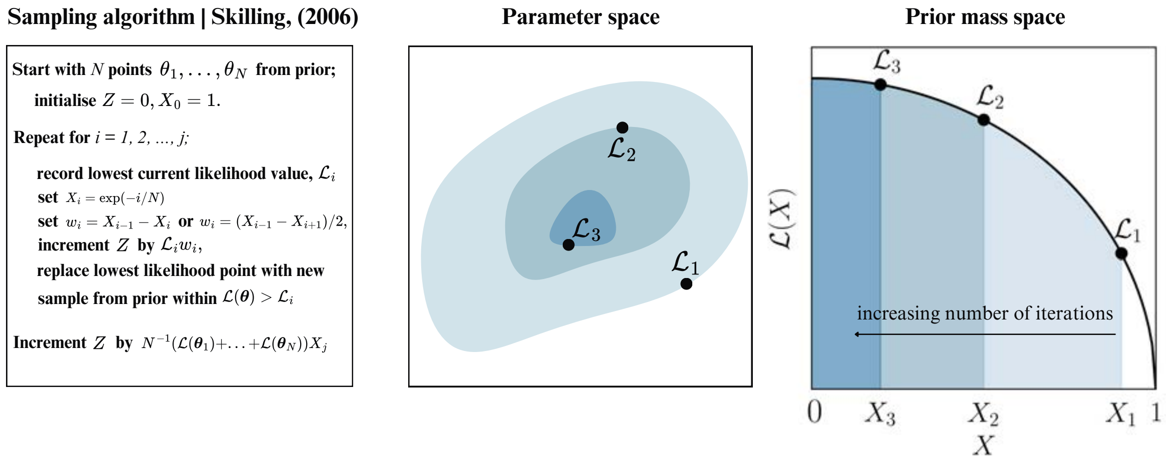

FIGURE 4.1
The nested sampling algorithm of John Skilling [603], outlined in the left panel, systematically generates nested likelihood shells (middle panel), leading to a progressive reduction of the prior mass space with an increasing number of iterations (right panel).

Evidence estimation: The procedure starts with drawing N_{live} so-called *live points* from the prior, $\pi(\boldsymbol{\theta})$, associated with a prior volume X_0, with $X_0 = 1$. Each live point has a likelihood $\mathcal{L}_i = p(d|\boldsymbol{\theta}_i))$. At each iteration, the lowest-likelihood point $\mathcal{L}_i$ among the live points is identified and removed (referred to as a *dead point*) and a new point is sampled from the prior constrained to have likelihood greater than $\mathcal{L}_i$. At the i-th iteration, the prior volume is a random variable distributed as $X_i = t_i X_{i-1}$, where t_i follows the distribution $P(t) = N_{\text{live}} t^{\text{N}_{\text{live}}-1}$. The weights w_i can be evaluated by simply computing $w_i = X_{i-1} - X_i$ or using the trapezoidal rule $w_i = \frac{1}{2}(X_{i-1} - X_{i+1})$. This process continues until the entire prior volume is explored, with live points moving through nested likelihood shells as the prior volume decreases (cf. right panel in Figure 4.1).

Stopping criterion: The nested sampling algorithm will terminate when the contribution of the remaining live points to the evidence becomes negligible and falls below a specific tolerance, estimated as [603]

$$\mathcal{L}_{\text{max}} X_j < f \mathcal{Z}_j \,, \tag{4.19}$$

in which f represents the tolerance, given as a fraction of $\mathcal{Z}$, and the index j corresponds to the total number of iterations used for the sampling yielding N_j dead points. The choice of the tolerance value is arbitrary.

Posterior reconstruction: As the prior volume decreases, the sequence of discarded points forms a representative posterior sample. Posterior samples can be inferred from these dead points, each weighted as

$$p_i = \frac{\mathcal{L}_i w_i}{\sum_j \mathcal{L}_j w_j} = \frac{\mathcal{L}_i w_i}{Z}. \tag{4.20}$$

These weighted samples enable the computation of key posterior statistics such as means, variances, and covariances. Nested sampling techniques that estimate both the evidence and the posterior distributions are implemented in software packages such as `dynesty` [611] and `MultiNest` [135], facilitating parameter estimation for GW and EM data, respectively.

MCMC sampling: In contrast to nested sampling, MCMC sampling methods are designed to directly estimate the posterior probability distribution. MCMC is a type of Monte Carlo method that creates a *Markov chain* designed to produce samples from a target probability distribution once it reaches equilibrium. A *Markov chain* is a sequence of random variables $x_1, x_2, x_3, \ldots,$ where the probability of transitioning to the next state depends only on the current state, not on past states. This property is called the Markov property: $P(x_{t+1}|x_1, x_2, ..., x_{t-1}, x_t) = P(x_{t+1}|x_t)$. Let $p^{(t)}(\boldsymbol{x})$ denote the probability distribution of the state of a Markov chain estimator. The Markov chain is established by an initial probability distribution $p^{(0)}(\boldsymbol{x})$ and a transition probability $T(\boldsymbol{x}'|\boldsymbol{x})$. Then, the probability distribution at the $(t+1)$-th iteration of the Markov chain, $p^{(t+1)}(\boldsymbol{x})$ is given by [407]

$$p^{(t+1)}(\boldsymbol{x}') = \int d^N\boldsymbol{x}\ T(\boldsymbol{x}'|\boldsymbol{x})p^{(t)}. \tag{4.21}$$

For an MCMC method to be effective, the Markov chain must satisfy i) ergodicity, meaning that it should be possible to reach any state from any other state, and ii) aperiodicity, meaning that the chain should not get trapped in cycles. Together, these conditions ensure that iii) the target distribution is the unique stationary distribution of the chain. Once these conditions are satisfied and the chain reaches approximate stationarity, a *burn-in* phase discards initial draws to ensure that the chain has converged to the target distribution. Furthermore, *thinning* the chain by only keeping a subset of samples helps to reduce autocorrelation and produce a more representative set of samples from the stationary distribution.

Metropolis-Hastings algorithm: A common algorithm in MCMC sampling is the Metropolis-Hastings algorithm [434, 299] and enables efficient exploration in complex and high-dimensional parameter spaces. To sample from a target probability function, the algorithm starts with some arbitrary state $\boldsymbol{\theta}^{(0)}$ and uses a proposal PDF $Q(\boldsymbol{\theta}^*|\boldsymbol{\theta}^{(t)})$ at iteration t in the chain to generate a new random candidate state $\boldsymbol{\theta}^*$. The new state $\boldsymbol{\theta}^*$ is accepted with a probability A when

$$A = \min\left(1, \frac{p(\boldsymbol{\theta}^*|d,\mathcal{H})\,Q(\boldsymbol{\theta}^{(t)}|\boldsymbol{\theta}^*)}{p(\boldsymbol{\theta}^{(t)}|d,\mathcal{H})\,Q(\boldsymbol{\theta}^*|\boldsymbol{\theta}^{(t)})}\right). \tag{4.22}$$

If the probability of the new state $\boldsymbol{\theta}^*$ exceeds that of $\boldsymbol{\theta}^{(t)}$, the proposed state is accepted and sets $\boldsymbol{\theta}^{(t+1)} = \theta^*$. Otherwise, acceptance is determined by drawing a random number, u, from a uniform distribution $\mathcal{U}(0,1)$ and accepts the proposed state $\boldsymbol{\theta}^*$, when $A \geq u$. Otherwise, the proposed state is rejected, and the chain keeps the current state $\boldsymbol{\theta}^{(t+1)} = \theta^t$. Since the posterior distribution is proportional to the likelihood and the prior, $p(\boldsymbol{\theta}|d,\mathcal{H}) \propto p(d|\boldsymbol{\theta},\mathcal{H})p(\boldsymbol{\theta})$, one only needs to compute the ratio of the posteriors $p(\boldsymbol{\theta^*|d,\mathcal{H}})/p(\boldsymbol{\theta^{(t)}|d,\mathcal{H}})$ up to a constant factor. This means that this method does not require computing the evidence, since it cancels out in the posterior ratio. As a result, MCMC directly targets the posterior distribution. While the MCMC/Metropolis-Hastings method offers broad applicability, flexibility in proposal design, it can produce correlated samples necessitating additional post-processing and careful tuning.

5

An updated nuclear-physics and multi-messenger astrophysics framework for binary neutron star mergers

CONTENTS

This chapter is based on the article by Peter T. H. Pang, Tim Dietrich, Michael W. Coughlin, Mattia Bulla, Ingo Tews, Mouza Almualla, Tyler Barna, Ramodgwendé Weizmann Kiendrebeogo, ***Nina Kunert****, Gargi Mansingh, Brandon Reed, Niharika Sravan, Andrew Toivonen, Sarah Antier, Robert O. VandenBerg, Jack Heinzel, Vsevolod Nedora, Pouyan Salehi, Ritwik Sharma, Rahul Somasundaram, and Chris Van Den Broeck published in Nature Communications 14 (2023) 1, 8352. I contributed to the joint multi-messenger simulations carried out for this article and demonstrated the performance scaling of the code as shown in the manuscript. Additional contributions include image visualizations, software development, and editing the manuscript.*

Editorial notes: The figure captions were reformatted to align with the current style of this work, and minor typographical errors in the text were corrected. Additional citations have been included beyond those in the published version.

Abstract: The multi-messenger detection of the gravitational-wave signal GW170817, the corresponding kilonova AT2017gfo and the short gamma-ray burst GRB170817A, as well as the observed afterglow has delivered a scientific breakthrough. For an accurate interpretation of all these different

messengers, one requires robust theoretical models that describe the emitted gravitational-wave, the electromagnetic emission, and dense matter reliably. In addition, one needs efficient and accurate computational tools to ensure a correct cross-correlation between the models and the observational data. For this purpose, we have developed the Nuclear-physics and Multi-Messenger Astrophysics framework NMMA. The code allows incorporation of nuclear-physics constraints at low densities as well as X-ray and radio observations of isolated neutron stars. In previous works, the NMMA code has allowed us to constrain the equation of state of supranuclear dense matter, to measure the Hubble constant, and to compare dense-matter physics probed in neutron-star mergers and in heavy-ion collisions, and to classify electromagnetic observations and perform model selection. Here, we show an extension of the NMMA code as a first attempt of analysing the gravitational-wave signal, the kilonova, and the gamma-ray burst afterglow simultaneously. Incorporating all available information, we estimate the radius of a $1.4M_{\odot}$ neutron star to be $R = 11.98^{+0.35}_{-0.40}$km.

5.1 Introduction

The study of the gravitational-wave (GW) and electromagnetic (EM) signals GW170817 [10], AT2017gfo [53, 174, 185, 242, 345, 352, 398, 428, 589, 625, 647], and GRB170817A [420, 255, 379] has already enabled numerous scientific breakthroughs, for example, constraints on the properties of neutron stars (NSs) and the dense matter equation of state (EOS) at supranuclear densities [83, 562, 529, 451, 183, 153, 214, 324], an independent measurement of the Hubble constant [7, 291, 317, 184, 214, 657], the verified connection between binary NS (BNS) mergers and at least some of the observed short gamma-ray bursts (GRBs) [11], and precise limits on the propagation speed of GWs [11]. These scientific achievements were enabled by the multi-messenger nature of GW170817.

Despite this enormous progress, results have been obtained by connecting constraints from individual messengers a posteriori, i.e., different messengers were analyzed individually and then combined within different multi-messenger frameworks to achieve the final results. Such frameworks and attempts include, among others, the work of Breschi et al.[129] performing Bayesian inference and model selection on the kilonova AT2017gfo, Nicholl et al.[471] developing a framework for predicting kilonova and GRB afterglow lightcurves using information from GW signals as input, and the multi-messenger framework developed by Raaijmakers et al.[525]. Similarly, to these works, our previous Nuclear physics - Multi-Messenger Astrophysics (NMMA) framework has been successfully applied to provide constraints on the EOS of NS matter and on the Hubble constant [214, 491], to investigate the nature of the compact binary merger GW190814 [631], to provide techniques to search for kilonova transients [54], to classify observed EM transients such as GRB200826A [44], and to combine information from multi-messenger observations with data from nuclear-physics experiments such as heavy-ion collisions [324].

Here, we upgrade our framework to allow for a simultaneous analysis of kilonova, GRB afterglow, and GW data capitalizing on the multi-messenger nature of compact-binary mergers.

5.2 Results

The full potential of our NMMA study becomes clear from Fig. 5.1 where we show a set of possible EOSs relating the pressure and baryon number density inside NSs. Different constraints can provide valuable information in different density regimes. For example, theoretical calculations of dense nuclear matter in the framework of chiral effective field theory (EFT) [401, 312, 223, 503, 348] or data

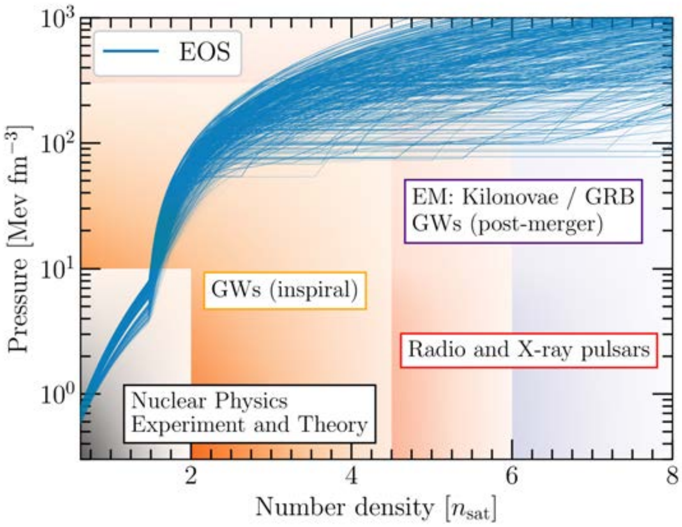

FIGURE 5.1
Overview of constraints on the EOS from different information channels. We show a set of possible EOSs (blue lines) that are constrained up to $1.5n_{\rm sat}$ by Quantum Monte Carlo calculations using chiral EFT interactions [630] and extended to higher densities using a speed of sound model [633]. Different regions of the EOS can then be constrained by using different astrophysical messengers, indicated by rectangulars: GWs from inspirals of NS mergers, data from radio and X-ray pulsars, and EM signals associated with NS mergers. Note, that the boundaries are not strict but depend on the EOS and properties of the studied system.

extracted from nuclear-physics experiments, e.g, heavy-ion collisions [563] or the recent PREX-II experiment at Jefferson Laboratory [37], provide valuable input up to about twice the nuclear saturation density, $n_{\rm sat} \approx 0.16\,{\rm fm}^{-3}$. GW signals emitted during the inspiral of a BNS or black-hole–NS (BHNS) systems contain information that probe the EOS at densities realized inside the individual NS components of the system, typically up to about five times $n_{\rm sat}$, but the exact density range probed in such mergers depends noticeably on the mass of the component stars. Furthermore, radio observations of NSs can be used to infer their masses, e.g., by measuring Shapiro delay in a binary system. In particular, radio observations of heavy NSs with masses of about $2M_\odot$, such as PSR J0348+0432 [57], PSR J1614-2230 [63], and PSR J0740+6620 [187], currently provide valuable information at larger densities than those probed by inspiral GW signals. In addition, these observations provide a valuable lower bound on the maximum mass of NSs. Matter at the highest densities in the universe could be created in the postmerger phase of a BNS coalescence, i.e., after the collision of the two NSs in the binary. This phase of the binary merger might be observed through future GW detections with more sensitive detectors. Alternatively, this phase can be probed by analyzing EM signals connected to a BNS merger, i.e., the kilonovae, GRBs, and their afterglows. Finally, at asymptotically high densities that are not shown in the figure, the EOSs can be calculated in perturbative QCD [371] and might be used to constrain the NS EOS [360]. The combination of all these various pieces of information provides a unique tool to unravel the properties of matter at supranuclear densities.

GW170817-AT2017gfo

With the NMMA framework, we analyze GW170817 simultaneously with the observed kilonova AT2017gfo. For the GW analysis, we have used the `IMRPhenomPv2_NRTidalv2` waveform model and analyzed the GW data obtained from the Gravitational Wave Open Science Center (GWOSC)[649] in a frequency range of 20Hz to 2048Hz, covering the detected BNS inspiral[16]. For the EM signal, we use the data set compiled in Coughlin et al.[182], where in this work, we include the optical,

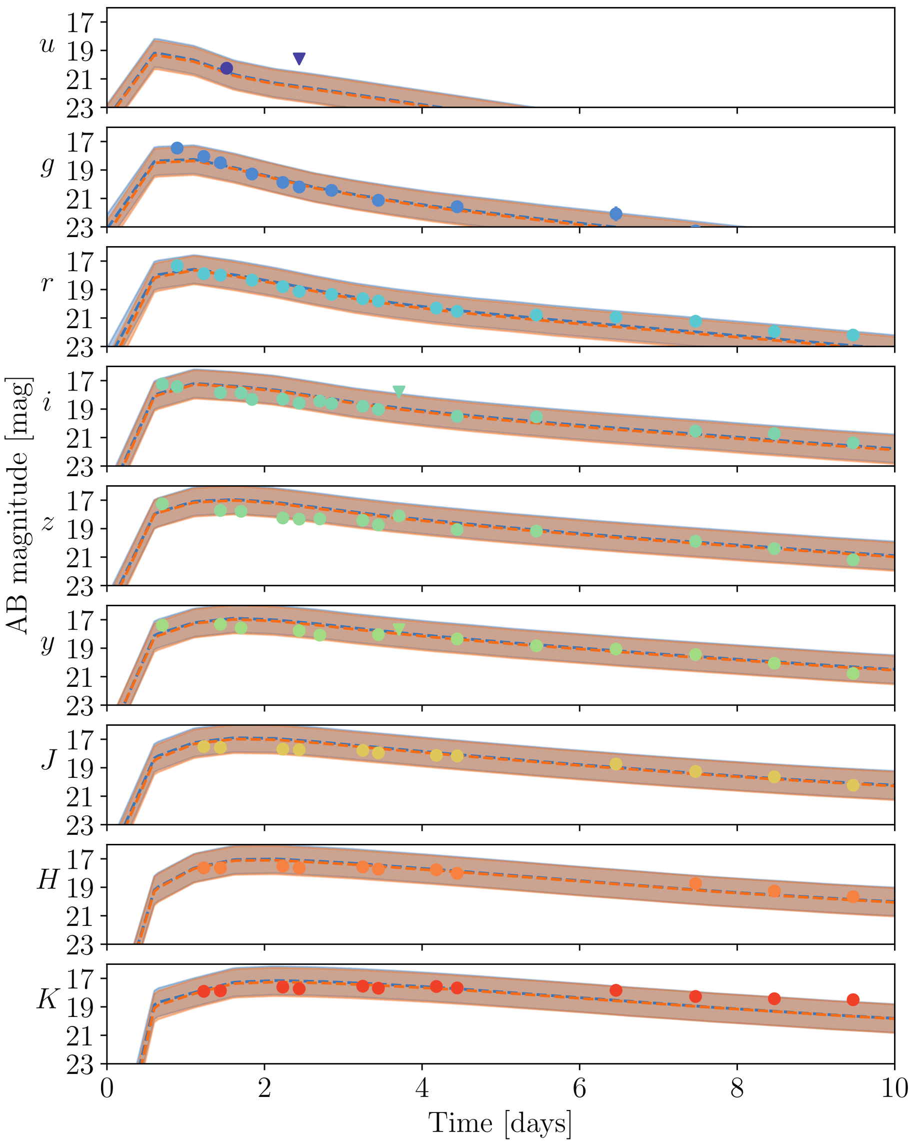

FIGURE 5.2
Best-fit early-time lightcurve from the analysis. The best-fit lightcurves (dashed, with the 1 magnitude uncertainty shown as the band) for AT2017gfo data when analysing GW170817-and-AT2017gfo (orange) or GW170817-and-AT2017gfo-and-GRB170817A (blue) simultaneously. We note that both bands overlap almost completely, i.e., for AT2017gfo the accuracy of the kilonova lightcurve description does not depend noticeably on the inclusion of a GRB afterglow component. For the analysis, we restrict our dataset to times between 0.5 days up to 10 days after the BNS merger to simplify the joint GW170817-and-AT2017gfo-and-GRB170817A study as discussed in the main text.

infrared, and ultraviolet data between 0.5 and 10 days after the merger. The corresponding data is analysed with a Gaussian Process Regression (GPR)-based kilonova model. For our analysis, we are presenting the best-fit lightcurve in Fig. 5.2, with its band representing a one magnitude uncertainty for the individual lightcurves. This one magnitude uncertainty is introduced during the inference and should account for systematic uncertainties in kilonova modelling. In Supplementary information, we

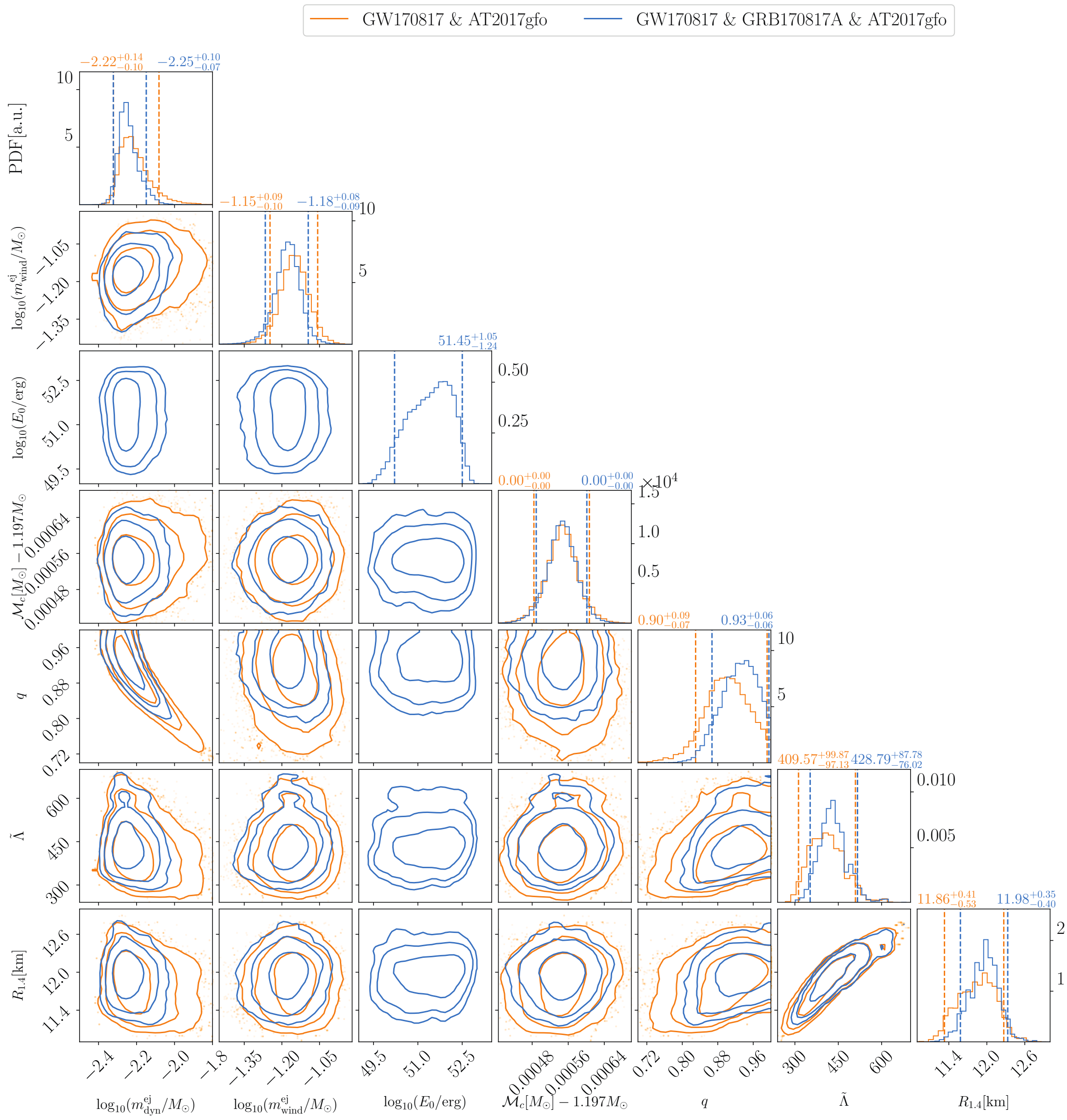

FIGURE 5.3
Visualization of the posterior of the GW170817-and-AT2017gfo and GW170817-and-AT2017gfo-and-GRB170817A analysis. Corner plot for the mass of the dynamical ejecta $m^{\mathrm{ej}}_{\mathrm{dyn}}$, the mass of the disk wind ejecta $m^{\mathrm{ej}}_{\mathrm{wind}}$, $\log_{10}$ of the GRB jet on-axis isotropic energy $\log_{10} E_0$, the detector-frame chirp mass $\mathcal{M}_c$, the mass ratio q, the mass-weighted tidal deformability $\tilde{\Lambda}$, and the radius of a 1.4 solar mass neutron star $R_{1.4}$ at 68%, 95% and 99% confidence. For the 1D posterior probability distributions, we mark the median (solid lines) and the 90% confidence interval (dashed lines) and report these above each panel. We show results that are based on the simultaneous analysis of GW170817-and-AT2017gfo (orange) and of GW170817-and-AT2017gfo-and-GRB170817A (blue).

show how smaller or larger assumed uncertainties change our conclusions and it show that the one-magnitude is a sensible choice. Such a finding is also consistent with Heinzel et al.[303]. Therefore, we focus particularly on one-magnitude uncertainties' results. Nevertheless further work would be needed to understand in detail uncertainties related to the ejecta geometry[303], assumed heating rates, thermalization efficiencies and opacities within the ejecta[139]. Furthermore, we point out that for Fig. 5.2, we explicitly restricted our data set to the times between 0.5 to 10 days after the BNS merger, since model predictions at earlier or later times are more uncertain, e.g., due to less accurate opacities during early times and a larger impact of Monte Carlo noise in the employed radiative transfer models at late times. While this does not affect the GW170817-AT2017gfo analysis, it has an impact when we will also incorporate the GRB afterglow. In fact, we find that not restricting us to this time ranges can cause problems in the joint inference and it takes noticeably longer until the sampler converges.
Fig. 5.3 summarizes our main findings and shows joint posteriors for the mass of the dynamical ejecta $m^{\rm ej}_{\rm dyn}$, the mass of the disk wind ejecta $m^{\rm ej}_{\rm wind}$, the chirp mass $\mathcal{M}_c$, the mass ratio q, the mass-weighted tidal deformability $\tilde{\Lambda}$, and the radius of a 1.4 solar mass neutron star $R_{1.4}$. In contrast to previous findings using simpler kilonova modelling (see Ref. [596] and references therein), we can fit AT2017gfo with masses for the dynamical (about $0.006\,M_\odot$) and disk-wind (about $0.07\,M_\odot$) ejecta components that are within the range of values predicted by numerical-relativity simulations [528].

While the parameters extracted are consistent with our previous findings [214], we observe a clear improvement on the parameter error bounds due to (i) performing a simultaneous analysis of the distinct messengers and (ii) employing a modified likelihood function when analysing the kilonova. For instance, the constraints on $R_{1.4} = 11.86^{+0.41}_{-0.53}$, a typical choice to quantify EOS constraints, is significantly improved compared to our previous result, $R_{1.4} = 11.75^{+0.86}_{-0.81}$ km[214]. The half-width of $R_{1.4}$'s 90% credible interval decreases from about 800m [214] to about 400m.

GW170817-AT2017gfo-GRB170817A
In addition to the combined analysis of GW170817 and AT2017gfo, we can also incorporate information obtained from the GRB afterglow of GW170817A, where we employ the data set collected in Troja et al.[640]. The GRB afterglow light-curve data are analyzed with the synthetic Gaussian jet-model lightcurve described before [651, 566]. Fig. 5.2 shows the corresponding best-fit lightcurve for the kilonova with a 1 magnitude uncertainty band as before. Moreover, we are also presenting the best-fit lightcurve, which includes kilonova and GRB afterglow, and the employed uncertainty band in Fig. 5.4. We find that both the kilonova AT2017gfo and the GRB afterglow GRB170817A are well described in our analysis.

Fig. 5.3 again summarizes our findings for the joint posteriors of the mass of the dynamical ejecta, the mass of the disk wind ejecta, the on-axis isotropic equivalent energy, the chirp mass, the mass ratio, the mass-weighted tidal deformability, and the radius of a 1.4 solar mass neutron star for this analysis, which is consistent with GW170817-and-AT2017gfo only. Compared to the analysis of GW170817-and-AT2017gfo only, the improvement on the parameter uncertainties is minimal, yet, noticeable when information from GRB170817A is added. Although no significant constraint on the EOS is imposed by the jet energy E_0 as the ratio ξ between it, E_0, and the disk mass $m_{\rm disk}$ is taken as a free parameter, the inclination constraint from the GRB plays a role in the constraint on EOS. For an anisotropic kilonova model, the inclination angle changes the observable kilonova light curves beyond scaling (e.g. Fig. 2 in Ref. [595]), which is correlated with the ejecta masses (e.g. Fig. 3 in Ref. [52]). Therefore the GRB's inclination measurement imposes a constraint on the EOS via the kilonova eject masses measurements. Moreover, for future studies, we expect that the inclusion of the GRB afterglow will be of great importance for measuring the Hubble constant.

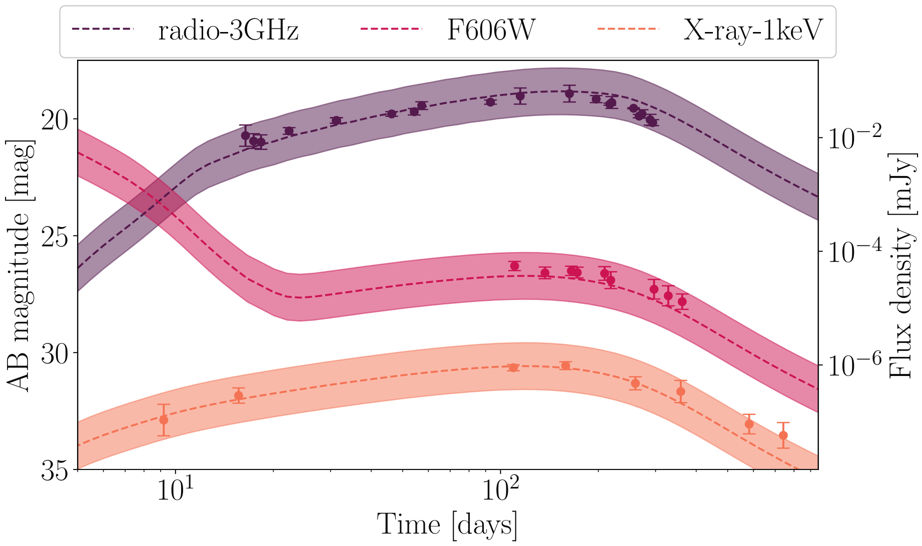

FIGURE 5.4
Best-fit late-time lightcurve from the analysis. The best-fit lightcurves (dashed, with the 1 magnitude uncertainty shown as the band) for the analysis of GRB170817A when simultaneously analysing GW170817, AT2017gfo, GRB170817A. We compare our model predictions with the observational data including the 1-sigma measurement uncertainty.

5.3 Discussion

We have developed a publicly available NMMA framework for the interpretation and analysis of BNS and BHNS systems. This framework allows for the simultaneous analysis of GW and EM signals such as kilonovae and GRB afterglows. In addition, our framework allows us to incorporate constraints from nuclear-physics calculations, e.g., by sampling over EOS sets constrained by chiral EFT, and to include radio as well as X-ray measurements of isolated NSs. By employing our framework to a combined analysis of GW170817, AT2017gfo, and GRB170817A, we find that the radius of a typical 1.4 solar mass NS lies within $11.98^{+0.35}_{-0.40}$ km; cf. Tab. 5.1 for a selection of studies from the literature. Based on our findings, our analysis is a noticeable improvement over previous works. However, additional uncertainties in our work lie in limited physics input in kilonova and semi-analytic GRB and models. Therefore, reliable astrophysical interpretations of future BNS detections will only be possible if not only parameter estimation infrastructure, as presented in this work, but also the astrophysical models describing transient phenomena advance further. Nevertheless, given the increasing number of multi-messenger detections of BNS and BHNS merger, we expect to use our framework to further increase our knowledge about the interior of NSs during the coming years.

TABLE 5.1
Comparison of radius measurements of a 1.4 $M_\odot$ neutron star for a selection of multi-messenger studies.

Reference	$R_{1.4}$ [km]
Dietrich et al. [214]	$11.75^{+0.86}_{-0.81}$ (90%)
Essick et al. [239]	$12.54^{+0.71}_{-0.63}$ (90%)
Breschi et al. [129]	$11.99^{+0.82}_{-0.85}$ (90%)
Nicholl et al. [471]	$11.06^{+1.01}_{-0.98}$ (90%)
Raaijmakers et al. [524]	$12.18^{+0.56}_{-0.79}$ (95%)
Miller et al. [447]	$12.45^{+0.65}_{-0.65}$ (68%)
Huth et al. [324]	$12.01^{+0.78}_{-0.77}$ (90%)
this work [NMMA]	$11.98^{+0.35}_{-0.40}$ (90%)

A selected list of radius measurements of a 1.4 $M_\odot$ neutron star from various multi-messenger studies is shown. We denote the corresponding credible interval in parenthesis.

5.4 Methods

5.4.1 Equation of State construction

The EOS describes the relation between energy density ε, pressure p, and temperature T of dense matter and additionally depends on the composition of the system. For NSs, thermal energies are much smaller than typical Fermi energies of the particles, and therefore, temperature effects can be neglected for isolated NSs or NSs in the inspiral phase of a merger. In these cases, the EOS simply relates ε and p.

The most general constraints on the EOS can be inferred from the slope of the EOS, the speed of sound, defined as

$$c_S = c\sqrt{\partial p/\partial \varepsilon}\,, \tag{5.1}$$

where c is the speed of light. Due to the laws of special relativity, the speed of sound has to be smaller than the speed of light, $c_S \leq c$. Furthermore, the speed of sound in a NS has to be larger than zero, $c_S \geq 0$, as NSs would otherwise be unstable. These constraints alone, however, allow for an extremely large EOS space.

At nuclear densities, additional information on the EOS can be inferred from laboratory experiments and theoretical nuclear-physics calculations. For example, this information was used to constrain the properties of stellar matter in the NS crust [86, 161], i.e., the outermost layer of NSs at densities below approximately $0.5n_{\rm sat}$. Above roughly $0.5n_{\rm sat}$, NS matter consists of a fluid of neutrons with a small admixture of protons. In this regime, the EOS can be constrained by microscopic calculations of dense nuclear matter. These calculations typically provide the energy per particle, $E/A(n,x)$, which is a function of density n and proton fraction $x = n_p/n$ with n_p being the proton density. From this, the EOS follows from

$$\varepsilon(n,x) = n\,\frac{E}{A}(n,x)\,, \tag{5.2}$$

and

$$p(n,x) = n^2\frac{\partial E/A(n,x)}{\partial n}\,. \tag{5.3}$$

The proton fraction $x(n)$ is then determined from the beta equilibrium condition, $\mu_n = \mu_p + \mu_e$, where μ_i is the chemical potential of particle species i, and n, p, and e refer to neutrons, protons, and electrons, respectively.

To calculate the energy per particle microscopically, one needs to solve the nuclear many-body problem, commonly described by the Schrödinger equation. This requires knowledge of the nuclear Hamiltonian describing the many-body system. Fundamentally, nuclear many-body systems are described by Quantum Chromodynamics (QCD), the fundamental theory of strong nuclear interactions. QCD describes the system in terms of the fundamental degrees of freedom (d.o.f.), quarks and gluons. Unfortunately, this approach is currently not feasible [632]. At densities of the order of $n_{\rm sat}$, however, the effective d.o.f. are nucleons, neutrons and protons, that can be treated as point-like nonrelativistic particles. Then, the nuclear Hamiltonian can be written generically as

$$H = T + \sum_{i<j} V_{ij}^{\rm NN} + \sum_{i<j<k} V_{ijk}^{\rm 3N} + \cdots \,, \tag{5.4}$$

where T denotes the kinetic energy of the nucleons, $V_{ij}^{\rm NN}$ describes two-nucleon (NN) interactions between nucleons i and j, and $V_{ijk}^{\rm 3N}$ describes three-nucleon (3N) interactions between nucleons i, j, and k. In principle, interactions involving four or more nucleons can be included, but initial studies have found these to be small compared to present uncertainties [365].

The derivation of the nuclear Hamiltonian (Eq. (5.4)) from QCD is not feasible due to its nonperturbative nature. In this work, we therefore use a common approach and choose nucleons as effective d.o.f. The interactions among nucleons can then be derived in the framework of Chiral Effective Field Theory (EFT) [236, 406]. Chiral EFT starts out with the most general Lagrangian consistent with all the symmetries of QCD in terms of nucleonic degrees of freedom. It explicitly includes meson-exchange interactions for the lightest mesons, i.e., the pions. This approach yield an infinite number of pion-exchange and nucleon-contact interactions which needs to be organized in terms of a hierarchical expansion in powers of a soft (low-energy) scale over a hard (high-energy) scale. In chiral EFT, the soft scale q is given by the nucleons' external momenta or the pion mass. The hard scale, also called the breakdown scale Λ_b, is of the order of $500-600$ MeV [222] and interaction contributions involving heavier d.o.f., such as the ρ meson, are integrated out. The chiral Lagrangian is then expanded in powers of q/Λ_b according to a power-counting scheme. Most current chiral EFT interactions are derived in Weinberg power counting [660, 661, 662, 236, 406]. One can then derive the nuclear Hamiltonian from this chiral Lagrangian in a consistent order-by-order framework that allows for an estimate of the theoretical uncertainties [237, 221, 222] and that can be systematically improved by increasing the order of the calculation. Chiral EFT Hamiltonian naturally include NN, 3N, and higher many-body forces, see Eq. (5.4), and chiral EFT predicts a natural hierarchy of these contributions. For example, 3N interactions start to contribute at third order (N^{2}LO) in the expansion. Typical state-of-the art calculations truncate the chiral expansion at N^{2}LO [401, 503, 233] or fourth order (N^{3}LO) [629, 223].

With the nuclear Hamiltonian at hand, one then needs to solve the many-body Schrödinger equation which requires advanced numerical methods. Examples of such many-body techniques include many-body perturbation theory (MBPT) [629, 312, 223], the self-consistent Green's function (SCGF) method [154], or the coupled-cluster (CC) method [292, 233]. Here, we employ Quantum Monte Carlo (QMC) methods [155], which provide nonperturbative solutions of the Schrödinger equation. QMC methods are stochastic techniques which treat the Schrödinger equation as a diffusion equation in imaginary time. In the QMC framework, one begins by choosing a trial wavefunction of the many-body system, which for nuclear matter can be described as a slater determinant of non-interacting fermions multiplied with NN and 3N correlation functions. This trial wavefunction is evolved to large imaginary times, projecting out high-energy excitations, and converging to the true ground state of the system as long as the trial wavefunction has a non-zero overlap with it. Among QMC methods, two well-established algorithms are Green's function Monte Carlo (GFMC), used to describe light atomic nuclei with great precision [155], and Auxiliary Field Diffusion Monte Carlo (AFDMC) [581], suitable to study larger systems such as nuclear matter. Here, we employ AFDMC calculations of neutron matter but our NMMA framework is sufficiently flexible to employ any low-density calculation for neutron-star matter. We then extend our neutron-matter calculations to neutron-star conditions by extrapolating the calculations to β equilibrium using phenomenological information on symmetric nuclear matter and constructing a consistent crust reflecting the uncertainties of the calculations [628]. This crust includes a description of the outer crust [86] and uses the Wigner-Seitz approximation to calculate the inner-crust EOS consistently with our AFDMC calculations.

At nuclear densities, chiral EFT together with a suitable many-body framework provides for a reliable description of nuclear matter with systematic uncertainty estimates. With increasing density, however, the associated theoretical uncertainty grows fast due to the correspondingly larger nucleon momenta approaching the breakdown scale. The density up to which chiral EFT remains valid is not exactly known but estimates place it around $2n_{\rm sat}$ [630, 222]. Hence, chiral EFT calculations constrain the EOS only up to these densities but to explore the large EOS space beyond the breakdown of chiral EFT, one requires a physics-agnostic extension scheme. Here, physics-agnostic implies that no model assumptions, e.g., about the existence of certain d.o.f. at high densities, are made. Instead, the EOS is only bounded by conditions of causality, $c_S \leq c$, and mechanical stability, $c_S \geq 0$, mentioned before. There exist several such extension schemes in literature: parametric ones, like the polytropic expansion [536, 300, 55] or expansions in the speed of sound [633, 290], and nonparametric approaches [240]. To extend the AFDMC calculations employed here, we employ a parametric speed-of-sound extension scheme. Working in the c_S versus n plane, the speed of sound $c_S(n)$ is determined with theoretical uncetainty estimates by chiral EFT up to a reference density below the expected breakdown density. From this uncertainty band, we sample a speed-of-sound curve up to the reference density. Beyond this density, we create a typically non-uniform grid in density up to a large density $\approx 12n_{\rm sat}$, well beyond the regime realized in NSs. For each grid point, we sample random values for $c_s^2(n_i)$ between 0 and c^2 (we set $c = 1$ in the following). We then connect the chiral EFT draw for the speed of sound with all points $c_{s,i}^2(n_i)$ using linear segments. The resulting density-dependent speed of sound can be integrated to give the EOS, i.e., the pressure, baryon density, and energy density. In the interval $n_i \leq n \leq n_{i+1}$,

$$p(n) = p(n_i) + \int_{n_i}^{n} c_s^2(n')\mu(n')dn' \,, \tag{5.5}$$

$$\epsilon(n) = \epsilon(n_i) + \int_{n_i}^{n} \mu(n')dn' \,, \tag{5.6}$$

where $\mu(n)$ is the chemical potential that can be obtained from the speed of sound using the relation

$$\mu(n) = \mu_i \exp\left[\int_{\log n_i}^{\log n} c_s^2(\log n')d\log n'\right] . \tag{5.7}$$

For each reconstructed EOS, constrained by Chiral EFT at low densities and extrapolated via the c_S extension to larger densities, the global properties of NSs can be calculated by solving the Tolman–Oppenheimer–Volkoff (TOV) equations. This way, we determine the NS radii (R) and dimensionless tidal deformabilities (Λ) as functions of their masses (M). We repeat this approach for a large number of samples to construct EOS priors for further analyses of NS data.

This approach is flexible and additional information on high-density phases of QCD can be included straightforwardly. For example, pQCD calculations at asymptotically high densities [371], of the order of $40 - 50n_{\rm sat}$, might be used to constrain the general EOS extension schemes even further [55, 360]. However, the exact impact of these constraints at densities well beyond the regime realized in NSs needs to be studied in more detail. While our NMMA framework currently does not have this capability, we are planning to add this in the near future. Similarly, instead of using general extension models, one can employ specific high-density models accounting for quark and gluon d.o.f. One such model is the quarkyonic-matter model [429, 332, 586, 417], which describes the observed behavior of the speed of sound in NSs [630]: a rise of the speed of sound at low densities to values above the conformal limit of $c/\sqrt{3}$, followed by a decrease to values below the conformal limit at higher densities. In future work, we will address quarkyonic matter and other models in our NMMA framework.

The construction of the EOS, as detailed above, is implemented in the NMMA code under the class `EOS_with_CSE`. This class allows for (a) an exploration of theoretical uncertainties in the low-density EOS and (b) constructs the high-density EOS using a c_S extrapolation. (a) Low-density uncertainties are implemented by requiring two tabulated EOS files for the lower and upper bound of the uncertainty band as inputs, containing the pressure, energy density and number density up to the chosen breakdown density of the model. By default, the results of a QMC calculation using local chiral EFT interactions at N^{2}LO [630] with theoretical uncertainties are provided. Upon initiation of the class, a sample is drawn from the low-density uncertainty band using a 1-parameter sampling technique. In this approach, a uniform random number ω is sampled uniformly between 0 and 1, and the interpolated EOS is given as

$$p(n) = p_{\mathrm{soft}}(n) + \omega(p_{\mathrm{stiff}}(n) - p_{\mathrm{soft}}(n)), \tag{5.8}$$

$$\varepsilon(n) = \varepsilon_{\mathrm{soft}}(n) + \omega(\varepsilon_{\mathrm{stiff}}(n) - \varepsilon_{\mathrm{soft}}(n)), \tag{5.9}$$

where the subscripts "soft" and "stiff" refer to the lower and upper bounds of the EFT uncertainty band, respectively. This sampling technique assumes that pressure and energy density are correlated but we have found that releasing this assumption and using a four-parameter form suggested by Gandolfi et al. [270] does not change our results appreciably. In future, we will explore additional schemes, e.g., using Gaussian processes [239].

(b) The EOS given by Eqs. (5.8) and (5.9) is used up to a breakdown density determined by the user. By default, this density is set to $2n_{\mathrm{sat}}$. Beyond this density, the class constructs the EOS using a c_S extension. The maximum density up to which the EOS is extrapolated and the number of linear line segments can be adjusted by the user, with the default values being $12n_{\mathrm{sat}}$ for the former and 5 line segments for the latter. The code then solves Eqs. (5.5), (5.6) and (5.7) to give the extrapolated EOS. The pressure, energy density, and number density describing the full EOS are accessible as attributes of the `EOS_with_CSE` class.

Finally, the method `construct_family` solves the stellar structure equations (TOV equations and equations for the quadrupole perturbation of spherical models), and returns a sequence of NSs with their masses, radii and dimensionless tidal deformabilities as arrays.

5.4.2 Prior weighting to incorporate radio and X-ray observations of single neutron stars

To incorporate mass measurements of heavy pulsars and mass-radius measurements of isolated pulsars, the associated likelihood is calculated and taken as the prior probability for an EOS for further analysis. For instance, the radio observations on PSR J0348+4042 [57], and PSR J1614-2230 [63] provide a lower bound on the maximum mass of a NS. The likelihood for a mass-only measurement is given by

$$\mathcal{L}_{\mathrm{PSR-mass}}(\mathbf{E}) = \int_0^{M_{\mathrm{TOV}}} dM\ \mathcal{P}(M|\mathrm{PSR}), \tag{5.10}$$

where $\mathcal{P}(M|\mathrm{PSR})$ is the posterior distribution of the pulsar's mass and M_{TOV} is the maximum mass supported by the EOS with parameters $\mathbf{E}$. The posterior distributions of pulsar masses are typically well approximated by Gaussians [214].

Recent X-ray observations of millisecond pulsars by NASA's Neutron Star Interior Composition Explorer (NICER) mission have been used to simultaneously determine the mass and radius of these

NSs [667, 446, 547, 447, 548]. The corresponding likelihood is given by

$$\begin{aligned}
&\mathcal{L}_{\rm NICER}(\mathbf{E}) \\
&= \int dM \int dR\ \mathcal{P}_{\rm NICER}(M,R)\frac{\pi(M,R|\mathbf{E})}{\pi(M,R|I)} \\
&\propto \int dM \int dR\ \mathcal{P}_{\rm NICER}(M,R)\delta(R-R(M;\mathbf{E})) \\
&\propto \int dM\ \mathcal{P}_{\rm NICER}(M,R=R(M;\mathbf{E})),
\end{aligned} \tag{5.11}$$

where $\mathcal{P}_{\rm NICER}(M,R)$ is the joint-posterior distribution of mass and radius as measured by NICER and we use the fact that (i) the radius is a function of mass for a given EOS, and (ii) that without further EOS information, e.g., through chiral EFT, the prior for the radius given mass is taken to be uniform.

5.4.3 Gravitational-wave inference

5.4.3.1 GW models

A complex frequency-domain GW signal is given by

$$h(f) = A(f)e^{-i\psi(f)}, \tag{5.12}$$

with the amplitude $A(f)$ and the GW phase $\psi(f)$. Because of the NS's finite size and internal structure, BNS and BHNS waveform models have to incorporate tidal contributions for an accurate interpretation of the binary coalescence. Such tidal contributions account for the deformation of the stars in their companions' external gravitational field [193, 309] and, once measured, allow to place constraints on the EOS governing the NS interior [11, 13, 20, 156]. They are attractive because they convert energy from the orbital motion to a deformation of the stars, and lead to an accelerated inspiral. In the case of non-spinning compact objects, the leading-order tidal contribution depends on the tidal deformability

$$\tilde{\Lambda} = \frac{16}{13}\frac{(m_1+12m_2)m_1^4\Lambda_1+(m_2+12m_1)m_2^4\Lambda_2}{(m_1+m_2)^5} \tag{5.13}$$

with the individual tidal deformabilities $\Lambda_{1,2} = \frac{2}{3}k_2^{1,2}/C_{1,2}^5$ and the individual masses $m_{1,2}$. Here, $k_2^{1,2}$ are the Love numbers describing the static quadrupole deformation of one body inside the gravitoelectric field of the companion and $C_{1,2}$ are the individual compactnesses $C_{1,2} = m_{1,2}/R_{1,2}$ in isolation.

To date, there are three different types of BNS or BHNS models for the inspiral GW signal that are commonly used: Post-Newtonian (PN) models [195, 33, 380, 333], effective-one-body (EOB) models[142, 194, 315, 310, 47, 96, 215, 456, 616], and phenomenological approximants [347, 210, 213, 212, 635]. In the NMMA framework, we make use of the LALSuite [395] software package, in particular LALSimulation, so that the BNS and BHNS models used by the LIGO-Virgo-Kagra Collaborations can be easily employed. This includes:

- PN models such as `TaylorT2, TaylorT4,` or `TaylorF2` where a PN descriptions for the point-particle BBH baseline as well as the tidal description is employed,
- the most commonly used tidal EOB models `SEOBNRv4T` [310, 615, 616], its frequency-domain surrogate model [375], as well as the `TEOBResumS` model [457, 47] including its post-adiabatic accelerated version [458] which enables it being used during parameter estimation,

- and phenomenological models such as `IMRPhenomD_NRTidal` [322, 349, 626, 210, 213], `SEOBNRv4_ROM_NRTidal` [118, 521, 210, 213], `IMRPhenomPv2_NRTidal` [322, 349, 210, 213], `IMRPhenomD_NRTidalv2` [322, 349, 626, 212], `SEOBNRv4_ROM_NRTidalv2` [118, 521, 212], `PhenomNSBH` [635], `IMRPhenomPv2_NRTidalv2`, [210, 213, 212], and `SEOBNRv4_ROM_NRTidalv2_NSBH` [635, 212, 426].

5.4.3.2 GW analysis

By assuming stationary Gaussian noise, the GW likelihood $\mathcal{L}_{\mathrm{GW}}(\boldsymbol{\theta})$ that the data d is a sum of noise and a GW signal h with parameters $\boldsymbol{\theta}$ is given by [652]

$$\mathcal{L}_{\mathrm{GW}} \propto \exp\left(-\frac{1}{2}\langle d - h(\boldsymbol{\theta}) | d - h(\boldsymbol{\theta})\rangle\right), \tag{5.14}$$

where the inner product $\langle a|b\rangle$ is defined as

$$\langle a|b\rangle = 4\Re \int_{f_{\mathrm{low}}}^{f_{\mathrm{high}}} \frac{\tilde{a}(f)\tilde{b}^*(f)}{S_n(f)} df. \tag{5.15}$$

Here, $\tilde{a}(f)$ is the Fourier transform of $a(t)$, * denotes complex conjugation, and $S_n(f)$ is the one-sided power spectral density of the noise. The choice of f_{low} and f_{high} depends on the type of binary that we are interested in. In our study, we will set f_{low} and f_{high} to 20 Hz and 2048 Hz, respectively. This is sufficient for capturing the inspiral up to the moment of merger for a typical BNS system in the advanced GW detector era.

5.4.4 Electromagnetic Signals

5.4.4.1 Kilonova models

Kilonova models are extracted using the 3D Monte Carlo radiative transfer code POSSIS [138]. The code can handle arbitrary geometries for the ejected material and produces spectra, lightcurves and polarization as a function of the observer viewing angle. Given an input model with defined densities ρ and compositions (i.e., electron fraction Y_e), the code generates Monte Carlo photon packets with initial location and energy sampled from the energy distribution from radioactive decay of r-process nuclei within the model. The latter depends on the mass/density distribution of the model and the assumed nuclear heating rates and thermalization efficiencies. The frequency of each Monte Carlo photon packet is sampled according to the temperature T in the ejecta, which is calculated at each time-step [427, 408]. Photon packets are then followed as they diffuse out of the ejected material and interact with matter via either electron scattering or bound-bound line transitions. Time- and wavelength-dependent opacities $\kappa_\lambda(\rho, T, Y_e, t)$ from Tanaka et al. [623] are implemented in the code and depend on the local properties of the ejecta (ρ, T, and Y_e). Spectral time series are extracted using the technique described by Bulla et al. [141] and used to construct broad-band lightcurves in any desired filter.

5.4.4.2 Supernova models

Templates available within the `SNCosmo` library [76] are used to model supernova spectra. Currently, the `salt2` model for Type Ia supernovae and the `nugent-hyper` model for hypernovae associated with long GRBs are implemented in the framework and have been used in the past [44]. However, the framework is flexible enough such that additional templates for different types of supernovae can be added with minimal effort.

5.4.4.3 Kilonova/Supernova Inference

Our EM inference of kilonovae and GRB afterglows is based on the AB magnitude for a specific filter j, $m_i^j(t_i)$. We assume these measurements to be given as a time series at times t_i with a corresponding statistical error $\sigma_i^j \equiv \sigma^j(t_i)$. The likelihood function $\mathcal{L}_{\rm EM}(\boldsymbol{\theta})$ then reads [181]:

$$\mathcal{L}_{\rm EM} \propto \exp\left(-\frac{1}{2}\sum_{ij}\frac{(m_i^j - m_i^{j,\rm est}(\boldsymbol{\theta}))^2}{(\sigma_i^j)^2 + \sigma_{\rm sys}^2}\right), \tag{5.16}$$

where $m_i^{j,\rm est}(\boldsymbol{\theta})$ is the estimated AB magnitude for the parameters $\boldsymbol{\theta}$ and $\sigma_{\rm sys}$ is the additional error budget for accounting the systematic uncertainty within the electromagnetic signal modeling. The inclusion of $\sigma_{\rm sys}$ is equivalent to adding a shift of Δm to the light curve, for which marginalized with respect to a zero-mean normal distribution with a variance of $\sigma_{\rm sys}^2$.

This likelihood is equivalent to approximating the probability distribution of the spectral flux density f_ν to be a Log-normal distribution. The Log-normal distribution is a 2-parameter maximum entropy distribution with its support equals to the possible range for $f_\nu \in (0, \infty)$. There are two advantages of approximating f_ν with a Log-normal distribution: (i) if the uncertainty is larger or comparable to the measured value, it avoids having non-zero support for the nonphysical $f_\nu < 0$; (ii) if the uncertainty is much smaller than the measured value, the Log-normal distribution approaches the normal distribution.

For kilonovae, we use the same model presented in Dietrich et al. [214]. The model is controlled by four parameters, namely, the dynamical ejecta mass $m_{\rm dyn}^{\rm ej}$, the disk wind ejecta mass $m_{\rm wind}^{\rm ej}$, the half-opening angle of the lanthanide-rich component Φ, and the viewing angle $\theta_{\rm obs}$. Both the dynamical ejecta and the disk wind ejecta are described in methods section 5.4.4.5.

5.4.4.4 GRB Afterglows

In our framework, the computation of the GRB afterglow lightcurves is until now based on the publicly available semi-analytic code `afterglowpy` [651, 566]. The inclusion of other afterglow models is currently ongoing.

The GRB afterglow emission is produced by relativistic electrons gyrating around the magnetic field lines. These electrons are accelerated by the Fermi first-order acceleration (diffusive shock acceleration) and the magnetic field is assumed to be of turbulent nature, amplified by processes acting in collision-less shocks. The complex physics of electron acceleration at shocks is approximated by the equipartition parameters, ϵ_e and ϵ_B, denoting the fraction of the shock energy that goes into the relativistic electrons and magnetic field, respectively, and p, and the slope of the electron energy distribution $dn/d\gamma \propto \gamma^{-p}$, with n being the electron number density and γ being the electron Lorentz factor. The flux density of the curvature radiation is

$$F_\nu = \frac{1}{4\pi d_L^2}\int d\theta d\phi R^2 \sin(\theta)\frac{\epsilon_\nu}{\alpha_\nu}(1 - e^{-\tau}), \tag{5.17}$$

where τ is the optical depth and ϵ_ν and α_ν are the impassivity coefficient and absorption coefficient, respectively. For a fixed power-law distribution of electrons these can be approximated analytically [575]. The synchrotron self-absorption is neglected in this work.

In order to capture the possible dependence of the GRB properties on the polar angle, the jet is discretized into a set of lateral axisymmetric (conical) layers, each of which is characterized by its initial velocity, mass, and angle. Several prescriptions for the initial angular distribution of the jet energy are available in the code. As default, we use the Gaussian jet model with $E \propto E_0 \exp(-\frac{1}{2}(\frac{\theta}{\theta_c})^2)$, where θ_c characterizes the width of the Gaussian. The jet truncation angle is θ_w. We assume the GRB jet to be powered by the accretion of mass from the disk onto the remnant black hole [229, 486, 432, 462]. Consequently, the jet energy is proportional to the leftover disk mass,

$$E_0 = \epsilon \times (1 - \xi) \times m_{\rm disk}, \tag{5.18}$$

where ξ is the fraction of disk mass ejected as wind and ϵ is the fraction of residual disk mass converted into jet energy.

The dynamical evolution of these layers is computed semi-analytically using the "thin-shell approximation" casting energy-conservation equations and shock-jump conditions into a set of evolution equations for the blast wave velocity and radius. Within blast waves, the pressure gradient perpendicular to the normal leads to lateral expansion [650, 286]. In other words, the transverse pressure gradient adds the velocity along the tangent to the blast wave surface, forcing the latter to expand. The lateral expansion is important for late-time afterglow and is included in the code.

Finally, the flux density, F_ν, is obtained by equal arrival time surface integration, Eq. (5.17), taking into account relativistic effects, i.e., that the observed F_ν is composed of contributions from different blast waves that has emitted at different comoving time and at different frequencies.

5.4.4.5 Connecting Electromagnetic Signals to Source properties

To connect the observed GRB, kilonova, and GRB afterglow properties to the binary properties, we rely on phenomenological relations, i.e., fits based on numerical-relativity simulations. For our work, we use the fits presented in Kruger et al. [364] and Dietrich et al. [214] but emphasize that a variety of other fitting formulas exist in the literature [217, 182, 528, 183, 466].

In NMMA, the dynamical ejecta mass $m^{\mathrm{ej}}_{\mathrm{dyn}}$ is connected to the binary properties through the phenomenological relation [364]

$$\frac{m^{\mathrm{ej}}_{\mathrm{dyn,fit}}}{10^{-3}M_\odot} = \left(\frac{a}{C_1} + b\left(\frac{m_2}{m_1}\right)^n + cC_1\right) + (1 \leftrightarrow 2), \tag{5.19}$$

where m_i and C_i are the masses and the compactness of the two components of the binary with best-fit coefficients $a = -9.3335$, $b = 114.17$, $c = -337.56$, and $n = 1.5465$. This relation enables an accurate estimation of the ejecta mass with an error well-approximated by a zero-mean Gaussian with a standard deviation $0.004M_\odot$[364]. Therefore, the dynamical ejecta mass can be approximated as

$$m^{\mathrm{ej}}_{\mathrm{dyn}} = m^{\mathrm{ej}}_{\mathrm{dyn,fit}} + \alpha, \tag{5.20}$$

where $\alpha \sim \mathcal{N}(\mu = 0, \sigma = 0.004M_\odot)$. To determine the disk mass m_{disk}, we follow the description of Dietrich et al. [214],

$$\log_{10}\left(\frac{m_{\mathrm{disk}}}{M_\odot}\right) = \tag{5.21}$$

$$\max\left(-3, a\left(1 + b\tanh\left(\frac{c - (m_1+m_2)M^{-1}_{\mathrm{threshold}}}{d}\right)\right)\right), \tag{5.22}$$

with a and b given by

$$a = a_o + \delta a \cdot \Delta\,, \qquad b = b_o + \delta b \cdot \Delta\,, \tag{5.23}$$

where a_o, b_o, δa, δb, c, and d are free parameters. The parameter Δ is given by

$$\Delta = \frac{1}{2}\tanh\left(\beta\left(q - q_{\mathrm{trans}}\right)\right)\,, \tag{5.24}$$

where $q \equiv m_2/m_1 \leq 1$ is the mass ratio and β and q_{trans} are free parameters. The best-fit model parameters are $a_o = -1.581$, $\delta a = -2.439$, $b_o = -0.538$, $\delta b = -0.406$, $c = 0.953$, $d = 0.0417$, $\beta = 3.910$, $q_{\mathrm{trans}} = 0.900$. The threshold mass $M_{\mathrm{threshold}}$ for a given EOS is estimated as [40]

$$M_{\mathrm{threshold}} = \left(2.38 - 3.606\frac{M_{\mathrm{TOV}}}{R_{1.6}}\right)M_{\mathrm{TOV}}, \tag{5.25}$$

where M_{TOV} and $R_{1.6}$ are the maximum mass of a non-spinning NS and the radius of a $1.6M_\odot$ NS.

We note that we assume that the disk-wind ejecta component is proportional to the disk mass, i.e., $m^{\rm ej}_{\rm wind} = \xi \times m_{\rm disk}$.

5.4.4.6 Bayesian statistics

Based on Bayes' theorem, the posterior distribution of the parameters $p(\boldsymbol{\theta}|d,\mathcal{H})$ under hypothesis $\mathcal{H}$ with data d is given by

$$p(\boldsymbol{\theta}|d,\mathcal{H}) = \frac{p(d|\boldsymbol{\theta},\mathcal{H})p(\boldsymbol{\theta}|\mathcal{H})}{p(d|\mathcal{H})} \equiv \frac{\mathcal{L}(\boldsymbol{\theta})\pi(\boldsymbol{\theta})}{\mathcal{Z}(d)}, \tag{5.26}$$

where $\mathcal{L}(\boldsymbol{\theta})$, $\pi(\boldsymbol{\theta})$, and $\mathcal{Z}(d)$ are the likelihood, prior, and evidence, respectively. The prior describes our knowledge of the source or model parameters prior to the experiment or observation. The likelihood and evidence quantify how well the hypothesis describes the data for a given set of parameters and over the whole parameter space, respectively. Throughout our NMMA pipeline, all data analyses use Bayes' theorem but differences appear due to the functional form of the likelihood and its specific dependence on the source parameters. For example, the GW likelihood is evaluated with a cross-correlation between the data and the GW waveform and the EM signal analysis employs a χ^2 log-likelihood between the predicted lightcurves with the observed apparent magnitude data, however, from a Bayesian viewpoint their treatment is equivalent only with different likelihood functions.

In addition to the posterior estimation, the evidence $\mathcal{Z}$ carries additional information on the plausibility of a given hypothesis $\mathcal{H}$. The evidence is given by

$$\mathcal{Z}(d|\mathcal{H}) = \int d\boldsymbol{\theta} p(d|\boldsymbol{\theta},\mathcal{H})p(\boldsymbol{\theta}|\mathcal{H}) = \int d\boldsymbol{\theta}\mathcal{L}(\boldsymbol{\theta})\pi(\boldsymbol{\theta}), \tag{5.27}$$

which is the normalization constant for the posterior distribution. Moreover, we can compare the plausibilities of two hypotheses, $\mathcal{H}_1$ and $\mathcal{H}_2$, by using the odd ratio $\mathcal{O}^1_2$, which is given by

$$\mathcal{O}^1_2 = \frac{\mathcal{Z}_1}{\mathcal{Z}_2}\frac{p(\mathcal{H}_1)}{p(\mathcal{H}_2)} \equiv \mathcal{B}^1_2\Pi^1_2, \tag{5.28}$$

where $\mathcal{B}^1_2$ and Π^1_2 are the Bayes factor and prior odds, respectively. If $\mathcal{O}^1_2 > 1$, $\mathcal{H}_1$ is more plausible than $\mathcal{H}_2$, and vice versa.

5.5 Supplementary material

5.5.1 Computing generic kilonova lightcurves

Gaussian Process Regression:

Because we are given vectors of photometry or spectra from radiative transfer simulations, we require methods to interpolate between these grids. If we denote the parameters of the models as $\boldsymbol{\Theta}^j$ and the vectors of data as τ, parameterized by the i-th time index, we can create matrices of simulations as $\mathcal{T}_{ij} = [\tau_i(\boldsymbol{\Theta}^j)]$. From these matrices, there are a variety of ways to interpolate these vectors, including direct interpolation of the vectors. Here, instead, we interpolate the principal components of each τ_i. To compute the principal components, we take the singular value decomposition (SVD) of this matrix

$$\mathcal{T} = V\Sigma U^\top. \tag{5.29}$$

The SVD computes orthonormal basis vectors in the columns and rows of V and U. With this new basis, we can project our original τ_i onto the left-singular vector basis

$$s_k(\boldsymbol{\theta}^j) = V_{ki}^\top \tau_i(\boldsymbol{\theta}^j), \tag{5.30}$$

where s_k are the weights of the principal components of the input data $\mathcal{T}_{ij}$. This method has the benefit of maximizing the variance in each subsequent basis vector, meaning we can truncate this sum to minimize computational resources; in our case, we find that using the first 10 basis vectors is sufficient for a reliable representation of the lightcurves.

To interpolate the principal component eigenvalues, we use Gaussian process regression (GPR) [532], which relies on the assumption that the correlation between neighboring values can be represented by a multivariate Gaussian distribution. The covariance between function values is known as a "kernel" function, with many kernel functions commonly used in the literature; in our analysis, we use a rational-quadratic kernel function implemented in `sci-kit learn` [497]:

$$k(\boldsymbol{\theta}^i, \boldsymbol{\theta}^j) = \left(1 + \frac{d(\boldsymbol{\theta}^i, \boldsymbol{\theta}^j)^2}{2\alpha l^2}\right)^{-\alpha} \tag{5.31}$$

where $\alpha = 0.1$ and $l = 1.0$ for our implementation.

As is common in GPR-based interpolation, we first normalize the components of $s_k(\boldsymbol{\theta}^j)$ by subtracting the minimum value and dividing by the difference between the maximum and minimum value. After the interpolation, the de-whitened values are projected back into the time domain:

$$\tau_i(\boldsymbol{\theta}^j) = V_{ik} s_k(\boldsymbol{\theta}^j) \tag{5.32}$$

Finally, the interpolated $\tau_i(\boldsymbol{\theta}^j)$ is then used for the computation of the likelihood.

Neural Networks:

Another alternative method for the grid interpolation is a feed-forward neural network (NN) which can predict the kilonova lightcurves based on the input parameters used by the chosen model [49]. The main advantage of this approach is it to reduce the memory footprint for the lightcurves computation.

To train the NN, we use about 2000 lightcurves computed with the full radiative transfer code POSSIS [138]. These lightcurves are split into a training data set of 90% and an evaluation dataset that contains 10% of all lightcurves. In the pre-processing stage, all the data was normalized between 0 and 1 via the usual MinMax normalization method, and similar to the GPR method, we used PCA data reduction to reduce the dimensions of the output parameter space to 10 components. In addition, we use simple linear interpolation for the cases in which the requested time interval is larger than the original in-hand data.

To develop our NN, we used Keras API from TENSORFLOW[5]. Our NN comprises an input layer with the same number of neurons as the input parameter space, three dense hidden layers with 64, 128, and 128 neurons each, and an output layer with ten neurons for the bolometric luminosity and the nine observational bands. We use the Adam optimizer with a learning rate of 0.01 and a Rectified linear unit as activation function. Finally, the NN is trained using a batch size of 32, epoch count of 15, and mean squared error (MSE) as loss function. To reconstruct the real lightcurves, a series of inverse transformations is applied with respect to the PCA and the normalization. Overall a MSE of 0.0022 is achieved.

The table summarizes the intrinsic parameters for the multi-messenger observation of a BNS merger. In the fourth column, we report median posterior values at 90% credibility for the joint inference of GW170817-and-AT2017gfo-and-GRB170817A. $\mathcal{U}(a,b)$ refers to uniform distribution between a and b. $\log\mathcal{U}(a,b)$ refers to the log-uniform (of base 10) distribution, i.e. if $X \sim \log\mathcal{U}(a,b)$, $\log_{10} X \sim \mathcal{U}(a,b)$. $\mathcal{N}(\mu,\sigma)$ refers to a normal distribution with mean μ and variance of σ^2.
The table summarizes the intrinsic parameters for the multi-messenger observation of a BNS merger

TABLE 5.2
Posterior of and prior used for the GW170817-and-AT2017gfo and GW170817-and-AT2017gfo-GRB170817A analysis.

Parameter	Name	Connection with other parameters	prior	Posterior
m_i	Component mass	-	$\mathcal{U}(0.5M_\odot, 4.3M_\odot)$	$m_1 = 1.41^{+0.05}_{-0.05}M_\odot$
				$m_2 = 1.31^{+0.04}_{-0.04}M_\odot$
EOS	Equation-of-state of nuclear matter	-	$\mathcal{U}(1, 5000)$	$\text{EOS} = 4734.09^{+253.85}_{-304.07}$
$\mathbf{s}_i$	Component spin	-	Uniform on a sphere	$\mathbf{s}_1 = (0.00^{+0.02}_{-0.02}, 0.00^{+0.02}_{-0.02}, 0.00^{+0.01}_{-0.01})$
			with $\|\mathbf{s}_i\| < 0.05$	$\mathbf{s}_2 = (0.00^{+0.02}_{-0.02}, 0.00^{+0.02}_{-0.02}, 0.00^{+0.01}_{-0.01})$
Λ_i	Tidal deformability	$\Lambda(m_i; \text{EOS})$	-	$\Lambda_1 = 352.71^{+107.84}_{-114.83}$
			-	$\Lambda_2 = 530.26^{+135.03}_{-116.34}$
C_i	Compactness	$C_i = C(m_i; \text{EOS})$	-	$C_1 = 0.17^{+0.01}_{-0.01}$
			-	$C_2 = 0.16^{+0.01}_{-0.01}$
α	Dynamical ejecta mass fitting error	-	$\mathcal{N}(0M_\odot, 0.0004M_\odot)$	$\alpha = -0.00005^{+0.0005}_{-0.0006}M_\odot$
$m^{\text{ej}}_{\text{dyn}}$	Dynamical ejecta mass	$m^{\text{ej}}_{\text{dyn}} = m^{\text{ej}}_{\text{dyn,fit}}(m_i, C_i) + \alpha$	-	$\log_{10}(m^{\text{ej}}_{\text{dyn}}/M_\odot) = -2.25^{+0.10}_{-0.07}$
$M_{\text{threshold}}$	Threshold mass	$M_{\text{threshold}} = M_{\text{threshold}}(\text{EOS})$	-	$M_{\text{threshold}} = 3.76^{+0.10}_{-0.09}M_\odot$
m_{disk}	Disk mass	$m_{\text{disk}} = m_{\text{disk}}(m_i, M_{\text{threshold}})$	-	$\log_{10}(m_{\text{disk}}/M_\odot) = -0.76^{+0.02}_{-0.01}$
ξ	Fraction of the disk mass ejected as wind	-	$\mathcal{U}(0, 1)$	$\xi = 0.61^{+0.18}_{-0.17}$
$m^{\text{ej}}_{\text{wind}}$	Wind ejecta mass	$m^{\text{ej}}_{\text{wind}} = \xi \times m_{\text{disk}}$	-	$\log_{10}(m^{\text{ej}}_{\text{wind}}/M_\odot) = -1.18^{+0.08}_{-0.09}$
Φ	Lanthanide-rich composition opening angle	-	$U(15\text{deg}, 75\text{deg})$	$\Phi = 68.69^{+4.77}_{-4.61}\text{deg}$
ϵ	Fraction of leftover disk mass converted to GRB jet energy	-	$\log\mathcal{U}(-7, -0.3)$	$\epsilon = 0.04^{+0.23}_{-0.04}$
E_0	GRB jet on-axis isotropic energy	$E_0 = \epsilon \times (1 - \xi) \times m_{\text{disk}}$	$\log\mathcal{U}(48, 60)$	$\log_{10}(E_0/\text{erg}) = 51.45^{+1.05}_{-1.24}$
θ_c	Half-width of the jet core	-	$\mathcal{U}(0.01\text{rad}, \pi/2\text{rad})$	$\theta_c = 0.37^{+0.60}_{-0.29}$ rad
θ_w	Truncation angle of the jet	-	$\mathcal{U}(0.01\text{rad}, \pi/2\text{rad})$	$\theta_w = 0.24^{+0.11}_{-0.09}$ rad
n_0	Number density of ISM	-	$\log\mathcal{U}(-6, 0)$	$\log_{10}(n_0/\text{cm}^{-3}) = -3.96^{+1.62}_{-1.73}$
p	Electron distribution power-law index	-	$\mathcal{U}(2, 5)$	$p = 2.11^{+0.07}_{-0.06}$
ϵ_e	Thermal energy fraction in electrons	-	$\log\mathcal{U}(-4, 0)$	$\log_{10}\epsilon_e = -0.77^{+0.77}_{-1.05}$
ϵ_B	Thermal energy fraction in magnetic field	-	$\log\mathcal{U}(-5, 0)$	$\log_{10}\epsilon_B = -2.39^{+2.26}_{-1.64}$
$R_{1.4}$	Radius of a $1.4M_\odot$ neutron star	$R_{1.4}(\text{EOS})$	-	$R_{1.4} = 11.98^{+0.35}_{-0.40}\text{km}$

TABLE 5.3
Posterior of and prior used for the GW170817-and-AT2017gfo and GW170817-and-AT2017gfo-GRB170817A analysis with the model from Ref.[342].

Parameter	Name	Connection with other parameters	prior	Posterior
m_i	Component mass	-	$\mathcal{U}(0.5M_\odot, 4.3M_\odot)$	$m_1 = 1.46^{+0.07}_{-0.08} M_\odot$
				$m_2 = 1.28^{+0.07}_{-0.06} M_\odot$
EOS	Equation-of-state of nuclear matter	-	$\mathcal{U}(1, 5000)$	$\text{EOS} = 4686.33^{+289.78}_{-432.21}$
$\mathbf{s}_i$	Component spin	-	Uniform on a sphere	$\mathbf{s}_1 = (0.00^{+0.02}_{-0.02}, 0.00^{+0.02}_{-0.02}, 0.00^{+0.01}_{-0.01})$
			with $\lvert\mathbf{s}_i\rvert < 0.05$	$\mathbf{s}_2 = (0.00^{+0.02}_{-0.02}, 0.00^{+0.02}_{-0.02}, 0.00^{+0.01}_{-0.01})$
Λ_i	Tidal deformability	$\Lambda(m_i; \text{EOS})$	-	$\Lambda_1 = 272.25^{+118.90}_{-117.36}$
			-	$\Lambda_2 = 594.23^{+178.28}_{-156.80}$
C_i	Compactness	$C_i = C(m_i; \text{EOS})$	-	$C_1 = 0.18^{+0.01}_{-0.01}$
			-	$C_2 = 0.16^{+0.01}_{-0.01}$
α	Dynamical ejecta mass fitting error	-	$\mathcal{N}(0M_\odot, 0.0004M_\odot)$	$\alpha = -0.00002^{+0.0005}_{-0.0006} M_\odot$
$m^{\text{ej}}_{\text{dyn}}$	Dynamical ejecta mass	$m^{\text{ej}}_{\text{dyn}} = m^{\text{ej}}_{\text{dyn,fit}}(m_i, C_i) + \alpha$	-	$\log_{10}(m^{\text{ej}}_{\text{dyn}}/M_\odot) = -2.17^{+0.16}_{-0.13}$
$M_{\text{threshold}}$	Threshold mass	$M_{\text{threshold}} = M_{\text{threshold}}(\text{EOS})$	-	$M_{\text{threshold}} = 3.05^{+0.08}_{-0.09} M_\odot$
m_{disk}	Disk mass	$m_{\text{disk}} = m_{\text{disk}}(m_i, M_{\text{threshold}})$	-	$\log_{10}(m_{\text{disk}}/M_\odot) = -0.93^{+0.18}_{-0.19}$
ξ	Fraction of the disk mass ejected as wind	-	$\mathcal{U}(0, 1)$	$\xi = 0.26^{+0.13}_{-0.12}$
$m^{\text{ej}}_{\text{wind}}$	Wind ejecta mass	$m^{\text{ej}}_{\text{wind}} = \xi \times m_{\text{disk}}$	-	$\log_{10}(m^{\text{ej}}_{\text{wind}}/M_\odot) = -1.52^{+0.11}_{-0.11}$
$m^{\text{ej}}_{\text{tot}}$	Total ejecta mass	$m^{\text{ej}}_{\text{tot}} = m^{\text{ej}}_{\text{dyn}} + m^{\text{ej}}_{\text{wind}}$	-	$\log_{10}(m^{\text{ej}}_{\text{tot}}/M_\odot) = -1.43^{+0.09}_{-0.09}$
v^{ej}	Ejecta velocity	-	$\log\mathcal{U}(-1, -0.6)$	$\log_{10}(v^{\text{ej}}/c) = -0.74^{+0.06}_{-0.07}$
X_{lan}	Lanthanide mass fraction	-	$\log\mathcal{U}(-5, -2)$	$\log_{10} X_{\text{lan}} = -3.38^{+0.13}_{-0.12}$
ϵ	Fraction of leftover disk mass converted to GRB jet energy	-	$\log\mathcal{U}(-7, -0.3)$	$\epsilon = 0.01^{+0.12}_{-0.01}$
E_0	GRB jet on-axis isotropic energy	$E_0 = \epsilon \times (1 - \xi) \times m_{\text{disk}}$	$\log\mathcal{U}(48, 60)$	$\log_{10}(E_0/\text{erg}) = 51.33^{+1.17}_{-0.99}$
θ_c	Half-width of the jet core	-	$\mathcal{U}(0.01\text{rad}, \pi/2\text{rad})$	$\theta_c = 0.12^{+0.36}_{-0.06}$ rad
θ_w	Truncation angle of the jet	-	$\mathcal{U}(0.01\text{rad}, \pi/2\text{rad})$	$\theta_w = 0.42^{+0.28}_{-0.19}$ rad
n_0	Number density of ISM	-	$\log\mathcal{U}(-6, 0)$	$\log_{10}(n_0/\text{cm}^{-3}) = -2.87^{+1.56}_{-1.53}$
p	Electron distribution power-law index	-	$\mathcal{U}(2, 5)$	$p = 2.11^{+0.06}_{-0.06}$
ϵ_e	Thermal energy fraction in electrons	-	$\log\mathcal{U}(-4, 0)$	$\log_{10}\epsilon_e = -0.61^{+0.61}_{-1.09}$
ϵ_B	Thermal energy fraction in magnetic field	-	$\log\mathcal{U}(-5, 0)$	$\log_{10}\epsilon_B = -2.44^{+1.85}_{-1.9}$
$R_{1.4}$	Radius of a $1.4M_\odot$ neutron star	$R_{1.4}(\text{EOS})$	-	$R_{1.4} = 11.86^{+0.37}_{-0.49}$km

using the kilonova model described in Ref. [342]. In the fourth column, we report median posterior values at 90% credibility for the joint inference of GW170817-and-AT2017gfo-and-GRB170817A. $\mathcal{U}(a,b)$ refers to uniform distribution between a and b. $\log\mathcal{U}(a,b)$ refers to the log-uniform (of base 10) distribution, i.e., if $X \sim \log\mathcal{U}(a,b)$, $\log_{10} X \sim \mathcal{U}(a,b)$. $\mathcal{N}(\mu,\sigma)$ refers to a normal distribution with mean μ and variance of σ^2.

5.5.2 EOS Sampling

For a set of EOSs, such as our sets constrained by chiral EFT, our framework is able to directly sample over EOSs instead of sampling over the masses and tidal deformabilities independently. Since these EOSs relate masses and tidal deformabilities based on nuclear-physics information, the tidal deformabilities can be computed for a given mass and EOS according to

$$p(\Lambda_i|m_i,\mathrm{EOS}) = \delta(\Lambda_i - \Lambda(m_i;\mathrm{EOS})). \tag{5.33}$$

This feature enables the possibility to include more physical information on the NS sources during parameter estimation ab initio and can be used through the installation of additional BILBY and PARALLEL BILBY patches that come along with our NMMA framework. Another advantage of this functionality is that information from multiple simulations can be combined to compute a combined posterior because the EOS is a common parameter for all NSs [370].

5.5.3 Combined Sampling

To extract most information from the GW and the EM data, we perform a full parameter estimation combining both likelihoods. The 'full' likelihood $\mathcal{L}$ is given by

$$\mathcal{L}(\boldsymbol{\theta}) = \mathcal{L}_{\mathrm{GW}}(\boldsymbol{\theta}_{\mathrm{GW}}) \times \mathcal{L}_{\mathrm{EM}}(\boldsymbol{\theta}_{\mathrm{EM}}), \tag{5.34}$$

where $\boldsymbol{\theta} = \{\boldsymbol{\theta}_{\mathrm{GW}}, \boldsymbol{\theta}_{\mathrm{EM}}\}$. Because the lightcurve models and the GW waveform models depend on different sets of parameters, simply sampling over all of the parameters would not yield a stronger constraint on the parameters of interest. Therefore, it is key to use connections between different parameters at the prior level. In particular, a few parameters describing the EM signals can be determined by the binary masses and the EOS. For instance, the dynamical ejecta mass $m^{\mathrm{ej}}_{\mathrm{dyn}}$ and the disk mass m_{disk} are connected to the binary properties through the relations discussed in the methods section. The details for all the parameters are summarized in Supplementary Tab. 5.2.

5.5.4 Scaling

Due to the enormous computational burden of simultaneously analysing both the EM and GW signals, we have to ensure a good parallelization of our code. For the NMMA framework, the parallelization is achieved by taking advantage of the flexibility of `dynesty` [611] and based on the interface presented in `parallel_bilby` [606].

In particular, the nested sampling process is parallelized using a head/worker strategy. The "head" organizes the live/dead points, and validates if the stopping criteria are reached, while the "workers" find new live points under the likelihood constraint. The theoretical scaling performance of such a strategy is given by [296]

$$T(N_{\mathrm{cores}}) = T(N_{\mathrm{core}_{\mathrm{ref}}}) \times \frac{\ln(1 + N_{\mathrm{core}_{\mathrm{ref}}}/n_{\mathrm{live}})}{\ln(1 + N_{\mathrm{cores}}/n_{\mathrm{live}})}, \tag{5.35}$$

where $T(N_{\mathrm{cores}})$ is the runtime using N_{cores} cores and $T(N_{\mathrm{core}_{\mathrm{ref}}})$ is the reference time using $N_{\mathrm{core}_{\mathrm{ref}}}$ cores. The parameter n_{live} denotes the number of live points.

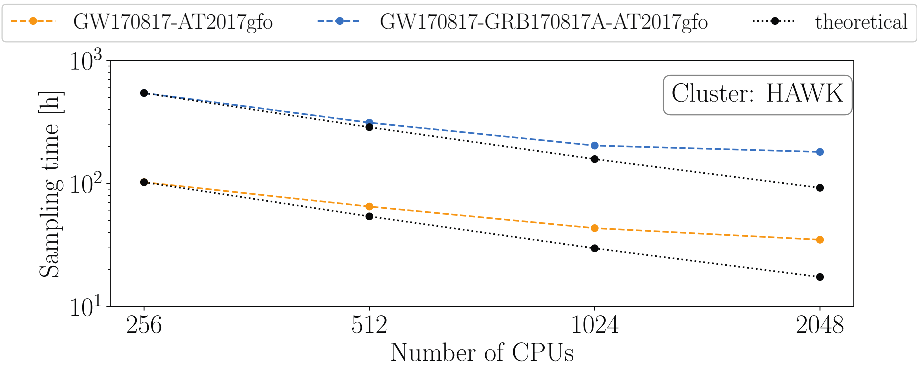

FIGURE 5.5
Scaling performance of the NMMA framework. Theoretical against measured scaling performance for the inference runs of GW170817-AT2017gfo and GW170817-GRB170817A-AT2017gfo on 256, 512, 1024, and 2048 cores, respectively. The theoretical scaling is computed for 256 cores using the reference time $T(N_{\mathrm{core}_{\mathrm{ref}}}) = 102.49$ h for GW170817-AT2017gfo and $T(N_{\mathrm{core}_{\mathrm{ref}}}) = 543.45$ h for GW170817-GRB170817A-AT2017gfo.

To validate if such a scaling is achieved, we performed intensive scaling tests on SuperMUC_NG at the Leibniz Supercomputing Centre (Munich), Lise and Emmy of the North German Supercomputing Alliance, and on HAWK of the High-Performance Computing Center Stuttgart. We show results for scaling tests performed on HAWK using AMD EPYC 7742 processors. The tests are based on a full joint inference of GW170817-and-AT2017gfo and GW170817-and-GRB170817A-and-AT2017gfo which includes intermediate checkpointing and all necessary I/O-operations. The strong scaling for such simulations is shown in Supplementary Fig. 5.5 and is compared to the theoretical scaling mentioned of Eq. (5.35).

5.5.5 Modelling Uncertainty

Overall, the obtained multi-messenger constraints depend noticeably on the robustness and accuracy of the individual GW, kilonova, and GRB afterglow models but also on the uncertainty and accuracy of the underlying equations of state and nuclear physics computations. In the past, there have been numerous studies considering the effect of GW-model uncertainties, e.g., [572, 573, 370] and we have already employed multiple GW models in one of our previous studies also to investigate uncertainties with the conclusion that with the current amount of observational data, we are mainly limited by statistical and not systematic uncertainties [214]. As an example of the influence of the particular choice of the kilonova model, we employ two different kilonova models with different assumptions about the geometry and composition of the ejecta. In particular, we compare the results for our standard kilonova model as presented in Supplementary Tab. 5.2 with the results based on the model of Kasen et al. [342] in Supplementary Tab. 5.3. While we find that individual parameters can be different, we find a similar neutron star radius of $R_{1.4} = 11.86^{+0.37}_{-0.49}$km.

5.5.6 Effect of systematic uncertainty budget

To investigate the effect of the value chosen for the systematics uncertainty budget, the analysis on the GW170817-AT2017gfo-GRB170817A event has been conducted with three different values of σ_{sys}, namely, 0.5mag, 1mag and 2mag.
To gauge the effect on the final equation-of-state constraint, the resulting posterior of the radius of

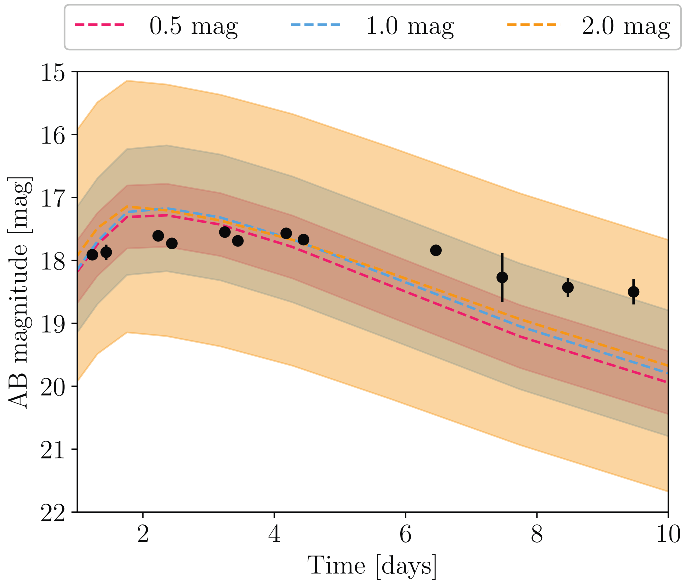

FIGURE 5.6
Best-fit early-time lightcurve from the analysis with various σ_{sys}. The best-fit K-filter lightcurve (dashed, with the one magnitude uncertainty shown as the band) for AT2017gfo data when analysing GW170817-and-AT2017gfo-and-GRB170817A simultaneously with different σ_{sys}.

a $1.4M_{\odot}$ neutron star, $R_{1.4}$, for these different σ_{sys} are compared. The median values with the 90% credible interval as uncertainties, are shown in Supplementary Tab. 5.4.

TABLE 5.4
Comparison of radius measurements of a $1.4M_{\odot}$ neutron star for different σ_{sys}.

σ_{sys} [mag]	$R_{1.4}$ [km]
0.5	$12.05^{+0.35}_{-0.45}$
1.0	$11.98^{+0.35}_{-0.40}$
2.0	$11.76^{+0.41}_{-0.49}$

The resulting radius measurements of a $1.4M_{\odot}$ neutron star for σ_{sys} being 0.5, 1.0 and 2.0 are shown.

With lower values of σ_{sys}, the estimated $R_{1.4}$ is skewed towards higher values, with the minimal uncertainty at 1mag. Therefore, it hints that

- the information from difference channels are more coherent at 1mag as compare to 0.5mag
- the information is not over diluted in 1mag as compare to 2mag.

To verify the above claim, we investigate into the estimated best-fit lightcurves. In particular, the best-fit lightcurves with the associated error budget for filter K is shown at Supplementary Fig. 5.6. One can see that the 0.5mag is underestimating the systematic uncertainty and failed to account for the data after 6 days after the merger, while the 2mag is overcompensating for the systematic uncertainty. Based on the above observations, we concluded that the σ_{sys} of 1mag is a sensible choice.

Part IV

The impact of gravitational waveform model systematics

6

Quantifying modeling uncertainties when combining multiple gravitational-wave detections from binary neutron star sources

CONTENTS

*This chapter is based on the article by **Nina Kunert**, Peter T. H. Pang, Ingo Tews, Michael W. Coughlin, Tim Dietrich published in Physical Review D (2022), Vol. 105, L061301. I carried out parameter estimation simulations in collaboration with Dr. Peter Pang, performed data analysis, visualized results, and authored the manuscript. Preliminary findings were presented in my master's thesis, while the final publication provides a refined analysis and extended investigations to evaluate the impact of systematic biases.*

Editorial notes: Appendix A has been integrated in the Section 6.2 and additional citations have been included beyond those in the published version.

Abstract: With the increasing sensitivity of gravitational-wave detectors, we expect to observe multiple binary neutron-star systems through gravitational waves in the near future. The combined analysis of these gravitational-wave signals offers the possibility to constrain the neutron-star radius and the equation of state of dense nuclear matter with unprecedented accuracy. However, it is crucial to ensure that uncertainties inherent in the gravitational-wave models will not lead to systematic biases when information from multiple detections are combined. To quantify waveform systematics, we perform an extensive simulation campaign of binary neutron-star sources and analyse them with a set of four different waveform models. Based on our analysis with about 38 simulations, we find that statistical uncertainties in the neutron-star radius decrease to ± 250m (2% at 90% credible interval) but that systematic differences between currently employed waveform models can be twice as large. Hence, it will be essential to ensure that systematic biases will not become dominant in inferences of the neutron-star equation of state when capitalizing on future developments.

6.1 Introduction

Gravitational waves (GWs) emitted from binary neutron-star (BNS) coalescences allow us to probe the equation of state (EOS) of dense nuclear matter. This was successfully demonstrated by the LIGO-Virgo Collaboration and other research groups following the first GW observation of a BNS system, GW170817, using Bayesian analyses of the GW signal [10, 16, 13, 15, 200]. Such constraints have been further improved in numerous multi-messenger analyses, e.g., Refs. [83, 55, 451, 13, 526, 188, 311, 153, 214, 388, 524, 324], by incorporating data from associated electromagnetic observations, AT2017gfo and GRB170817A [9], nuclear-physics computations [300, 55, 630], nuclear-physics experiments [196, 563, 37], as well as radio and X-ray observations of isolated neutron stars (NSs) [57, 63, 256, 446, 547, 447, 548].

Extracting information from observational data always requires certain modeling assumptions. For example, to infer information from the measured GW data, it is necessary to cross-correlate the observed GW signal with theoretical models describing the compact binary coalescence for various binary parameters. Following this approach, the matching introduces systematic uncertainties that originate from the approximations made to describe the general relativistic two-body problem. These approximations range from an analytical description using the Post-Newtonian (PN) framework [108], the effective-one-body (EOB) model [142, 143] to numerical-relativity simulations, e.g., Refs. [69, 216]. Since it is expected that statistical uncertainties will be reduced for high signal-to-noise ratio (SNR) signals or when multiple signals are combined, systematic uncertainties introduced by the waveform models will become increasingly prominent and it is crucial to understand all sources of systematic uncertainties for a reliably quantification of EOS constraints.

Previous studies have shown that EOS constraints based on tidal deformabilities extracted from GW170817 were dominated by statistical uncertainties, e.g., Ref. [13], and that systematic biases were under control, i.e., noticeably smaller than statistical ones. For example, Ref. [225] performed an injection study to investigate systematic uncertainties from different GW models and found systematic biases for GW170817 to be small. However, for similar sources observed at Advanced LIGO and Advanced Virgo design sensitivity, different waveform models can lead to noticeable biases, i.e., the recovered 90% credible intervals would not contain the injected values. Similarly, Ref. [572] used simulated, non-spinning GW170817-like sources measured at design sensitivity and found that for unequal masses the obtained tidal parameters can get noticeably biased. This work was extended by Ref. [573] by studying the imprint of precession and source localization obtained through a possible electromagnetic counterpart. Ref. [269] found that existing GW waveform models used for the analysis of GW170817 will be dominated by systematic uncertainties for SNRs above 80. Finally, very recently, Ref. [167] discussed numerous systematic biases that enter GW analyses outlining the importance of waveform systematics.

As pointed out in, e.g., Refs. [204, 39, 376, 673], even low SNR signals can be used and combined to constrain the tidal deformability parameter to an accuracy of $\sim 10\%$ with only a few tens of detections; cf. also Refs. [246, 655]. Using such a procedure, systematic biases are introduced through "stacking," i.e., combining multiple GW measurements. However, to our knowledge no study to date has addressed waveform systematics introduced through the stacking of signals within a realistic injection study. Here, we address this issue and determine at which point systematic biases dominate. We use a set of 38 simulated signals analysed with four different waveform models and perform a total of 152 BNS parameter estimation simulations assuming Advanced GW detectors at design sensitivity [1, 34]. Throughout this work, geometric units are used by setting $G = c = 1$. Further notations are $M = M_A + M_B$ for a system's total mass, $q = M_A/M_B$ for the mass ratio, and Λ_A, Λ_B for individual tidal deformabilities of the stars in a binary.

6.2 Methodology

By using Bayes' theorem, the posterior $p(\vec{\theta}|d,\mathcal{H})$ on the parameters $\vec{\theta}$ under hypothesis $\mathcal{H}$ and with data d is given by

$$p(\vec{\theta}|d,\mathcal{H}) = \frac{p(d|\vec{\theta},\mathcal{H})p(\vec{\theta}|\mathcal{H})}{p(d|\mathcal{H})}, \tag{6.1}$$

where $p(d|\vec{\theta},\mathcal{H})$, $p(\vec{\theta}|\mathcal{H})$, and $p(d|\mathcal{H})$ are the likelihood, prior, and evidence, respectively. The prior describes our knowledge of the parameters before the observation. It also naturally acts as a gateway for additional observations to be included as part of the analysis. The likelihood quantifies how well the hypothesis describes the data at a given point θ in the parameter space and the evidence marginalizes over the whole parameter space. By assuming Gaussian noise, the likelihood $p(d|\vec{\theta},\mathcal{H})$ of a GW signal $h(\vec{\theta})$ with parameters $\vec{\theta}$ embedded in the data d is given by [652]

$$p(d|\vec{\theta},\mathcal{H}) \propto \exp\left(-2\int_{f_{\rm low}}^{f_{\rm high}} \frac{|\tilde{d}(f) - \tilde{h}(f;\vec{\theta})|^2}{S_n(f)}df\right), \tag{6.2}$$

where $\tilde{n}(f)$ and $\tilde{h}(f)$ are the Fourier transform of $n(t)$ and $h(t;\vec{\theta})$, $S_n(f)$ is the one-sided power spectral density of the noise. In our study, all simulations are performed in stationary Gaussian noise assuming Advanced LIGO [1] and Advanced Virgo [34] design sensitivity and we set $f_{\rm low}$ and $f_{\rm high}$ to 20 Hz and 2048 Hz.

The evidence $p(d|\mathcal{H})$ is given by

$$p(d|\mathcal{H}) = \int_{\mathcal{V}} p(d|\vec{\theta},\mathcal{H})p(\vec{\theta}|\mathcal{H})d\vec{\theta}, \tag{6.3}$$

which is the normalization constant for the posterior distribution. The landscape of the likelihood function is explored using the nested sampling algorithm [603] implemented in PARALLEL BILBY [606].

6.2.1 Combining information from multiple detections

Extracting tidal effects from GW data requires information about the EOS. In this study, we will use EOSs that are constrained by chiral effective field theory (EFT) at low densities [630, 633]. Chiral EFT is a systematic theory for nuclear forces that provides an order-by-order scheme for the interactions among neutrons and protons [236, 406]. These interactions can then be used in microscopic studies of dense matter up to densities of ~ 2 times the nuclear saturation density ($n_{\rm sat} = 0.16\,{\rm fm}^{-3}$). In Ref. [214], 5000 EOSs constrained by quantum Monte Carlo calculations using chiral EFT interactions up to $1.5n_{\rm sat}$ were computed. For this article, we employ the most-likely EOS of Ref. [214] for all of our BNS injections. During the parameter estimation, instead of sampling masses and tidal deformabilities independently, we sample from the same set of 5000 EOSs. These EOSs relate masses and tidal deformabilities based on nuclear-physics information. The tidal deformabilities are then computed for a given mass and EOS via

$$p(\Lambda_i|m_i,{\rm EOS}) = \delta(\Lambda_i - \Lambda(m_i;{\rm EOS})), \tag{6.4}$$

with m_i and Λ_i denoting the mass and tidal deformability of the stars.

In addition to the tidal behavior, the EOS also determines the maximum allowed mass $M_{\rm max}$ for NSs. Therefore, we choose a uniform NS mass distribution given by

$$p(m_1,m_2|{\rm EOS}) = \frac{2\Theta(m_1-m_2)\Theta(M_{\rm max}-m_1)}{(M_{\rm max}-M_{\rm min})^2}, \tag{6.5}$$

where $M_{\rm min}$ is the minimum NS mass and Θ is the Heaviside step function. We choose $M_{\rm min}$ to be $0.5M_\odot$.

For the EOS prior probability, the mass measurements of PSR J0348+0432 [57], PSR J1614-2230 [63], and PSR J0740+6620 [256] are taken into account, similar to the approach outlined in Ref. [214]. The prior gives rise to $R_{1.4} = 12.24^{+1.21}_{-1.44}$km (at 90% credibility). In contrast to [214], the NICER observation of PSR J0030+0451 [446, 547] and the upper bound on $M_{\max}$ derived from GW170817 [542] are not included here to avoid masking the systematic uncertainties in the GW analysis by additional information.

Since the EOS is a common parameter, we can combine the information from multiple simulations to compute the combined posterior, $p_c(\vec{\theta})$. With $N_{\rm obs}$ detections $\{d_i\}$ it is given as

$$p_c(\mathrm{EOS}|\{\vec{d_i}\}) = p(\mathrm{EOS})^{1-N_{\rm obs}} \prod_{i=1}^{N_{\rm obs}} p_i(\mathrm{EOS}|\{\vec{d_i}\}), \tag{6.6}$$

in which $p_i(\mathrm{EOS}|\{d_i\})$ is the EOS posterior given the i-th simulation and $p(\mathrm{EOS})$ refers to the prior employed. To correct the selection bias introduced by non-uniform detectability across sources, we follow Ref. [414] to compute the joint posterior for the EOS as

$$p_c(\mathrm{EOS}|\{\vec{d_i}\}) = p(\mathrm{EOS})^{1-N_{\rm obs}} \prod_{i=1}^{N_{\rm obs}} \frac{p_i(\mathrm{EOS}|\{\vec{d_i}\})}{\int d\vec{\theta} p_{\rm det}(\vec{\theta}) p(\vec{\theta}|\mathrm{EOS})}, \tag{6.7}$$

where $p_{\rm det}(\vec{\theta})$ is the probability of detecting the GW signal corresponding to the source parameters $\vec{\theta}$. In this work, a threshold SNR of 7 is enforced for the detections and we estimate $p_{\rm det}(\vec{\theta})$ using a neural-network classifier as described in Ref. [277] trained on the BNS parameter distributions.

6.2.2 Waveform models

The frequency-domain representation of a gravitational waveform can be written as

$$\tilde{h}(f) = \tilde{A}(f) e^{-\mathrm{i}\psi(f)}, \tag{6.8}$$

with the frequency f, the amplitude $\tilde{A}(f)$, and GW phase $\psi(f)$. The phase can be further decomposed into

$$\psi(f) = \psi_{\rm pp}(f) + \psi_{\rm SO}(f) + \psi_{\rm SS}(f) + \psi_{\rm T}(f) + \cdots, \tag{6.9}$$

with $\psi_{\rm pp}$ being the non-spinning point-particle contribution, $\psi_{\rm SO}$ corresponding to contributions caused by spin-orbit coupling, $\psi_{\rm SS}$ to contributions caused by spin-spin effects, and $\psi_{\rm T}$ denoting the tidal effects present in the GW phase. We note that higher-order effects, e.g., cubic-in-spin, could also be included.

The dominant quantity describing EOS-related tidal effects on the GW signal is the mass-weighted tidal deformability [309, 308, 246]

$$\tilde{\Lambda} = \frac{32}{39} \left[\left(1 + 12\frac{X_B}{X_A}\right) \left(\frac{X_A}{C_A}\right)^5 k_2^A + (A \leftrightarrow B) \right], \tag{6.10}$$

with the compactness parameters of the individual undisturbed stars $C_{A,B} = M_{A,B}/R_{A,B}$, the Love numbers $k_2^{A,B}$ [308, 193, 104], and $X_{A,B} = M_{A,B}/(M_A + M_B)$. The leading-order PN contribution to the tidal phase, proportional to $\tilde{\Lambda}$, starts at the 5PN order, i.e., becomes most relevant at the late inspiral; cf. Fig. 2 of Ref. [216]. To quantify the modelling systematics, we employ four different GW waveform models: TaylorF2 (TF2), IMRPhenomD_NRTidal (PhenDNRT), IMRPhenomD_NRTidalv2 (PhenDNRTv2), SEOBNRv4_ROM_NRTidalv2 (SEOBNRTv2). These models are based on different point-particle and tidal descriptions and, hence, lead to different estimates on the intrinsic source properties. The variety of GW models allows us to disentangle the effects of the tidal contribution, comparing PhenDNRT vs. PhenDNRTv2, and the point-particle information, comparing PhenDNRTv2 vs. SEOBNRTv2. The comparison with TF2 serves as a "worst case" scenario

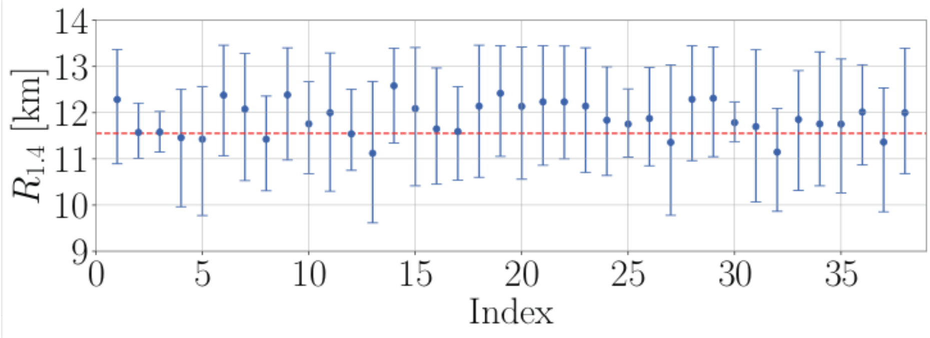

FIGURE 6.1
Constraints on the radius of a typical NS, $R_{1.4}$, from simulated raw data for the injection model PhenDNRTv2. The radius for the injected EOS is shown as red dashed line.

since point-particle and tidal contributions are varied with respect to the injected waveform set (see Appendix 6.5).

An easy interpretation of the tidal contribution for our employed models can be extracted from Figs. 3 and 4 of Ref. [212]. NRTidalv2 predicts larger tidal effects than TaylorF2 and smaller tidal effects than NRTidal for the same tidal deformability. Hence, it is expected that NRTidal models will predict smaller NS radii and TaylorF2 will potentially predict larger radii with respect to our reference model NRTidalv2. Considering the differences in the employed point-particle contributions, we refer to Fig. 3 of Ref. [572], where it was found that when using the same tidal contribution, both TaylorF2 and SEOBNRv4_ROM lead to smaller estimated tidal deformabilities than IMRPhenomD. A summary of the expected biases and the final results is given in Tab. 6.1.

6.2.3 Injection setup

We simulate a network of interferometers consisting of Advanced LIGO and Advanced Virgo at design sensitivity [1, 34]. The BNS sources in our injection set are uniformly distributed in a co-moving volume with the optimal network SNR $\rho \in [7, 100]$. The sources' sky locations (α, δ) and orientations (ι, ψ) are placed uniformly on a sphere. Based on the observed BNS population, the spins of NSs are expected to be small [481]. We restrict the spin magnitudes of the two stars (a_1, a_2) to be uniformly distributed, $a_i \in [-0.05, 0.05]$. The component masses are sampled from a uniform distribution of $m_{1,2} \in [1, 2]\ M_\odot$. For our 38 BNS setups, we have used PhenDNRTv2 as injection model and employed the most-likely EOS of Ref. [214], leading to an injected radius of a typical $1.4 M_\odot$ NS, $R_{1.4}$, of ~ 11.55km, corresponding to a dimensionless tidal deformability of $\Lambda_{1.4} \sim 292.5$. We have used the four different models for the recovery, leading to a total of 152 inference runs.

6.3 Results

6.3.1 Radius measurements and intrinsic biases

In Fig. 6.1, we present our preliminary results for the NS radius, $R_{1.4}$, for the injection model PhenDNRTv2 for each individual injected GW event denoted through a random identifier (index). The uncertainties reflect the 90% confidence intervals. Depending on the source properties, the SNR and the particular noise realisation, different GW events place tighter or weaker constraints on the neutron star radius. To improve our radius estimate on the underlying EOSs, one can combine multiple GW events. In Fig. 6.2, we show the $R_{1.4}$ results for successively combined GW events. Fig. 6.2(a) clearly shows that the combination of multiple GW events significantly reduces the uncertainty of a NS radius measurement. Furthermore, in order to avoid an arbitrary ordering effect in our simulated BNS population, we randomly shuffle the order (indexed events as shown in Fig. 6.1) of the 38 simulated events for 1000 times and compute the median over all permutations; cf. Fig. 6.2(b).

At this stage, our study still includes an additional selection bias in our BNS population due to our inability of detecting arbitrarily weak GW signals [414]. Therefore, we are systematically more sensitive to sources with higher SNRs. This means that more massive binaries are favoured due to their high SNRs[1]. Because these systems also correspond to lower tidal deformabilities, this selection effect could lead to smaller $R_{1.4}$-predictions. When correcting for this selection bias using the neural network classifier of Ref. [277], we obtain our final result for $R_{1.4}$ shown in Fig. 6.2(c). As can be seen in Fig. 6.2(b)-(c), we recover the expected $\sim 1/\sqrt{N}$ falloff of the statistical uncertainty of the radius measurement, where N denotes the number of combined GW detections. When all GW events are combined, we obtain a final NS radius estimate for the injection model PhenDNRTv2 of $11.55^{+0.24}_{-0.25}$km which is in perfect agreement with the injected value of 11.55 km (red dashed line). The injection set corrections illustrated in the panels of Fig. 6.2 were likewise applied to the other waveform models used in this study. The final NS radius measurements for all models are listed in Tab. 6.1 and are shown in Fig. 6.3. From our NS radius measurement for the injection model PhenDNRTv2, we confirm the findings of Ref. [204] that the tidal deformability can be measured with a statistical uncertainty of $\sim 10\%$ after a few tens of detections.

TABLE 6.1
Overview of expected and measured NS radius measurements, $R_{1.4}$, and systematic shifts, $\Delta R_{1.4}$, for our selected GW models with respect to PhenDNRTv2. $\circ$ marks no expected bias, $\Uparrow$ a larger expected radius estimate, $\Downarrow$ a smaller expected radius, and $\Updownarrow$ denotes cases in which competing effects are present. The injected NS radius is 11.55 km. Our results for $\Delta R_{1.4}$ in the last column are based on the shift of the median value from the injected value.

Model	$\psi_{\rm pp}$	$\psi_{\rm T}$	ψ	$R_{1.4}$ [km]	$\Delta R_{1.4}$ [m]
PhenDNRTv2	$\circ$	$\circ$	$\circ$	$11.55^{+0.24}_{-0.25}$	-3
PhenDNRT	$\circ$	$\Downarrow$	$\Downarrow$	$11.22^{+0.26}_{-0.30}$	-329
SEOBNRTv2	$\Downarrow$	$\circ$	$\Downarrow$	$11.12^{+0.28}_{-0.25}$	-437
TF2	$\Downarrow$	$\Uparrow$	$\Updownarrow$	$11.71^{+0.24}_{-0.26}$	$+158$

[1]We note that although the extrinsic parameters affect the SNR, they do not contribute to an uneven detectability for given intrinsic parameters.

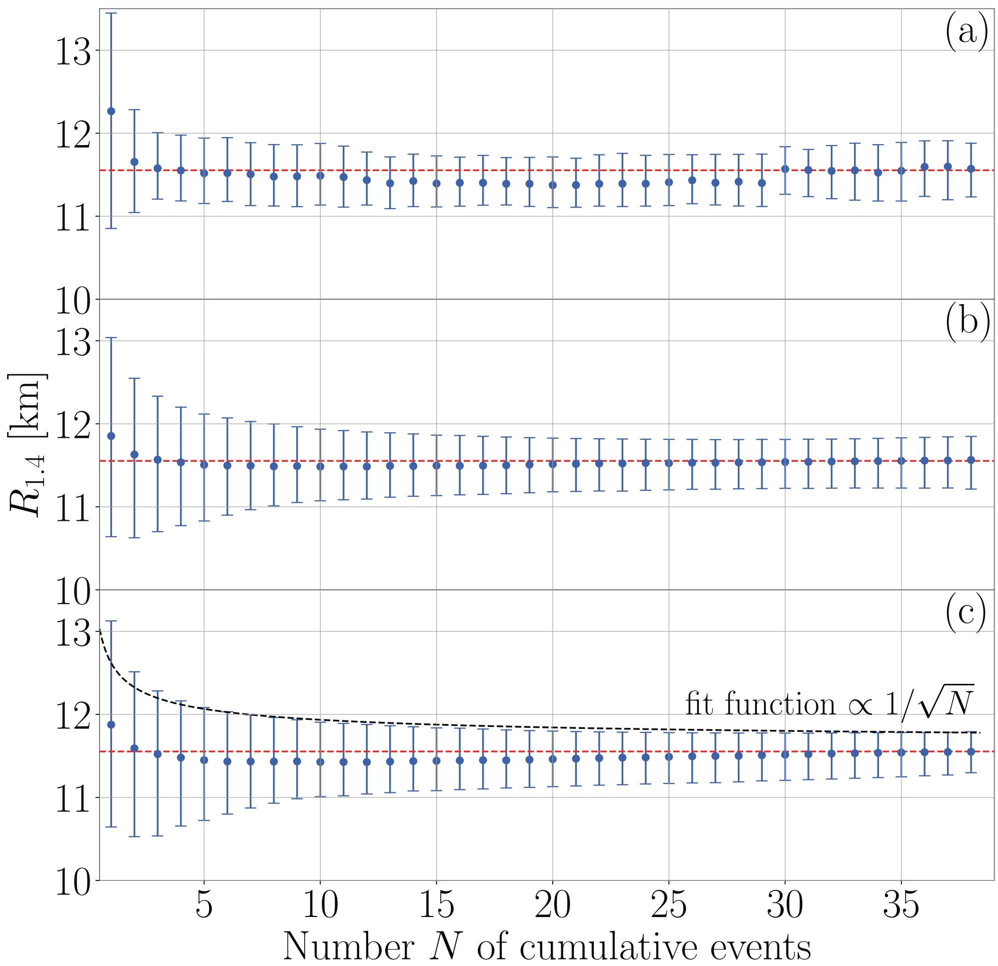

FIGURE 6.2
Overview of applied corrections for injection model PhenDNRTv2: (a) combined injection data, (b) combined and randomly reshuffled injection data, and (c) same data as before but corrected for selection effects as detailed in Sec. 5.4. The injected NS radius is 11.55 km (red-dashed line).

6.3.2 Waveform-model systematics

In Tab. 6.1, we show our expectations of potential systematic biases originating from different modelling assumptions, which we compare with our results for all waveform models in Fig. 6.3.

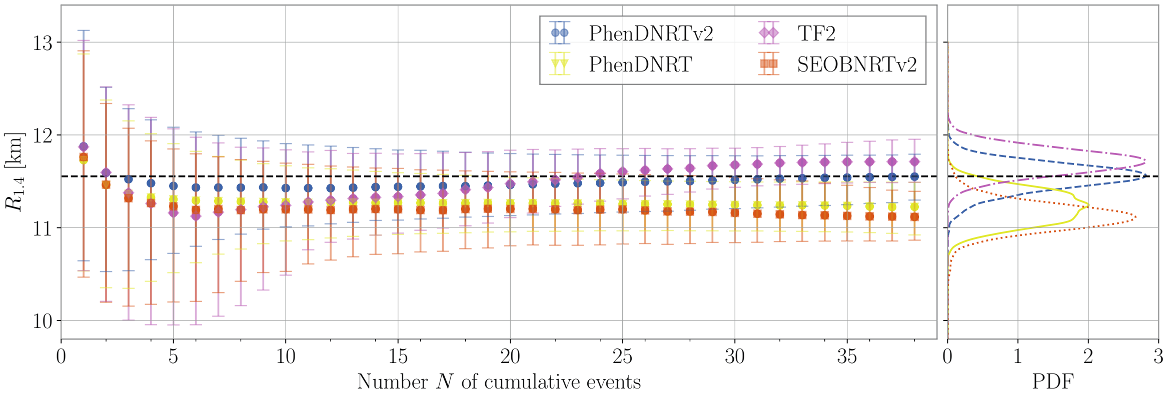

FIGURE 6.3
Left: radius constraints of a typical NS with $1.4M_{\odot}$, $R_{1.4}$, versus number of successively combined GW signals for the GW models PhenDNRT, TF2, SEOBNRTv2, and the injection model PhenDNRTv2. Right: posterior distribution function (PDF) for each GW model when all GW signals are combined. The injected EOS value is shown as black-dashed line.

The injection model PhenDNRTv2 perfectly recovers the injected value, but all other models employed, introduce a considerable bias in the NS radius measurement. PhenDNRT predicts lower NS radii which can be explained by the different tidal descriptions in the PhenDNRT and PhenDNRTv2, leading to overall smaller tidal deformabilities, and, hence, to smaller NS radii. Due to this systematic bias and decreasing statistical uncertainties, the model recovers the injected value within the 90% credible interval only when less than 20 GW events are combined. Combining all 38 GW events, PhenDNRT recovers a NS radius of $11.22^{+0.26}_{-0.30}$km which is lower than the injected value by $\sim$ 300m. We note that the bell-shaped PDF for PhenDNRT in Fig. 6.3 is an effect of our selection bias correction and is not present when excluding this correction. We find the same trend towards smaller NS radii for SEOBNRTv2. Here, the different point-particle phase description in the model predicts smaller tidal deformabilities and, hence, smaller NS radii. From the results in Fig. 6.3, we find that the model is able to recover the injected NS radius in the 90% credible interval when less than 30 GW events are combined. The SEOBNRTv2 model predicts a final NS radius of $11.12^{+0.28}_{-0.25}$km when all injections are combined, resulting in a systematic shift of $\sim$ 400m towards smaller NS radii. In comparison to the injection model PhenDNRTv2, the systematic biases present in PhenDNRT and SEOBNRTv2 lead to overall smaller NS radii when all GW events are combined. However, our analysis of the injection raw data shows that for some individual simulations PhenDNRT predicts slightly larger NS radii than PhenDNRTv2.

Finally, TF2 shows an indefinite trend for $R_{1.4}$, giving smaller NS radii for a smaller number of combined GW events, whereas with more than 23 combined GW events TF2 overestimates the injected NS radius. Notably, this model shows the largest uncertainties when less than 10 GW events are combined. Using all 38 detections, TF2 predicts a NS radius of $11.71^{+0.24}_{-0.26}$km which is larger than the injected value by $\sim$ 150m. The trend of the TF2 model could be explained by the different point-particle and tidal-phase descriptions compared to the injection model PhenDNRTv2. Because in TF2 the point-particle sector is described up to 3.5PN order whereas tidal effects are included up to 7.5 PN order, the uncertainties of $\psi_{\rm pp}$ will dominate for smaller numbers of combined GW events, leading to smaller NS radii, while uncertainties of $\psi_{\rm T}$ at 7.5PN order begin to dominate when larger numbers of GW events are combined, leading to larger NS radii. Therefore, the combined $R_{1.4}$-estimate for

TF2 underestimates waveform systematics because competing effects balance out; see Tab. 6.1 and Fig. 6.3.

Notably, the $R_{1.4}$-estimates when combining the first few events in Fig. 6.3 follow the same pattern regardless which waveform model is employed. The first event results in an overestimation of $R_{1.4}$ because it is largely driven by our heavy-pulsar prior. The non-zero support of $\Lambda = 0$ for low Λ injections results in an underestimation of $R_{1.4}$ when including a few additional events.

We find that our extracted systematic shifts of the NS radius of up to ~ 400m are smaller than shifts $\sim \mathcal{O}(1\text{km})$ estimated in previous studies [269, 514]. From a mock analysis of 15 sources, Ref. [269] found that systematic errors of that order dominate over statistical errors for signals with SNR $\gtrsim$ 80 for current advanced detectors at design sensitivity. Ref. [514] found a similar result when neglecting dynamical tidal effects in their BNS population. The differences with our findings could originate from the fact that in our parameter estimation runs we directly sample over an EOS set restricted by nuclear physics to obtain combined $R_{1.4}$-estimates. Refs. [269, 514], instead, used methods such as spectral parametrizations and universal relations for the EOS to translate binary tidal parameters into NS EOS and radius information. Consequently, our parameter estimation accounts for more physical information on the NS radius which affects systematic biases. Moreover, systematics can become more pronounced once information across several events are combined. Appendix 6.5 shows that we do not find significant systematic biases when estimating mass and spin parameters with our waveform models.

6.4 Conclusions

In this work, we performed a large injection campaign with a total of 152 BNS parameter estimation simulations to understand how the combination of information from multiple BNS detections will decrease statistical measurement uncertainties in the NS radius and to quantify the impact of waveform model systematics. For this purpose, we used four different waveform models with different point-particle and tidal phase descriptions. Based on 152 BNS simulations, our main findings are summarized below:

(i) We verified that both the combination of multiple GW sources and GW detections with high SNR will be influenced by the different modelling assumptions of existing GW models.

(ii) From a total number of 38 combined simulations, one might be able to constrain the NS radius with an accuracy of ± 250m for our injection model.

(iii) Our results showed that systematic effects substantially affect the NS radius measurement. In this work, these are strongest for the models PhenDNRT and SEOBNRTv2 (up to ~ 440m). Hence, these models cannot recover the injected NS radius in their 90% credible interval when more than 20 or 30 GW events are combined, respectively.

Overall, with increasing GW detector sensitivity and the projected BNS merger rate of 10^{+52}_{-10} detections per year estimated by Ref. [22] or 9–88 forecasted by Ref. [501] for O4, waveform model systematics will influence the extraction of NS properties. Moreover, it might be possible that systematic uncertainties in GW modelling could lead to inconsistencies of the measured NS properties between different messengers, in particular, when information from electromagnetic counterparts of potential multi-messenger observations or tighter constraints from future X-ray observations similar to Ref. [446, 447] are included. In fact, given the expectations of $1 - 13$ well-localized ($\leq 100\,\text{deg}^2$ at 90% credible areas) GW detections for BNS systems with corresponding kilonova detection rates of $0.5 - 4.8$ events per year in O4 [501], one can expect systematic effects when using currently available waveform models during the next observing runs.

6.5 Appendix

Waveform Models

Throughout this article, we used four different waveform approximants that are described in more detail below:

TaylorF2 (TF2) is a purely analytical model derived within the Post-Newtonian approximation, see Ref. [108] for a review. The model includes point-particle [578, 110, 192, 111, 112, 448] and aligned spin terms [444, 61, 117, 448] up to 3.5PN order as well as tidal effects up to 7.5PN order [194, 654, 103, 195].[2]

IMRPhenomD_NRTidal (PhenDNRT) uses a binary black hole (BBH) baseline given by the phenomenological frequency-domain model IMRPhenomD, which was introduced in Refs. [322, 349] and calibrated to untuned EOB waveforms [626], as well as numerical-relativity hybrids. The model describes spin-aligned systems throughout the inspiral, merger, and ringdown. The BBH model is augmented by the NRTidal phase description of Refs. [210, 213], which is based on analytical PN knowledge up to 6PN order, a tidal EOB model [456, 96], and numerical-relativity simulations. In PhenDNRT, no additional contributions from EOS-dependent spin-spin or cubic-in-spin effects are included.

IMRPhenomD_NRTidalv2 (PhenDNRTv2) uses the same underlying BBH model as PhenDNRT, but has a different description of the tidal sector and the NRTidalv2 phase contribution is employed [212]. This tidal description incorporates PN information up to 7.5PN order and is calibrated to an updated set of tidal EOB and NR waveforms as outlined in Ref. [212]. These updates also include tidal contributions to the GW amplitude as well as the EOS-dependence on the quadrupole and octupole moment in the spin-spin (up to 3PN order) and cubic-in spin (up to 3.5PN order) contributions.

SEOBNRv4_ROM_NRTidalv2 (SEOBNRTv2) also uses the NRTidalv2 description for the tidal sector which includes amplitude- and EOS-dependent spin effects. However, in contrast to PhenDNRTv2, the waveform model is based on an effective-one body description. The underlying BBH waveform model SEOBNRv4 was introduced in Ref. [118] and its reduced-order model SEOBNRv4_ROM is constructed following the methods outlined in Ref. [521]. The differences between PhenDNRTv2 and SEOBNRTv2 will enable us to understand the importance of the underlying BBH model for the inference of the EOS parameters.

Assessment on systematic biases on mass and spin parameters

In order to investigate potential biases in the recovery of sources' mass and spin parameters, i.e., the chirp mass $\mathcal{M}_c$, the mass ratio q, and the effective spin parameter $\chi_{\rm eff}$, we used a percentile-percentile (pp) test.

We expect our recovery to be unbiased when the pp-curve for each parameter follows the $x = y$ line, apart statistical fluctuations resulting from the Gaussian noise assumed in our BNS simulations. We find that associated parameters analyzed in Fig. 6.4 follow the expected $x = y$ relation, shown as black dashed line, and can be recovered within a 3-σ region (2-σ for PhenomDNRTv2). In order to quantify deviations seen in Fig. 6.4, we perform a Kolmogorov-Smirnov (KS) test for all models. Our KS statistic results, D_n, confirm that the deviations for the chirp mass, mass ratio, and the effective spin parameter are smallest for our injection model ranging up to $D_{n,\mathcal{M}_c} = 0.1$, $D_{n,q} = 0.17$, and $D_{n,\chi_{\rm eff}} = 0.1$, respectively.

As PhenomDNRT has the same point-particle description as PhenomDNRTv2, one expect it to

[2] We note that we employ the existing publicly available TF2 implementation in LALSuite that was used for the analysis of previous GW detections but does not incorporate recently updated 7PN and 7.5PN order terms [305, 464].

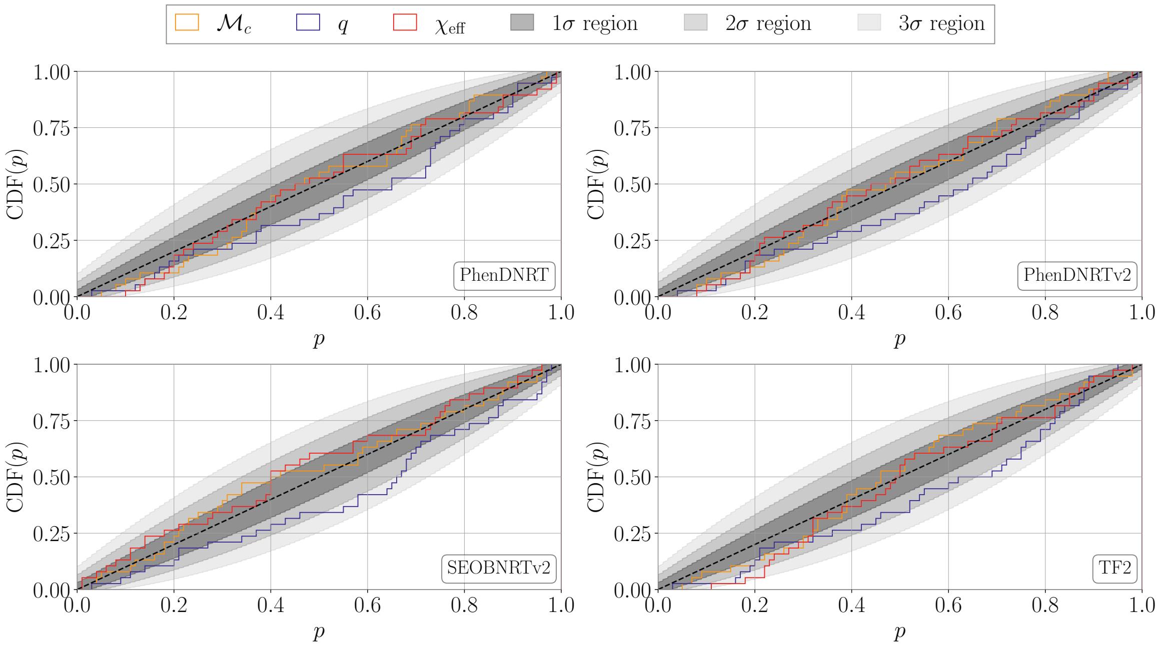

FIGURE 6.4
Percentile-percentile plot for chirp mass $\mathcal{M}_c$, mass ratio q, and $\chi_{\rm eff}$ for all waveform models. p is the probability contained in a given credible interval and CDF(p) is the fraction of the injections with their injected values laying inside that interval. The black dashed lines indicates the ideal 1-to-1 relation for the recovery of unbiased parameters. Shaded regions refer to 1-, 2-, and 3-σ regions.

have similar degree of performance as PhenomDNRTv2. Indeed, the PhenomDNRT's KS statistic are close to the one of PhenomDNRTv2. The KS statistic for chirp mass, mass ratio, and effective spin parameter are $D_{n,\mathcal{M}_c} = 0.11$, $D_{n,q} = 0.2$, and $D_{n,\chi_{\rm eff}} = 0.11$.

Because PhenomD reduces to TF2 at low frequency, the systematics induced by using TF2 should be less than the one by using SEOB. This matches our results with the TF2's KS statistic for chirp mass, mass ratio and effective spin parameter being $D_{n,\mathcal{M}_c} = 0.12$, $D_{n,q} = 0.19$, and $D_{n,\chi_{\rm eff}} = 0.12$, respectively. Because the tidal contribution is only included up to 7PN order for PhenomDNRT, while TF2 has included up to 7.5PN order, that could contributed to the marginally stronger systematics for mass ratio in PhenomDNRT.

While the largest deviation from the $x = y$ relation is present for SEOBNRTv2 ranging up to 0.12 for $\mathcal{M}_c$, 0.22 for q, and up to 0.17 for $\chi_{\rm eff}$, we conclude that systematics are not pronounced for these source parameters regardless of waveform model in use.

7

Impact of gravitational waveform model systematics on the measurement of the Hubble constant

CONTENTS

This chapter is based on the article by ***Nina Kunert****, Jonathan Gair, Peter T. H. Pang, and Tim Dietrich published in Physical Review D (2024), Vol. 110, 4, 043520. The analysis in this study builds upon data from my previous work [Phys. Rev. D, 105(6):L061301, 2022]. I conducted data analysis under guidance of Dr. Jonathan Gair, visualized the results, and authored the manuscript.*

Editorial notes: Additional citations and explanations have been included beyond those in the published version.

Abstract: Matching GW observations of binary neutron stars with theoretical model predictions reveals important information about the sources, such as the masses and the distance to the stars. The latter can be used to determine the Hubble constant, the rate at which the universe expands. One general problem of all astrophysical measurements is that theoretical models only approximate the real underlying physics, which can lead to systematic uncertainties introducing biases. However, the extent of this bias for the distance measurement due to uncertainties of gravitational waveform models is unknown. In this study, we analyze a synthetic population of 38 binary neutron star sources measured with Advanced LIGO and Advanced Virgo at design sensitivity. We employ a set of four different waveform models and estimate model-dependent systematic biases on the extraction of the Hubble constant using the bright siren method. Our results indicate that systematic biases are below statistical uncertainties for the current generation of GW detectors.

7.1 Introduction

The measurement of the local expansion rate of the Universe, also known as the Hubble constant, H_0, is one of the most intriguing problems in cosmology. The knowledge of the cosmological expansion rate at different times, given through the Hubble-Lemaître parameter, is essential for understanding the history of the Universe and to infer its age and composition.

A big puzzle in cosmology is to piece together the measurements from the early and late Universe. While the SH0ES Collaboration [546] using the cosmic distance ladder method constrained the local expansion rate to $H_0 = 74.03 \pm 1.42$ km s^{-1}Mpc^{-1}, the Planck Collaboration [43] estimated $H_0 = 67.4 \pm 0.5$ km s^{-1}Mpc^{-1} at 68% credibility from observations of the CMB radiation. This leads to the well-known Hubble-Lemaître tension with a discrepancy at a 4.4 sigma level [546].

This discrepancy has spurred scientific efforts, with researchers proposing numerous independent studies to elucidate the underlying cause. The use of acoustic baryonic oscillations [404], the gravitational lensing method [105], or calibrating the tip of the red giant branch (TRGB) to Type Ia supernovae [261] exemplify prominent attempts to resolve this enigma. Meanwhile, the possibility of a need for new physics is actively debated, suggesting that a new cosmological model may be necessary to reconcile the distinct measurements [93, 115, 412, 510].

Using GW observations as a probe to infer the cosmic expansion rate was first proposed by Schutz in 1986 [583]. The GW emission of compact binary coalescences involving black holes or neutron stars can serve as cosmic distance indicators or so-called standard sirens and provide a measurement of the luminosity distance of the source. The landmark detection of GW170817 [10, 16], a BNS merger, by the LIGO and Virgo detectors [1, 34] along with its associated EM counterparts, GRB170817A and AT2017gfo ([11] and refs. therein), marked a pivotal milestone in the field of cosmology. This event enabled the first direct measurement of the Hubble constant using a GW standard siren [7, 23]. Although current constraints from GW observations are not yet able to resolve the Hubble tension, future observations could place further constraints on this cosmological parameter [170, 247, 245, 248]. Multi-messenger observations especially hold significant promise for improving the accuracy of Hubble constant determinations. This advantage arises from being able to combine the GW measurement of the distance to the source with an electromagnetic measurement of its redshift [7, 291, 317, 657, 214, 140, 489].

While the standard siren methodology offers the advantage of not requiring recalibration, as is common practice in the distance ladder method, there are different sources of systematic uncertainties that must be addressed. Previous studies such as Ref. [319] investigated the impact of instrumental calibration uncertainties on Hubble constant measurements. They found that for single BNS events with a SNR of 50 for a network consisting of Advanced LIGO and Advanced Virgo operating at design sensitivity, the introduced bias is smaller than statistical uncertainties, but could accumulate as more events are detected. Reference [644] examined the influence of galaxy redshift uncertainties using different galaxy redshift uncertainty models, with particular emphasis on photometric redshifts, which are known to exhibit substantial errors. Their findings indicate that while there may exist a potential bias, it remains smaller than statistical uncertainties. Furthermore, systematic uncertainties arising from the viewing angle of BNS mergers and EM selection effects can be major challenges [169, 171, 411]. Building on [209], this work explores the systematic biases introduced by BBH waveform models. The analysis reveals that these biases become more pronounced with increasing detector-frame total mass, binary asymmetry, and spin-precession effects. Notably, the study demonstrates on the basis of three high SNR events (golden events) that current waveform models lead to biased measurement of the Hubble constant, even for current detectors.

In contrast to Ref. [209], our study delves into the issue of systematic uncertainties originating from BNS waveform models potentially influencing the determination of the distance to the source and, hence, the Hubble constant. Until now, this question remains, up to the best of our knowledge, unanswered. We analyze a synthetic population of 38 BNS sources, previously published in Ref. [370], with a set of four different waveform models and study model-dependent systematic errors. We employ the most recent Planck CMB measurement [43] as a benchmark and investigate whether estimating H_0 using different models than the one used to generate the data introduces a systematic bias. As our results will demonstrate, GW model-dependent biases have a minimal influence on the inferred value of the Hubble constant for current detector networks.

This chapter is organized as follows. Section 7.2 provides details on modeling GW standard sirens, the simulated BNS source population, and on the Bayesian framework employed to extract estimates of H_0. Our results of combined H_0 estimates are presented in Sec. 7.3 and Sec. 7.4 summarizes the key takeaways.

7.2 Methodology

The standard siren method utilizes the detection of GW signals and their correlation with EM observations of the same astrophysical events to infer the Hubble constant. When a source's redshift can be measured directly or through an association with its host galaxy, it is denoted as a bright siren. When an EM counterpart is absent, statistical methods can be used to ascertain possible redshifts of the source. Notable examples of these techniques include the galaxy catalog method [203, 170, 252, 287, 29, 289, 288, 425, 122], the cross correlation method [477, 455, 92], and the spectral siren technique [245, 424, 454, 243].

In our study, we will employ the bright siren technique to infer a joint estimate of the local expansion rate of the Universe, assuming the standard ΛCDM cosmology. In accordance, we utilize the latest Planck CMB measurement [43] as a reference value for our Bayesian analysis.

7.2.1 Modeling standard sirens

Gravitational waveform models describe the amplitude $\tilde{A}$ and the phase ϕ of standard sirens emitted from coalescing compact objects like neutron stars and black holes. The evolution of a gravitational waveform $\tilde{h}(f)$ over frequency can be written as

$$\tilde{h}(f) = \tilde{A}(f) \exp(-i\phi(f)), \tag{7.1}$$

in which both, the amplitude as well as the phase carry information about the intrinsic source properties. GW detectors measure a linear combination of two polarizations of the GW signal. At leading order, these can be written as [287]

$$\tilde{h}_{+}(f) \propto \frac{\mathcal{M}_z^{5/6}}{D_L} \frac{1+\cos^2(\iota)}{2} f^{-7/6} \exp(i\phi(\mathcal{M}_z, f)), \tag{7.2}$$

$$\tilde{h}_{\times}(f) \propto \frac{\mathcal{M}_z^{5/6}}{D_L} \cos\iota f^{-7/6} \exp(i\phi(\mathcal{M}_z, f) + i\pi/2), \tag{7.3}$$

where $\mathcal{M}_z \equiv \mathcal{M}(1+z)$ denotes the detector-frame (or "red-shifted") chirp mass, which is better constrained by the signal's phase as compared its amplitude, and f represents the redshifted frequency. It can be seen that the amplitude of a GW signal decreases in proportion to the luminosity distance D_L of its source. This inverse relationship is a fundamental property of GWs and plays a crucial role in their detection and interpretation. On the other hand, gravitational waveform models including only the quadrupole mode show a limited capability to accurately infer the luminosity distance to an astrophysical source due to its interdependence with the inclination angle ι. This degeneracy fundamentally limits our ability to measure both parameters so that the dominant uncertainty in the signal's amplitude arises from the uncertainties on the luminosity distance and the inclination angle. The inclusion of higher-order modes can be a way to break this degeneracy, as shown in Ref. [148].

7.2.2 Population of synthetic BNS sources

In this study, we use the large set of mock data obtained in Ref. [370] and exploit the inferred posterior on the luminosity distance to study the impact of model uncertainties on the estimation of the Hubble constant. Below, we recap the key elements of the study.

The population of 38 synthetic binary neutron star sources was simulated with stationary Gaussian noise into a network of interferometers assuming Advanced LIGO [1] and Advanced Virgo [34] design sensitivity. In light of current observations suggesting a uniform distribution for neutron star masses in gravitational-wave binaries [382], we adopt a uniform prior sampled within $m_{1,2} \in [1, 2]\ M_{\odot}$. All sources were uniformly sampled in comoving volume with an optimal network SNR, ρ, ranging within $\rho \in [7, 100]$ and lie within a maximum or threshold luminosity distance of $D_L^{\mathrm{thr}} = 100$ Mpc. Hence, the population lies within a volume in which cosmology can be well modeled under the linear Hubble relation (for redshifts $z \ll 1$) given as

$$D_L(z) \approx \frac{cz}{H_0}, \tag{7.4}$$

in which c is the speed of light. For all BNS signals in our population, we employed IMRPhenomD_NRTidalv2 (PhenDNRTv2) [212] as our reference model that we use for the creation of the simulated data. We performed parameter estimation runs using parallel bilby [606] for all sources in the population with four different models, which were TaylorF2 (TF2) [578, 110, 192, 111, 112, 448, 444, 61, 117, 448, 194, 654, 103, 195], IMRPhenomD_NRTidal (PhenDNRT) [322, 349, 626, 210, 213, 456, 96], IMRPhenomD_NRTidalv2 (PhenDNRTv2) [322, 349, 626, 456, 96, 212], and SEOBNRv4_ROM_NRTidalv2 (SEOBNRTv2) [118, 521, 212] resulting in a total of 152 simulations. For further details on our simulation setup, we refer the interested reader to Ref. [370].

7.2.3 Bayesian framework

In this section, we outline our method for estimating the Hubble constant by utilizing the posterior distributions on luminosity distance obtained for the discussed BNS population. In order to compute the posterior probability distribution of the Hubble constant for a set of GW events $\{x_{\mathrm{GW}}\}$, we employ Bayes' theorem

$$p(H_0|\,\{x_{\mathrm{GW}}\}) \propto p(H_0)p(\{x_{\mathrm{GW}}\}\,|H_0) \tag{7.5}$$

where $p(H_0)$ is the prior on H_0 and $p(\{x_{\mathrm{GW}}\}\,|H_0)$ is the likelihood of the measured GW data given a certain value of H_0.

Our analysis follows the bright siren approach, which utilizes the joint information from GW detections $\{x_{\mathrm{GW}}\}$ and electromagnetic observations providing information on the redshift $\{\hat{z}\}$ [7]. Consequently, we determine the joint posterior, $p(H_0|\,\{x_{\mathrm{GW}}, \hat{z}\})$, for N_{obs} events in our population as follows

$$p(H_0|\,\{x_{\mathrm{GW}}, \hat{z}\}) \propto \frac{p(H_0)}{N_{\mathrm{s}}(H_0)^{N_{\mathrm{obs}}}} \prod_{i=1}^{N_{\mathrm{obs}}} \int_{\vec{\lambda}} \int_{D_L} p(x^i_{\mathrm{GW}}|D_L, H_0, \vec{\lambda}) p(\hat{z}_i|D_L, H_0) p(D_L) p(\vec{\lambda}) dD_L d\vec{\lambda}, \tag{7.6}$$

where $p(D_L)$ is the prior on the luminosity distance, and other waveform parameters are denoted by $\vec{\lambda}$, similar to the notation employed in Ref. [7]. Hence, $p(\vec{\lambda})$ relates to priors for other GW parameters. Analogous to the approach used in Ref. [7], $N_s(H_0)$ incorporates the selection effect imposed by the finite sensitivity of GW detectors and is

$$N_s(H_0) = \int_{\mathrm{det}} p(x_{\mathrm{GW}}|D_L, H_0, \vec{\lambda}) p(D_L) p(\vec{\lambda}) dD_L d\vec{\lambda} dx_{\mathrm{GW}}, \tag{7.7}$$

integrated over the prior probability distributions of the parameters $D_L, \vec{\lambda}$ and over "detectable" GW datasets. This factor is constructed on the assumption that the choice of whether or not an event is included in the analysis is a property purely of the observed data, x_{GW}. In this analysis (as in [7]) we assume that selection effects are dominated by the GW data; i.e., there are no selection effects for the EM counterpart. Additionally, we assume that GW detection is based on the observed SNR of the source.[1] At the distances to which BNS events can be observed with current GW detectors, such a selection becomes a threshold in the luminosity distance of the source, which is what the GW detectors measure. As a consequence, the selection function has no dependence on the unknown cosmological parameters and so can be set to unity.

Since our dataset lacks direct redshift measurements for each BNS merger event, we need to model this information. We consider all EM observations as securely detected and, hence, neglect a correction for EM selection effects. In the absence of actual electromagnetic observational data for redshifts, we simulate a redshift measurement $\hat{z}$ for the ith BNS merger event using a Gaussian probability density function

$$p(\hat{z}_i|D_L, H_0) = \frac{1}{\sqrt{2\pi}\sigma_z} \exp\Big[-\frac{1}{2}\Big(\frac{\hat{z}-z}{\sigma_z}\Big)^2\Big]. \tag{7.8}$$

This allows us to associate each BNS source with a simulated measured redshift sampled from a Gaussian distribution centered on its true redshift value. We use the same Gaussian likelihood in Eq. (7.6) to obtain our Hubble constant posteriors. We examine the dependence of our analysis on the choice of the fractional error term, C, which contributes to the overall redshift uncertainty, σ_z, defined by the linear relationship $\sigma_z = z \cdot C$. This aims to quantify the sensitivity of our results to variations in the assumed fractional error value and, hence, in the precision of the EM measurement of the redshift. To infer joint constraints on H_0, we convert the measured redshift values to luminosity distances using Eq. (7.4). In our study, we do not explore different redshift uncertainty models as demonstrated in [644]. Their work showed that the impact of different uncertainty models is much smaller than the current statistical errors. Hence, we expect that different redshift uncertainty models will not alter our results, which we will present in the next section.

7.3 Results

In accordance with the methodology detailed in Sec. 7.2.3, we obtained combined H_0 estimates for each GW model. As described, we aim to investigate the sensitivity of our results to variations in the fractional redshift error value C, which we explore for $C = 0.5\%$ and 3%. Our choice of the fractional error is driven by the inherent differences in redshift measurement techniques. Spectroscopic redshifts offer increased precision compared to photometric redshifts. Typical uncertainties for spectroscopic redshifts can be as low 0.01% [614], while photometric redshift uncertainties can range up to 10% or more [644]. Hence, we intend to mimic a more precise spectroscopic and a less precise photometric measurement of the redshift.

First of all, we study how our estimate on H_0 changes with the number of successively combined GW signals for each BNS event for $C = 0.03$, i.e., a 3% fractional error in the modeling of the observed redshift. The result is shown in Fig. 7.1 and shows that all models recover the Planck measurement at $H_0 = 67.4$ kms^{-1}Mpc^{-1} within their uncertainty bands at 95% credible interval. Consistent with theoretical expectations, incorporating more GW events gradually decreases the uncertainties associated with the H_0 estimates. Among 38 combined GW events, PhenDNRTv2 (the "true" model) and PhenDNRT align best with the Planck value, while SEOBNRTv2 and TF2 show slightly larger deviations. From Fig. 7.1, we find that systematic biases in the extraction of the Hubble constant are below statistical uncertainties.

[1] In practice, we impose selection on the true, rather than the observed, luminosity distance of the source. This is the approach used widely in the literature. Selection on source parameters rather than observed data should really be treated differently [266], but in practice this approximation does not change the results.

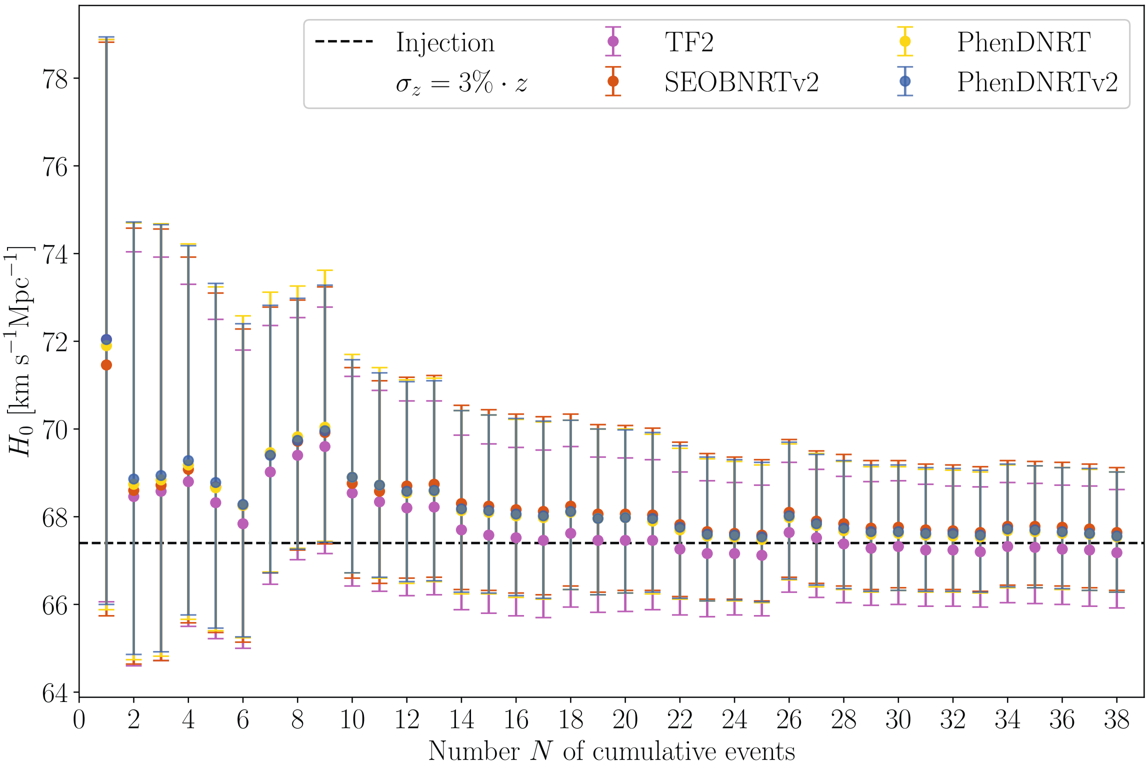

FIGURE 7.1
H_0 results versus the number of successively combined GW events for the GW models PhenDNRT (yellow), TF2 (purple), SEOBNRTv2 (orange), and the reference model PhenDNRTv2 (blue). Constraints on H_0 are reported at 95% credible interval. The reference value of the Planck measurement [43] is shown as a black dashed line. For this result, we modeled a 3% uncertainty on the true redshift as described in Sec. 7.2.3.

Second, we show the results for a 0.5% fractional error in Fig. 7.2, i.e., assuming more precise EM measurements of the observed redshift. We find that our reference model, PhenDNRTv2, recovers the Planck measurement within 95% credible interval. Likewise, analyses employing the GW models, PhenDNRT and TF2, recover this value when considering the combined data from all BNS events. The only exception is the model SEOBNRTv2 which does not recover the reference value when data from roughly 30 BNS events have been combined. Moreover, we find that there is a slight overestimation for all models when comparing with the Planck measurement. This is most likely due to a combination of statistical fluctuations and GW model-dependent differences in estimating the luminosity distance (as seen for TF2 in Fig. 7.1). The initial selection of GW events within our sample introduces another source of statistical fluctuation. However, the present bias is not significant for our conclusions as the true value lies within the posterior uncertainty.

At this point, it is crucial to acknowledge that our recovered H_0 values presented in Fig. 7.2 depend upon the specific random realization of observed redshifts generated through Eq. (7.8). This implies that any variation in the random realization of redshift measurements for each event would lead to a corresponding change in the inferred H_0 posterior. While we present a single realization in Fig. 7.2, we investigated the dependence of our results concerning different random realizations of the redshift measurement. Notably, while maintaining a fixed fractional error of 0.5%, we observed that the final, combined H_0 estimates exhibit a tendency to converge closer to the reference value of the Planck measurement under certain realizations (not shown in Fig. 7.2).

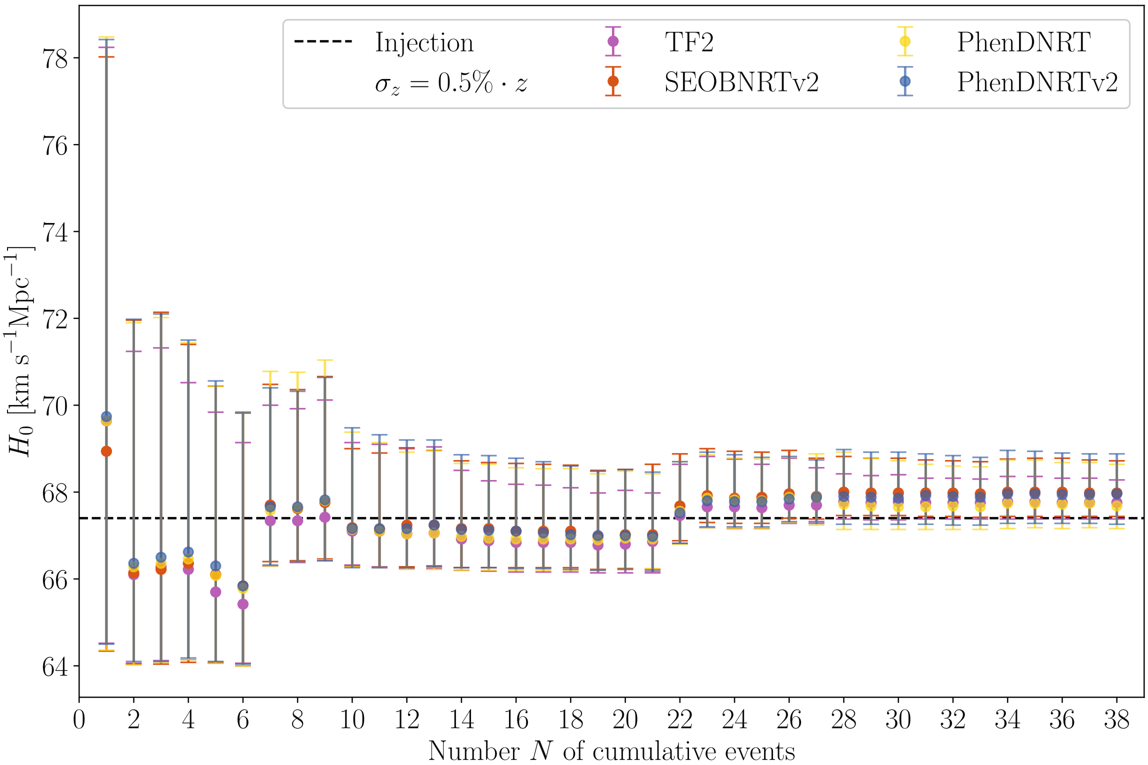

FIGURE 7.2
H_0 results versus the number of successively combined GW events for the GW models PhenDNRT (yellow), TF2 (purple), SEOBNRTv2 (orange), and the reference model PhenDNRTv2 (blue). Constraints on H_0 are reported at 95% credible interval. The Planck measurement [43] is shown as a black dashed line. For this result, we modeled a 0.5% uncertainty on the true redshift as described in Sec. 7.2.3.

In order to minimize the impact of stochastic redshift realizations and of specific BNS event orderings in our sample, we implement a double randomization procedure.[2] In this procedure, we draw 100 random redshift values assuming a Gaussian distribution with a 0.5% uncertainty for each BNS event within the sample. Equation (7.6) is then used to compute the combined H_0 value for 100 times. In each iteration, the order of the BNS events is randomized, and a different drawn redshift value is used for each event. This procedure yields 100 independent realizations of the combined H_0 posterior distribution. Finally, we compute the median of the distribution to extract the final results of H_0. The results are shown in Fig. 7.3, for which we modeled a 0.5% uncertainty on the true redshift. Our result depicts a convergence towards the Planck value for all GW models. Consistent with prior findings, it also reveals a progressive uncertainty reduction and that all GW models recover the Planck measurement.

From Figs. 7.2 and 7.3, we find that PhenDNRT tends to yield smaller H_0 values as compared to PhenDNRTv2. This could result from the fact that the PhenDNRTv2 includes an amplitude tidal correction term [212], while this is not the case for PhenDNRT. Because of this correction, the amplitude for PhenDNRT waveforms will be larger as compared to PhenDNRTv2. In order to compensate, PhenDNRT needs to go to higher luminosity distances and, hence, will predict smaller

[2] Despite this procedure, our GW posteriors are not randomized, which can lead to slight offsets or biases as we can see in our study.

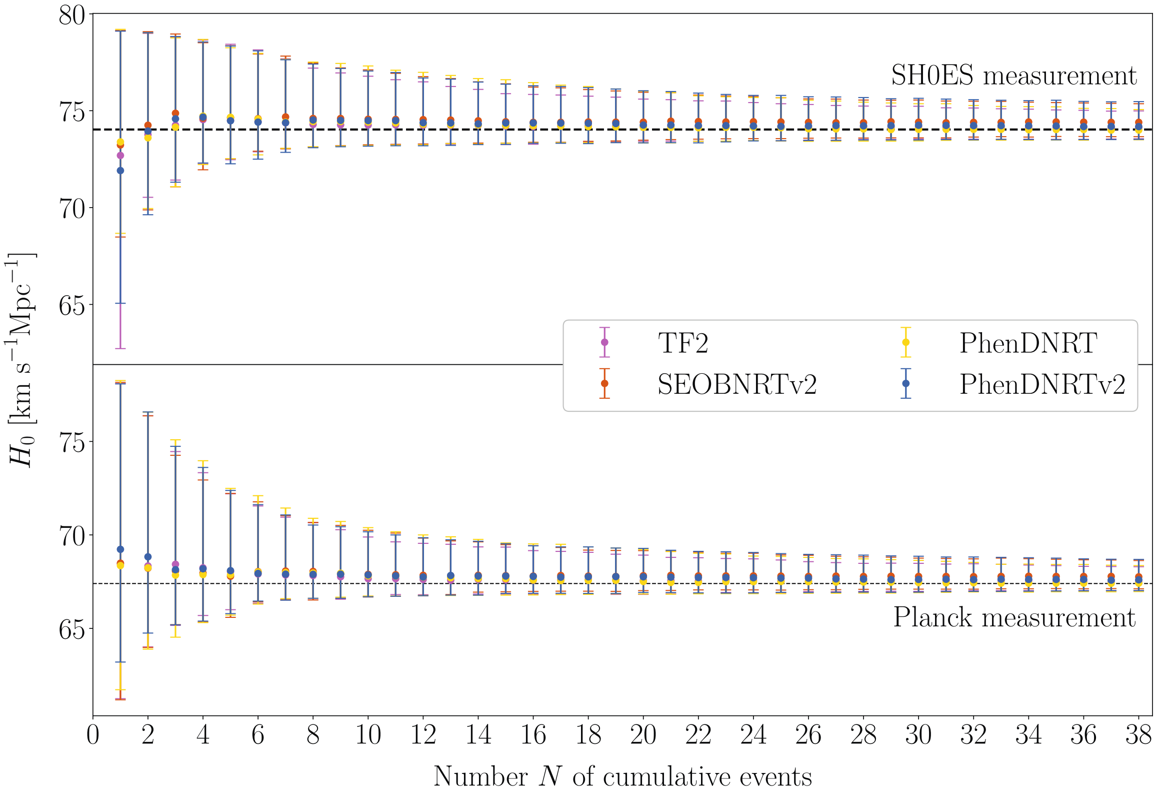

FIGURE 7.3
H_0 results versus the number of successively combined GW events for the GW models PhenDNRT (yellow), TF2 (purple), SEOBNRTv2 (orange), and the reference model PhenDNRTv2 (blue) for both, using the SH0ES measurement of $H_0 = 74.03 \pm 1.42$ km s^{-1}Mpc^{-1} (top panel) [546] and the Planck measurement of $H_0 = 67.4 \pm 0.5$ km s^{-1}Mpc^{-1} (bottom panel) [43] as reference values. We use the same credible interval and fractional error on the redshift uncertainty as in Fig. 7.2, but randomly shuffled the order of BNS events in our sample for 100 times, while employing 100 random realizations of redshift measurements.

values for the Hubble constant. Another distinctive feature is that the uncertainty is smallest for TF2 when all data has been taken into account. To investigate this observation, we computed the Fisher information matrix (FIM) for both TF2 and PhenDNRTv2 across all events using GWFAST [325, 326]. The FIM analysis revealed that 55% of the events exhibited a lower distance error for TF2 as compared to PhenDNRTv2. This finding suggests that TF2 can achieve a narrower posterior width or lower variance. However, we would still expect it to have a larger bias, which would eventually dominate the uncertainty once sufficiently many events have been combined. Moreover, we repeat the analysis employing the Hubble constant measurement reported by the SH0ES Collaboration [546] as the reference value, $H_0 = 74.03 \pm 1.42$ km s^{-1}Mpc^{-1}. Figure 7.3 shows that we obtain consistent results compared to the scenario where we utilize the Planck measurement. Consequently, our primary conclusions remain unchanged.

Overall, our results indicate that waveform model-dependent biases on the extraction of the Hubble constant are small for current detectors. Ascribing the subtle discrepancies observed in the combined H_0 estimates solely to specific model descriptions or assumptions presents a significant challenge. First, GW models only possess a limited capability to accurately infer the distance and, consequently, the Hubble constant, so we are dominated by statistical rather than systematic uncertainties. Second, our employed GW models exhibit interdependencies within specific regimes, which hamper an unambiguous explanation attributable to individual models.

Finally, we use our results compared to the Planck measurement shown in Fig. 7.3 to estimate how many cumulative BNS events will be required to achieve a statistical uncertainty that falls below the waveform model systematics. To understand how much the final measurement of the Hubble constant might be affected by the choice of a certain model, we calculate the difference between the final H_0 value obtained using our reference model PhenDNRTv2 and the final values obtained using all the other models. The largest systematic shift of $\Delta H_0 = 0.18$ km s^{-1}Mpc^{-1} is present when comparing to PhenDNRT, while the final result of TF2 has the smallest shift with $\Delta H_0 = 0.08$ km s^{-1}Mpc^{-1}. As the statistical uncertainty drops as $\sim 1/\sqrt{N_{\rm obs}}$, we can estimate the number of BNS events required to fall below the above-reported values. For our reference model PhenDNRTv2 to possess statistical uncertainties smaller than the systematic shift of $\Delta H_0 = 0.18(0.08)$ km s^{-1}Mpc^{-1} roughly 3500 (16,500) BNS observations would be required with the current generation of GW detectors.

7.4 Conclusions

In this study, we investigated the impact of gravitational waveform systematics on the extraction of the Hubble constant. Employing the bright siren approach, we obtained combined estimates on the Hubble constant by using previous simulated GW data from a population containing 38 BNS sources published in [370] and by modeling a corresponding EM observation to provide information on the redshift. Overall, our analysis reveals that the uncertainty in the luminosity distance arising from GW models exerts a negligible influence on the determination of the Hubble constant for the current generation of GW detectors. However, our analysis is limited because our employed GW models are based on the quadrupolar mode and do not include any higher-order modes. While current systematic biases on the Hubble constant are below statistical uncertainties, this picture will change with upcoming third generation detectors like the Einstein Telescope (ET) [520, 410, 128] or the Cosmic Explorer (CE) [541, 241]. Projected BNS detection rates of 10^4 BNS/year for ET [538, 601, 128] or 10^5 BNS/year for a network consisting of ET and CE [656] imply diminishing statistical uncertainties, necessitating an increased focus on reducing systematic biases in the future.

Part V

Exploring progenitors: Bayesian multi-wavelength analyses of gamma-ray bursts

8

Bayesian model selection for GRB 211211A through multi-wavelength analyses

CONTENTS

This chapter is based on the article by ***Nina Kunert****, Sarah Antier, Vsevolod Nedora, Mattia Bulla, Peter T. H. Pang, Shreya Anand, Michael W. Coughlin, Ingo Tews, Jennifer Barnes, Thomas Hussenot-Desenonges, Brian Healy, Theophile Jegou du Laz, Meili Pilloix, Weizmann Kiendrebeogo, and Tim Dietrich published in Monthly Notices of the Royal Astronomical Society, Volume 527, Issue 2, January 2024, Pages 3900–3911. I collected and processed the X-ray data, while the remaining observational data were primarily compiled by my colleagues, Dr. Sarah Antier and Prof. Dr. Michael Coughlin. I conducted all parameter estimation simulations, performed data analysis, visualized the results, and authored the manuscript.*

Editorial notes: Table 8.1 has been updated to include the correct number of model parameters for the core collapse supernova scenario.

Abstract: Although GRB 211211A is one of the closest GRBs, its classification is challenging because of its partially inconclusive electromagnetic signatures. In this paper, we investigate four different astrophysical scenarios as possible progenitors for GRB 211211A: a binary neutron-star merger, a black-hole–neutron-star merger, a core-collapse supernova, and an r-process enriched core collapse of a rapidly rotating massive star (a collapsar). We perform a large set of Bayesian multi-wavelength analyses based on different models describing these scenarios and priors to investigate which astrophysical scenarios and processes might be related to GRB 211211A. Our analysis supports previous studies in which the presence of an additional component, likely related to r-process nucleosynthesis, is required to explain the observed light curves of GRB 211211A, as it can not solely be explained as a GRB afterglow. Fixing the distance to about 350 Mpc, namely the distance of the possible host galaxy SDSS J140910.47+275320.8, we find a statistical preference for a binary neutron-star merger scenario.

8.1 Introduction

The joint detection of gravitational waves (GWs) and electromagnetic (EM) signatures originating from the merger of BNSs on August 17th 2017 [10, 11] has been a breakthrough in multi-messenger astronomy. In addition to the GW signal GW170817, an associated kilonova, AT2017gfo, and a gamma-ray burst, GRB 170817A, were observed [11]. This multi-messenger detection allowed for an independent way of measuring the expansion rate of the Universe [7], placed new constraints on the properties of supranuclear-dense matter [83, 562, 529, 451, 183, 153, 214, 324], and proved that at least some short GRBs are connected to compact binary mergers [9]. However, it was also reported that short GRBs could originate from collapsars [45], indicating that the classification of astrophysical scenarios associated with GRBs is more complex [684, 554]. Additional signatures associated with GRBs and their afterglows, such as kilonovae, significantly help to identify the origin of the progenitors. The kilonova AT2017gfo was certainly an exemplary case for such an EM signal, and spectral features connected to the creation of new elements [658, 218] in the outflowing material have possibly been observed. In addition to AT2017gfo, there is a large number of kilonova candidates that could be connected to other GRB observations, e.g., GRB 060614, GRB 130603B, GRB 150101B, GRB 150424A, GRB 160821B, GRB 060505 e.g., [624, 95, 677, 335, 254, 639, 378, 344, 336, 641, 337]; cf. e.g. [64] for a review about some of these kilonova candidates. The most recent example that has to be added to the list is the kilonova candidate connected to GRB 211211A.

This GRB signal was discovered on the 11th December 2021 at 13:09:59 (UTC) by the Burst Alert Telescope of the Swift Observatory and its optical and near-infrared counterpart observed by, e.g., [533] and [642]. This GRB signal is characterized by a complex emission phase lasting approximately 50 s and shows several overlapping pulses lasting for about $\sim$ 12 s [533]. Given this duration, GRB 211211A would be classified as a long GRB typically arising from the core-collapse of massive stars (e.g., [613, 393]) and not from compact binary mergers. Hence, for a scenario such as GRB 211211A, one would not necessarily expect to observe an associated kilonova. Based on intensive follow-up observations [533, 642], it seems plausible that SDSS J140910.47+275320.8 was the host galaxy of GRB 211211A, at 98.6% confidence [533].

Numerous groups, e.g., [533, 642, 678, 430], and also other groups explained these observations by invoking a kilonova in association with GRB 211211A. This was suggested for different reasons: (i) the profile of the prompt emission showed an initially complex structure followed by an extended softer emission, (ii) a predominant signature of a supernova was lacking for up to 17 days post-discovery, (iii) the color evolution of the optical counterpart had similar properties as AT2017gfo, and (iv) the offset of the GRB location concerning the center of the host galaxy was larger than for typical long GRBs.

The origin of GRB 211211A is highly debated, e.g., [678] suggested that it has similar properties as GRB 060614, another event associated with a kilonova candidate. They conclude that the significant excess in the near-infrared and optical afterglow at late observations points more towards a neutron star-white dwarf merger which leaves behind a rapidly spinning magnetar as a central engine providing additional heating to the ejecta. [620] mentioned a possible gamma-ray precursor before the main emission which was caused by the resonant shattering of one star's crust prior to the merger. In contrast, [272] concluded the presence of a strong magnetic field from the precursor surrounding the central engine of the GRB. This would result in the prolongation of the accretion process and, thus, could explain the duration of the hard spiky emission detected for GRB 211211A. Similarly, [674] supposes that a magnetar participated in the merger and caused a quasi-periodic precursor. [283] analyzed the spectra of the prompt emission of GRB 211211A by using synchrotron spectrum models and concluded that the rapid evolution of synchrotron emission is the main driver its extended emission. While the kilonova observed for GRB 211211A argues for a BNS merger, a NSBH scenario cannot be fully ruled out. Finally, [80] investigated the possibility that collapsars could explain the origin of GRB 211211A and found that the afterglow-subtracted emission of GRB 211211A is in best agreement for collapsar models with high kinetic energies.

Following the discussion in the literature, we will use our `NMMA` framework [492][1] to explore different astrophysical scenarios for the origin of GRB 211211A. We will consider the possibility of two merger scenarios, a BNS merger and an NSBH merger, and in addition two supernova scenarios, a core-collapse supernova, and an r-process enriched collapsar. At this point, we emphasize that while multiple scenarios (e.g. different supernova types) could possibly explain the origin of GRB 211211A, we restrict our study to the four scenarios mentioned above, and to particular models representing such scenarios. Hence, our study will only provide estimates for this narrow parameter space of possible scenarios. For our model selection study, the `NMMA` framework allows us to simultaneously fit the observed data across the full electromagnetic range with multiple models, e.g., we can simultaneously employ GRB afterglow and kilonova models without the need of splitting the observational data in chunks and processing them separately.

8.2 Observational data

In order to perform our model selection, we collect a set of multi-wavelength data observed for GRB 211211A. However, we do not use any data from the prompt emission phase of the GRB in our analysis since our framework is, at the current stage, not able to handle such high-energetic emission. With regard to the X-ray data, we use the available information from the *Swift* X-ray Telescope. In particular, we use the 0.3 - 10 keV flux light curve observed at late times ($t = 10^4$ s after BAT trigger time) and convert it to 1 keV flux densities following [274]. For our optical study in UV, we use results from Swift-UVOT of Tab. 2 provided by [533] in the bands v, b, u, $uvw1$, $uvm2$, $uvw2$, and *white*. To supplement these UVOT data, we incorporate measurements from "supplement Table 1" provided by [642]. Whenever measurements overlap within a 30-minute window in the same band between [642] and [533], we remove duplicates, as such measurements represent variations in analysis binning during the early epoch between the two publications.[2] For the remaining optical data, we exclusively utilize measurements directly analyzed by [533] (cf. Tab. 1 in the appendix, references (1)).

We follow a similar approach for the published data from [642]. (cf."supplement Table 1"). Furthermore, we augment our dataset with measurements exclusively published in General Coordinates Network[3] (GCNs) [494, 415] for instance. In this manner, we try to obtain an almost complete set encompassing available optical data for this particular GRB, including the latest publicly accessible measurements when possible. The data were all corrected from the foreground Galactic extinction $A_V = 0.048$ mag [580].

Furthermore, we use the 6 GHz radio detection of GRB 211211A observed 6.27 days after the initial trigger with a 5σ upper limit flux density of 16 μJy [533]. With regard to available GeV data, as reported in [685] and [430], we do not include this data since our employed GRB model does not provide mechanisms to explain their origin.

8.3 Methods

Our analysis is based on the nuclear physics and multi-messenger astronomy framework `NMMA` [492] that allows us to perform joint Bayesian inference runs of multi-messenger events containing GWs,

[1] `https://github.com/nuclear-multimessenger-astronomy`

[2] Moreover, we ensure in this way that the statistical analysis will not be biased by including redundant data, which would give more weight to specific bands during the likelihood estimation.

[3] `https://gcn.gsfc.nasa.gov/other/211211A.gcn3`

kilonovae, supernovae, and GRB afterglow signatures. For this article, we extended the code infrastructure to include the description of r-process enriched collapsars following the model of [79].

We use the EM data of GRB 211211A to investigate which model or which combination of models describe the observational data best.

8.3.1 Bayesian Inference

According to Bayes' theorem, we compute posterior probability distributions, $p(\vec{\theta}|d,\mathbf{M})$, for model source parameters $\vec{\theta}$ under the hypothesis or model $\mathbf{M}$ with data d as

$$p(\vec{\theta}|d,\mathbf{M}) = \frac{p(d|\vec{\theta},\mathbf{M})p(\vec{\theta}|\mathbf{M})}{p(d|\mathbf{M})} \rightarrow \mathcal{P}(\vec{\theta}) = \frac{\mathcal{L}(\vec{\theta})\pi(\vec{\theta})}{\mathcal{Z}(d)}\,, \tag{8.1}$$

where $\mathcal{P}(\vec{\theta})$, $\mathcal{L}(\vec{\theta})$, $\pi(\vec{\theta})$, and $\mathcal{Z}(d)$ are the posterior, likelihood, prior, and evidence, respectively. In order to investigate the plausibility of competing models, we evaluate the odds ratio $\mathcal{O}^1_2$ for two models $\mathbf{M}_1$ and $\mathbf{M}_2$ which is given by

$$\mathcal{O}^1_2 = \frac{p(d|\mathbf{M}_1)}{p(d|\mathbf{M}_2)}\frac{p(\mathbf{M}_1)}{p(\mathbf{M}_2)} \equiv \mathcal{B}^1_2\Pi^1_2, \tag{8.2}$$

where $\mathcal{B}^1_2$ and Π^1_2 are the Bayes factor and the prior odds, respectively. Under the assumption that the different astrophysical scenarios considered here are equally likely to explain GRB 211211A, we impose unity prior odds, i.e., $\Pi^1_2 = 1$, for all comparisons of models describing these scenarios. Therefore, we simply compute the Bayes factor $\mathcal{B}^1_2$. In our study, we report the natural logarithm of the Bayes factor,

$$\ln \mathcal{B}^1_{\text{ref}} = \ln\left(\frac{p(d|\mathbf{M}_1)}{p(d|\mathbf{M}_{\text{ref}})}\right)\,, \tag{8.3}$$

relative to our best fitting model as a reference (ref.), which we will denote as $\ln \mathcal{B}_{\text{ref}}$ hereafter. Following [331] and [346], we interpret $\ln \mathcal{B}^1_{\text{ref}}$ as the evidence favoring our reference model as:

$\ln[\mathcal{B}^1_{\text{ref}}] < -4.61$	decisive evidence,
$-4.61 \leq \ln[\mathcal{B}^1_{\text{ref}}] \leq -2.30$	strong evidence,
$-2.30 \leq \ln[\mathcal{B}^1_{\text{ref}}] \leq -1.10$	substantial evidence,
$-1.10 \leq \ln[\mathcal{B}^1_{\text{ref}}] \leq 0$	no strong evidence.

However, we point out that these classifications should only be considered as estimates and that the Bayes factor is generally a continuous quantity. In addition to the Bayes factor, we also provide information about the ratio of the maximum likelihood, or the difference of the maximum log-likelihood point estimates $\ln[\mathcal{L}^1_2(\hat{\theta})]$ supporting our analysis in Sec. 8.4.1. We will denote this as $\ln[\mathcal{L}_{\text{ref}}(\hat{\theta})]$ when we compare the maximum log-likelihood against our reference model.

8.3.2 Employed models

As described in the introduction, we investigate four different scenarios in our study from which GRB 211211A could have emerged. In particular, we consider two merger scenarios: a BNS merger and an NSBH merger, and two supernova cases: a phenomenological long GRB supernova template and an r-process enriched collapsar scenario. As a word of caution, we emphasize that all these scenarios can only be considered when employing characteristic models describing such a scenario. Strictly speaking, our results will only favor or disfavor particular models employed for the analysis, but we will not be able to rule out an entire astrophysical scenario, e.g., disfavoring the employed SN98bw and rCCSNe will not be sufficient to rule out the supernova origin completely.

BNS scenario: For this case, we use the kilonova models of [214] (hereafter 'BNS-KN-Bulla') and of [342] (hereafter 'BNS-KN-Kasen'). BNS-KN-Bulla is based on the time-dependent three-dimensional Monte Carlo radiation transfer code `possis` [138, 139], which computes light curves, spectra, and luminosities for kilonovae depending on the viewing-angle $\theta_{\rm Obs}$. The ejected material is classified through the dynamical ejecta mass, $M_{\rm ej}^{\rm dyn}$, and the disk-wind ejecta mass, $M_{\rm ej}^{\rm wind}$. The tidal dynamical ejecta component is assumed to be distributed within a half opening angle Φ. In the same way, BNS-KN-Kasen uses the multi-dimensional Monte Carlo code `sedona` that solves the multi-wavelength radiation transport equation in a relativistically expanding medium [343, 558]. In this paper, we use the one-dimensional model provided by [342], which assumes spherical symmetry and uniform composition for our analysis. The model, 'BNS-KN-Kasen', depends on the ejecta mass, $M_{\rm ej}$, a characteristic expansion velocity, $v_{\rm ej}$, and the mass fraction of lanthanides, $X_{\rm lan}$, which affects the opacity.

NSBH scenario: For this case, we also use a `possis` model grid of KN spectra tailored to NSBH mergers which was used in the study of [51] (hereafter 'NSBH-KN-Bulla'). This model depends on the same model parameters as BNS-KN-Bulla but excludes the dependence on the half opening angle of the dynamical ejecta, fixed to $\Phi = 30°$.

Supernova: In order to assess the possibility of a typical core-collapse supernova (CCSN) associated with a long GRB, we use the `nugent-hyper` model from `sncosmo` [392] with the absolute magnitude, $S_{\rm max}$, as the main free parameter. This model is a template constructed from observations of the supernova SN1998bw associated with the long GRB 980425 and is hereafter abbreviated as 'SN98bw'.

***r*-process enriched Collapsar**: Rapidly rotating massive star core collapses [145, 523] are another possible astrophysical site for r-process nucleosynthesis. As massive stars undergo a core collapse, material is disrupted and forms an accretion disk which can become neutron-rich through weak interactions [90] and can launch winds which power emission of r-process-enriched core-collapse SNe (rCCSNe). We use the semi-analytic model for rCCSNe of [79] (hereafter denoted as 'SNCol'). The model depends on five free parameters: the total ejecta mass, $M_{\rm ej}$, a characteristic ejecta velocity, $v_{\rm ej}$, the ^{56}Ni mass, $M_{\rm Ni}$, the r-process material mass, $M_{\rm rp}$, and the mixing coordinate, $\Psi_{\rm mix}$. The ejecta are assumed to be spherically symmetric, with r-process elements of mass $m_{\rm rp}$ concentrated in an inner core whose total mass is $\Psi_{\rm mix} m_{\rm ej}$, with $\Psi_{\rm mix} \leq 1$. An r-process-free envelope surrounds the core, and 56-Ni is distributed uniformly throughout the core and the envelope. The velocity $v_{\rm ej}$ is defined such that the total kinetic energy of the ejecta $E_{\rm kin}$ is equal to $\frac{1}{2} M_{\rm ej} v_{\rm ej}^2$.[4]

GRB afterglow: For modeling the GRB afterglow light curves, we employ the semi-analytic model of [651] and [566], available in the public `afterglowpy` library (denoted as 'GRB-M'). The model computes GRB afterglow emission and takes the following free parameters as input: the isotropic kinetic energy, $E_{\rm K,iso}$, the viewing angle, $\theta_{\rm Obs}$, the half-opening angle of the jet core, θ_c, the outer truncation angle of the jet, θ_w, the interstellar medium density, n, the electron energy distribution index, p, and the fractions of the shock energy that go into electrons, ϵ_e, and magnetic fields, ϵ_B. The model allows for several angular structures of the GRB jet. For our simulations, we assume a Gaussian or a top-hat jet structure (hereafter, 'Gauss' and 'top')[5]. It is important to note that, while we try to be agnostic concerning GRB 211211A's origin, the GRB-M model that we employ has some limitations. Specifically, it does not include the emission from the reverse shock that might be important at early times. Additionally, it does not include the wind-like interstellar medium, which is expected in the case of a collapsar.

In Fig. 8.1, we summarize our approach to analyze GRB 211211A based on the data set described in Sec. 8.2. We employ two different priors for the luminosity distance, i.e., a narrow Gaussian luminosity distance prior centered around 350 Mpc as reported by [533] and a uniform prior on the luminosity distance ranging between 0 and 3 Gpc. This allows us to investigate the potential influence of the distance on the GRB classification. Furthermore, we employ five models or model combinations to

[4] [80] also compared rCCSNe with observational data from GRB 211211A. However, not within a Bayesian approach as employed here and with an updated version of their model originally described in [79].

[5] In addition, we tested a power law jet structure for which we found consistent results.

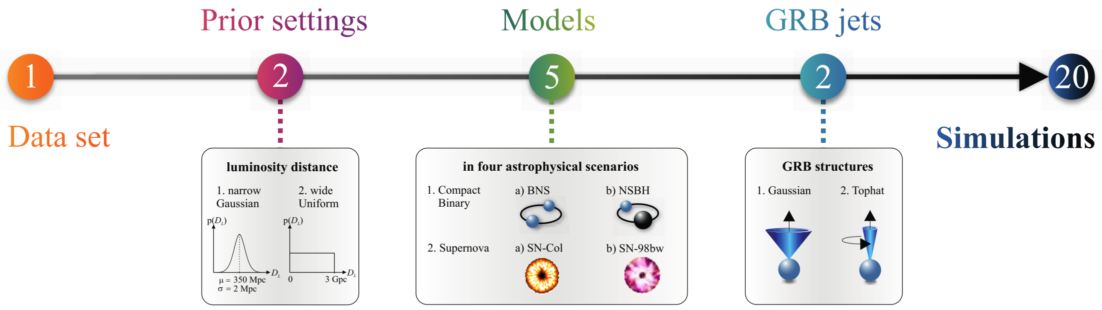

FIGURE 8.1
Schematic illustration of our comprehensive Bayesian inference campaign performed to analyze GRB 211211A. We use one observational data set as described in Sec. 8.2, two prior settings in which we mainly vary the luminosity distance prior while prior settings for other model parameters remained fixed and are reported in Table 8.2, five models (including two different BNS kilonova models) or model combinations for four different astrophysical scenarios, and two GRB jet types (Gaussian and top-hat), totaling in 20 Bayesian inferences.

describe the different astrophysical scenarios. For the choice of a Gaussian luminosity distance prior, we report the prior settings for all parameters of the employed models in Table 8.2. Moreover, we use two different GRB jet types, totaling in 20 Bayesian inference simulations.

8.4 Multi-wavelength Analyses

In the following three subsections, 8.4.1-8.4.3, we discuss our results for a narrow Gaussian prior on the luminosity distance in order to compare with previous studies. In subsection 8.4.4, we will investigate the influence of the distance prior choice and employ a wide uniform prior on the luminosity distance.

8.4.1 Model Comparison

As indicated in the introduction, one of the main differences between previous studies and our work is that most previous works fitted first the X-ray and radio data with a GRB afterglow model, and then used the afterglow-subtracted optical and near-infrared photometry for fitting a kilonova model. In contrast, but similar to [678] we perform a joint analysis of the GRB afterglow and a possible additional contribution such as a kilonova signature or emission from a rCCSN or CCSN. Moreover, in order to consider systematic uncertainties arising from different assumptions made in each model, we employ a 1 mag uncertainty in our simulations.
In Table 8.1, we summarize our main findings for the investigated astrophysical scenarios. We found that the BNS-GRB-$\mathrm{M}^{\mathrm{Kasen}}_{\mathrm{top}}$ model describes the observational data best, and hence, we pick it as our reference model. Consequently, the Bayes factors and likelihood ratios in Table 8.1 are reported relative to this best-fit inference run. With reference to Table 8.1, we show the maximum log-likelihood light curve fits in Fig. 8.2 for each assessed scenario, which we will refer to as "best-fitting light curves" hereafter.

Comparing only the two different BNS kilonova models, we find differences in the log-Bayes factors of about 4, disfavouring the BNS-GRB-$\mathrm{M}^{\mathrm{Bulla}}_{\mathrm{Gauss/top}}$ model compared to our reference model. Different GRB afterglow models lead only to a change of about 1 in the log-Bayes factor. Similarly, the employed GRB afterglow model has only a very small imprint of the maximum log-likelihood values, while different kilonova models lead to a change of order 3. These differences can be seen in Fig. 8.3

Name	Astrophysical Processes	GRB Jet Structure	Model dimension	Bayes factor $\ln[\mathcal{B}^1_{\rm ref}]$	Likelihood $\ln[\mathcal{L}^1_{\rm ref}(\hat{\theta})]$
BNS-GRB-$M^{\rm Kasen}_{\rm top}$	Kilonova + GRB	Tophat	11	ref.	ref.
BNS-GRB-$M^{\rm Kasen}_{\rm Gauss}$	Kilonova + GRB	Gaussian	12	-1.21 ± 0.12	0.04
BNS-GRB-$M^{\rm Bulla}_{\rm top}$	Kilonova + GRB	Tophat	11	-4.51 ± 0.12	-3.24
BNS-GRB-$M^{\rm Bulla}_{\rm Gauss}$	Kilonova + GRB	Gaussian	12	-6.26 ± 0.12	-3.31
NSBH-GRB-$M_{\rm top}$	Kilonova + GRB	Tophat	11	-8.41 ± 0.12	-9.30
NSBH-GRB-$M_{\rm Gauss}$	Kilonova + GRB	Gaussian	12	-10.56 ± 0.12	-8.99
SNCol-GRB-$M_{\rm top}$	rCCSNe + GRB	Tophat	14	-15.24 ± 0.13	-8.41
SNCol-GRB-$M_{\rm Gauss}$	rCCSNe + GRB	Gaussian	15	-16.97 ± 0.13	-8.34
SN98bw-GRB-$M_{\rm top}$	CCSNe + GRB	Tophat	9	-12.66 ± 0.12	-14.69
SN98bw-GRB-$M_{\rm Gauss}$	CCSNe + GRB	Gaussian	10	-12.59 ± 0.12	-13.01
GRB-$M_{\rm top}$	GRB	Tophat	8	-12.47 ± 0.12	-13.01
GRB-$M_{\rm Gauss}$	GRB	Gaussian	9	-12.65 ± 0.12	-14.67

TABLE 8.1
Results for the logarithmic Bayes factors, $\ln[\mathcal{B}^1_{\rm ref}]$, and maximum logarithmic likelihood ratios, $\ln[\mathcal{L}^1_{\rm ref}(\hat{\theta})]$, relative to the best-fit, joint inference using BNS-GRB-$M^{\rm Kasen}_{\rm top}$ (ref.). The four investigated scenarios of possible astrophysical origins (BNS, NSBH, SNCol, and SN98bw) are each being assessed assuming a Gaussian or a Top-hat jet structure. As reference, we list results for a stand-alone GRB-M investigation for both jet structures.

especially in the bands bessel-v, ps1-i, 2massj, and 2massks. Although the maximum likelihood light curve for the BNS-GRB-$M^{\rm Kasen}_{\rm Gauss}$ simulation is slightly favored as compared to our reference scenario, the difference is of the order of the statistical uncertainties. It is worth pointing out that statistical uncertainties, as stated in the table, are noticeably smaller than model differences, i.e., our results are dominated by systematic uncertainties in the underlying light curve models.

Considering the differences between the NSBH and BNS scenarios, we find strong evidence that GRB 211211A was connected to a BNS rather than an NSBH system. This is reflected both in Bayes factors as well as maximum log-likelihood values as shown in Table 8.1. Comparing the respective best fitting light curves in Fig. 8.2, we see that NSBH-GRB-$M^{\rm Bulla}_{\rm top}$ fits the NIR-band data worse compared to BNS-GRB-$M^{\rm Kasen}_{\rm top}$.

With regard to the relative Bayes factors for the collapsar scenario, we find that there is decisive evidence that a BNS scenario is preferred over a collapsar origin for GRB 211211A when employing the light curves models outlined in the previous section. However, it is important to note that the collapsar model depends on more parameters. Because of this, Occam's razor penalizes the model.

As indicated by [533], and confirmed by our study, we find that a Ni-powered SN event or an SN98bw-GRB-M scenario is noticeably less favored compared to a BNS merger. This is depicted in Fig. 8.2 in which SN98bw-GRB-$M^{\rm Bulla}_{\rm top}$ fails to fit late-time NIR data, resulting in a larger, negative log-likelihood ratio. Moreover, the upper SN limits reported for the r- and i-band in [642] rule out other supernova models.

Finally, our study confirms that the BNS-GRB-$M^{\rm Kasen}_{\rm top}$ scenario provides decisive evidence when compared with GRB-$M_{\rm top}$ simulations, even though the latter sampled over fewer parameters in respective parameter estimation runs. Considering the impact of the choice of a Gaussian vs. top-hat jet structure on our Bayes factor results, we find a slight preference for the top-hat jet structure for all assessed scenarios, except for SN98bw-GRB-$M_{\rm top}$.

8.4.2 Presence of an additional component

Given the overall narrative that GRB 211211A was a GRB connected to a kilonova, we study the ability of the GRB-M with top-hat jet structure to describe the observational data and compare this

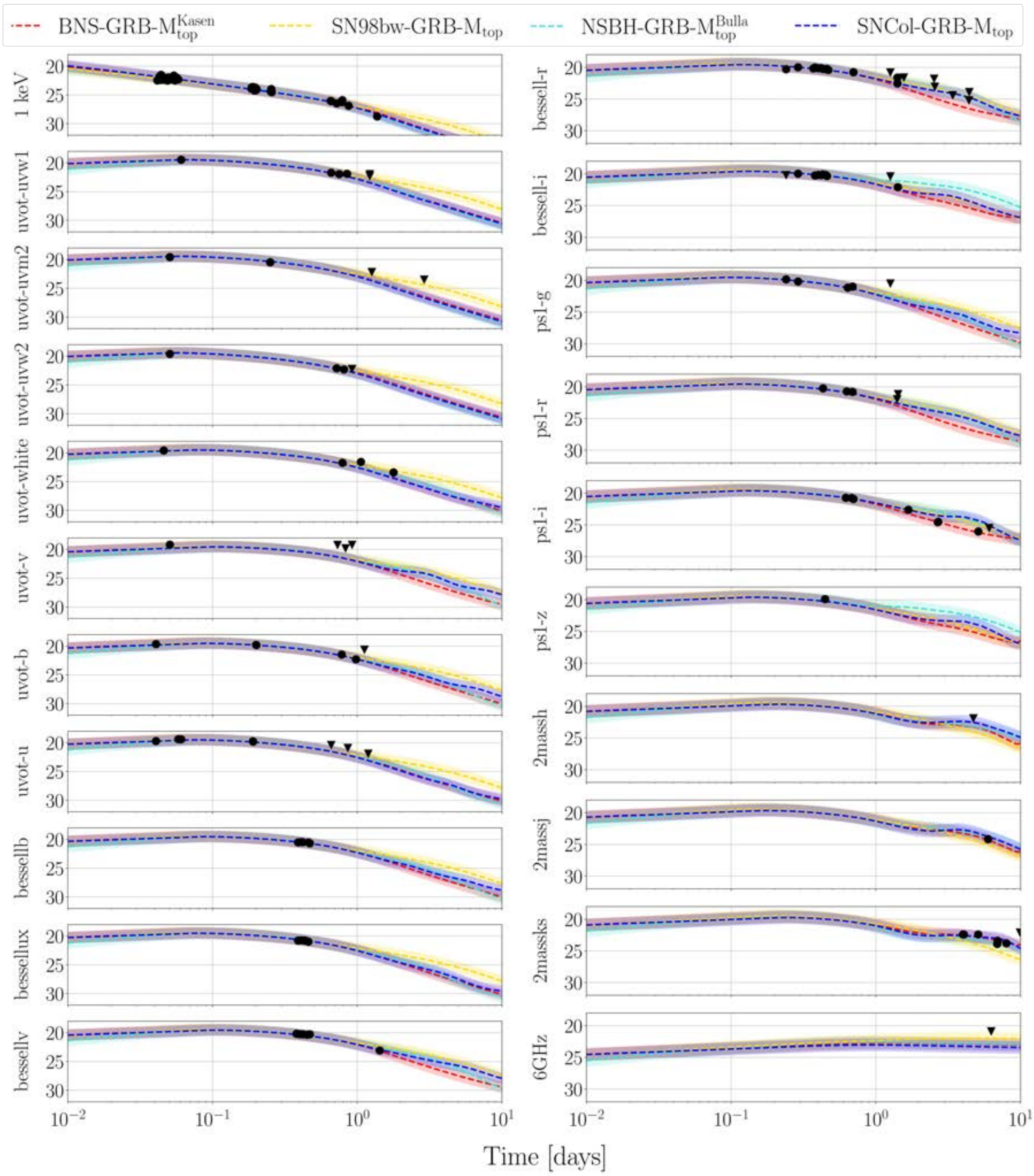

FIGURE 8.2
Best fitting light curve from joint Bayesian inferences listed in Table 8.1 for possible scenarios: BNS-GRB-M$_{top}^{Kasen}$ (red), NSBH-GRB-M$_{top}$ (cyan), SNCol-GRB-M$_{top}$ (orange), and SN98bw-GRB-M$_{top}$ (blue). The observational data of GRB 211211A in X-ray-1keV, radio-6GHz, UV, optical, and NIR band as discussed in Sec. 8.2 are shown as black dots, whereas black triangles refer to upper detection limits. Note that we are employing the naming convention of the `sncosmo` library [75] for our work.

with two BNS merger scenarios. For this purpose, we show the best-fitting light curves for BNS-GRB-$\mathrm{M}_{\mathrm{top}}^{\mathrm{Bulla}}$, BNS-GRB-$\mathrm{M}_{\mathrm{top}}^{\mathrm{Kasen}}$, and $\mathrm{GRB}_{\mathrm{top}}$ in Fig. 8.3 for a selection of the most informative bands.

We find that the GRB-M achieves a good representation of the data in the X-ray and UV bands (not all are shown in Fig. 3). However, the optical bands such as uvot-b and bessel-v already show that an additional component is required to describe the dimmer observational data observed roughly one day after trigger time. This becomes even more pronounced in NIR bands especially in the ps1-i and 2massks band where our reference model achieves the best representation. Overall, the joint model inferences of BNS-GRB-$\mathrm{M}_{\mathrm{top}}^{\mathrm{Bulla}}$ and BNS-GRB-$\mathrm{M}_{\mathrm{top}}^{\mathrm{Kasen}}$ achieve a better representation in the mentioned bands and the observational data points lie within the estimated 1 magnitude uncertainty (shaded band) of the best-fit light curves. Hence, our analysis suggests that an additional source of energy generation is required to generate bright light curves in optical and NIR bands and to fit the observed data.

8.4.3 Source properties of the potential compact binary mergers

For the scenario that GRB 211112A was connected to a compact binary merger, which is favored by our analysis, we now determine the source properties of the potential progenitor system. For this purpose, we use the inferred GRB afterglow and kilonova properties for both BNS-KN-Kasen and BNS-KN-Bulla and connect information about the ejecta and debris disk to the BNS properties following [214]; cf. [304] for a recent discussion about uncertainties in the employed numerical-relativity informed phenomenological relations.

In Fig. 8.4, we show our inference results for a possible BNS source using BNS-GRB-$\mathrm{M}_{\mathrm{top}}^{\mathrm{Kasen}}$, BNS-GRB-$\mathrm{M}_{\mathrm{Gauss}}^{\mathrm{Kasen}}$, and BNS-GRB-$\mathrm{M}_{\mathrm{top}}^{\mathrm{Bulla}}$ and contrast these to the prior probability regions for each parameter, in order to show how constraining the observational data is. Comparing inference results for BNS-GRB-$\mathrm{M}_{\mathrm{Top}}^{\mathrm{Kasen}}$ and BNS-GRB-$\mathrm{M}_{\mathrm{Gauss}}^{\mathrm{Kasen}}$, we find that estimated source masses and tidal deformabilities are very similar. For the BNS-GRB-$\mathrm{M}_{\mathrm{Top}}^{\mathrm{Kasen}}$ simulation, we find that a BNS merger with a primary mass of $1.52^{+0.49}_{-0.38}M_{\odot}$ and a secondary mass of $1.30^{+0.24}_{-0.32}M_{\odot}$ was the likely progenitor. The associated dimensionless tidal deformability of the system lies within $\tilde{\Lambda} = 348^{+855}_{-320}$. With regard to a similar analysis for BNS-GRB-$\mathrm{M}_{\mathrm{Top}}^{\mathrm{Bulla}}$, we find a primary mass of $1.57^{+0.34}_{-0.28}M_{\odot}$ and a secondary mass of $1.32^{+0.19}_{-0.24}M_{\odot}$. The corresponding tidal deformability is 320^{+426}_{-218}. Comparing estimated masses for BNS-GRB-$\mathrm{M}_{\mathrm{Top}}^{\mathrm{Kasen}}$ and BNS-GRB-$\mathrm{M}_{\mathrm{Top}}^{\mathrm{Bulla}}$, we find overall good agreement within the stated uncertainties.

Overall, our estimated masses are consistent with [533], who concluded that GRB 211211A originated from a 1.4 $M_{\odot}$+1.3 $M_{\odot}$ BNS merger. We expect that the remaining small differences are caused by the different analyses of the observed GRB 211211A data and by the fact that [533] assumed the inclination angle, under which the binary was observed, to be zero. Moreover, [533] assumed a fixed equation of state from the EOS set of [214] using additional information from [471]. In contrast, we leave the inclination angle as a free parameter in our analysis and use the updated EOS set of [324]. This set incorporates information from theoretical nuclear-physics computations and from astrophysical observations of neutron stars such as [214], but also heavy-ion collision experimental data. With regard to investigated binary merger scenarios, we find that the inferred inclination angle is around $\theta_{\mathrm{Obs}} \approx 0.02^{+0.02}_{-0.02}$rad, while a larger inclination angle of $\theta_{\mathrm{Obs}} \approx 0.04^{+0.03}_{-0.02}$rad is estimated for the considered supernova scenario (see Table 8.2).
[533] deduced a total r-process ejecta mass of $M_{\mathrm{ej}} = 0.047^{+0.026}_{-0.011}M_{\odot}$, of which 0.02 $M_{\odot}$ correspond to lanthanide-rich ejecta, 0.01 $M_{\odot}$ to intermediate-opacity ejecta, and 0.01 $M_{\odot}$ to lanthanide-free material. In addition, [678] reported a total ejecta mass of $M_{\mathrm{ej}} = 0.037^{+0.008}_{-0.004}\mathrm{M}_{\odot}$. With our reference inference result from BNS-GRB-$\mathrm{M}_{\mathrm{top}}^{\mathrm{Kasen}}$, we find a total ejecta mass of $M_{\mathrm{ej,Kasen}}^{\mathrm{BNS}} = 0.016^{+0.013}_{-0.009}\mathrm{M}_{\odot}$ which is smaller than the result estimated by [533]. Concerning our analysis based on BNS-GRB-$\mathrm{M}_{\mathrm{top}}^{\mathrm{Bulla}}$, we found a total ejecta mass of $M_{\mathrm{ej}}^{\mathrm{BNS}} = 0.022^{+0.021}_{-0.013}\mathrm{M}_{\odot}$, of which 0.012$\mathrm{M}_{\odot}$ can be attributed to lanthanide-rich ejecta, 0.006$\mathrm{M}_{\odot}$ to intermediate-opacity mass, and 0.001$\mathrm{M}_{\odot}$ to lanthanide-free material. We note that during our analysis of GRB 211211A, we have also performed simulations not including the Swift-UVOT data. In such a case, we find larger total ejecta masses of

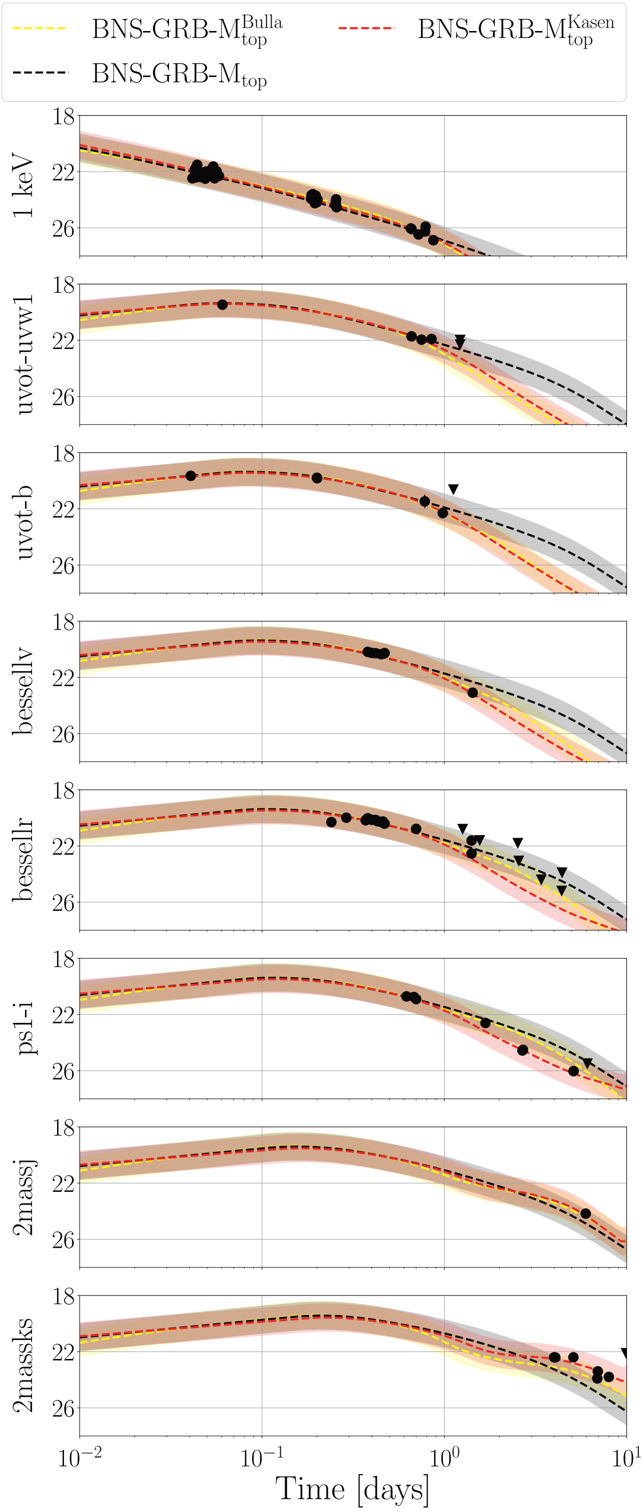

FIGURE 8.3
Best-fitting light curves from joint Bayesian inferences of BNS-GRB-M_{top}^{Bulla} (yellow) and BNS-GRB-M_{top}^{Kasen} (red) compared to a stand-alone GRB-M_{top} inference (black) for X-ray, UV, optical and NIR bands on a logarithmic time scale in days since trigger time.

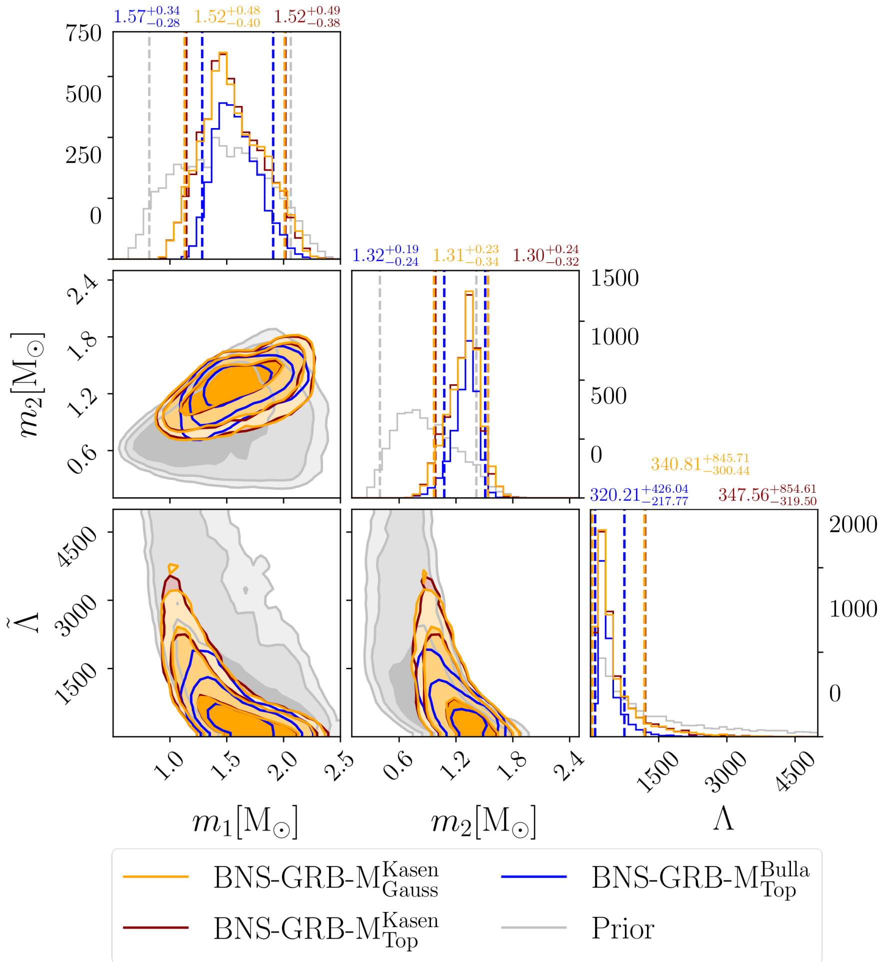

FIGURE 8.4
Component masses $m_{1,2}$ and the dimensionless tidal deformability $\tilde{\Lambda}$ based on our inference results of BNS-GRB-$\mathrm{M}^{\mathrm{Kasen}}_{\mathrm{Gauss}}$ (orange), BNS-GRB-$\mathrm{M}^{\mathrm{Kasen}}_{\mathrm{Top}}$ (red) and BNS-GRB-$\mathrm{M}^{\mathrm{Bulla}}_{\mathrm{Top}}$ (blue). Different shadings mark the 68%, 95%, and 99% confidence intervals. For the 1D posterior probability distributions, we give the 90% confidence interval (dashed lines) and report median values above each panel. Grey shaded areas give the prior probability regions.

$M^{\mathrm{BNS}}_{\mathrm{ej,Kasen}} = 0.021^{+0.017}_{-0.013}\mathrm{M}_\odot$ and $M^{\mathrm{BNS}}_{\mathrm{ej,Bulla}} = 0.031^{+0.033}_{-0.018}\mathrm{M}_\odot$ comparable to [533] and [678]. This finding sheds some light on the impact of different data sets being used to analyze astronomical sources such as GRB 211211A in a Bayesian context.

For completeness, we have performed a similar investigation for our NSBH-GRB-$\mathrm{M}_{\mathrm{top}}$ and NSBH-GRB-$\mathrm{M}_{\mathrm{Gauss}}$ models to infer the corresponding NSBH properties by making use of the relations provided in [259] and [364]. Although the observational data does not provide a strong constraint on the NSBH source properties, our NSBH-GRB-$\mathrm{M}_{\mathrm{top}}$ analysis suggests that an NSBH merger with a BH mass of $3.11^{+5.53}_{-2.23}M_\odot$ and an NS mass of $1.40^{+0.74}_{-0.81}M_\odot$ could have been the progenitor of GRB 211211A, with a total ejecta mass of $M^{\mathrm{NSBH}}_{\mathrm{ej}} = 0.006^{+0.006}_{-0.004}\ M_\odot$. Likewise, the BH spin is weakly constrained to $\chi_1 = 0.00^{+0.59}_{-0.60}$ for the NSBH-GRB-$\mathrm{M}_{\mathrm{top}}$ inference. Our inferred NS masses are in agreement with previous GW population analyses [30, 25, 15] and with the maximum non-spinning NS mass of $2.7^{+0.5}_{-0.4}M_\odot$ estimated at 90% credibility by [679]. Within the estimated uncertainties, the inferred BH mass is close to the NSBH mass gap for which the lightest BH masses were estimated to be $\sim 5M_\odot$ [690, 244].

8.4.4 Influence of the prior choice

Finally, we discuss the influence of a different luminosity distance prior on our results. The distance of GRB 211211A was relatively precisely estimated based on the redshift of the potential host galaxy, $z = 0.0763 \pm 0.0002$ [533]. However, we are generally interested in the influence of a wide uniform luminosity distance prior on our results. For this reason, we widen the prior range and allow a distance between 0 and 3 Gpc.

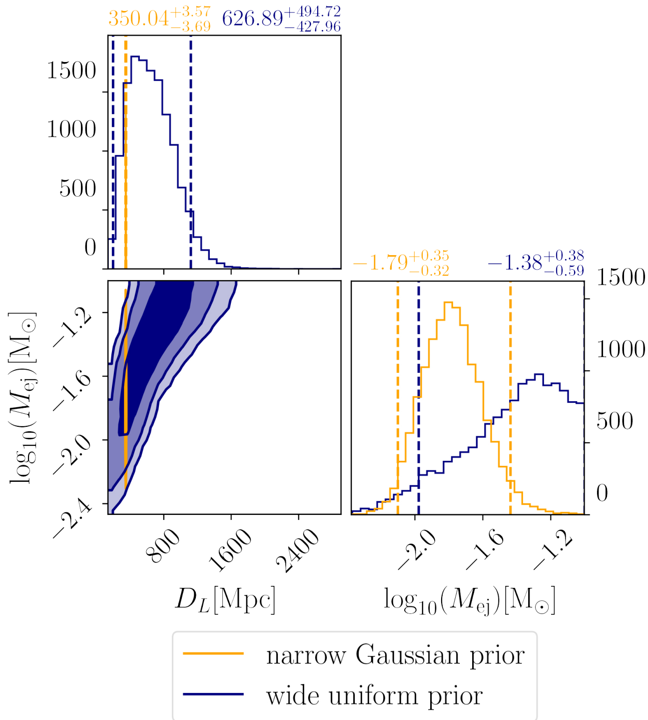

FIGURE 8.5
Corner plot for BNS-GRB-$M_{\rm top}^{\rm Kasen}$ with a narrow Gaussian luminosity distance prior centered around 350 Mpc (orange) and a wide uniform luminosity distance prior ranging up to 3 Gpc (blue). The inferred model parameters are shown at 68%, 95%, and 99% confidence (shadings from light to dark). For the 1D posterior probability distributions, we report the median values and show the 90% confidence intervals as dashed lines.

Following the procedure in Sec. 8.4.1, we have computed the logarithmic Bayes factors and found that BNS-GRB-$M_{\rm top}^{\rm Kasen}$ remains to be the best-fitting model. Moreover, the differences in logarithmic Bayes factors between BNS-KN-Bulla and BNS-KN-Kasen remain the same. The Bayes factors are slightly smaller for all assessed scenarios when comparing to the results in Tab. 8.1. Interestingly, the SN98bw-GRB-$M_{\rm Gauss/top}$ and the GRB-$M_{\rm Gauss/top}$ are least favored, while the NSBH and collapsar scenario are more favored. Overall, our main conclusions remain valid also for the wider distance prior.

We have investigated the posterior probability distributions obtained for a wide uniform distance prior and compare these with the ones obtained for a narrow Gaussian distance prior setting. In Fig. 8.5, we show an example for the obtained luminosity distance and the total ejecta mass distributions using BNS-GRB-$M_{\rm top}^{\rm Kasen}$. As can be seen, the wide distance prior leads to a noticeably weaker constraint on the distance and the total ejecta mass. The latter is caused by a degeneracy between the luminosity distance and the ejecta mass. Generally, larger ejecta masses could compensate for larger distances and vice versa, which explains the shape of the 2D correlation plot of Fig. 8.5. Similarly (not shown in the figure), also the SNCol model predicts higher ejecta masses for larger distances. With respect to the SN-GRB and the GRB inferences, the GRB isotropic energy, $\log_{10}(E_{\mathrm{K,iso}})$, tends to increase for larger distances, which is expected as brighter signals can be detected to further distances.

8.5 Conclusion

In this paper, we have performed multiple multi-wavelength analyses for GRB 211211A assuming four different scenarios, i.e., a BNS merger, an NSBH merger, an rCCSN, as well as a CCSN. On the basis of joint multi-wavelength Bayesian inferences combining respective kilonova or SN models with a gamma-ray burst afterglow model, we studied for which scenario we find the highest statistical evidence to explain the data detailed in Sec. 8.2. While emphasizing again that our study is only considering a small part of possible astrophysical scenarios and thus our results need to be considered with caution, we summarize our main conclusions below:

1. On the basis of the four assessed scenarios and the employed models, we find statistical evidence for a BNS merger scenario; cf. Table 8.1. However, we can not fully rule out other scenarios.
2. Our study confirms that GRB 211211A can not solely be explained as a GRB afterglow and that an additional emission process (likely related to r-process nucleosynthesis) is required for a good description of the observational data, mostly in optical and NIR bands (cf. Fig. 8.3). This emphasizes that near-infrared data at late times are essential to investigate the astrophysical origin of interesting transient objects.
3. Assuming a BNS origin, our study suggests that this system was a $1.52^{+0.49}_{-0.38}M_{\odot}$ - $1.30^{+0.24}_{-0.32}M_{\odot}$ binary, leading to a total ejecta mass of $M^{\mathrm{BNS}}_{\mathrm{ej,Kasen}} = 0.016^{+0.013}_{-0.009}\mathrm{M}_{\odot}$. Assuming a NSBH origin of GRB 211211A, our study suggests a $3.11^{+5.53}_{-2.23}M_{\odot}$ - $1.40^{+0.74}_{-0.81}M_{\odot}$ system with a total ejecta mass of $M^{\mathrm{NSBH}}_{\mathrm{ej}} = 0.006^{+0.006}_{-0.004}\ M_{\odot}$.

8.6 Appendix

Inference settings: All parameter estimation runs were performed using the nuclear physics and multi-messenger astronomy framework `NMMA` [492]. In this framework, joint Bayesian inferences of electromagnetic signals are carried out on the basis of the nested sampling algorithm implemented in PYMULTINEST ([135]). Each simulation used 2048 live points, and the prior settings for each of the employed models, as well as the median values and 90% credible ranges, are provided in Table 8.2.

Inference results: In the following, we present the posterior distribution for our reference model $\mathrm{GRB}^{\mathrm{Kasen}}_{\mathrm{top}}$ employing a narrow distance prior centered around 350 Mpc. Figure 8.6 summarizes our results. As discussed in the main text, we obtain an average velocity of $10^{-0.92^{+0.46}_{-0.45}}$c and a total ejecta mass of $10^{-1.79^{+0.35}_{-0.32}}\ \mathrm{M}_{\odot}$, whereas the latter is slightly smaller as compared to previous findings in the literature. Interestingly, our analysis prefers a higher lanthanide fraction compared to the one inferred for AT2017gfo using the same kilonova models [182], i.e., we predict a slightly redder kilonova (similar to [533] who predict a larger mass of the red component, but opposite to e.g. [430]).

Parameter	Prior	Posterior BNS-GRB-M_{top}^{Bulla}	BNS-GRB-M_{top}^{Kasen}	NSBH-GRB-M_{top}	SNCol-GRB-M_{top}	SN98bw-GRB-M_{top}
GRB-M						
$\log_{10}(E_{K,iso})$ [erg]	[47, 55]	$50.74^{+1.03}_{-0.86}$	$50.63^{+0.90}_{-0.86}$	$50.79^{+1.13}_{-0.94}$	$50.72^{+0.99}_{-0.89}$	$50.40^{+1.01}_{-0.70}$
θ_{Obs} [rad]	[0, $\frac{\pi}{4}$]	$0.02^{+0.02}_{-0.02}$	$0.02^{+0.02}_{-0.02}$	$0.02^{+0.02}_{-0.02}$	$0.02^{+0.02}_{-0.02}$	$0.04^{+0.03}_{-0.02}$
θ_c [rad]	[0.01, $\frac{\pi}{10}$]	$0.03^{+0.03}_{-0.02}$	$0.03^{+0.03}_{-0.02}$	$0.03^{+0.03}_{-0.02}$	$0.03^{+0.03}_{-0.02}$	$0.06^{+0.05}_{-0.03}$
$\log_{10}(n)$ [cm^{-3}]	[-6, 2]	$-5.00^{+1.46}_{-1.00}$	$-5.05^{+1.29}_{-0.95}$	$-4.96^{+1.58}_{-1.04}$	$-5.05^{+1.30}_{-0.95}$	$-4.77^{+1.15}_{-1.23}$
p	[2.01, 3]	$2.42^{+0.19}_{-0.18}$	$2.47^{+0.19}_{-0.18}$	$2.42^{+0.19}_{-0.19}$	$2.45^{+0.19}_{-0.17}$	$2.49^{+0.18}_{-0.17}$
$\log_{10}(\epsilon_e)$	[-5, 0]	$-0.10^{+0.10}_{-0.22}$	$-0.09^{+0.09}_{-0.17}$	$-0.10^{+0.10}_{-0.24}$	$-0.09^{+0.09}_{-0.19}$	$-0.08^{+0.08}_{-0.18}$
$\log_{10}(\epsilon_B)$	[-10, 0]	$-0.66^{+0.66}_{-1.43}$	$-0.59^{+0.59}_{-1.25}$	$-0.72^{+0.72}_{-1.55}$	$-0.65^{+0.65}_{-1.30}$	$-0.59^{+0.59}_{-1.28}$
D_L[Mpc]	$\mathcal{N}(350, 2)$	$350.13^{+3.49}_{-3.63}$	$350.04^{+3.57}_{-3.69}$	$350.32^{+3.81}_{-3.56}$	$350.28^{+3.75}_{-3.47}$	$350.00^{+3.60}_{-3.77}$
BNS-KN-Bulla						
$\log_{10}(M_{dyn}^{ej})$ [$M_\odot$]	[-3, -1]	$-1.89^{+0.66}_{-0.49}$				
$\log_{10}(M_{wind}^{ej})$ [$M_\odot$]	[-3, -0.5]	$-2.23^{+0.48}_{-0.72}$				
Φ [deg]	[15, 75]	$69.78^{+5.22}_{-16.11}$				
BNS-KN-Kasen						
$\log_{10}(M_{ej})$ [$M_\odot$]	[-2.5, -1]		$-1.79^{+0.35}_{-0.32}$			
$\log_{10}(v_{ej})$ [c]	[-1.8, -1]		$-0.92^{+0.46}_{-0.45}$			
$\log_{10}(X_{lan})$	[-4.5, -1]		$-1.69^{+0.69}_{-0.82}$			
NSBH-KN-Bulla						
$\log_{10}(M_{dyn}^{ej})$ [$M_\odot$]	[-3, -1]			$-2.56^{+0.49}_{-0.44}$		
$\log_{10}(M_{wind}^{ej})$ [$M_\odot$]	[-3, -0.5]			$-2.56^{+0.50}_{-0.40}$		
SNCol						
M_{ej} [$M_\odot$]	[0, 0.5]				$0.02^{+0.06}_{-0.02}$	
M_{Ni} [$M_\odot$]	[0, 0.03]				$0.00^{+0.00}_{-0.00}$	
v_{ej} [c]	[0, 0.21]				$0.20^{+0.01}_{-0.02}$	
M_{rp} [$M_\odot$]	[0, 0.05]				$0.01^{+0.02}_{-0.01}$	
Ψ_{mix}	[0, 0.9]				$0.84^{+0.06}_{-0.13}$	
SN98bw						
S_{max}	[0, 60]					$34.41^{+24.54}_{-24.81}$

TABLE 8.2
Model parameters and prior bounds employed in our Bayesian inferences. We report median posterior values at 90 % credibility from simulations that were run with Top-hat jet structure and with a narrow Gaussian luminosity distance prior $\mathcal{N}(\mu, \sigma)$, with mean $\mu = 350$ Mpc and standard deviation $\sigma = 2$ Mpc. We employ a conditional prior on the inclination angle depending on the jet core opening angle, $p(\theta_{Obs}|\theta_c)$, using a truncated Gaussian distribution, $\mathcal{N}_T(\mu, \sigma)$, where $\mu = 0$ and $\sigma = \theta_c$.

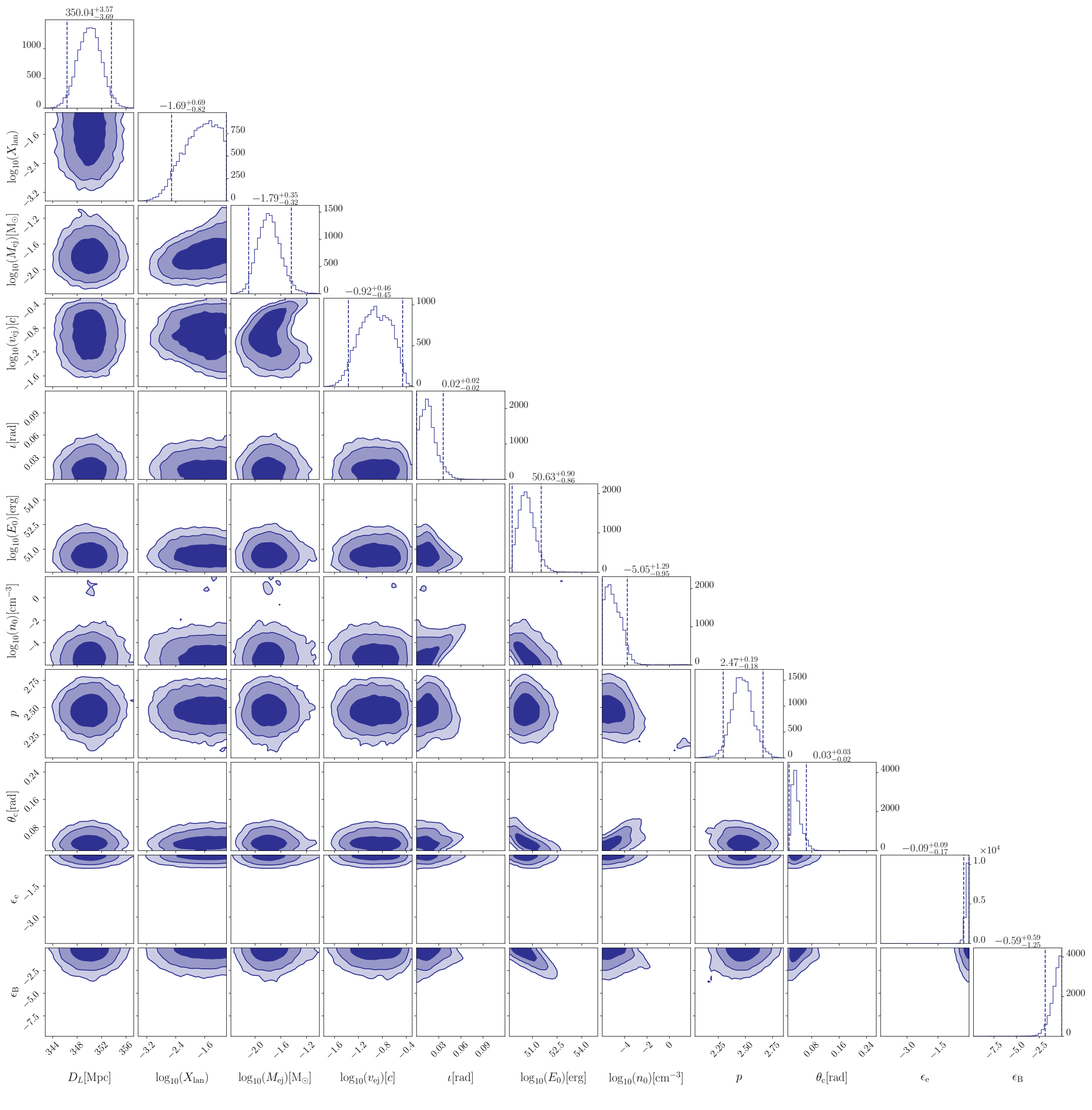

FIGURE 8.6
Corner plot for BNS-GRB-$\mathrm{M}^{\mathrm{Kasen}}_{\mathrm{top}}$ with a narrow Gaussian luminosity distance prior centered around 350 Mpc, in which we show the inferred parameters at 68%, 95%, and 99% confidence (shadings from light to dark). For the 1D posterior probability distributions, we report the median values and show the 90% confidence intervals as dashed lines.

Part VI

Binary neutron star mergers as probes of nuclear and dark matter

9

Revealing the strength of three-nucleon interactions with the Einstein Telescope

CONTENTS

*This chapter is based on the article by Henrik Rose, **Nina Kunert**, Tim Dietrich, Peter T. H. Pang, Rory Smith, Chris Van Den Broeck, Stefano Gandolfi, and Ingo Tews published in Phys.Rev.C 108 (2023) 2, 025811. My contributions to this article include conducting parameter estimation simulations, providing support for the data analysis presented in this study, and contributing to the manuscript.*

Editorial notes: Additional citations have been included beyond those in the published version.

Abstract: Nuclear systems, ranging from atomic nuclei to dense matter probed in neutron stars, are governed by strong interactions. Three-nucleon forces have been found to be a crucial ingredient for the reliable description of these systems. Here, we explore how astrophysical data on neutron stars and their mergers from current and next-generation observatories will enable us to distinguish nuclear Hamiltonians. In particular, we investigate two different nuclear Hamiltonians that have been adjusted to reproduce two-nucleon scattering data and properties of light nuclei, but differ in the three-nucleon interactions among neutrons. We find that no significant constraints can be obtained from current data, but that the proposed Einstein Telescope could provide strong evidence to distinguish among these Hamiltonians.

9.1 Introduction

Neutron stars (NSs) are among the most extreme objects in the universe [385, 161, 691, 271] and contain observable matter at the highest densities realized anywhere in nature. Inside NSs, densities up to several times the nuclear saturation density, corresponding to $\rho_{\text{sat}} \approx 2.7 \times 10^{14}$ g cm^{-3} can be reached. However, the structural properties of typical NSs, i.e., their masses, radii, and deformabilities, are determined to a large extent by dense matter up to $2-3\,\rho_{\rm sat}$. At these densities, neutron-star matter consists mainly of neutrons and protons whose microscopic interactions determine the macroscopic properties of NSs. The macroscopic NS properties can, in turn, be extracted from analyses of data from astrophysical observations, for example gravitational wave (GW) [10, 13, 16] and electromagnetic (EM) signals [83, 529, 451, 183, 214] from NS mergers, or EM observations of isolated NSs, e.g., from the Neutron star Interior Composition Explorer (NICER) [547, 446, 548, 447]. Hence, by comparing predictions of theoretical models for dense nuclear matter and astrophysical data on typical neutron stars, one can infer properties of microscopic nuclear interactions.

In the previous decade, tremendous progress has been made in calculating the properties of nuclear systems from microscopic nuclear theory. This progress was driven mainly by the development of systematic interactions from chiral effective field theory (EFT) [236, 406] as well as improvements to many-body computational methods. These methods solve the many-body Schrödinger equation numerically for a system described by a nuclear Hamiltonian that entails the kinetic energy of the particles as well as their interactions, $\mathcal{H} = T + V_{NN} + V_{3N} + \cdots$, where V_{NN} denotes two-nucleon (NN) interactions, V_{3N} denotes three-nucleon (3N) interactions, and the dots indicate additional many-body forces. Calculations of properties of atomic nuclei and isotopic chains [482, 665], and studies of nuclear matter [199, 223, 400] have shown that 3N interactions are an important ingredient in nuclear Hamiltonians and crucial to accurately describe data.

In chiral EFT, 3N interactions are usually constructed to reproduce properties of light nuclei [465, 300, 402] and then used to study heavier atomic nuclei and neutron-rich matter relevant for astrophysics. The latter requires the extrapolation of these interactions from nearly symmetric to almost pure neutron systems, which might suffer from systematics if interactions among neutrons are poorly constrained. Hence, it is desirable to investigate if one can constrain these interactions directly in neutron-rich systems. In this article, we examine how well we can distinguish between nuclear Hamiltonians that include different 3N interactions by analyzing GW signals of NS mergers, fully taking into account present uncertainties in nuclear theory. We probe how different tidal properties, due to the different 3N contributions, can be extracted from a catalogue of synthetic signals as observed in future third-generation detectors, e.g., the Einstein Telescope (ET) [519, 307].

9.2 Methods

9.2.1 Equations of state for different three-nucleon interactions

To analyze the impact of 3N interactions on the equation of state (EOS) of NSs, we follow Ref. [633] and construct two EOS sets constrained by auxiliary field diffusion Monte Carlo calculations [581, 155, 403] of pure neutron matter for two local Hamiltonians from chiral EFT [278, 279, 401]. These Hamiltonians differ in their 3N interactions in pure neutron matter (the interactions of Ref. [401] named TPE and $V_{E,\mathbb{1}}$[1]), but they give a similar description in atomic nuclei [399].

The difference in the neutron-matter description originates from regulator artifacts in the EOS due to the 3N contact interaction V_E [401]. In pure neutron matter, without any regulators, the two-pion–exchange (TPE) interaction is the only 3N contribution because the shorter-range one-pion-exchange–contact interaction V_D and 3N contact V_E vanish due to their spin-isospin structure and the Pauli principle, respectively [301]. However, when local regulators are applied, the contact interactions acquire a finite range and start to contribute also to pure neutron systems [401, 323]. Here,

[1]We do not investigate the $V_{E,\tau}$ interaction of Ref. [401] because it leads to negative pressure in pure neutron matter below $2\,\rho_{\rm sat}$.

we use these regulator artifacts to our advantage to test the sensitivity of the EOS to different 3N interactions[2]. The first Hamiltonian only contains the TPE interaction, while the second Hamiltonian additionally contains a repulsive 3N contact piece with the identity operator, $V_{E,\mathbb{1}}$.

For both Hamiltonians, we calculate the EOS up to $2\,\rho_{\mathrm{sat}}$ and estimate the truncation uncertainties according to the description used in Ref. [401]. We stress that this choice for the upper EFT density is less conservative but will enable us to demonstrate more clearly the impact of third-generation detectors. We extend these calculations to beta equilibrium and include a crust following the description of Ref. [628]. This crust model includes EFT uncertainties. We translate this to a band in the density–speed-of-sound plane from which we sample 3000 low-density EOSs for each Hamiltonian. For simplicity, we refer to the two sets as TPE and $V_{E,\mathbb{1}}$, too. We can then extend each of them to higher densities using the speed-of-sound extrapolation scheme introduced in Ref. [633]. For the extension, the prior in the radius of a typical $1.4M_{\odot}$ NS is "natural", i.e., we directly use the generated EOSs as prior and do not post-select EOSs to generate a certain prior shape. Hence, both EOS sets enable us to explore the impact of different 3N interaction strengths while taking into account all theoretical uncertainties.

Including these uncertainties is key in answering the question of whether current and future observations can distinguish between nuclear Hamiltonians and, in our case, can reveal the strength of 3N interactions. First, uncertainties in the nuclear EOS are not solely originating from unknown 3N interactions, which is reflected by the truncation uncertainty separately estimated for each Hamiltonian employed here. Second, at higher densities in the core of NSs, a description in terms of nucleonic degrees of freedom alone might fail as exotic forms of matter might appear. Using the speed-of-sound extrapolation allows us to account for all possible density behavior at high densities. Both uncertainties soften the constraining power of multimessenger data but are crucial to make robust statements about prospects of constraining nuclear Hamiltonians.

Our approach, thus, differs significantly from Refs. [423, 567], who first investigated the impact of GW measurements with current and future GW detectors on inferring 3N forces in the nuclear Hamiltonian. In contrast to our work, Refs. [423, 567] employed phenomenological NN and 3N Hamiltonians and constructed a set of EOSs by varying one parameter that quantifies the strength of the phenomenological 3N contact potential. Here, instead, we use two realistic nuclear Hamiltonians based on chiral EFT that are both adjusted to reproduce experimental data on atomic nuclei and for which we can estimate theoretical uncertainties. Furthermore, Refs. [423, 567] assumed their nuclear models to be valid throughout the whole density range of NSs, neglecting the possibility of changes to the high-density equation of state due to novel phases of matter. We, instead, include such uncertainties by using a general EOS extension scheme. Finally, they assumed a noise-free realization of GW measurements in their injection campaign, whereas we include detector noise.

9.2.2 Injection campaign

The EOS links to GW measurements of NS mergers due to tidal deformations of the stars during the inspiral phase. This leaves a characteristic imprint on the observable gravitational waveform [165]. It is most commonly expressed by the (effective) tidal deformability

$$\tilde{\Lambda} := \frac{16}{13}\frac{(M_1 + 12M_2)M_1^4\Lambda_1 + (1 \longleftrightarrow 2)}{(M_1+M_2)^5}, \tag{9.1}$$

a mass-weighted average of both components' tidal deformability $\Lambda := \frac{2k_2R^5}{3M^5}$. Here k_2 denotes the tidal Love number which, like the radius R, depends on the EOS [308]. Together with the component masses M_i, the EOS is therefore sufficient to determine $\tilde{\Lambda}$. Conversely, $M-\Lambda$ and $M-R$ relations directly map back to the EOS. Three-nucleon interactions increase the pressure in the EOS, leading to an increase in the tidal deformability compared to NN interactions only. As different 3N interaction

[2]In principle, these regulator artifacts can be thought of as sub-leading 3N contact interactions, appearing first at $\mathrm{N^4LO}$ in chiral EFT.

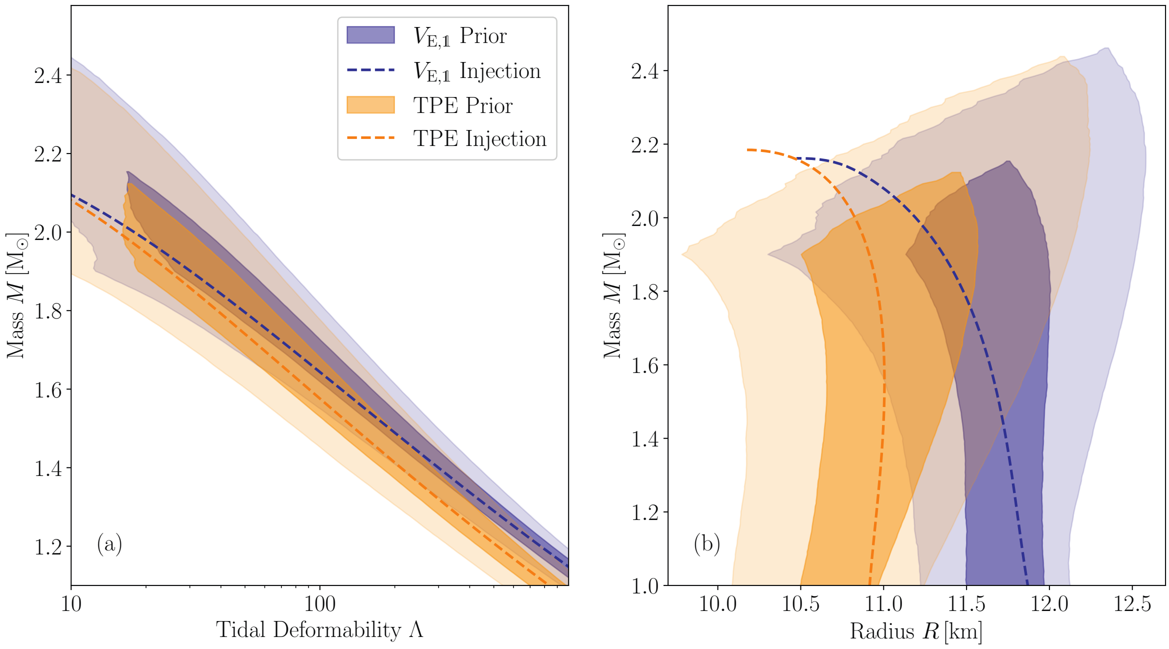

FIGURE 9.1
M-Λ (a) and M-R relation (b) for EOS prior and injections. Shaded bands indicate regions in prior space covered by 90% and 50% of EOSs, respectively. The two sets are well distinguishable at low masses. As central densities and masses rise, smaller sections of the stars are governed by the EFT regime and the parameter spaces increasingly overlap by construction. The injected EOS from each set (dashed lines) is therefore chosen based on the Λ-distribution at a relatively low mass of 1.2 $M_\odot$. We inject the EOS from the distribution's 50th percentile which has a TOV-mass closest to a fiducial value of 2.2 $M_\odot$.

models do this to a different degree, we can use information on the tidal deformability to constrain 3N forces. The EOSs in the $V_{E,\mathbb{1}}$ set are stiffer at low densities due to the additional repulsion term in the nuclear Hamiltonian. This usually leads to a larger radius at low masses and the stars are more susceptible to deformations, i.e., we generally expect to observe a higher $\tilde{\Lambda}$ than for the softer TPE set. Four-nucleon forces, on the other hand, have been shown to be small and can safely be neglected [629, 365]. The contour lines in Fig. 9.1 indicate the 50 and 90%-range of both $M-\Lambda$ and $M-R$ relations allowed by either EOS set.

A re-analysis of the GW transient GW170817 with respect to 3N interactions proves uninformative, though (see appendix 9.5.1 for details). In principle, the EOS is linked to EM observables, too, as it determines NS radii and, thus, affects the properties of ejected matter. Intricate models of this connection to EM counterparts are under development, but current uncertainties do not allow stringent constraints on 3N interactions. These modelling efforts will profit from additional multimessenger events observed with the present detector generation [34, 1]. Yet event rates are highly uncertain and kilonova rates are especially poorly constrained [30, 26, 501, 178]. We conclude that significantly improved constraints may not be expected before future detector technology becomes operational [484]. In the GW sector, this refers to the third-generation ET [519] in Europe and the proposed Cosmic Explorer (CE) [541] in the US. We, therefore, explore synthetic GW signals detected with ET. To that end, we choose an example EOS for both Hamiltonians and perform a volume-limited injection study that analyzes 20 realistic NS mergers [691]. For each injected signal, we compare Bayesian parameter estimation over the TPE and $V_{E,\mathbb{1}}$ set, amounting to a total of 80 inference runs. Subject to the population model under consideration, the detection of 20 such systems will amount to at least two years of observations at ET [32, 413].

The injected component masses $M_{1,2}$ are drawn from a Gaussian distribution $\mathcal{N}(\mu = 1.33, \sigma = 0.09)$ that is characteristic for galactic BNS systems [691]. They cover a range from 1.14 $M_\odot$ to 1.53 $M_\odot$. The systems are uniformly distributed in a comoving volume with a distance cutoff at 200 Mpc. In a larger random sample of 1000 binaries within 500 Mpc, the detections' average chirp mass settles at this distance near the injected distribution's mean, indicating that the volume is sufficiently large to characterize the underlying distribution. We further limit our analysis to systems with a signal-to-noise ratio (SNR) above 30. This value is sufficiently high to expect measurements of significant tidal contributions without introducing a bias towards higher masses, where tidal effects would again become less prominent. The dimensionless aligned spins $\chi_{1,2}$ are constrained to a uniform distribution subject to $|\chi_i| < 0.05$, as implied for realistic sources of NS mergers [618, 146]. We leave the sky location (declination and right ascension), inclination angle θ_{JN}, orbital phase at coalescence ϕ, and polarization angle ψ totally unconstrained.

From our two EOS sets, we select one EOS each for the injection campaigns with 20 binaries according to the following considerations. We naturally expect to obtain the strongest constraints on 3N interactions from low-mass binaries because the densities explored in these systems are closer to the densities that can comfortably be described by nucleonic models of matter. They are, therefore, more influenced by the EFT calculations and less so by the high-density extrapolations. Fig. 9.1 shows how the parameter spaces of the EOS sets largely overlap at high masses, corresponding to core densities far beyond the breakdown of the chiral EFT approach. In order to minimize biases resulting from the choice of injection EOS, we base our selection on both sets' associated Λ-distribution at a relatively low mass of 1.2 $M_\odot$. This mass is supported by observations and neutron star formation theories [422, 621]. We then choose to inject the EOS from each distribution's 50th percentile which has a TOV mass[3] closest to a fiducial value of 2.2 $M_\odot$. In that sense, the chosen EOS is representative for its EFT Hamiltonian in a low-mass regime and it is sufficiently realistic at high masses. We use the IMRPhenomD_NRTidalv2 approximant to generate a measurable gravitational wave from these parameters in the frequency range 30 Hz to 2048 Hz [322, 349, 626, 212]. This is then superposed by random detector noise to simulate a realistic GW strain in ET.

9.2.3 Parameter estimation

We analyze the resulting strain in the framework of Bayesian inference. This makes use of Bayes' theorem,

$$p(\theta|d) = \frac{L(d|\theta)\pi(\theta)}{\mathcal{Z}(d)}, \text{ with} \tag{9.2}$$

$$\mathcal{Z}(d) = \int_\Theta L(d|\theta)\pi(\theta)\,\mathrm{d}\theta, \tag{9.3}$$

to determine a posterior distribution $p(\theta|d)$ in the multi-dimensional parameter space Θ that characterizes an event's GW signal. We obtain the posterior by reweighting a parameter set's prior probability $\pi(\theta)$ by the likelihood L that the parameter set describes the data d. In the context of GW analyses, we determine how well a waveform model computed from various input parameters matches the observed GW strain. The likelihood evaluations follow the usual matched filter approach with the IMRPhenomD_NRTidalv2 approximant to efficiently and robustly generate waveforms including tidal effects [322, 349, 626, 212]. Because this reweighting cannot be done analytically, we have to resort to a statistical approximation by numerically sampling over Θ. The sampling parameters that describe the waveform space of our injection study are given in table 9.1.
These include observational parameters (e.g., luminosity distance d_L, phase, inclination angles of the merger) and intrinsic binary parameters (e.g., chirp mass $\mathcal{M}$, mass ratio, tilts). We considerably

[3]The TOV mass is the limiting mass above which the neutron star structure equations have no stable solution.

	parameter	symbol	prior bounds	
observational	luminosity distance [Mpc]	d_{L}	5	– 500
	inclination	cos θ_{JN}	-1	– 1
	phase [rad]	ϕ	0	– 2π
	polarization [rad]	ψ	0	– π
	right ascension [rad]	α	0	– 2π
	declination [rad]	δ	$-\pi$	– π
orbital	chirp mass [$\mathrm{M}_\odot$]	$\mathcal{M}$	*1.20*	*– 1.30**
	source chirp mass [$\mathrm{M}_\odot$]	$\mathcal{M}_s$	1.15	– 1.30*
	mass ratio	q	0.125	– 1
	source comp. mass [$\mathrm{M}_\odot$]	$M_{i,s}$	*>0.5*	
	aligned component spin	χ_i	-0.15	– 0.15
hyper	Equation of State	EOS	1	– 3000

TABLE 9.1
GW Sampling Parameters in the ET-Analysis: Most priors are uniform within given bounds. The declination δ is uniform in cosine, and the luminosity distance d_{L} is uniform within a co-moving volume of the specified dimension. The EOS prior is weighted by the ability to support massive pulsars. Prior ranges in italics indicate constraints that are not used as sampling parameters. Starred priors are adjusted to the injected signal.

extend the range above the injection distribution for the luminosity distance and aligned spins in order to avoid boundary effects from the prior distribution. This comes at the cost of a bias towards unequal mass ratios in the parameter estimation, though. As stated above, each EOS uniquely defines the tidal deformabilities, which are required as input to the waveform approximant, for any given component mass. We can, therefore, use the EOS as a sampling parameter that is constrained by tidal terms in the observed waveform. The EOS prior is weighted conservatively by incorporating a lower bound on the TOV mass in agreement with precise pulsar observations [57, 63, 256] (compare Fig. S1 of Ref. [214]).

In order to reduce the significant computational cost of waveform evaluations during the likelihood computation, we apply a Reduced-Order-Quadrature (ROQ) rule [605]. This requires limiting the chirp mass space to 0.1 $M_\odot$ intervals. ROQs apply to the observed signal and hence to mass parameters as seen in a detector frame. It is redshifted against the source frame of the system, whose non-redshifted masses determine the tidal effects. As we sample over chirp masses in the source frame, we invoke a corresponding prior adapted to the injected signal in order to avoid computational issues. Since the chirp mass is by far the most accurately measured quantity, the prior is still wide enough to avoid the introduction of prior-driven artifacts in the parameter estimation.

Due to this high dimensionality of the GW parameter space, parameter estimation is a computationally challenging problem for which we use nested sampling [603, 636]. Nested sampling algorithms aim at calculating the evidence $\mathcal{Z}$ and yield the posterior *en passant*. We employ the implementation of PARALLEL-BILBY with 2048 live points [606]. This is an efficient parallelization package relying on nested sampling routines from BILBY [603, 65], with some minor modifications to accommodate EOS sampling. The frequency range of 30 Hz to 2048 Hz is chosen to reduce computational costs with signals lasting less than two minutes[4]. In this setting, each inference run requires about 80 000 hours of computing time.

[4]While tidal effects are hardly measurable before, ET will certainly be able to detect a GW signal below 10 Hz. From this frequency range, most information on other GW parameters can be obtained [216]. We discuss the consequences of this choice in 9.3.2.

9.2.4 Model selection

The big advantage of nested sampling is that we can use it not only for parameter estimation, but also for model selection. This relies on the observation that a higher evidence $\mathcal{Z}$ can only be achieved by the more complex (i.e., with a less compact prior π) among two competing models if it matches the data significantly better. Treating both models of 3N interaction beforehand as equally likely, we follow common practice to express model preference for the TPE or $V_{E,\mathbb{1}}$ Hamiltonians by a Bayes factor $\mathcal{B}_{\text{TPE}}^{V_{E,\mathbb{1}}} = \frac{\mathcal{Z}_{V_{E,\mathbb{1}}}}{\mathcal{Z}_{\text{TPE}}}$ or its logarithm $\ln \mathcal{B}_{\text{TPE}}^{V_{E,\mathbb{1}}} = \ln \mathcal{Z}_{V_{E,\mathbb{1}}} - \ln \mathcal{Z}_{\text{TPE}}$. Moreover, the strength of 3N interactions is a universal property. The evidence for either model explaining a suite of N independent observations is given by

$$\mathcal{Z} = \int \prod_{i=1}^{N} L_i(\theta_i, \text{EOS}_i)\pi(\theta_i, \text{EOS}_i)\, \text{d}\theta_i \text{dEOS}_i \tag{9.4}$$

$$= \prod_{i=1}^{N} \int L_i(\theta_i, \text{EOS}_i)\pi(\theta_i, \text{EOS}_i)\, \text{d}\theta_i \text{dEOS}_i \tag{9.5}$$

$$= \prod_{i=1}^{N} \mathcal{Z}_i. \tag{9.6}$$

This has subsumed all system parameters besides the EOS in θ_i. The corresponding Bayes factor

$$\mathcal{B}_{\text{TPE}}^{V_{E,\mathbb{1}}} = \prod_{i=1}^{N} \frac{\mathcal{Z}_{V_{E,\mathbb{1}},i}}{\mathcal{Z}_{\text{TPE},i}} \tag{9.7}$$

then expresses the statistical support for the notion that the N systems are characterized by the $V_{E,\mathbb{1}}$ description instead of TPE.

We highlight that this is a statement on the EOS *set* and hence the 3N interactions we explore, not on the EOS itself. In principle, all neutron stars should be described by the same EOS. This assumption is built into our EOS sampling because the algorithm always tests one EOS on both stars. We may therefore treat the EOS as a hyperparameter and derive a joint posterior $p(\text{EOS})$. Its distribution after observing N systems is given by

$$p(\text{EOS}) = \text{const.} \cdot \frac{\prod_{\text{i=1}}^{\text{N}} \text{p}_\text{i}(\text{EOS})}{\pi(\text{EOS})^{\text{N}-1}}, \tag{9.8}$$

with $p_i(\text{EOS})$ denoting the posterior distribution obtained from the i-th event, marginalized over all parameters but the EOS. We can use this to define posteriors of EOS-associated quantities, e.g., a 1.4 $M_\odot$ NS's radius $R_{1.4} := R(\text{EOS}, M = 1.4\ M_\odot)$ or tidal deformability $\Lambda_{1.4} := \Lambda(\text{EOS}, M = 1.4\ M_\odot)$. However, one needs to be cautious when including this knowledge in the computation of Bayesian evidence for either EOS model. The EOS parameter space conveys present modeling uncertainties in nuclear theory. This leads to unequal prior densities in the associated observables. Hence, an EOS set of which only one model EOS survives after the inference might be erroneously favored over a set where multiple EOSs remain. We further discuss this subtlety in appendix 9.5.2.

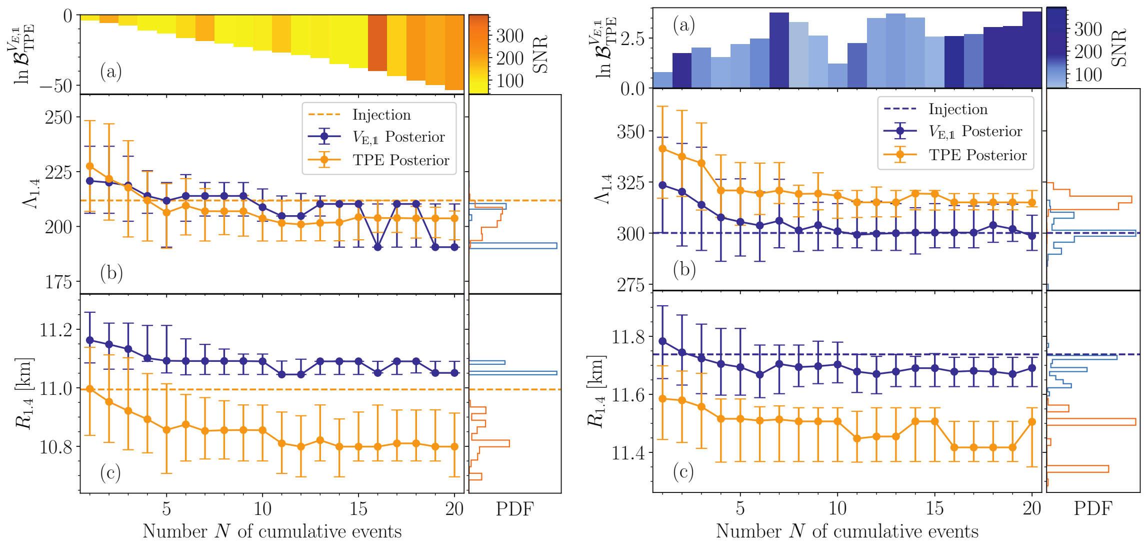

FIGURE 9.2
Joint EOS posteriors and Bayes Factors. For a TPE (left) and $V_{E,\mathbb{1}}$ (right) injection, we show model preference as expressed by a cumulative Bayes factor (a), color-coded by the event's signal-to-noise ratio (SNR). While the evidence in favor of a TPE injection piles up almost linearly, some runs with low SNR disfavor the $V_{E,\mathbb{1}}$ set when injected. Below, we show for each injected EOS the results of parameter estimation with both EOS sets. Joint posteriors on the observable tidal deformability Λ (b) and radius R (c) of a 1.4 $M_\odot$ NS are displayed as a function of total signals observed in random order. The smaller windows show the same posteriors as a probability density function (PDF) after all 20 events.

9.3 Results

9.3.1 Population analysis

Combining the information from each event into a cumulative EOS posterior using Eq. 9.8 and a joint model evidence using Eq. 9.6, we obtain the results illustrated in Fig. 9.2. On the left, we show the EOS posterior – expressed by the observable tidal deformability $\Lambda_{1.4}$ (middle) and the radius $R_{1.4}$ (bottom) of a fiducial 1.4 $M_\odot$ NS – for both EOS sets when injecting a TPE EOS. Evidence in favor of the TPE Hamiltonian accumulates very quickly and essentially independent of further system parameters (top). Particularly, we see no correlation with the color-coded SNR. We obtain $\ln \mathcal{B}^{V_{E,1}}_{\mathrm{TPE}} = -53.5 \pm 1.3$ after all 20 mergers, i.e., strong preference for the injected TPE model, although the injected EOS has only 0.04% weight in the joint TPE posterior.

Some considerations are in order to properly interpret these findings. As an increasing amount of observations is made, the TPE posterior (orange) narrows down continuously and the median estimate for $\Lambda_{1.4}$ decreases until it settles at $\Lambda_{1.4,\mathrm{TPE}} = 204^{+4}_{-10}$ (90% CI). This falls just below the corresponding injection value $\Lambda_{1.4,\mathrm{inj}} = 212$. In contrast, the posterior obtained from individual runs typically overestimates the injected tidal deformability. This relates to our conservative prior choice which only penalizes low TOV masses. EOSs that allow for higher TOV masses are typically associated with higher Λ values, too. Individual runs are therefore biased towards overestimates of Λ

at any reference mass. The joint estimate approaches a more realistic limit only as data from more runs and a wider range of component masses is included.

That the injection value is not recovered within 90% CI of the joint posterior is primarily due to a systematic overestimate of the luminosity distance d_{L} or, equivalently, the redshift. The observed mass parameters are degenerate in redshift, while Λ is determined by the component masses in their source frame (i.e., not redshifted). The overestimate in d_{L} leads to an underestimate of these masses. Low masses correspond to higher deformability, an effect that the sampling algorithm will naturally compensate by selecting EOSs of more compact NSs to match the measured tidal effects. The even larger underestimate of a 1.4 $M_{\odot}$ NS's radius with $R_{1.4,\mathrm{TPE}} = 10.80^{+0.12}_{-0.10}$ km is aided by the fact that our injection EOS happens to exhibit the highest radius ($R_{1.4,\mathrm{inj}} = 11.0$ km) among the EOSs that live in a narrow Λ-band around the injection value at 1.4 $M_{\odot}$. Since observations of the inspiral signal are not radius sensitive, we would thus expect a radius underestimate even if we had observed a more accurate Λ recovery. This highlights the fact that the NS radius and its tidal deformability are not fully equivalent quantities.

Similar arguments apply to the overall trend in the $V_{E,\mathbb{1}}$ posterior (blue). It overestimates the tidal deformability at the reference mass 1.4 $M_{\odot}$ for individual runs and decreases as we include data from additional observations. However, the overall capability of this set to explain the injected TPE signals is very low. The soft injection covers a low-Λ regime that is only sparsely populated by the on-average stiffer $V_{E,\mathbb{1}}$ EOSs. It requires a very peculiar extrapolation in the high-density end for a $V_{E,\mathbb{1}}$ EOS to soften sufficiently already for medium-mass stars to provide decent agreement with the TPE injection while still allowing for a sufficiently high TOV mass. This explains the strong preference for the TPE Hamiltonian. The tighter and better fit of the $V_{E,\mathbb{1}}$ posterior therefore must not be mistaken for evidence of better agreement with the observational data. To the contrary, this indicates the narrow range and low number of EOSs that provide a mildly plausible description of the data. After the 13th detection, only two EOSs populate more than 90% of the $V_{E,\mathbb{1}}$ posterior space and cause the apparent jumps of the observables' median estimate. The seemingly better agreement with the injection, particularly for $R_{1.4}$, should therefore not lead us astray: ET's high resolution effectively rules out $V_{E,\mathbb{1}}$ after a sufficient amount of signals.

Conversely, the corresponding plot for the $V_{E,\mathbb{1}}$ injection on the right of Fig. 9.2 demonstrates a much weaker model preference at $\ln \mathcal{B}^{V_{E,\mathbb{1}}}_{\mathrm{TPE}} = 3.8 \pm 1.3$ (top, note the different scales). This links to the fact that the TPE model naturally provides better support for the $V_{E,\mathbb{1}}$ set's Λ distribution than vice versa: As the $V_{E,\mathbb{1}}$ set is characterized by higher tidal deformability at lowest masses, the injected Λ values are then best matched by EOSs in the TPE set that stiffen considerably and early-on in comparison to the full prior. These are likely to yield high TOV masses which our prior does not penalize due to the lack of confidently measured upper bounds, in contrast to the softening $V_{E,\mathbb{1}}$ EOSs in case of the TPE injection.

The six events with the lowest SNR even seem to favor the TPE model to various degree. A low SNR in the considered distance range is typically related to low inclination angles. Due to the well-known inclination-distance degeneracy, these systems are especially prone to overestimates of the luminosity distance. In the apparent source frame, component masses appear then lower than injected. If we knew the true EOS, we could use tidal deformability measurements to break this degeneracy. But as we explore the EOS, these observations erroneously indicate a soft EOS which favors the TPE model.

Nevertheless, the joint $V_{E,\mathbb{1}}$ posterior after all runs is at $\Lambda_{1.4,V_{E,\mathbb{1}}} = 299^{+10}_{-7}$ in good agreement with $\Lambda_{1.4,\mathrm{inj}} = 300$ (dashed line), while the TPE posterior overestimates it at $\Lambda_{1.4,\mathrm{TPE}} = 315^{+6}_{-3}$. Fig. 9.3 illustrates the reason for this. It shows the ten most likely EOSs from each set together with the $V_{E,\mathbb{1}}$ injection. Fainter lines correspond to subdominant posterior contributions and background contours match the prior ranges (90% CI) in Λ (left) as well as radius (right). Since merging binaries form a distinct sub-population of all NSs, our injection was guided by the mass distribution of galactic BNS systems. We see that Λ is best recovered around that distribution's mode at 1.33 $M_{\odot}$ [691]. TPE EOSs matching this value despite their lower deformability at low mass 'overshoot' the $V_{E,\mathbb{1}}$ injection in the M-Λ plane above 1.33 $M_{\odot}$. That the joint TPE posterior overestimates $\Lambda_{1.4}$ is therefore indicative

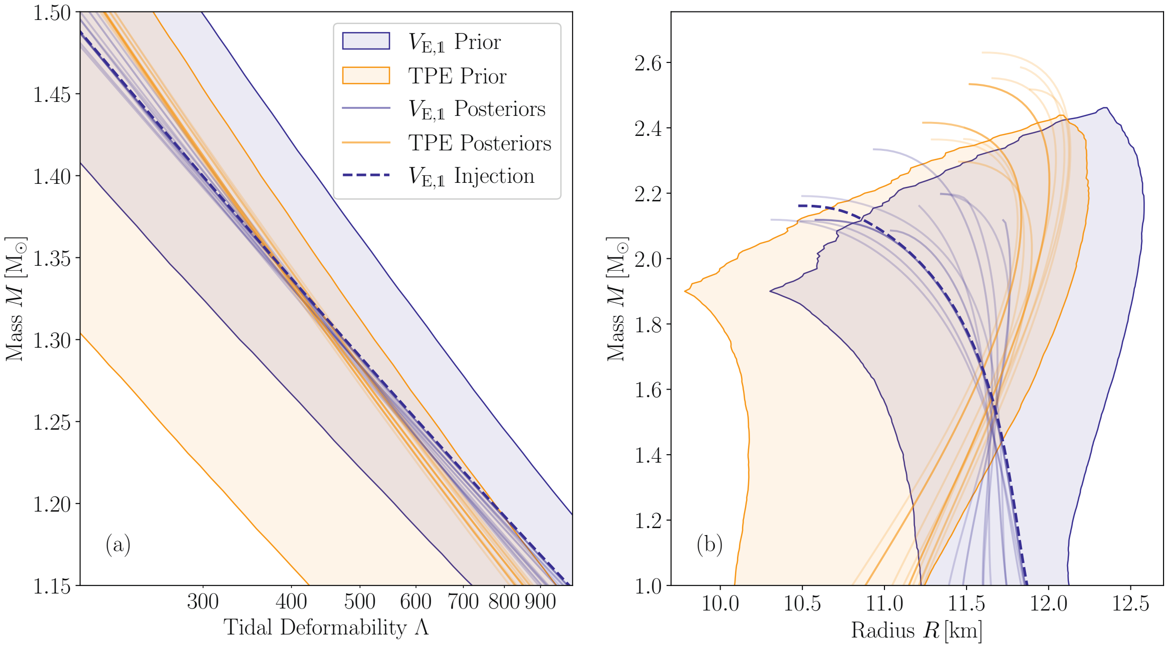

FIGURE 9.3
M-Λ (a) and M-R relation (b) for EOS prior and posterior. Similar to Fig. 9.1, shaded bands indicate regions in prior space covered by 90% of EOSs. We show the $V_{E,\mathbb{1}}$ injection as a dashed line alongside the ten dominant EOSs in each set's corresponding posterior. Note how the tidal deformability is best constrained around the mean mass of the underlying mass distribution.

of the probed mass range. It does not contradict the fact that TPE provides in general softer EOSs. The latter is further indicated by the lower radius estimate in case of the TPE model. Here, too, the final posterior is dominated by a very low number of remaining EOSs.

9.3.2 Validation

As we have discussed above, the lack of symmetry in the degree of model preference for the respective injection is linked to our prior choice. The $V_{E,\mathbb{1}}$ model's ability to reproduce the TPE injection is limited due to the prior penalty on low TOV masses. However, there is some evidence for the formation of a short-lived hypermassive NS in the GW170817 merger [542, 416, 591, 562]. Its rapid collapse to a black hole would be in conflict with the most preferred TPE EOSs in case of the $V_{E,\mathbb{1}}$ injection. We see in the mass-radius plot in Fig. 9.3 that these EOSs mostly have TOV masses of 2.4 $M_\odot$ and above. While we consider a maximum limit on the TOV mass too uncertain at the moment to include it in our more conservative main analysis, we acknowledge that new observations could provide a more confident upper limit on this mass. A corresponding penalty in the EOS prior could reduce the erroneous TPE preference and shift the Bayes factor in favor of the injection. We therefore reanalyze a signal with particularly poor parameter estimation in the $V_{E,\mathbb{1}}$ injection, using a different EOS prior that additionally penalizes TOV limits above $2.16^{+0.17}_{-0.15}\,\mathrm{M}_\odot$ [542]. This step does not significantly improve the $V_{E,\mathbb{1}}$ estimation for observable parameters, while it does lead to a modified EOS posterior. The TPE sampling, in contrast, does not converge within acceptable runtime because the adjusted prior effectively outlaws EOSs that previously provided suitable waveform descriptions. This makes it much harder for the nested sampling algorithm to find parameters with better likelihood. Enforcing convergence by allocating significantly more computing resources would certainly have removed the model preference for TPE against the injection.

Significantly better data will be available in real observations. We based our analysis on observations above 30 Hz where tidal effects begin to contribute. Inference on the full detection band would have further increased the high computational cost of this study by orders of magnitude. The mass and spin parameters of a compact binary, however, are best determined at 5 Hz to 9 Hz in ET [216]. Measuring them with high precision in this range would naturally constrain the inference of other parameters, too. Similarly, a signal recorded by a GW detector network or even identified in optical counterparts would constrain the sky location much tighter. To mimic these effects, we re-analyze the same signal with our usual priors, but under the assumption, that a) mass parameters and sky location were tightly constrained – as expected from a full bandwidth detection in a GW detector network –, and that b) the luminosity distance was known to high precision, as expected from the identification of the host galaxy to an EM counterpart.

Fig. 9.4 shows that option a) already leads to a more accurate description of the tidal effects. In our original analysis, the distance overestimate drives the EOS sets to EOSs with lower tidal deformability to counter the underestimate in the (redshifted) source-frame mass parameters. These are associated with more compact neutron stars that typically have a lower TOV limit. Because our prior penalizes low TOV limits, good waveform fits had previously worse prior support, particularly for $V_{E,\mathbb{1}}$. Properly identifying the detected mass within narrow margins of 0.01 $M_\odot$ reduces this source of uncertainty considerably and resolves the erroneous model preference for TPE against the injected $V_{E,\mathbb{1}}$ EOS. Constraining the luminosity distance even further in b), for instance by identifying a host galaxy, does not improve the estimation of other parameters and in particular $\tilde{\Lambda}$. These findings support the conclusion that realistic GW detections in the ET era with improved priors from upcoming detections will be capable of quickly distinguishing 3N interactions.

9.3.3 Discussion

Our analysis comes with some caveats. First, Ref. [370] has shown in a comparable framework how systematic errors in available waveform approximants affect the determination of tidal effects. Given the greatly increased sensitivity of ET and the prospect of advances in waveform modelling in the upcoming years, we are optimistic that these uncertainties will be reduced significantly when analyzing future detections.

Second, we have drawn the component masses from a $\mathcal{N}(\mu = 1.33, \sigma = 0.09)$-distributed population. In principle, the impact of three-nucleon interactions on the observable structure is strongest for low masses, and high-mass systems will be less constraining. The relatively tight distribution from which we have drawn masses is based on observations of close NS binaries in the milky way. Its difference to the mass distribution of isolated NSs indicates peculiar formation channels which benefit our study [627]. The fact that the only other confidently measured NS merger GW190425 contained at least one component with significantly higher masses could indicate selection effects in current radio surveys and the underestimation of other formation channels in population evolution studies [19, 267]. Nevertheless, a higher fraction of massive NSs does not harm our analysis: It would only take longer to reach a desired level of confidence with less constraining high-mass mergers. Moreover, for the low- to medium-mass range of our study, we found the quality of the strain (i.e., SNR) to outweigh effects due to the component masses.

Third, our analysis naturally depends on the true EOS, too. If it exhibited extremely low (or high) tidal effects that the $V_{E,\mathbb{1}}$ (or TPE) model cannot reproduce, the amount of detections necessary to reach a desired level of model preference will drastically reduce. If, by contrast, the true EOS covered just the middle of both models' associated $M - \Lambda$-space, a misidentification could only be avoided by studying extremely low-mass systems or by employing more advanced modelling.

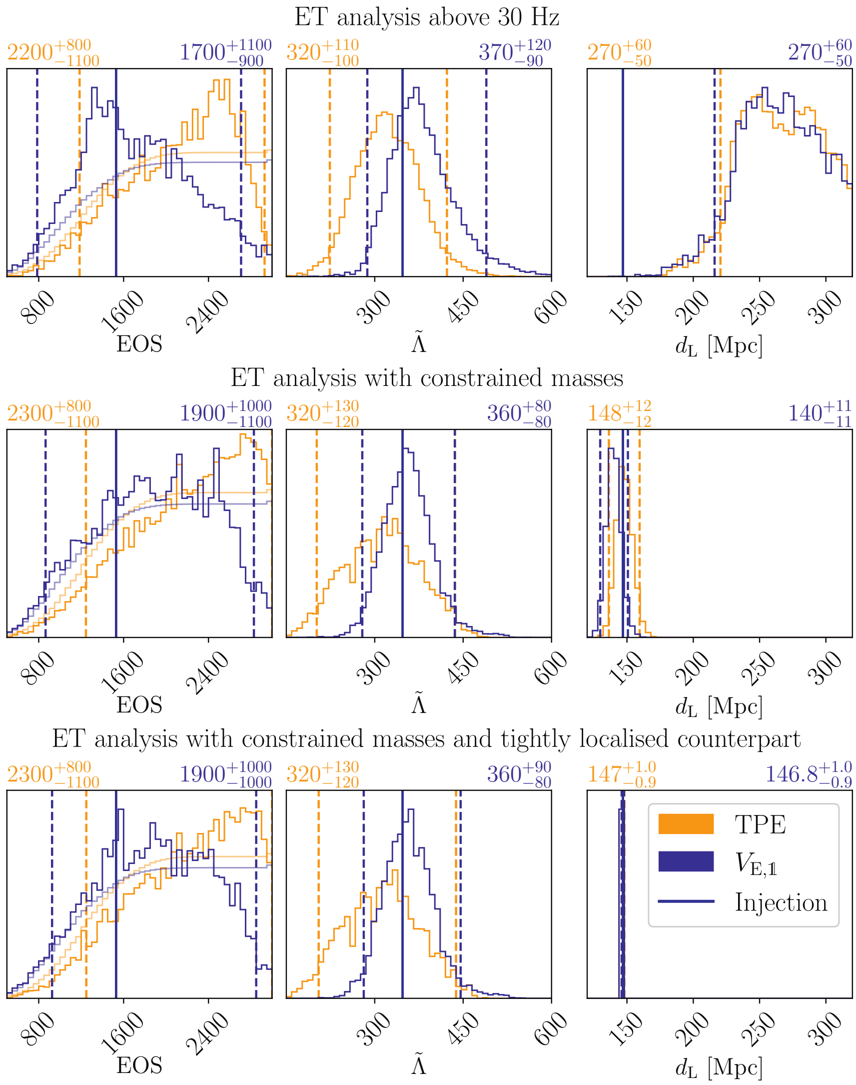

FIGURE 9.4
Selected posteriors with adapted priors: We show the posteriors for the EOS indices (left), the associated tidal deformability (center), and luminosity distance (right) in our original set-up (top), with tightly constrained mass parameters as expected from realistic network operation (middle), and with known distance as expected from the localization of an EM counterpart (bottom). The fainter lines in the EOS plots indicate the indices' prior weight. Note how the distance estimate and the tidal description improve when assuming knowledge on the mass parameters. Further limiting the luminosity distance does not improve the quality of other parameters.

9.4 Conclusions

We have performed an ET injection study to investigate if future GW observations can help to constrain the nuclear Hamiltonian in NS matter. For our TPE and $V_{E,\mathbb{1}}$ injection choices, constrained by chiral EFT at low densities and observations at high densities, we have found $\ln \mathcal{B}_{\mathrm{TPE}}^{V_{E,\mathbb{1}}} = -53.5 \pm 1.3$ and $\ln \mathcal{B}_{\mathrm{TPE}}^{V_{E,\mathbb{1}}} = 3.8 \pm 1.3$, respectively. The strength of model preference will naturally change for more or less extreme EOSs as well as for denser EOS sets.

These outcomes need to be seen in context of computational limitations and our rather conservative approach. We performed inference on the frequency domain above 30 Hz to limit this study's computational cost. While tidal terms are hardly distinguishable below, this has in fact cut the most promising information on the mass parameters which contribute most information in ET around 5 Hz to 9 Hz [216]. Additionally, we have only taken a detection by ET alone into consideration. Network operation with CE and other GW detectors as well as sky localization by detection of EM counterparts would greatly improve inference on GW parameters, including the luminosity distance, under realistic conditions and reduce the observed bias towards the TPE model. Moreover, upper limits on the TOV mass will be refined by further multi-messenger detections of NS mergers. We can therefore be optimistic to achieve significantly better constraints in actual science runs.

That we have not recovered our injected EOSs in our inference runs, but closely similar models, reminds us that we only probe the limited mass range of merging NSs. While we will be able to mitigate some systematic effects by taking into account other aspects of the expected multi-messenger signals, we cannot expect to fully recover our injections.

However, even under our conservative assumptions, we found clear evidence in support of either injected Hamiltonian, particularly when considering the systems with high SNR. This suggests that observations with 3rd generation GW detectors alone will be able to amass the required data to decisively distinguish nuclear Hamiltonians. Joint detections then reduce the amount of necessary events to surpass a desired level of confidence, underlining the potential of multi-messenger astronomy to inform nuclear theory. Naturally, if the true EOS proves more extreme, our results will be more constraining than if the true EOS can be described well by either Hamiltonian. Notwithstanding, our approach is not limited to 3N interactions but can in principle be used to constrain other parts of the Hamiltonian, too.

9.5 Appendix

9.5.1 Re-analysis of GW170817

For a re-analysis of GW170817 [28], we use the available information on the GRB afterglow and kilonova, motivating the modified prior distribution given in Table 9.2. We also use a more informative EOS prior that is weighted by minimum mass constraints from precise pulsar observations [552, 63, 57, 256], evidence for the formation of a hypermassive neutron star in the merger [542, 416], and NICER analysis of millisecond pulsars [547, 548, 446, 447]. Each measurement is assumed to be subject to Gaussian errors characterized by the respectively published uncertainty.
Fig. 9.5 displays the recovered spread of several key parameters which are consistent with the original findings and recent re-analysis [10, 463]. The luminosity distance peaks sharply near 46 Mpc, matching the spread in source chirp mass. This is slightly lower than originally reported. We can associate this effect with the wide spread of mass ratios, falling even below 0.6. The low mass ratios correspond to the

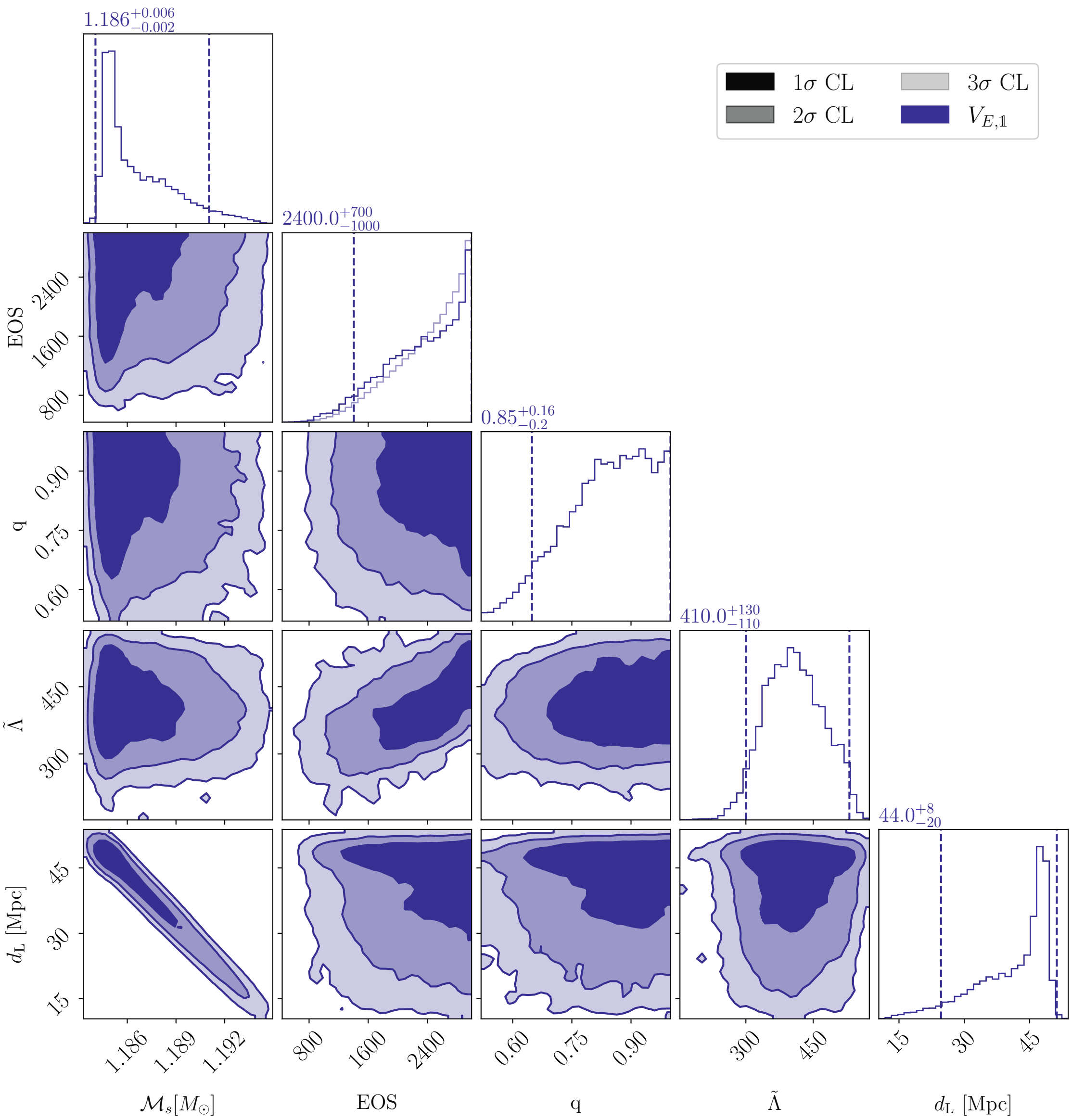

FIGURE 9.5
Important System Parameters for GW170817: We show a corner plot of (in reading direction) chirp mass, EOS index, mass ratio, tidal deformability, and luminosity distance. The blue contours represent the $V_{E,\mathbb{1}}$ recovery. A TPE recovery is not included because the low information gain in the EOS posterior (as indicated by the marginal deviation from the prior, shown in the corresponding histogram as a faint line) suggests that no constraints can be won. Dashed lines in the top histograms mark the 90% CI, contours indicate 1-, 2-, and 3-σ confidence levels in the 2D-histograms.

	parameter	symbol	prior bounds	
observational	lum. distance [Mpc]	d_{L}	1	– 75
	inclination	$\cos\ \theta_{JN}$	-1	– 1
	phase [rad]	ϕ	0	– 2π
	polarization [rad]	ψ	0	– π
	right ascension [rad]	α	3.44616	(exact)
	declination [rad]	δ	-0.408084	(exact)
orbital	chirp mass [$M_\odot$]	$\mathcal{M}$	1.18	– 1.21
	mass ratio	q	0.125	– 1
	component mass [$M_\odot$]	M_i	*>1.0*	
	aligned component spin	χ_i	-0.15	– 0.15
hyper	Equation of State	EOS	1	– 3000

TABLE 9.2
GW Sampling Parameters in GW170817-Analysis: Most priors are uniform within given bounds. Luminosity distance d_{L} is uniform within a comoving volume of the specified radial dimension. The EOS prior is weighted by the ability to support mass constraints from high-mass pulsars, NICER observations, and the kilonova observations that suggested the formation of a hypermassive NS. The component mass prior indicates a constraint that is not used as a sampling parameter.

extended prior range for the aligned spin components in comparison with Ref. [10] that considered the case $|\chi_i| < 0.05$. Since we find the spins (not shown) to deviate only slightly from the prior distribution and to be strongly anti-correlated, we conclude that there is no evidence for significant spin effects. The tidal deformability is relatively tightly constrained, falling way below the limits in nuclear-physics agnostic analysis of the original discovery [13, 200, 16] and matching findings of $80 \leq \tilde{\Lambda} \leq 580$ in a similar chiral EFT framework [633]. This is a prior-driven conclusion, though, and we find that the EOS distribution has hardly relaxed from the prior. This is due to the fact that GW170817 and chiral EFT up to $2\,\rho_{\mathrm{sat}}$ provide similar information on the EOS [153]. Since this run at the upper limit of plausible deformabilities is uninformative, no better constraints can be expected from a TPE recovery on these data. This analysis does, therefore, suggest no preference for any particular realization of 3N interactions. Other GW detections with neutron stars have so far proven even less informative with respect to tidal effects. Further measurements of NS mergers are expected in the next observing runs, but current population models make it unlikely that these include signals that are considerably stronger than GW170817.

9.5.2 Computation of evidence

Equation 9.6 does not incorporate the fact that all neutron stars should be described by only one EOS. Including this knowledge leads to a slightly different expression for the resulting evidence:

$$\mathcal{Z} = \int \prod_{i=1}^{N} L_i(\theta_i, \mathrm{EOS}_i)\pi(\theta_i, \mathrm{EOS}_i) \cdot \delta(\mathrm{EOS}_i - \mathrm{EOS}_1)\, \mathrm{d}\theta_i\, \mathrm{dEOS}_i \tag{9.9}$$

$$= \int \prod_{i=1}^{N} L_i(\theta_i, \mathrm{EOS})\pi(\theta_i, \mathrm{EOS})\, \mathrm{d}\theta_i\, \mathrm{dEOS} \tag{9.10}$$

$$= \int \prod_{i=1}^{N} \mathcal{Z}_i p_i(\mathrm{EOS})\, \mathrm{dEOS} \tag{9.11}$$

$$= \prod_{j=1}^{N} \mathcal{Z}_j \int \prod_{i=1}^{N} p_i(\mathrm{EOS})\, \mathrm{dEOS}. \tag{9.12}$$

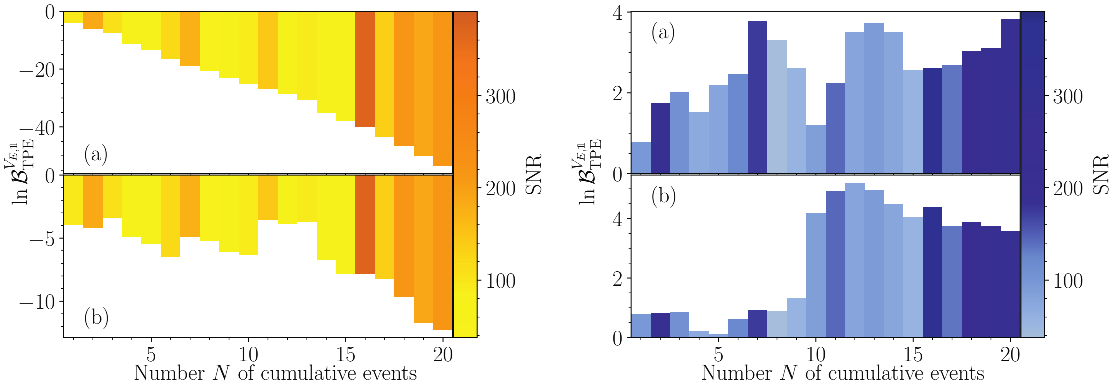

FIGURE 9.6
Comparison of Bayes Factors. Bayes factors as in Fig. 9.2, using eq. 9.6 (a) and eq. 9.12 (b), respectively. Note the different scales. For the TPE (top) injection, the model preference becomes less decisive and the inclusion of some runs favors the $V_{E,\mathbb{1}}$ model when assuming that all observations result from the same EOS. For the $V_{E,\mathbb{1}}$ injection (bottom), the overall model preference remains nearly constant, while the contribution of some runs varies greatly.

However, this prescription is misleading for the purpose of selecting among competing nuclear models. Consider, for instance, a segment of Λ space at relatively low mass that is only approximately met by a single TPE EOS, whereas multiple $V_{E,\mathbb{1}}$ EOS provide similarly good agreement with observations. This would naturally happen if $V_{E,\mathbb{1}}$ described the true EOS, independent of the total number of EOSs in each set. After some mergers with near-solar-mass NSs, eq. 9.12 would still suggest model preference for the inappropriate TPE description because it matches the expectation of a single true EOS better.

We see this effect in Fig. 9.6. The model preference in case of the TPE injection reduces massively. Even more prominent is the effect for the tenth event in case of the $V_{E,\mathbb{1}}$injection. In our analysis, it leads to a reduction of the cumulative Bayes factor because of the distance overestimate which suggests lower component masses in the source frame. If, however, we include the demand that all observations should be explained by the same EOS, we observe that the same detection has the opposite effect. This traces back to the circumstance that this system contained the most massive primary star and the second highest chirp mass in our sample. It therefore probes a low Λ regime that is not probed by other measurements. While the effects of a distance overestimate as discussed above favor the TPE model in this individual run, there are virtually no remaining TPE EOSs that agree decently with data from the lower-mass detections, too.

10

Impact of dark matter on tidal signatures in neutron star mergers with the Einstein Telescope

CONTENTS

This chapter is based on the article by Hauke Koehn, Edoardo Giangrandi, ***Nina Kunert****, Rahul Somasundaram, Violetta Sagun, and Tim Dietrich published in Phys.Rev.D 110 (2024) 10, 103033. My contributions include consultation during data analysis and contributing to the manuscript through review and proofreading.*

Abstract: If dark matter (DM) accumulates inside neutron stars (NS), it changes their internal structure and causes a shift of the tidal deformability from the value predicted by the dense-matter equation of state (EOS). In principle, this shift could be observable in the gravitational-wave (GW) signal of binary neutron star (BNS) mergers. We investigate the effect of fermionic, noninteracting DM when observing a large number of GW events from DM-admixed BNSs with the precision of the proposed Einstein telescope (ET). Specifically, we study the impact on the recovery of the baryonic EOS and whether DM properties can be constrained. For this purpose, we create event catalogs of BNS mock events with DM fraction up to 1%, from which we reconstruct the posterior uncertainties with the Fisher matrix approach. Using this data, we perform joint Bayesian inference on the baryonic EOS, DM particle mass, and DM particle fraction in each event. Our results reveal that when falsely ignoring DM effects, the EOS posterior is biased toward softer EOSs, though the offset is rather small. Further, we find that within our assumptions of our DM model and population, ET will likely not be able to test the presence of DM in BNSs, even when combining many events and adding Cosmic Explorer (CE) to the next-generation detector network. Likewise, the potential constraints on the DM particle mass will remain weak because of degeneracies with the fraction and EOS.

10.1 Introduction

The detection of gravitational waves (GW) from compact binary mergers involving neutron stars (NSs) has provided the opportunity to constrain the equation of state (EOS) for dense, strongly interacting matter [13, 529, 451, 531, 416, 542], also in combination with additional recent data from nuclear and astrophysics [524, 357, 324, 153, 107, 56]. Due to their finite size, NSs experience tidal distortion if placed in an inhomogeneous gravitational field. During the inspiral of a binary neutron star (BNS) or black-hole-neutron-star binary (BHNS), this distortion causes a phase shift on the emitted GW signal. When this phase shift is measured, Bayesian inference allows for the recovery of the tidal deformability parameter Λ which in turn restricts the underlying EOS for NSs.

The usual assumption in the aforementioned studies is to consider compact stars in a vacuum. Yet, it has been suggested that NSs might be embedded in a dark matter (DM) halo or rapidly accrete DM clumps while passing through an overdense region in a subhalo [126]. The latter scenario is supported by many cosmological models predicting formation of primordial DM gravitationally collapsed objects residing in subhalos [238, 136]. In fact, because of their extreme gravity, NSs may accumulate a significant amount of DM over their lifetime [124, 550, 99, 201], especially when located close to the respective galactic center [202]. Furthermore, it is possible that upon the creation of the NS, DM is inherited from the progenitor star [612, 442, 162]. In particular, BNS systems could have a relatively high amount of DM, since they are old systems that went through several stages of stellar evolution and the joint gravitational pull of the binary traps more DM particles in comparison to an isolated NS [89].

DM in the NS interior would alter the interior structure and thereby impact properties such as radius, mass, and tidal deformability [205, 99, 341, 197, 391, 281, 338], for a recent review see Ref. [127]. This makes NS potential probes for DM [235] but it also complicates the analysis in regards to the EOS for strongly interacting matter, because more unknown parameters with possible degeneracies need to be considered [568, 281]. In Ref. [565], the authors examined how future mass-radius measurements of NS with next-generation X-ray telescopes can be used to detect bosonic asymmetric dark matter, finding that with present uncertainties about the baryonic EOS, constraining intrinsic DM properties will not be feasible. In Ref. [569] it was shown that the reported low mass and radius for HESS J1731-347 can be explained by asymmetric, noninteracting DM and several values for the particle masses and fractions for DM would be possible.

In the present article, we investigate how future tidal deformability measurements of DM-admixed BNS with next-generation GW observatories impact the inference of the underlying baryonic EOS and whether they can be used to study intrinsic properties of DM. Next-generation observatories are necessary for this purpose, since the precision of current GW measurements is not sufficient to identify the small offset in the tidal deformability induced by DM. With two detected BNS mergers [10, 19] and three BHNS candidates [27, 3], detector sensitivity limits have only allowed for meaningful constraints on Λ in the case of GW170817 [524, 357]. Depending on the vicinity and rate of occurring events, tighter EOS constraints may be achieved during the advanced LIGO-Virgo observational runs O4 and O5 [251, 74], though the next major leap in precision will arise from next-generation detectors, such as the proposed Einstein telescope (ET) [307, 519, 577, 128] or Cosmic Explorer (CE) [8, 541, 241]. Several studies for next-generation observations show that these facilities will be able to infer the EOS with high accuracy [484, 251, 656, 74, 518, 327]. In particular, the effective tidal deformability

$$\tilde{\Lambda} = \frac{16}{13} \frac{(1 + 12q)\Lambda_1 + (12 + q)q^4 \Lambda_2}{(1 + q)^5} \tag{10.1}$$

in a binary with mass ratio q and component deformabilities $\Lambda_{1,2}$ will be measurable with an uncertainty of $\sim \mathcal{O}(10)$ at the 90% credibility limit [518, 517, 128, 327]. For comparison, the 90%-credible interval from GW170817 is set at $\tilde{\Lambda} = 356^{+479}_{-217}$ [15]. Hence, the question arises how to disentangle the contributions from DM and the unknown EOS, when tidal deformabilities can be determined with high precision in next-generation detectors.

For this purpose, we create BNS mock events where the tidal deformabilities are determined by an injected EOS together with DM effects taken into account. The posteriors on $\tilde{\Lambda}$ that would be recovered by the next-generation GW observatories are approximated through the Fisher matrix approach [649]. This mock posterior data is then used to perform a subsequent Bayesian analysis to infer the baryonic EOS jointly with the parameters of the DM model. We focus mainly on BNS measurements with ET, while we provide conclusions for a joint detector network of ET and CE in the Appendix.

We consider asymmetric, noninteracting, fermionic DM that does not annihilate, and, therefore, steadily accumulates inside the compact stars. Asymmetric DM is consistent with the ΛCDM model predicting cold (nonrelativistic) collisionless DM particles and reproduces the existing observational data [43]. The amount of accrued DM in BNSs depends on the surrounding medium, particularly the DM particle density, and could differ for each system [362]. This aspect poses a complication to the analysis of the observational data, but also offers the potential to firmly detect DM when significant variation in the tidal signatures is observable after comparing many events. The present study addresses this question by considering BNS merger events with different DM fractions up to 1%, reflecting deviations of DM density in each galaxy and at different distances from the galactic center [202].

The present article is organized as follows: In Sec. 10.2, we describe our baryonic EOS set and how we add the effects of DM for the determination of the tidal deformability. Thereafter in Sec. 10.3, we describe how we create the mock event data and lay out the details of the subsequent Bayesian statistical analysis. In Sec. 10.4, we present our findings for the impact of DM on the inference of the EOS and assess whether ET will be able to distinguish between populations of BNSs with and without DM. Finally, we summarize and discuss our findings in Sec. 10.5.

10.2 Constructing NS with DM

10.2.1 EOS construction

We construct our set of nucleonic EOSs using the metamodel of Refs. [418, 419]. The construction is similar to that of Ref. [357] but with the difference that, in this work, we use the metamodel at all densities, i.e., we do not allow for the presence of non-nucleonic degrees of freedom in NSs. The EOS predicted by the metamodel is determined by the nuclear empirical parameters which are given by the expansion of the energy per particle in symmetric nuclear matter $\mathcal{E}(n)$, and the symmetry energy $\mathcal{S}(n)$, around the nuclear saturation density, $n_{\rm sat}$,

$$\mathcal{E}(n) = E_{\rm sat} + \frac{1}{2}K_{\rm sat}x^2 + \frac{1}{6}Q_{\rm sat}x^3 + \frac{1}{24}Z_{\rm sat}x^4 + \dots\,, \tag{10.2}$$

$$\mathcal{S}(n) = E_{\rm sym} + L_{\rm sym}x + \frac{1}{2}K_{\rm sym}x^2 + \frac{1}{6}Q_{\rm sym}x^3 + \frac{1}{24}Z_{\rm sym}x^4 + \dots\,, \tag{10.3}$$

where $x = \frac{n-n_{\rm sat}}{3n_{\rm sat}}$. In this work, we fix $E_{\rm sat} = -16$ MeV and $n_{\rm sat} = 0.16$ fm^{-3}. The higher-order isoscalar parameters are varied uniformly in the ranges specified in Table 10.1. Similarly, Table 10.1 also contains the ranges for the isovector parameters. By drawing the nuclear empirical parameters from the specified ranges, we create a large set of EOS candidates from the metamodel. Furthermore, we require that our EOS candidates satisfy the following constraints:

1. A maximum mass of $M_{\rm TOV} > 1.97\,{\rm M}_\odot$ to account for the radio observations of heavy pulsars [206, 187, 256].

2. Positive symmetry energy $\mathcal{S}(n) > 0$ at all NS densities, see Ref. [419].
3. Causality in the speed of sound, $c_s \leq c$ for $n < 1.2\, n_{\rm TOV}$, where $n_{\rm TOV}$ is the central density of a NS with the maximum mass $M_{\rm TOV}$.

Metamodel draws that do not satisfy the above criteria are discarded. In this manner, we generate a set of 5000 nucleonic EOSs that constitute our EOS prior.

TABLE 10.1
The distributions from which the empirical parameters are drawn to generate the EOS candidates. The parameters $E_{\rm sat}$ and $n_{\rm sat}$ are fixed at -16 MeV and 0.16 fm^{-3}, respectively. We denote uniform distributions by $\mathcal{U}$.

Parameter	Distribution
$K_{\rm sat}$ [MeV]	$\mathcal{U}(210, 260)$
$Q_{\rm sat}$ [MeV]	$\mathcal{U}(-1000, 1000)$
$Z_{\rm sat}$ [MeV]	$\mathcal{U}(-1000, 1000)$
$E_{\rm sym}$ [MeV]	$\mathcal{U}(28, 35)$
$L_{\rm sym}$ [MeV]	$\mathcal{U}(30, 100)$
$K_{\rm sym}$ [MeV]	$\mathcal{U}(-200, 200)$
$Q_{\rm sym}$ [MeV]	$\mathcal{U}(-1000, 1000)$
$Z_{\rm sym}$ [MeV]	$\mathcal{U}(-1000, 1000)$

10.2.2 Adding DM to the NS properties

We model the DM component as a relativistic Fermi gas of noninteracting spin-one-half particles minimally coupled to Standard Model particles. This model has been extensively studied in the literature, for instance in Refs. [467, 328]. Hence, the DM pressure is given by

$$p(\mu_\chi) = \frac{m_\chi^4 c^5}{24\pi^2 \hbar^3} \left(x\sqrt{x^2-1}(2x^2-5) + 3\log\left(x + \sqrt{x^2-1}\right) \right), \tag{10.4}$$

where x is the ratio of the chemical potential μ_χ to the DM particle mass m_χ. By adopting the noninteracting Fermi gas model, we keep the number of parameters needed to describe DM to just two: the particle mass and fraction, while preserving the essential physics. In this way, the fermionic pressure is sufficient to balance the gravitational pull of DM, allowing for stable configurations and preventing DM-admixed NSs from collapsing into black holes, aligning with the observation of old compact stars.

The relation between NS mass, radius, and tidal deformability is determined by solving the two-fluid Tolman–Oppenheimer–Volkoff (TOV) and Love equations, discussed in detail in [328]. Note, that the star's tidal deformability is obtained considering the effective speed of sound derived in Ref. [281]. Unlike the one-fluid case, where the mass-radius curve is solely determined by the EOS, here the possible NS configurations will also depend on the DM particle mass m_χ and the fraction f_χ of (gravitational) DM mass over the total (gravitational) mass of the NS. For each of our 5000 baryonic EOS candidates, we calculate the stable NS configurations on a grid of 12×12 combinations for the DM particle masses and fractions. The possible grid values are distributed log-uniformly between 170–3000 MeV and 0.01–1% and listed in Table 10.2. The two-fluid TOV equations are solved up to

TABLE 10.2
Grid values for the DM particle mass m_χ and DM fraction f_χ for which NS configurations were determined. In total this amounts to 12×12 combinations. The values are distributed log-uniformly.

m_χ in MeV		f_χ in %
170		0.01
221		0.015
286		0.023
372		0.035
483	$\times$	0.053
627		0.081
814		0.123
1056		0.187
1371		0.285
1780		0.433
2311		0.658
3000		1

the point where the NS mass starts to decrease with higher central density to ensure stability of the NS against radial perturbations [559].

The choice of the DM particle mass range is motivated by previous studies [328, 564] where it was shown that light fermionic DM with $m_\chi \lesssim 170$ MeV forms an extended halo around the NS. Similar configurations could be obtained for most bosonic DM models, the range of parameters across different models is essentially equivalent [341]. Such extended DM halos could overlap at the late inspiral phase of the merger which makes existing waveform models inapplicable (for details see [564]). We thus focus on DM core configurations, considering only small changes in tidal deformability and assuming that the waveform description remains otherwise unaltered. As typical DM fractions for NS remain unknown, the choice for the range of f_χ remains arbitrary, though for instance Ref. [328] argue that considering only the Bondi accretion of DM onto an NS close to the Galactic center could yield $f_\chi = 0.01\%$. Higher fractions could occur through the other mechanisms mentioned in Sec. 10.1 and we consider 1% as a realistic upper limit. We note that other works also have investigated NS configurations with higher fractions [565, 443, 281].

10.3 EOS inference through BNS mergers

For our analysis, we create sixteen distinct catalogs of mock ET events, each encompassing 500 BNS events with a signal-to-noise ratio (SNR) larger than 100. The catalogs are identical in terms of the underlying population model, i.e., the NS masses and distances stay the same, but differ in terms of the injected baryonic EOS, DM particle mass, or DM fraction population. Specifically, for each catalog we pick one baryonic EOS, one value for m_χ and decide whether the DM fraction f_χ is sampled log-uniformly or uniformly between 10^{-4} and 10^{-2}. In total, we inject two different EOSs with four possible values m_χ (170 MeV, 483 MeV, 1056 MeV, or 3000 MeV), which then with the choice for the f_χ distribution amounts to $2 \times 4 \times 2$ combinations that represent our sixteen different catalogs. We show the distribution of the event parameters for one of our catalogs in Fig. 10.1. For the purpose of background checking, we also create two event catalogs that do not contain any DM effects. In these catalogs, the tidal deformability is solely determined by the baryonic EOS. We refer to them as "no DM" catalogs.

TABLE 10.3
Distributions from which the parameters for the individual events are drawn. Our event catalogs are created by sampling from these distributions and discarding any event with an SNR lower than 100. The event catalogs only differ in the choice for the EOS, m_χ and the distribution for f_χ. The draws for the masses, spins, and observational parameters remain the same.

	parameter	symbol	distribution
intrinsic	Component mass [M$_\odot$]	m_1, m_2	Eq. (10.5)
	Spin magnitude	a_1, a_2	$\mathcal{U}(0, 0.05)$
	DM fraction	f_χ	Log or $\mathcal{U}(10^{-4}, 10^{-2})$
	Tidal deformability	Λ_1, Λ_2	from EOS, m_χ, f_χ
observational	Luminosity distance [Mpc]	d_L	$\mathcal{U}_{\text{com. vol.}}(1, 1000)$
	Sky position [rad]	φ, θ	$\mathcal{U}(0, 2\pi)$, $\text{Cos}(0, \pi)$
	Trigger time [GPS]	t_c	$\mathcal{U}(1\text{ yr})$
	Phase [rad]	ϕ_c	$\mathcal{U}(0, 2\pi)$
	Inclination [rad]	ι	$\text{Cos}(0, \pi)$
	Polarization [rad]	ψ	$\mathcal{U}(0, 2\pi)$

From these events, we create mock posteriors on the tidal deformability using GWFAST [326, 325] and use those to perform inference on our EOS candidate set. The following two subsections first provide more details on how we draw the events for our catalogs and then about the statistical analysis of our Bayesian inference of the EOS.

10.3.1 Creating mock events

To create a mock GW detection for ET, we need to specify a parameter vector $\vec{\theta}$ for each event. This parameter vector encompasses the masses and tidal deformabilities of the NSs, their spins and other observational parameters. We list the distributions from which we draw each quantity in Table 10.3. The mass function for merging BNSs is largely unconstrained, therefore, we use the following distribution

$$P(m_1, m_2) \propto \begin{cases} (m_2/m_1)^2 & \text{if} \quad 1.1\,\mathrm{M}_\odot \leq m_2 < m_1 \leq 2\,\mathrm{M}_\odot \\ 0 & \text{else} \end{cases} \tag{10.5}$$

based on the analysis of GW170817 and GW190425 in Ref. [382]. The tidal deformabilities are determined through the combination of baryonic EOS, m_χ and f_χ. We inject one of two baryonic EOSs that were arbitrarily chosen from our candidate set. We refer to one as the "stiffer" EOS. For a canonical 1.4 $M_\odot$ NS without any DM this EOS predicts a tidal deformability of $\Lambda_{1.4}^{(\text{bar})} = 534$. The superscript here indicates that it is the expectation from the baryonic EOS alone and no DM effects are taken into account. The other EOS is the "softer" one with $\Lambda_{1.4}^{(\text{bar})} = 293$. The EOS and m_χ are fixed in each catalog, the DM fraction f_χ varies between individual events. We assume that both NSs in a binary have the same fraction f_χ that is either drawn from a log-uniform distribution between 0.01% and 1%, or from a uniform distribution in the same range.
To draw conclusions about the EOS from a BNS signal d_{GW}, one has to consider the posterior $P(\tilde{\Lambda}, \mathcal{M}, \eta | d_{\text{GW}})$ for the (source frame) chirp mass $\mathcal{M}$, symmetric mass ratio η, and effective tidal deformability $\tilde{\Lambda}$. This posterior is usually inferred from a full Bayesian sampling with a likelihood

given by

$$\ln \mathcal{L}(\vec{\theta}|d_{\rm GW}) = -\,2 \int_{f_{\rm min}}^{f_{\rm max}} \frac{|d_{\rm GW}(f) - h(f,\vec{\theta})|^2}{S(f)}\, df\,. \tag{10.6}$$

Here, $h(f,\vec{\theta})$ is the waveform model prediction for the parameter point $\vec{\theta}$, and $S(f)$ denotes the detector power spectral density. However, especially for long high-SNR signals, sampling over the entire parameter space turns out to be rather expensive. Instead, for the type of loud signals we are interested in, we assume that $P(\tilde{\Lambda}, \mathcal{M}, \eta|d_{\rm GW})$ is well approximated by a Gaussian centered around the injected (true) value. The Fisher matrix

$$F_{jk} = \mathbb{E}\left(\frac{\partial \ln \mathcal{L}(\vec{\theta}|d_{\rm GW})}{\partial \theta_j}\frac{\partial \ln \mathcal{L}(\vec{\theta}|d_{\rm GW})}{\partial \theta_k}\right)\,, \tag{10.7}$$

is then used to construct the uncertainty of this posterior. Specifically, the covariance matrix for $P(\tilde{\Lambda}, \mathcal{M}, \eta|d_{\rm GW})$ is the inverse F_{jk}. To determine Eq. (10.7) and its inverse, we use the GW-FAST package [326, 325]. The waveform model for the determination of the likelihood was set to `IMRPhenomD_NRTidalv2` [322, 349, 212]. For the ET detector, we assume the triangle configuration located in Sardinia [518, 128], the power spectral density was taken from Ref. [102].

When assessing the detection probabilities of DM, it is necessary to compare against the case when no DM is present in the events. For this reason, we also create two event catalogs in a similar manner as described here, but the tidal deformabilities are solely determined by the baryonic EOS. For each of these two "no DM" catalogs we use either the stiff or soft EOS from above.

10.3.2 Analyzing the events

The probability to observe a posterior $P(\tilde{\Lambda}, \mathcal{M}, \eta|d_{\rm GW})$ from an event $d_{\rm GW}$ when taken an EOS, a value f_χ for the DM fraction, and a value m_χ for the DM particle mass as given, is proportional to

$$\mathcal{L}({\rm EOS}, m_\chi, f_\chi|d_{\rm GW}) = \int d\mathcal{M}\; d\eta\; P(\tilde{\Lambda}(\mathcal{M},\eta), \mathcal{M}, \eta|d_{\rm GW}) \tag{10.8}$$

Here, the relationship $\tilde{\Lambda}(\mathcal{M},\eta)$ is determined through the EOS, f_χ, and m_χ. We are interested in the posterior probability for an EOS given a mock observation. From the likelihood in Eq. (10.8) it can be derived as

$$\begin{aligned} P({\rm EOS}|d_{\rm GW}) &= \int dm_\chi\; df_\chi\; P({\rm EOS}, m_\chi, f_\chi|d_{\rm GW}) \\ &\propto \int dm_\chi\; df_\chi\; \mathcal{L}({\rm EOS}, m_\chi, f_\chi|d_{\rm GW})\; \pi({\rm EOS}, m_\chi, f_\chi)\,. \end{aligned} \tag{10.9}$$

For the prior $\pi({\rm EOS}, m_\chi, f_\chi)$, we assume all the baryonic EOSs to be of equal prior likelihood, whereas the prior in m_χ is taken to be log-uniformly distributed between 170–3000 MeV. The prior for f_χ is chosen to match the distribution used to generate the events, i.e., either log-uniform or uniform between 0.01–1 %. Therefore, we may approximate Eq. (10.9) by taking the log-uniform samples $\{m_{\chi,j}\}$ and $\{f_{\chi,k}\}$ from Table 10.2 and sum over them

$$P({\rm EOS}|d_{\rm GW}) \approx \frac{1}{N_{m_\chi} N_{f_\chi}} \sum_{j,k} \mathcal{L}({\rm EOS}, m_{\chi,j}, f_{\chi,k}|d_{\rm GW}). \tag{10.10}$$

The number of samples for m_χ and f_χ from Table 10.2 is $N_{m_\chi} = N_{f_\chi} = 12$. In those cases where we want a uniform prior on f_χ, the summation over the fraction samples is performed with corresponding weights. It is worth pointing out that when combining multiple events $d^{(1)}_{\rm GW}$, $d^{(2)}_{\rm GW}$, one has

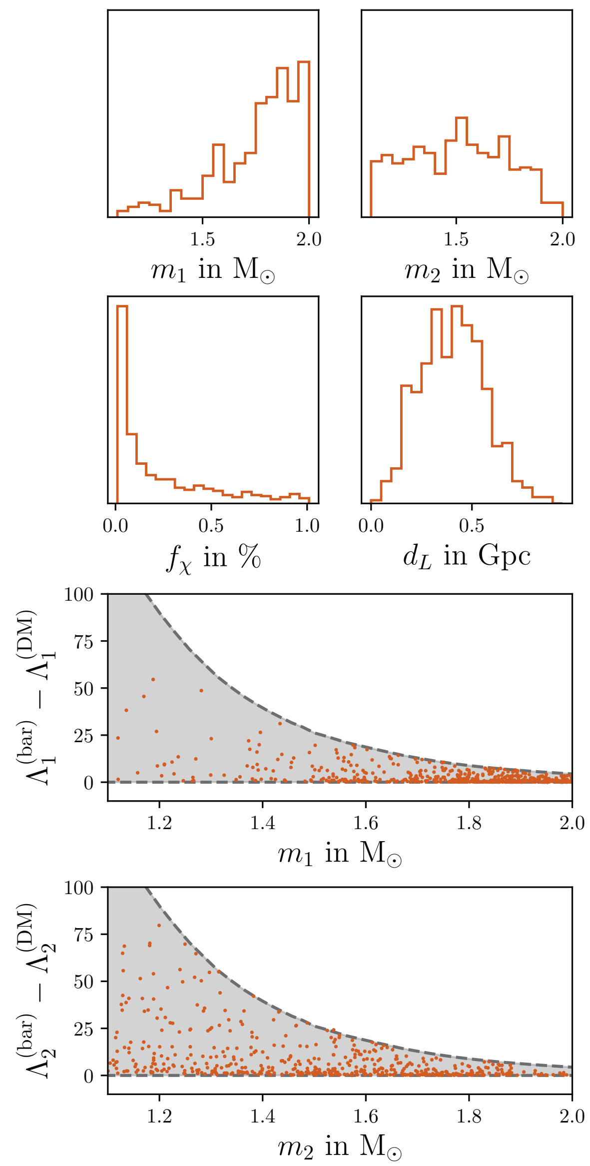

FIGURE 10.1
Overview of the 500 mock BNS events. The upper panels show the distribution of the component masses m_1, m_2, and luminosity distance d_L, these values remain the same across all event catalogs. The bottom panels show the difference between $\Lambda^{(\mathrm{bar})}$, i.e., the tidal deformability expected from the baryonic EOS, and the actual tidal deformability when accounting for the presence of DM. The upper dashed gray line shows the limit on the deviation of the tidal deformability from the baryonic value, i.e., from the M-Λ relationship for a NS with 1% DM. For this plot, we chose the event catalog with the stiff baryonic EOS, $m_\chi = 483$ MeV and the fraction f_χ was distributed log-uniformly.

to marginalize over the fraction for each event individually, i.e.,

$$\mathcal{L}(\mathrm{EOS}, m_{\chi,j}|d_{\mathrm{GW}}^{(1)}) \approx \frac{1}{N_{f_\chi}} \sum_k \mathcal{L}(\mathrm{EOS}, m_{\chi,j}, f_{\chi,k}^{(1)}|d_{\mathrm{GW}}^{(1)}) \,, \tag{10.11}$$

$$\begin{aligned}\mathcal{L}(\mathrm{EOS}, m_{\chi,j}|d_{\mathrm{GW}}^{(1)}, d_{\mathrm{GW}}^{(2)}) = \\ \mathcal{L}(\mathrm{EOS}, m_{\chi,j}|d_{\mathrm{GW}}^{(1)})\ \mathcal{L}(\mathrm{EOS}, m_{\chi,j}|d_{\mathrm{GW}}^{(2)}) \,.\end{aligned} \tag{10.12}$$

The posterior on the EOS is simply obtained by marginalizing the likelihood with a log-uniform prior on the DM particle mass:

$$P(\mathrm{EOS}|d_{\mathrm{GW}}^{(1)}, d_{\mathrm{GW}}^{(2)}) \propto \frac{1}{N_{m_\chi}} \sum_j \mathcal{L}(\mathrm{EOS}, m_{\chi,j}|d_{\mathrm{GW}}^{(1)}, d_{\mathrm{GW}}^{(2)})\,. \tag{10.13}$$

To obtain a posterior on the DM particle mass instead, we can also marginalize Eq. (10.12) with a uniform prior on the baryonic EOS. We establish two hypotheses, to explore the potential biases when analyzing the DM-admixed BNSs without accounting for the effects of DM:

- $\mathcal{H}_0$: The null-hypothesis states that for a given set of BNS events, the data is simply described by one baryonic EOS.
- $\mathcal{H}_1$: The alternative hypothesis claims that the BNS events are best described by DM-admixed BNS and the $\tilde{\Lambda}(\mathcal{M}, \eta)$ relationship experiences some variation from event to event.

The hypothesis $\mathcal{H}_1$ corresponds to using the likelihood in Eq. (10.8), whereas for $\mathcal{H}_0$ the likelihoods need to be determined with

$$\mathcal{L}(\mathrm{EOS}|d_{\mathrm{GW}}) = \int d\mathcal{M}\ d\eta\ P(\tilde{\Lambda}^{(\mathrm{bar})}(\mathcal{M}, \eta), \mathcal{M}, \eta|d_{\mathrm{GW}})\,, \tag{10.14}$$

i.e., the relationship for the tidal deformability is simply given by the baryonic EOS without any DM effects.

10.4 Results

For each event in our 16 catalogs, we determine the likelihood in Eq. (10.8) across our EOS candidates and the parameter grid for m_χ and f_χ from Table 10.2. From these likelihood values we obtain the posterior distribution on the baryonic EOS as described in Eq. (10.13). Similarly, we also obtain a posterior on the DM particle mass m_χ and further determine the Bayes factor for $\mathcal{H}_1$ vs. $\mathcal{H}_0$. In this section, we summarize the findings of our Bayesian analysis.

10.4.1 Recovering the underlying baryonic EOS

For the DM model and DM parameter ranges we consider in the present article, the tidal deformabilities of BNS are systematically lowered. Hence, over many events a bias toward softer baryonic EOSs could arise if one were to analyze a set of DM-admixed BNS events simply through a baryonic set of EOS candidates. Our analyses confirm that small biases in the EOS recovery appear, if the events in a catalog with DM are analyzed according to $\mathcal{H}_0$, i.e., ignoring DM effects. Figure 10.2 compares how the posterior estimate on the canonical baryonic tidal deformability $\Lambda_{1.4}^{(\mathrm{bar})}$ evolves over the course of multiple BNS events, when the DM effects are included in the inference vs. when they are ignored. Note that $\Lambda_{1.4}^{(\mathrm{bar})}$ here refers to the tidal deformability without any DM effects, as we simply use this quantity as an indicator to describe the recovery of the injected baryonic EOS.

The strength of the bias depends on whether the population for the DM fraction is log-uniform or uniform. In case of the latter, more BNS events will have a higher f_χ and already after around 50–100 events, a discrepancy between the $\mathcal{H}_0$-analyses and the injected true EOS is noticeable. At the same time, this bias is generally small, as the posterior estimates deviates from the true $\Lambda_{1.4}^{(\mathrm{bar})}$ in the range of 10–20. When the DM fraction in the BNS events is log-uniformly distributed, the discrepancy between the injected value and the analysis without DM is even smaller and the 95% credible region excludes the true EOS only after $\gtrsim 150$ events. The analyses for the event catalogs

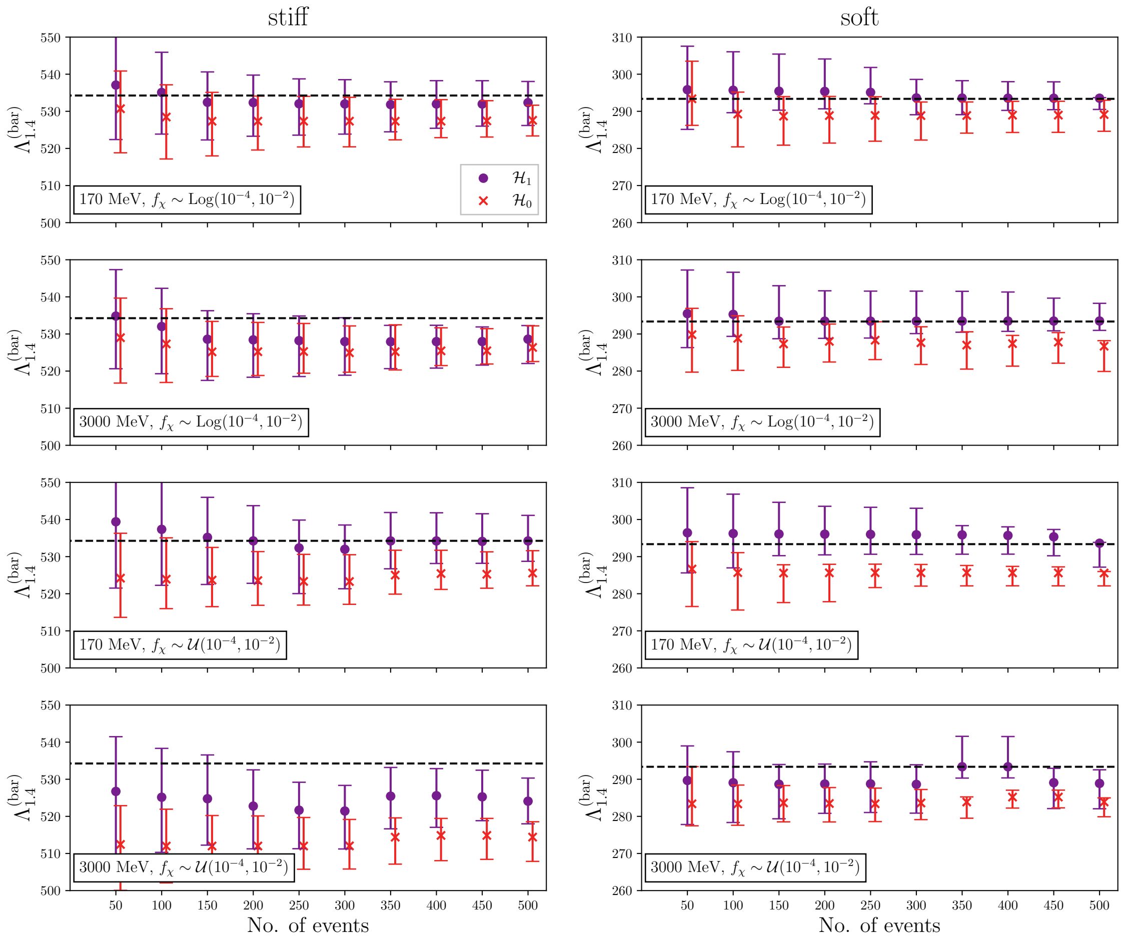

FIGURE 10.2
Evolution of the posterior estimate for the baryonic $\Lambda_{1.4}^{(\mathrm{bar})}$ with rising number of observed BNS events. The purple bands show the 95% credibility interval when the events are analyzed according to $\mathcal{H}_1$, i.e., when DM effects are included, whereas the red band indicates the credibility interval if DM effects are not accounted for, corresponding to $\mathcal{H}_0$. The circle and cross indicate the posterior medians, respectively. The panels correspond to distinct event catalogs, where the injected DM particle mass and the population for the DM fraction are described in the bottom left label. The panels of the left side correspond to those catalogs, where the injected baryonic EOS is stiffer, the panels on the right to the softer EOS. The true value for $\Lambda_{1.4}^{(\mathrm{bar})}$ from the injected baryonic EOS is shown as black dashed line.

with injected $m_\chi = 483$ MeV, and $m_\chi = 1056$ MeV are not shown in Fig. 10.2 but show the same trend.

However, we note that even the $\mathcal{H}_1$-inference is not always successful at recovering the true EOS. This happens in those cases where the injected particle mass is high, as seen in Fig. 10.2 for those catalogs where $m_\chi = 3000$ MeV. The reason is that the core configurations get more compact with higher DM particle mass, hence the reduction of the tidal deformability from the pure baryonic EOS is larger than for lower m_χ. However, this reduction in Λ can also be mimicked by EOSs that are softer than the actual injected EOS when they are combined with a low DM particle mass. Because we marginalize over all DM particle masses, and lower masses are preferred in the log-uniform prior, the final result is biased toward these slightly softer EOSs. The bias disappears when using a prior that is more favorable for higher m_χ. This indicates the sensitivity of the $\mathcal{H}_1$-inferences to the prior choice for the DM parameters.

Conversely to the bias we receive when $\mathcal{H}_1$ is true but we instead assume $\mathcal{H}_0$ in our analysis, we can also look at the bias that arises when we consider the events without any DM and analyze them according to $\mathcal{H}_1$. For this purpose we reran the analysis for our two "no DM" catalogs. Analyzing these events with $\mathcal{H}_0$, we found no bias at all in the recovery of the true baryonic EOS, as expected. When performing the analysis with $\mathcal{H}_1$, the posterior on $\Lambda_{1.4}^{(\mathrm{bar})}$ is biased toward stiffer EOSs than the true one, though the offset is only 5–15 and the true injected value leaves the 95% credible interval only after 400 events.

We point out that the uncertainties with which we determine $\Lambda_{1.4}^{(\mathrm{bar})}$ in the catalogs with the softer baryonic EOS (right panels in Fig. 10.2), are likely underestimated. This is because the softer EOS lies in a region of our EOS prior that is not very densely sampled, so after $\gtrsim 300$ events only few EOS with nonzero likelihood remain. Hence, the posterior on $\Lambda_{1.4}^{(\mathrm{bar})}$ is undersampled and the 95% credible intervals become too narrow.

10.4.2 Detectability of DM

To assess whether ET would allow the detection of DM from our BNS population, one may look at the Bayes factor $\mathcal{B}$ for $\mathcal{H}_1$ against $\mathcal{H}_0$. It is given as the evidence ratio of $\mathcal{H}_1$ over $\mathcal{H}_0$. We approximate the evidences by averaging the likelihood over the prior samples for m_χ, f_χ, and the EOS. The Bayes factor will change, depending on how many events are combined in the likelihood.
In the top panels of Fig. 10.3, we determine $\ln(\mathcal{B})$ for each event individually and plot the distribution. The individual log-Bayes-factors range mostly from -0.02 to 0.25. Thus, a single event is not very indicative whether DM was present in the NS or not. This is expected, as a single event only provides one data point for $\tilde{\Lambda}$ that likely can be well matched by some baryonic EOS.

However, even when combining multiple events together, the detectability of DM does not increase in our setup. In the middle and bottom panels of Fig. 10.3, we randomly group 10, respectively 20 events together, determine the Bayes factor for these batches and show the distribution. Generally, with growing number of combined events, the Bayes factor decreases and becomes mostly negative. The reason is that we average over the likelihood values with our prior to determine the evidence, and when multiple likelihoods from different events are combined, the average over the larger parameter space will generally decrease quicker than over the smaller one, when both models have the same ability to describe the data. The preference for the simpler model is a general property of the Bayes factor often attributed to Occam's razor. We note that the distribution of $\ln(\mathcal{B})$ is rather independent of the value for m_χ. When comparing the Bayes factors in a forward-background approach, we see that ET is not capable to distinguish between $\mathcal{H}_1$ and $\mathcal{H}_0$. The two "no DM" catalogs, i.e., the catalogs for which $\mathcal{H}_0$ is actually true, serve as background model and the distribution of their log-Bayes-factors are shown as gray patches in the panels of Fig. 10.3. They cover a similar range as the evidence ratios for the catalogs where DM is present, indicating that one cannot decide $\mathcal{H}_1$ over $\mathcal{H}_0$ based on $\mathcal{B}$. This is definitely true when f_χ is distributed log-uniformly, whereas $\ln(\mathcal{B})$ sometimes rises above the maximum from the background catalog when the fraction instead follows a uniform distribution. However, $\ln(\mathcal{B})$ stays close to 0 and for neither DM catalog it raises above the 5–σ level estimated

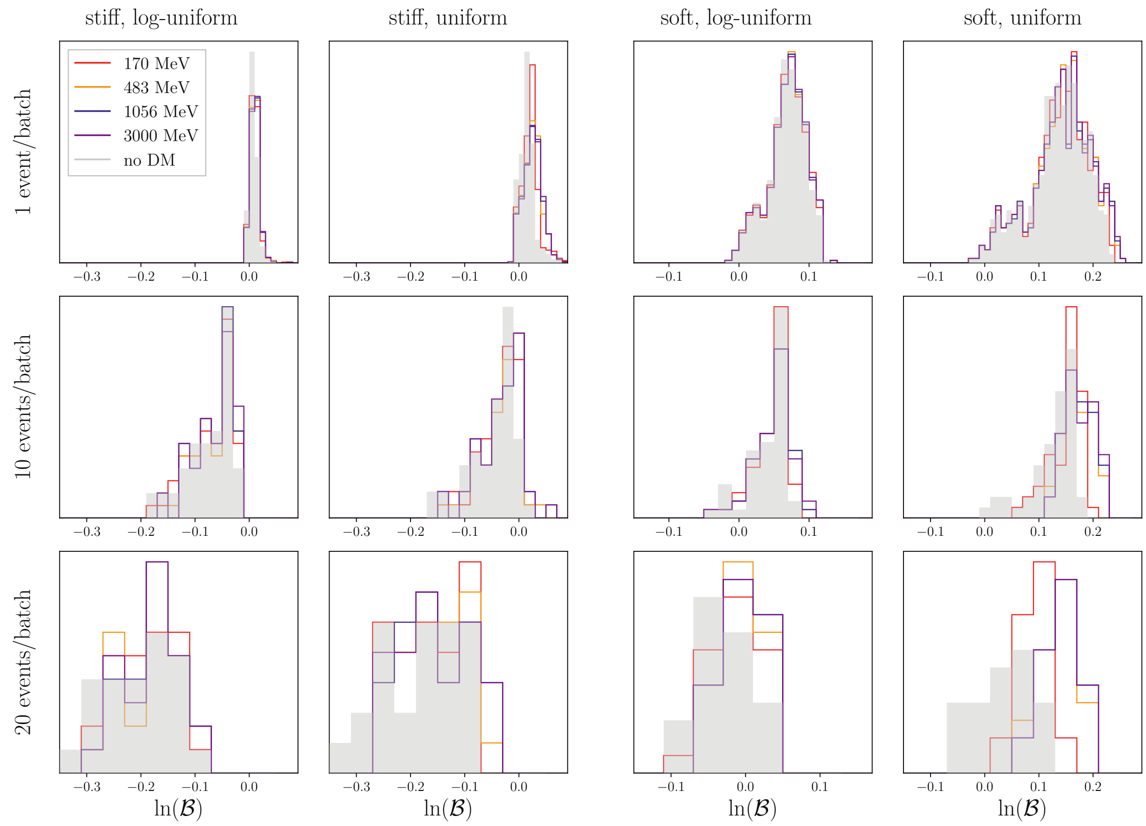

FIGURE 10.3
Distribution of $\ln(\mathcal{B})$ for the sixteen event catalogs with DM and the two event catalogs without DM. The top panels show how the Bayes factor is distributed when analyzing each of the 500 events individually, the middle panels show the distribution for batches of 10 events, the bottom panels for batches of 20 events. The first panel column refers to the event catalogs where the stiff EOS is used and f_χ is distributed log-uniformly. The different colors indicate the different injected m_χ-values, the gray patch refers to the evidence distribution when no DM is present in the events. Likewise, the second panel column uses the stiff EOS and a uniform f_χ-distribution, the third the soft EOS and a log-uniform f_χ-distribution, and the fourth the soft EOS and a uniform f_χ-distribution.

from the background model with kernel-density estimation. For the case of the soft EOS, there is an additional caveat: As discussed in Sec. 10.4.1, the soft EOS lies in a slightly undersampled region of the EOS prior. Therefore, the corresponding analyses assume stronger *a priori* knowledge about the EOS and are thus more capable of distinguishing between the tidal deformabilities from the baryonic and DM cases. The slightly stronger separation of $\ln(\mathcal{B})$ in case of the catalogs with the soft EOS indicates that potent constraints about the baryonic EOS, e.g., from nuclear physics or other data points, may enable detection of DM through tidal information from BNS, though it is unclear to which extent the baryonic EOS would need to be constrained. Yet, when inferring the EOS and DM properties simultaneously as we do in the present work, combining up to 20 BNS events will not be sufficient to observe the presence of DM from tidal signatures of BNS.

In Table 10.4 we show the values for $\ln(\mathcal{B})$ when combining all 500 events together. For all catalogs, the log-Bayes factor is negative, indicating that even with 500 events, $\mathcal{H}_0$ is equally capable of describing the data as $\mathcal{H}_1$. The expected number of BNS detections with SNR > 100 for ET is hard to assess due to uncertainties in the BNS population and the eventual detector design, but estimates

TABLE 10.4
Log-Bayes factors $\ln(\mathcal{B})$ for $\mathcal{H}_1$ against $\mathcal{H}_0$ after 500 events. The first column specifies which baryonic EOS was used in the respective event catalog, the second one whether f_χ was distributed log-uniform or uniform. The log-Bayes factors are listed in the columns for each injected m_χ and for the no-DM catalogs.

EOS	distribution for f_χ	m_χ in MeV				
		170	483	1056	3000	no DM
stiff	Log	−4.54	−4.32	−4.23	−4.23	−4.09
stiff	$\mathcal{U}$	−3.78	−2.41	−2.23	−2.16	−3.68
soft	Log	−1.98	−2.56	−2.62	−2.71	−2.53
soft	$\mathcal{U}$	−2.92	−2.93	−2.70	−2.65	−1.79

range from 50–150 per year [123, 241, 128]. Hence, we expect that ET will not be able to identify DM from tidal signatures of BNS within its first years of operation. In the Appendix we confirm that this assessment does not change, when the same set of events is analyzed in a detector network with ET and CE.

10.4.3 Inference of the DM particle mass

Since the DM particle mass impacts the change in tidal deformability of the NS, one could in principle infer the value of m_χ from the GW data. In practice however, we find that this is difficult to achieve when inferring the EOS and DM properties simultaneously. An individual event is only one data point about the tidal deformability, hence getting a useful estimate on m_χ and f_χ is infeasible. In Fig. 10.4, we show the distribution on m_χ and f_χ after one event, in one instance after the event with the highest SNR and in the other for an event with average SNR. When marginalizing over all prior EOS candidates, i.e.,

$$\mathcal{L}(m_\chi, f_\chi | d_{\mathrm{GW}}) = \sum_{\mathrm{EOS}} \mathcal{L}(m_\chi, f_\chi, \mathrm{EOS} | d_{\mathrm{GW}}) \,. \tag{10.15}$$

the likelihood is relatively constant across the m_χ-f_χ space, even for the high SNR event. Higher masses and fractions seem to have slightly higher likelihoods, though the variation is only on the order of a few percent. This offset of the maximum likelihood from the true values arises because DM reduces the tidal deformabilities in the signal by an interval $\approx \Delta\Lambda(m_\chi, f_\chi)$. The likelihood for a pair of m_χ and f_χ thus depends on how many baryonic EOSs are available within the range of the tidal deformability as measured plus $\Delta\Lambda(m_\chi, f_\chi)$. Our EOS prior set is not exactly uniform in tidal deformability and in this case there are just slightly more baryonic EOSs available to match the data when the values for m_χ and f_χ are high compared to when they are low, hence the offset arises.

To get an estimate of the DM particle mass, multiple events are needed to infer the true baryonic EOS simultaneously with the deviation in the observation away from it. In the bottom panel of Fig. 10.4 we show the likelihood for m_χ and f_χ after the event with modest SNR, where we only consider the contribution from the true injected EOS. On the one hand, it demonstrates that, when the true underlying EOS is known, the maximum likelihood aligns well with the true values of m_χ and f_χ. However, the variation in likelihood is still small, and even for high SNR events we find that it is only on the order of a couple $\sim 10\%$. Moreover, the bottom panel of Fig. 10.4 also exhibits a degeneracy between m_χ and f_χ. An event with high DM particle mass and low fraction may be equally well described by a low DM particle mass. When the DM particle mass is large, but the

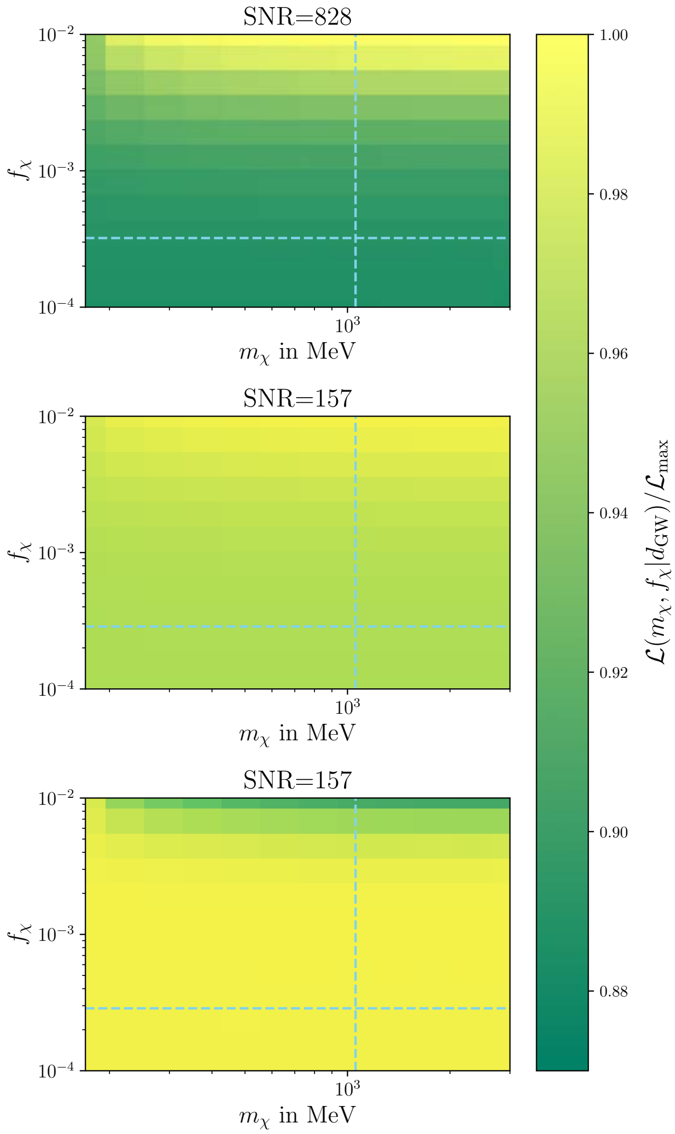

FIGURE 10.4
Likelihood across the m_χ-f_χ plane after individual events. The top panel shows the likelihood after one event with high SNR where $m_\chi = 1056$ MeV and $f_\chi = 0.032\%$ (both values shown as dashed blue lines), when marginalizing over all EOS candidates. Similarly, the middle panel shows an event with a modest SNR where $m_\chi = 1056$ MeV and $f_\chi = 0.029\%$. The bottom panel shows the same event as in the middle panel, but here the likelihood is just taken from the true EOS to showcase the degeneracy between low m_χ and high m_χ with small fractions.

fraction small, the shift in tidal deformability from the baryonic EOS is only slight. The likelihood of the large particle mass will only be high when the fraction is small. But the likelihood for the smaller DM particle mass will be high regardless the value of f_χ. By restricting the DM fraction to below 1%, the resulting DM profile for light DM particles does not exceed the baryonic radius, meaning that halo configurations are not possible. Instead, the formed DM core causes only a small shift in tidal deformability, which remains within the measurement uncertainty.

This is an inherent problem when trying to infer the DM particle mass from multiple events. Our event catalogs contain many events with small DM fraction. Since we marginalize over the fraction for each event individually, the events with low fraction will have a small preference for lower m_χ, as they are able to explain the data across all fractions. The preference is only very small, but can accumulate over many events, which after $\gtrsim 100$ events skews the combined posterior heavily toward lower masses. This effect can be seen in Fig. 10.5 for the posterior on m_χ after 500 events. Events with high fraction can correct the estimate again toward larger masses, however, even when the population of f_χ is uniform, there are not enough events with high fraction to overcome the opposite trend toward small m_χ. We point out that this problem remains even if the baryonic EOS was perfectly known, i.e., if one does not marginalize the likelihood Eq. (10.12) over the EOSs, but instead just considers the contribution from the true injected one.
This means that tidal signatures of BNS events alone are not sufficient to measure m_χ. However, we briefly note a method here how to deduce a lower limit $m_{\chi,\mathrm{min}}$ on the DM particle mass. Namely, when we assume that the maximum DM-fraction a BNS can have is $f_{\chi,\mathrm{max}}$, and we consider a particular baryonic EOS together with DM particle masses that yield core configurations, we can determine the minimum effective tidal deformability $\tilde{\Lambda}_{\mathrm{min}}$ a BNS can have. This will be a function of the chirp mass $\mathcal{M}$, symmetric mass ratio η and additionally depends on the EOS, as well as the DM parameter bounds $m_{\chi,\mathrm{min}}$ and $f_{\chi,\mathrm{max}}$, i.e.,

$$\tilde{\Lambda}_{\mathrm{min}}(\mathcal{M},\eta) = \tilde{\Lambda}(\mathcal{M},\eta,\mathrm{EOS},m_{\chi,\mathrm{min}},f_{\chi,\mathrm{max}})\,. \tag{10.16}$$

Now, when many events have been observed, one can select the single event $d^{(\star)}_{\mathrm{GW}}$ where the observed $\tilde{\Lambda}$ deviates the most from the expectation of the baryonic EOS. It is reasonable to assume that it had the maximum DM fraction $f_{\chi,\mathrm{max}}$, so we can then derive the probability that m_χ is smaller than the boundary $m_{\chi,\mathrm{min}}$ as

$$\begin{aligned} &P(m_\chi \leq m_{\chi,\mathrm{min}}|d^{(\star)}_{\mathrm{GW}}, f_{\chi,\mathrm{max}},\mathrm{EOS}) = \\ &\int d\mathcal{M}\int d\eta \int_{\tilde{\Lambda}_{\mathrm{min}}(\mathcal{M},\eta)}^{\infty} d\tilde{\Lambda}\; P(\mathcal{M},\eta,\tilde{\Lambda}|d^{(\star)}_{\mathrm{GW}})\,. \end{aligned} \tag{10.17}$$

The lower bound in the last integral is determined by Eq. (10.16). Typically, the higher one sets $f_{\chi,\mathrm{max}}$, the lower $m_{\chi,\mathrm{min}}$ can be. This is because a larger deviation from the baryonic EOS can also be explained by small DM particle masses when the DM fraction is high enough.

Note that this approach requires assumptions about the baryonic EOS and the maximum DM fraction in NS. However, one could for instance marginalize Eq. (10.17) over the EOS posterior from the 500 events and likewise marginalize with a prior on $f_{\chi,\mathrm{max}}$. An additional practical issue concerns the determination which event $d^{(\star)}_{\mathrm{GW}}$ has the highest deviation from the baryonic EOS. For our purposes here, we simply look at the posterior mean $\tilde{\Lambda}$ from the data and compare it to the value determined from the baryonic EOS alone with the posterior mean for $\mathcal{M}$ and η. We point out that in practice, determining $d^{(\star)}_{\mathrm{GW}}$ is potentially more difficult, since for real data the posterior mean does not always need to be well centered and other methods to identify $d^{(\star)}_{\mathrm{GW}}$ could be more suitable. Our results however show that the constraints on $m_{\chi,\mathrm{min}}$ remain weak anyway. Even when the true value for m_χ is 3000 MeV, we still find $P(m_\chi \leq 170\ \mathrm{MeV}|d^{(\star)}_{\mathrm{GW}}, f_{\chi,\mathrm{max}} = 1\%) = 34\%$. This indicates again that even the events that show the strongest signs for DM only restrict the particle mass weakly.

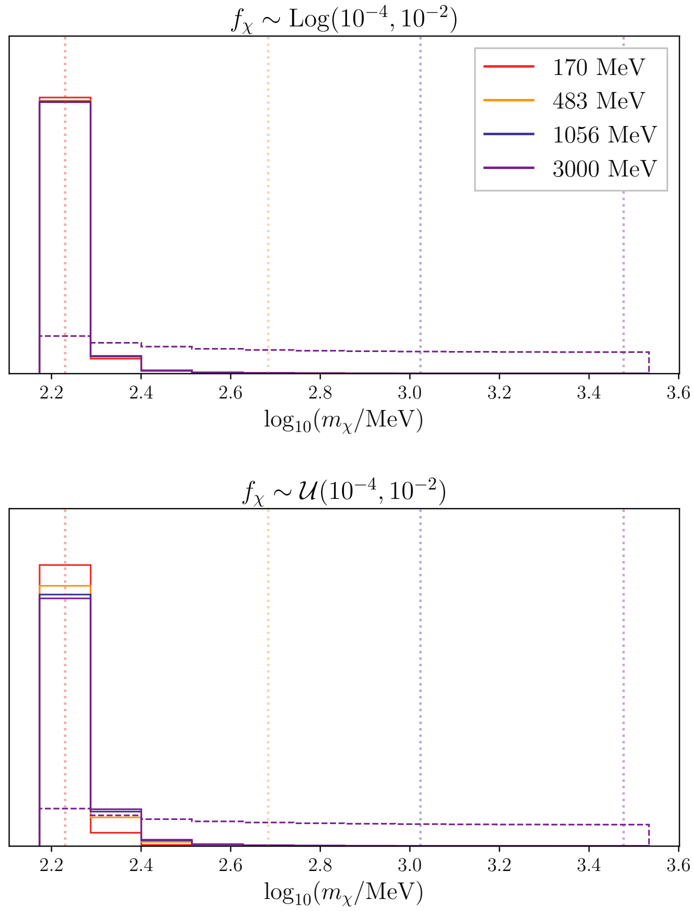

FIGURE 10.5
Posterior distributions on m_χ after 500 events. The colors indicate which DM particle mass was injected in the respective event catalog. The four different injection values are also drawn as vertical dotted lines. We only show event catalogs with the stiff EOS, the top panels considers those where f_χ was log-uniformly distributed, the bottom panel the ones where f_χ is uniform. The purple dashed lines show the posterior after 50 events with an injected DM particle mass of 3000 MeV to illustrate that the posterior skew to low masses is a cumulative effect from the degeneracy mentioned in the text.

10.5 Discussion and Conclusions

In the present article, we studied how ET measurements of the tidal deformability of DM-admixed NS can be used to recover the baryonic EOS and infer properties of DM. To this end, we created a catalog of 500 high-SNR BNS events and used the Fisher matrix approach to obtain estimates of the posterior uncertainties. In different instances of the catalog the injected baryonic EOS, injected DM particle mass, and the chosen distribution for the DM fraction were varied.

Using these event catalogs as our mock dataset, we performed joint Bayesian inference on the EOS, m_χ, and f_χ. We find that DM in BNS can bias the inference of the baryonic EOS when its presence is not accounted for, though the effect is very small. The offset in the tidal deformability $\Lambda_{1.4}^{(\mathrm{bar})}$ between the true baryonic EOS and the EOS posterior depends on the injected value for m_χ

as well as the population for f_χ, but is generally $\lesssim 20$. Similarly, the posterior on the canonical NS radius $R_{1.4}$ likewise is only off up to $\lesssim 0.1$ km. Note, that the effect could be stronger for heavier DM particles and higher fractions.

Even when DM is present in the data, we generally observe that the hypothesis for the presence of DM is disfavored by the Bayes factor when combining many events. This is because the observational signatures of DM are not strong and hence over many events the easier hypothesis requiring only the baryonic EOS is preferred. Comparison to a background analysis where the events actually lack DM reveals that the Bayes factor is not able to distinguish between the two cases. This is even true for the more favorable setups where f_χ is distributed uniformly instead of log-uniformly, though we also find indication that if the true EOS was perfectly known, ET might be able to deliver some evidence about the presence of DM.

Likewise, inferring the DM particle mass seems infeasible because of an inherent degeneracy between f_χ and m_χ. When the particle mass is large and the fraction low, the data may be equally well described by a small particle mass and higher DM fraction within the measurement uncertainty. Alternatively, we attempted to construct a lower limit on m_χ based on the assumed maximum DM fraction a BNS can have. In our setup though, this does not deliver any pertinent result either, since the statistical uncertainties on the event that deviates the most from the purely baryonic expectation are still too large.

The conclusions drawn in the present work depend on the choice of our DM model as well as on the assumptions about the ranges for the DM particle mass and DM fraction. Stronger observational signatures could be achieved with a different DM model, higher fractions, and different particle masses. Based on our results though, firm detection of DM would require a much larger variation of the NS tidal deformability than we consider in our event catalogs. Alternatively, if the baryonic EOS is well-constrained from other independent sources, DM detection might be possible. We leave the investigation into the necessary variability of tidal deformability or the required accuracy on the baryonic EOS for confident DM detection to future work.

While our analysis can be seen as cautious for the range of f_χ and m_χ, we point out that our statistical analysis benefits from some advantages a real-life application would not have. Namely, the NSs in our binary events always share the same fraction and we imposed the correct prior for f_χ based on the population distribution that we injected in the event catalog. Further, the Fisher matrix is generally considered a lower bound on the statistical uncertainties, and in a full Bayesian parameter estimation the uncertainty on $\tilde{\Lambda}$ can be significantly larger [327]. It has been shown that the Fisher matrix approach can also *overestimate* the uncertainty on certain parameters [551], though this mainly applies when parameters display mutual degeneracies or when the Fisher matrix implies support within a nonphysical range, e.g., negative values for the luminosity distance [226]. However, in our event catalogs, the Fisher matrix uncertainties on $\tilde{\Lambda}$ cover a range between 4–80, which agrees well with posterior estimates from full Bayesian parameter estimations for ET [518, 327]. Hence, we do not expect that our Fisher matrix approach overestimates the accuracy with which ET would recover the tidal deformability, especially when additionally considering systematic uncertainties in the waveform models [370, 535, 572, 483, 269]. Nevertheless, full Bayesian parameter estimation could be implemented in future to test if biases in other parameters arise when DM effects in BNSs are ignored.

Reduction of the tidal deformability in NS is not the only way DM could be observable through future GW telescopes. With the precision of next-generation detectors, several alternative possibilities for DM detection have been suggested, e.g., an additional feature in the BNS postmerger signal [234, 619], continuous GW signals around superradiant black holes [81], observing sub-2-$M_\odot$ black holes from DM-collapsed NS [600, 100, 198], or direct interaction of DM particles with the detector test masses [504, 643, 168]. However, based on our analysis we conclude that within our assumptions about the DM particle mass and DM fractions in NS, confident detection of DM cores through tidal measurements of BNSs by ET is unlikely.

10.6 Appendix

Including cosmic explorer in the detection network

The inference of BNS parameters from GW signals will have notably lower uncertainties if ET is joined by the other proposed third-generation detector CE. To see how our conclusions would change if CE was included in the detector network, we reran the analysis for some of our event catalogs. To obtain the reduced statistical uncertainties on $\mathcal{M}$, η, and $\tilde{\Lambda}$, one needs to simply add the Fisher matrices of the individual detectors

$$F_{jk} = F_{jk}^{(\mathrm{ET})} + F_{jk}^{(\mathrm{CE})}. \tag{10.18}$$

This is implemented directly in GWFAST. We assume that the CE detector is located in Idaho, with the PSD taken from Ref. [101]. With this setup, we recreate the mock posteriors for the event catalogs where the stiff baryonic EOS was injected and m_χ was set to 170 MeV or 3000 MeV. Hence, we consider ET and CE for $1 \times 2 \times 2$ DM catalogs plus one additional no-DM catalog. The subsequent Bayesian inference of the EOS and DM parameters is conducted in the same manner described in Sec. 10.3.

The recovery of the baryonic EOS shows similar behavior to Sec. 10.4.1, though the statistical uncertainties on the recovered baryonic EOS are now even further reduced. In particular, undersampling effects in our baryonic EOS prior now become noticeable even for the stiff EOS after $\gtrsim 300$ events. The detectability of DM however is not improved by the reduced uncertainties on $\tilde{\Lambda}$, $\mathcal{M}$, and η. In Fig. 10.6, we show the distribution of $\ln(\mathcal{B})$ for the four event catalogs we included CE in. The forward-background approach still shows that the Bayes factor will not allow to distinguish whether DM was present within 20 events. Moreover, $\mathcal{B}$ decreases the more events are added, similar to the cases with ET only. When we combine all events, excluding only the one with the highest SNR, we find $\ln(\mathcal{B}) = -9.01$ (-6.68) for the catalog with 170 MeV and where f_χ distributed log-uniformly (uniformly). Likewise, the log-Bayes factors for the catalog with 3000 MeV is -6.77 (-5.27) and -9.48 (-7.82) for the no-DM catalog.

We excluded here the one event with the highest SNR of 3158 which originates from an event with two 1.5 $M_\odot$ NSs at 41 Mpc distance. Its DM fraction is 0.07% and the Fisher matrix error on the tidal deformability lists at $\sigma_{\tilde{\Lambda}} = 1.4$. If this event was included, the log-Bayes factor for the event catalog with $m_\chi = 3000$ MeV and $f_\chi \sim \mathcal{U}(10^{-4}, 10^{-2})$ formally becomes 14.62 after all 500 events, correctly indicating positive support for $\mathcal{H}_1$. We note that the event on its own does not yield the detection of DM, in fact the Bayes factor only starts showing substantial support for $\mathcal{H}_1$ when it is combined with $\gtrsim 40$ other events.

While it might be possible that particular "golden" events with very accurate determination of $\tilde{\Lambda}$ warrant the detection of DM when combined with a sufficient amount of other data about the baryonic EOS, we note a couple of caveats. In the other event catalogs which include similar versions of this event, the log-Bayes factor remains negative, indicating that the formally positive $\ln(\mathcal{B})$ originates from undersampling effects in our EOS prior, i.e., the likelihood is so constraining that only a few of our EOS candidate samples remain. Hence, further research, preferably employing full Bayesian parameter estimation, seems needed to confirm if one "golden event" can indeed reverse the evidence. Furthermore, in the real-life application, systematic errors in the waveform models could potentially prevent the extraction of $\tilde{\Lambda}$ at such accuracy [370, 535, 572, 483, 269].

Overall, we therefore still conclude that even with a joint network of CE and ET, tidal BNS signatures would likely not enable the detection of the DM candidate adopted in the present work.

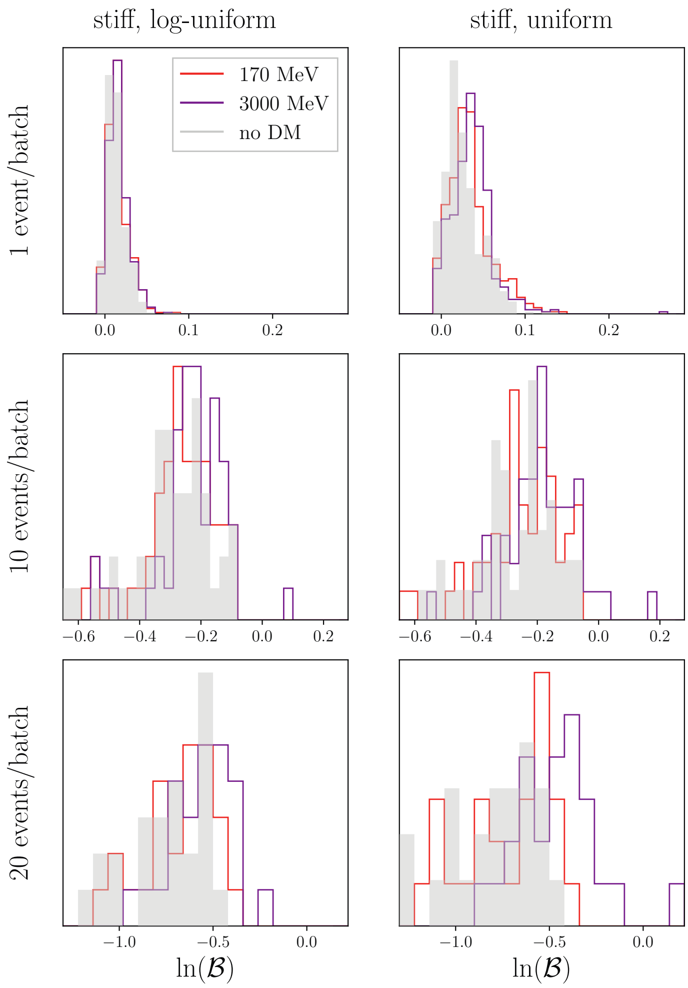

FIGURE 10.6
Distribution of ln($\mathcal{B}$) for the four event catalogs where we included CE into the detector network. Figure arrangement and color coding as in Fig. 10.3.

11

The Bright and the Dark: Exploring nuclear physics and dark matter constraints with binary neutron star mergers

CONTENTS

This chapter is based on an article in preparation by ***Nina Kunert****, Edoardo Giangrandi, Guilherme Grams, Anna Puecher, Hauke Koehn, Violetta Sagun, and Tim Dietrich. The abstract below provides an overview of preliminary key findings. I conducted all parameter estimation simulations, developed and implemented the new sampling routine to additionally sample dark matter parameters, and performed the data analysis.*

Abstract: The exact properties of the neutron star equation of state remain an open problem in astrophysics. Beyond the fundamental challenge of understanding the behavior of nuclear matter at extreme densities, an additional layer of uncertainty lies within the universe itself: dark matter. As binary neutron star mergers reside in galactic dark-matter halos, they may incorporate an additional non-luminous dark matter contribution in addition to their luminous baryonic matter. We simulate gravitational-wave observations of binary neutron star mergers and perform parameter estimation simulations to investigate the capability of next-generation detectors to constrain both nuclear and dark-matter properties. While the bright side is studied with different microphysical models describing the neutron star equation-of-state, the dark side assumes dark matter to be fermionic and interacting with baryonic matter only gravitationally. Our results indicate that moderate constraints for some nuclear-physics parameters could be expected from observations with next-generation detectors. Conversely, our results reveal no constraints on dark matter properties within the framework of our assumed model, suggesting that next-generation gravitational-wave detectors may have limited sensitivity to test the presence of dark matter in binary neutron star mergers.

11.1 Introduction

One of the primary open challenges in astrophysics is the determination of the properties of the neutron star (NS) equation-of-state (EOS), which encapsulates the behavior of matter under extremes of density and pressure and governs the internal structure and composition of NSs [385, 386, 383]. Understanding the EOS requires integrating information from both terrestrial experiments and astrophysical observations, each of which probes different density regimes and offers complementary insights into the nature of dense matter [492, 357].

Experimental constraints from terrestrial facilities, such as heavy-ion-collision experiments [563], the PREX-II [37] or CREX experiment [38] well as theoretical calculations of nuclear matter within the framework of chiral effective field theory (EFT) [401, 312, 223, 503, 348] have been essential for studying the behavior of nuclear matter in regimes up to about twice the nuclear saturation density, $n_{\rm sat} \approx 0.16\,{\rm fm}^{-3}$. However, the cores of NSs extend into significantly higher-density regimes, where direct experimental access is no longer possible. In these regimes, macroscopic observables such as NS masses, radii, and tidal deformabilities become key probes of the EOS, as they are sensitive to the properties of matter at densities of approximately $2-3\,n_{\rm sat}$. Astrophysical observations, most notably gravitational-wave (GW) detections from binary neutron star (BNS) mergers [10, 13, 16] and electromagnetic (EM) measurements of isolated NSs from missions such as NICER [547, 446, 548, 447], provide essential constraints in this higher-density domain. By confronting theoretical models of dense nuclear matter with such astrophysical data, it becomes possible to infer macroscopic NS properties and gain insight into the microscopic behavior of strongly interacting matter under extreme conditions.

The first multi-messenger observation of a BNS merger [11] through GWs (GW170817) [10] and EM waves (GRB 170817A and AT2017gfo) [9, 282, 186, 342, 58, 398, 648] allowed new constraints on the NS EOS [13, 83, 529, 451, 633, 182, 214, 324]. Using data from available GW observations, different studies investigated how nuclear-matter parameters are constrained with current-generation detectors. For example, the study of [686] showed that GW170817 when combined with NS mass and radius measurements allowed to constrain the nuclear symmetry energy, $E_{\rm sym}$, at twice saturation density to $E_{\rm sym}(2n_{\rm sat}) = 46.9 \pm 10.1$ MeV.

Next-generation GW detectors, such as the Einstein Telescope (ET) [519, 263, 306, 307] and Cosmic Explorer (CE) [8, 541, 241], are anticipated to significantly enhance our ability to constrain nuclear-physics parameters. Assuming two proposed designs for ET and simulating BNS coalescences with the Fisher information formalism (FIM) for different EOS models, the study of [327] showed that with $\geq$ 500 detections, NS properties and the underlying injected EOS can be recovered with great precision. Moreover, their results indicate the presence of interdependent degeneracies among nuclear matter parameters that cannot be resolved when relying solely on information from β-equilibrated matter, as was also shown in [449, 675].

Additional uncertainties may arise if the EOS is influenced not only by baryonic matter (BM) but also by dark matter (DM). Astrophysical observations leave little doubt about the cosmic abundance of DM, but its nature, properties, and interaction with BM remain largely unknown [688, 689, 560, 175, 421, 36, 43]. Although it is widely accepted that galaxies are embedded within DM halos, the distribution of DM, whether it is smoothly distributed throughout the Galactic halo or forms dense sub-halo structures [94, 126], remains an open question.

Several studies indicate that compact objects such as NSs may accrete DM as they move through regions of overdense DM regions, where scattering interactions could facilitate capture of DM [89, 94, 126]. Over time, this process can lead to substantial DM accumulation within NSs [550, 99, 201] with BNS systems possibly retaining more due to their extended lifetimes and stronger gravitational fields. DM, whether concentrated in the core or clustered around a NS, can alter its internal structure, affecting key properties such as mass, radius, and tidal deformability [99, 341, 328, 281, 338]. These structural modifications influence the NS EOS and leave distinct imprints on GW signals, making BNS mergers potential observational probes for the presence and effects of DM. The extent of these imprints is governed by the DM particle mass and the DM fraction. However, due to the current lack of information on both quantities, the resulting change to the tidal deformability, and hence the GW signal, may be minimal. Detecting such subtle effects requires the increased sensitivity of next-generation GW observatories, such as ET and CE. In our previous study [356], we investigated whether DM properties can be constrained with next-generation GW detectors, particularly focusing on ET. This study assumed asymmetric, noninteracting, fermionic DM and adopted a two-fluid approximation to model DM-admixed BNS mergers, used in previous studies, e.g., [467, 328, 361]. This analysis utilized posterior information derived using the FIM approximation.

This article aims to investigate both the 'bright side' of BNS mergers, referring to their composition of luminous BM, and the 'dark side', which considers the possibility that BNS mergers may contain an admixture of DM. Specifically, we investigate whether next-generation GW detectors can constrain nuclear matter parameters relevant for modeling the NS EOS, as well as properties of DM, thereby possibly offering insights into its unknown nature. In contrast to our previous study in [356], we perform full parameter estimation simulations to infer both BNS source parameters and DM properties, while assuming the same DM model and GW detector setup. This article is organized as follows: Sec. 11.2 outlines the methodology, including the Bayesian inference framework, the construction of baryonic and DM EOSs, the adopted dark-matter model, the GW data and detector configuration, and the approach used to infer information on nuclear matter and DM parameters. Sec. 11.3 presents preliminary findings of nuclear-physics constraints when analyzing BNS mergers with different microphysical models. Sec. 11.4 reports the results from our investigation of DM-admixed BNS mergers, aimed at constraining DM properties. Sec. 11.5 provides concluding remarks and an outlook on further planned investigations.

11.2 Methodology

To investigate GW observations of both baryonic and DM-admixed BNS mergers, we employ a Bayesian framework that allows us to incorporate information from nuclear and DM physics. In this Section, we recap the Bayesian methodology explained previously and outline the construction of baryonic EOS sets based on different nuclear models, the assumed dark matter model, the construction of DM EOSs, and the inference of posterior distributions of nuclear and DM parameters.

11.2.1 Bayesian inference

Adhering to a Bayesian approach, we employ Bayes' theorem

$$p(\boldsymbol{\theta}|d,\mathcal{H}) = \frac{p(d|\boldsymbol{\theta},\mathcal{H})p(\boldsymbol{\theta}|\mathcal{H})}{p(d|\mathcal{H})} \equiv \frac{\mathcal{L}(d|\boldsymbol{\theta})\pi(\boldsymbol{\theta})}{\mathcal{Z}}, \tag{11.1}$$

to obtain information on the posterior probability distributions $p(\boldsymbol{\theta}|d,\mathcal{H})$ of model parameters $\boldsymbol{\theta} = \{\boldsymbol{\theta}_{\rm BM}, \boldsymbol{\theta}_{\rm DM}\}$ describing either BM or BNS mergers admixed with DM, hereafter referred to as DM-admixed BNS mergers. In Eq. (11.1), $\mathcal{L}(\boldsymbol{\theta})$, $\pi(\boldsymbol{\theta})$, and $\mathcal{Z}$ refer to the likelihood, prior, and evidence, respectively. Assuming stationary Gaussian noise, the likelihood function for a GW signal $h(\boldsymbol{\theta})$ given observational data d is expressed as [652]:

$$\mathcal{L}_{\rm GW} \propto \exp\left(-\frac{1}{2}\langle d-h(\boldsymbol{\theta})|d-h(\boldsymbol{\theta})\rangle\right), \tag{11.2}$$

where the inner product $\langle a|b\rangle$ is defined as

$$\langle a|b\rangle = 4\Re\int_{f_{\rm low}}^{f_{\rm high}} \frac{\tilde{a}(f)\tilde{b}^*(f)}{S_n(f)}df, \tag{11.3}$$

where $\tilde{a}(f)$ representing the Fourier transform of $a(t)$, * denoting complex conjugation, and $S_n(f)$ corresponding to the one-sided power spectral density of the noise. The high-dimensional likelihood landscape is explored using nested sampling [603], as implemented within the Bayesian inference framework `Bilby` [65]. This library serves as a core component of the `NMMA` framework, a pipeline designed for multi-messenger analyses in nuclear physics and astrophysics [492]. In this study, we extend its capabilities to incorporate the inference of DM properties, operating under the assumption that BNS mergers may contain an admixture of DM.

To assess the degree of constraint on both nuclear-physics and DM parameters, we compare the posterior distributions with their corresponding priors. To quantitatively evaluate the extent to which the posterior deviates from the prior, we compute the Jensen–Shannon divergence (JSD). This metric provides a symmetrized and finite measure of the difference between two probability distributions p_1 and p_2 and is defined as [396],

$$D_{\mathrm{JS}}(p_1(x)||p_2(x)) = \frac{1}{2}\left[\sum_x p_1(x)\ln\Big(\frac{p_1(x)}{m(x)}\Big) + \sum_x p_2(x)\ln\Big(\frac{p_2(x)}{m(x)}\Big)\right], \tag{11.4}$$

in which $m(x) = 0.5(p_1(x) + p_2(x))$. A JSD of zero implies identical distributions, while larger values indicate increasing dissimilarity.

11.2.2 Construction of baryonic matter equation-of-states

Throughout this article, distinct models are utilized for modeling the NS EOS of baryonic nuclear matter, each capturing different microphysical properties.

i) Metamodel approach with phase transitions (MM-wPT): We employ the EOS set presented in previous studies [359, 357] based on the metamodel (MM) approach [418, 419]. Here, we recap main construction steps, while further details can be found in [357]. All EOSs in this set use the crust model from [219], which is applied up to its predicted crust-core transition density at 0.076 fm^{-3}. The EOS of the outer NS core assumes nucleonic matter in beta equilibrium up to a transition density n_{break}, randomly drawn from $1-2\ n_{\mathrm{sat}}$ to account for possible non-nucleonic degrees of freedom [609]. Below n_{break}, the MM of [418, 419] is used, a density functional approach incorporating nuclear-physics knowledge through Nuclear Empirical Parameters (NEPs) defined via a Taylor expansion of the energy per particle in symmetric matter, e_{sat}, and the symmetry energy, e_{sym}, around the saturation density n_{sat} as:

$$\begin{aligned} e_{\mathrm{sat}}(n) = E_{\mathrm{sat}} + K_{\mathrm{sat}}\frac{x^2}{2} + Q_{\mathrm{sat}}\frac{x^3}{3!} \\ +Z_{\mathrm{sat}}\frac{x^4}{4!} + \dots, \end{aligned} \tag{11.5}$$

$$\begin{aligned} e_{\mathrm{sym}}(n) = E_{\mathrm{sym}} + L_{\mathrm{sym}}x + K_{\mathrm{sym}}\frac{x^2}{2} + Q_{\mathrm{sym}}\frac{x^3}{3!} \\ +Z_{\mathrm{sym}}\frac{x^4}{4!} + \dots, \end{aligned} \tag{11.6}$$

where $x := (n - n_{\mathrm{sat}})/(3n_{\mathrm{sat}})$ is the expansion parameter. To account for nuclear-physics uncertainties and to generate a broad EOS prior, NEPs are varied uniformly within the ranges in Table 11.1. This defines the EOS for 0.12 fm^{-3} $< n < n_{\mathrm{break}}$, with the lower limit chosen arbitrarily. Above n_{break}, non-nucleonic degrees of freedom are incorporated using a modified speed-of-sound approach, originally introduced in [633] (see [357] for details). This framework allows for arbitrarily soft EOSs that emulate first-order phase transitions (PTs), leading to the designation of this EOS set as "MM-wPT."

Following this methodology, a set of 100,000 EOSs was generated and utilized in previous studies, including [359, 357]. Unless stated otherwise, most analyses are conducted on a subset presented in [357] to reduce computational costs, which excludes EOSs that are inconsistent with the most reliable constraints (cf. Refs. in [357]), such as heavy pulsar mass measurements via radio timing, and theoretical predictions from χEFT and perturbative QCD.

TABLE 11.1
The prior distributions for NEPs used for the construction of both EOS below $n_{\rm break}$ sets: MM-wPT and MM-wo-PT. Uniform priors are denoted by $\mathcal{U}$. For MM-wPT, the parameters $E_{\rm sat}$ and $n_{\rm sat}$ are fixed at -16 MeV and 0.16 fm^{-3}, respectively.

Parameter	**Prior**	
	MM-wPT	MM-wo-PT
$n_{\rm break}$ [$n_{\rm sat}$]	$\mathcal{U}(1,2)$	-
E_{sat} [MeV]	-	$\mathcal{U}(-17,-14.5)$
n_{sat} [fm^{-3}]	-	$\mathcal{U}(0.14,0.17)$
$K_{\rm sat}$ [MeV]	$\mathcal{U}(150,300)$	$\mathcal{U}(130,300)$
$Q_{\rm sat}$ [MeV]	$\mathcal{U}(-500,1100)$	$\mathcal{U}(-900,900)$
$Z_{\rm sat}$ [MeV]	$\mathcal{U}(-2500,1500)$	$\mathcal{U}(-1000,1000)$
$E_{\rm sym}$ [MeV]	$\mathcal{U}(28,45)$	$\mathcal{U}(28,60)$
$L_{\rm sym}$ [MeV]	$\mathcal{U}(10,200)$	$\mathcal{U}(25,160)$
$K_{\rm sym}$ [MeV]	$\mathcal{U}(-300,100)$	$\mathcal{U}(-300,200)$
$Q_{\rm sym}$ [MeV]	$\mathcal{U}(-800,800)$	$\mathcal{U}(-800,800)$
$Z_{\rm sym}$ [MeV]	$\mathcal{U}(-2500,1500)$	$\mathcal{U}(-1000,1000)$

ii) Metamodel approach without phase transitions (MM-wo-PT): We generate a second set of roughly 35,000 EOSs using the MM [418] approach mentioned in Section i). There are two main differences from the previous set: a) Here, we construct a unified EOS for the NS crust and core. The crust is modeled with a compressible liquid drop model (CLDM) as presented in [285] where the underlying NEP of the crust are the same as the NS core; b) We do not include phase transitions at higher densities. This construction assumes the nucleonic hypothesis and uses the MM at all densities. The NEPs are, therefore, explored in all regions of the star, from the crust to the core.

Figure 11.1 shows the different EOS sets in the mass-radius and mass-tidal deformability planes, respectively. The injected EOSs, which were selected based on the symmetry energy and its slope, as outlined in Subsec. 11.2.5, are represented by dashed lines.

11.2.3 Dark matter model

In this study, DM is modeled as a relativistic Fermi gas assuming minimal interaction with standard-model particles, interacting solely through gravity. Specifically, we adopt the two-fluid approximation, widely used in previous studies, e.g., [467, 328, 361], in which the two-fluid Tolman-Oppenheimer-

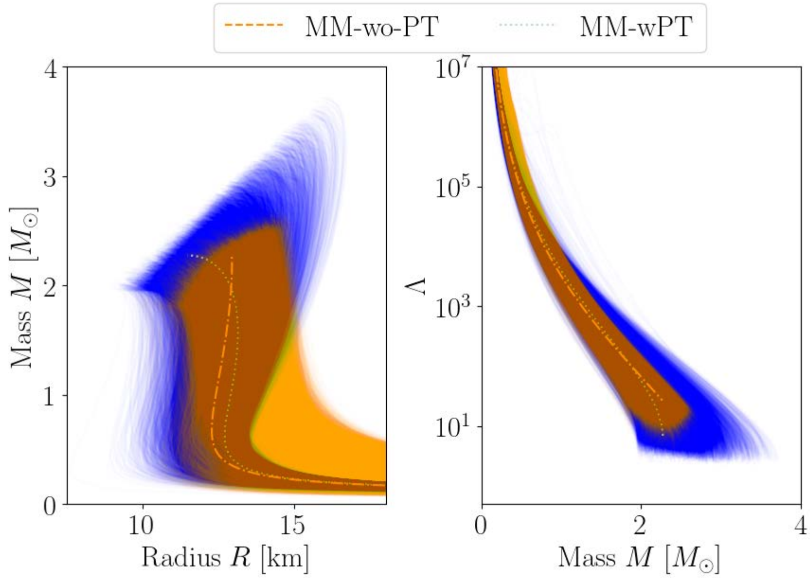

FIGURE 11.1
Overview of employed EOS sets illustrating their modeling of macroscopic NS properties. The left panel depicts the mass-radius relationship, while the right panel shows the mass-tidal deformability plane. The MM-wPT EOS set is represented in blue and the MM-wo-PT EOS set in orange. Injected EOSs within each set are indicated by dashed lines maintaining the same color scheme.

Volkoff (TOV) equations for a DM-admixed NS in hydrostatic equilibrium can be formulated as [328]

$$\frac{dp_j}{dr} = -\frac{(\epsilon_j + p_j)(M + 4\pi r^3 p)}{r^2(1 - 2M/r)}. \tag{11.7}$$

The subscript index j in Eq. (11.7) represents the different fluid components, namely baryonic and dark matter. Accordingly, the total mass and pressure are given by $M_{\text{tot}} = M_B(r) + M_D(r)$ and $p_{\text{tot}} = p_B(r) + p_D(r)$ respectively, where r denotes the radial distance from the center of the NS. The DM model is characterized by two parameters: the DM particle mass, m_χ, and the DM mass fraction, f_χ. The DM fraction,

$$f_\chi = \frac{M_D(R_D)}{M_{\text{tot}}}, \tag{11.8}$$

quantifies the proportion of DM mass relative to the total NS mass enclosed within its radius. The choice of these DM parameters yields two distinct configurations: the *core configuration*, where DM is entirely confined within the NS, and the *halo configuration*, where DM extends beyond the baryonic core, forming a diffuse halo surrounding the NS. Consequently, these configurations will affect NS properties such as mass, radius, and tidal deformability, as shown in [328, 281].

While core configurations generally lead to a reduction in the maximum mass, halo configurations result in an increase in the maximum NS mass at higher DM fractions. As extended DM halos may overlap during the late stages of BNS inspirals, DM-induced modifications in tidal deformabilities would need to be taken into account to accurately model GW signals for these systems. However, existing gravitational waveform models do not incorporate such effects. For this reason, this study completely focuses on core configurations, similar to our previous study [356].

11.2.4 Construction of dark matter equation-of-states

In order to obtain DM-informed NS masses, radii, and tidal deformabilities, we solve the two-fluid TOV and Love equations for different choices of DM particle masses and fractions, yielding DM-admixed NSs. In this study, we utilize the same set of DM EOS calculations derived in our previous work [356]. Consequently, we provide only a brief summary of the construction methodology.

The EOS for baryonic matter is formulated using the metamodel approach [418, 419], for which nuclear empirical parameters were sampled within the parameter ranges specified in Table 10.1 in Chapter 10. It is important to emphasize that the metamodel EOS set utilized here differs from those presented in Subsec. 11.2.2. The primary distinctions arise from variations in the parameter ranges used for sampling nuclear empirical parameters, as well as the inclusion or absence of phase transitions. Additional nuanced differences are discussed in detail in [356, 357]. Moreover, ongoing research efforts are directed toward achieving a more consistent usage of baryonic EOS sets.

The baryonic EOS set constructed with the metamodel in [356] comprises 5000 nucleonic EOSs, for which the two-fluid TOV and Love equations were solved over a 12 x 12 parameter grid of DM particle masses and fractions, as outlined in Table 10.2 in Chapter 10. The choice of DM parameter ranges, discussed in [356], is based on two key considerations: (i) DM-admixed NSs with particle masses $m_\chi \lesssim 170$ MeV exhibit halo-forming behavior and are therefore excluded [328, 564], and (ii) while DM mass fractions f_χ remain uncertain, estimates based on Bondi accretion suggest a lower bound of 0.01%, with other mechanisms allowing for values up to 1% [328].

This approach enables a systematic mapping of each underlying baryonic EOS to variations in DM particle mass and mass fraction, yielding insights into the DM-informed NS mass $m_{\rm DM}$ and DM-informed tidal deformability $\Lambda_{\rm DM}$. Integrating these quantities into existing gravitational waveform models allows us to simulate GW observations from DM-admixed BNS mergers.

11.2.5 Employed GW data and detector setup

This study explores GW signals from both baryonic and DM-admixed BNS mergers, with a focus on next-generation GW observatories such as the ET and CE. To generate synthetic GW data, we adopt a default configuration featuring a triangular ET design with a 10 km arm length, positioned in Limburg [128, 410, 102], and set a minimum frequency of $f_{\rm min} = 5$ Hz. Additionally, for selected BNS sources, we incorporate the baseline 40 km detector CE setup [8, 541, 241, 101], enabling analysis with a detector network comprising both ET and CE.

To this end, four different BNS configurations were simulated and analyzed. These configurations, along with their key characteristics, are listed in Table 11.2.
Concerning Event A, this BNS source is tailored to BNS parameters inferred from the multi-messenger observation of GW170817 [492], except for the tidal deformabilities, which are informed by the injected EOS from the different EOS sets described in Subsec. 11.2.2. The other BNS sources, associated with Events B-D, are drawn from one of the catalogs generated for the analysis presented in Chapter 10 [357].

The selection of injected EOSs from each EOS set is motivated by previous findings presented in [357], where the symmetry energy $E_{\rm sym}$ and its slope $L_{\rm sym}$ were estimated to be approximately $E_{\rm sym} \approx 32$ MeV and $L_{\rm sym} \approx 50$ MeV, respectively. For our analysis, we choose a slightly smaller value for $L_{\rm sym} \approx 45$ MeV, as shown in Figure 11.2.
In addition to synthetic data, we utilize GW data from GW170817 [10] to assess the capability of current-generation GW detectors [1, 34] in constraining DM properties. The result of this analysis is presented in Subsec. 11.4.1.

Furthermore, we note that all simulations of GW observations, excluding the analysis of observed data presented in Sec. 11.4.1, were conducted under the assumption of aligned-spin BNS configurations, utilizing the waveform model `IMRPhenomD_NRTidalv2` [322, 349, 626, 212]. A repeated analysis using the more recent waveform model `IMRPhenomXAS_NRTidalv3` [511, 2] confirms that the results presented in the following remain unaffected.

Parameter	Event A	Event B	Event C	Event D
$\mathcal{M}_c[M_\odot]$	1.19	1.32	1.28	1.41
q	0.96	0.97	0.97	0.67
a_1	0.00	0.03	0.02	0.04
a_2	0.00	0.05	0.04	0.04
D_L [Mpc]	40.00	609.45	41.20	116.09
δ [rad]	-0.41	2.72	2.14	2.02
α [rad]	3.45	5.20	1.18	6.28
$\cos\theta_N$ [rad]	-0.90	0.95	0.84	0.95
ψ [rad]	0.87	0.69	3.75	4.69
ϕ_c [rad]	1.22	0.29	2.04	0.88
$\rho_{\rm opt}^{\rm ET}$	643.03	123.15	813.31	573.12

TABLE 11.2
Overview of the BNS merger configurations analyzed in this study along with their key parameters. The quantity $\mathcal{M}_c[M_\odot]$ denotes the source-frame chirp mass, while tidal deformabilities are determined by the respective injected EOSs, as outlined in Subsec. 11.2.5, and are therefore omitted for brevity. The parameter $\rho_{\rm opt}^{\rm ET}$ refers to the optimal SNR as would be detected with a triangular ET design.

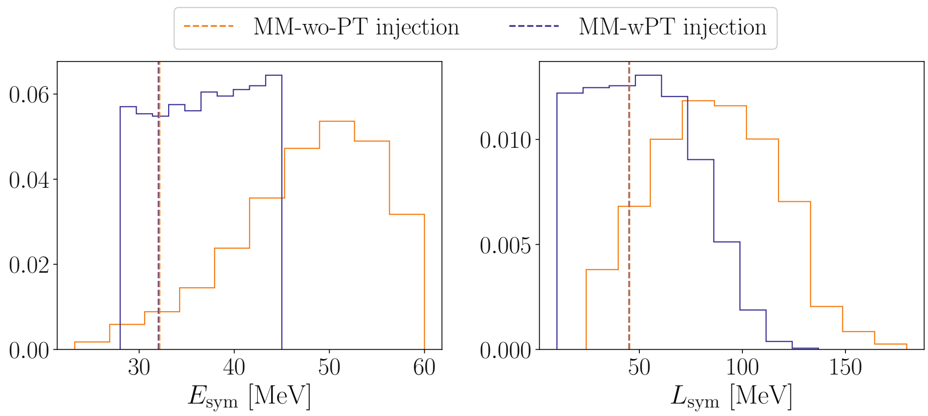

FIGURE 11.2
Normalized distribution of the symmetry energy $E_{\rm sym}$ and symmetry energy slope $L_{\rm sym}$ for the different EOS sets described in Subsec. 11.2.2. The selected EOS injections are shown as dashed lines for each of the EOS sets and are motivated through findings reported in [357].

11.2.6 Inference of nuclear and dark matter properties

The inference of nuclear-physics parameters is enabled through the joint sampling of EOS and binary parameters. This methodology allows for the integration of additional information on NS properties, provided by distinct nuclear-physics models, during parameter estimation. In particular, the BNS parameters, under the assumption that the binary consists of BM, are defined as,

$$\boldsymbol{\theta}_{\rm BNS}^{\rm BM} = \{m_i, a_{{\rm spin},i}, \Lambda_i^{\rm BM}(m_i;{\rm EOS}), D_L, t_c, \phi_c, \alpha, \delta, \iota, \psi\} \tag{11.9}$$

where $i = 1, 2$ indexes the two NSs in the binary. Here, m_i denote the binary masses composed of

BM, $a_{\rm spin,i}$ the aligned spin magnitudes, D_L the luminosity distance, t_c the coalescence time, ϕ_c the phase, (α, δ) the sky location, ι the inclination angle, and ψ the polarization. We note that we do not directly sample the tidal deformabilities, but instead sample the baryonic EOS and obtain $(\Lambda_{1,2}^{\rm BM})$ by interpolation for given masses m_i obtained in the sampling. Since the baryonic EOS is determined by the choice of nuclear parameters, mapping each posterior EOS sample back to its corresponding choice of nuclear parameters allows for the extraction of posterior distributions for these parameters.

Concerning the inference of DM properties, our DM model, as described in Sec. 11.2.3, introduces two parameters, i.e., the DM particle mass and fraction. To infer posteriors on DM quantities, we expand our sampling routine to sample on these two additional parameters. Consequently, the parameter vector for DM-admixed BNS mergers extends to

$$\boldsymbol{\theta}_{\rm BNS}^{\rm DM} = \{m_i, a_{\rm spin,i}, \Lambda_i^{\rm DM}(m_i; f_\chi, m_\chi, {\rm EOS}), D_L, t_c, \phi_c, \alpha, \delta, \iota, \psi\} \tag{11.10}$$

in which the EOS refers to the underlying baryonic EOS, which was used for solving the two-fluid TOV and Love equations, as detailed in Subsec. 11.2.4. To obtain DM-informed tidal deformabilities $\Lambda_i^{\rm DM}$, we gather a set of samples for the mass and the EOS. For a given EOS sample, $\Lambda_i^{\rm DM}$ is then obtained by interpolation in the parameter space $f_\chi - m_\chi$. These DM tidal deformabilities are incorporated into conventional GW models to analyze GW signals from DM-admixed BNS mergers, as GW waveform models that explicitly account for DM effects are currently unavailable.

Analyzing GW signals detected by next-generation GW detectors, which are expected to observe hours-long signals, significantly increases the computational burden associated with likelihood evaluations. Furthermore, the inclusion of two additional DM parameters further expands the dimensionality of the likelihood space, leading to considerable computational challenges and prolonged sampling times. To mitigate these computational demands and enhance sampling efficiency, we employ the parameter estimation acceleration technique proposed in [450], utilizing a multi-banding accuracy factor of $L = 50$.

11.3 The bright side: nuclear-physics constraints

In this section, we present a detailed analysis of our four BNS configurations, assuming a purely BM composition. The investigation is conducted using a range of microphysical EOS models, as introduced in Subsection 11.2.2. By mapping nuclear-physics parameters to their corresponding EOSs, we extract posterior distributions for these parameters, as detailed in Subsec. 11.2.6. This analysis aims to assess the constraints that GW observations with next-generation detectors could place on nuclear parameters and to investigate potential biases introduced by different microphysical EOS descriptions.

11.3.1 Studying constraints across different microphysical models

Analyzing BNS events with MM-wPT: Injecting all BNS events listed in Table 11.2 using the MM-wPT EOS and performing recovery with the same EOS set, we find that key BNS parameters, such as the source-frame chirp mass and the combined dimensionless tidal deformability under the assumption of purely BM, are tightly constrained and reliably recovered within their respective 90% credible intervals. A comparison between the posterior and prior distributions of the NEPs reveals slight constraints on $L_{\rm sym}$, $K_{\rm sym}$, and $Q_{\rm sat}$ across all events, whereas the remaining NEPs show no significant deviation from their prior distributions. In the following, we present and analyze these findings using Event A as a representative example, as shown in Figure 11.3.

We observe modest constraints on $L_{\rm sym}$, $K_{\rm sym}$, and $Q_{\rm sat}$, with the constraints on $L_{\rm sym}$ and $K_{\rm sym}$ being more pronounced relative to those on $Q_{\rm sat}$, as given by larger JSD values. This trend is consistent with expectations, as $Q_{\rm sat}$ represents a higher-order term in the expansion of the symmetry energy as

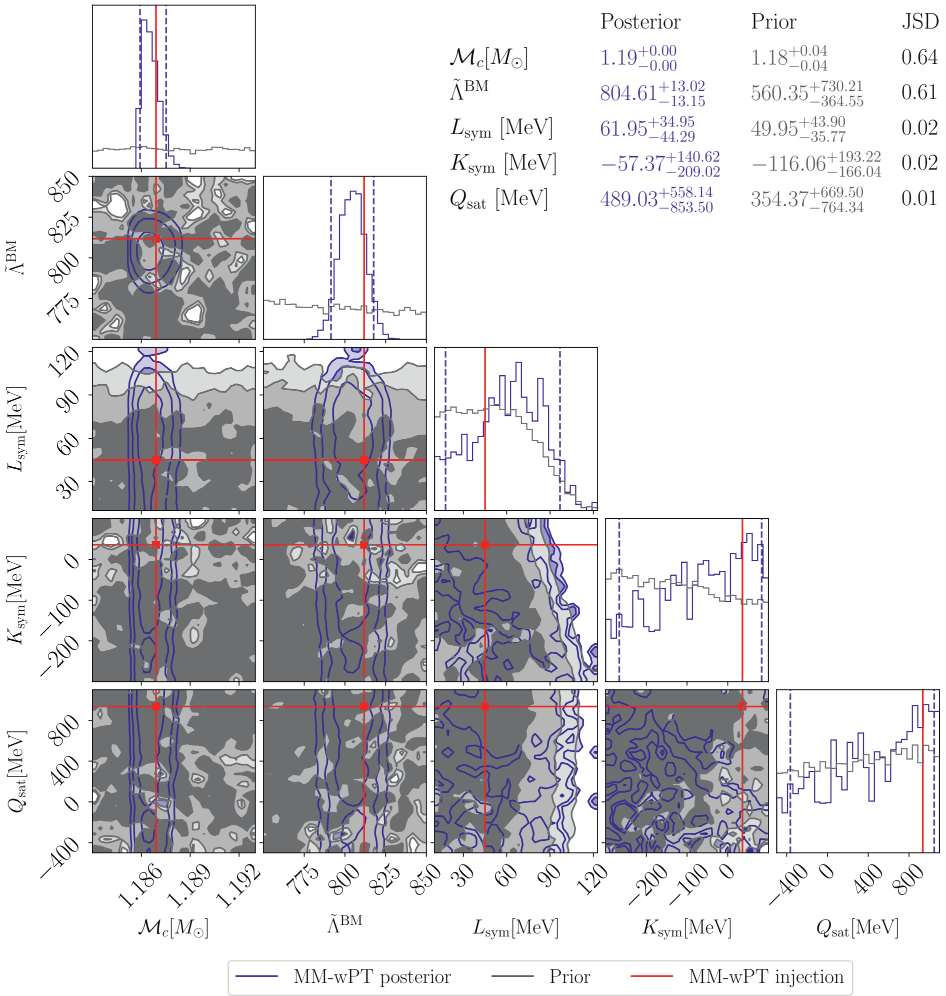

FIGURE 11.3
Corner plot of the simulated BNS Event A analyzed with ET under Gaussian-noise conditions injected and recovered with MM-wPT. The posterior distributions for the source-frame chirp mass $\mathcal{M}_c$, combined dimensionless tidal deformability of pure BM $\tilde{\Lambda}^{\rm BM}$ as well as nuclear parameters including $L_{\rm sym}$, $K_{\rm sym}$, and $Q_{\rm sat}$ are shown in blue. The prior is shown in gray and injected values as solid red lines. The median posterior values are reported at 90% credible interval and the JSD values are listed in the table for each parameter. Different shadings mark the 68%, 95%, and 99% confidence intervals.

compared to the other two parameters and is therefore less tightly constrained by the data. Applying this analysis to the other BNS with varying SNR events listed in Table 11.2, we obtain consistent results with JSD values remaining of the same order of magnitude.

Analyzing BNS events with MM-wo-PT: Injecting each BNS event with the MM-wo-PT EOS and performing the recovery with the same EOS set, we likewise tightly recover key BNS parameters within their respective 90% credible intervals such as the source-frame chirp mass and the combined dimensionless tidal deformability. In contrast to analyzing the different BNS events with the MM-wPT EOS set, constraints on nuclear parameters remain largely absent except for the symmetry energy slope. Figure 11.4 shows our results when analyzing Event A with the MM-wo-PT EOS set. The JSD values indicate that there is a moderate constraint on $L_{\rm sym}$ MeV, while posterior distributions of the

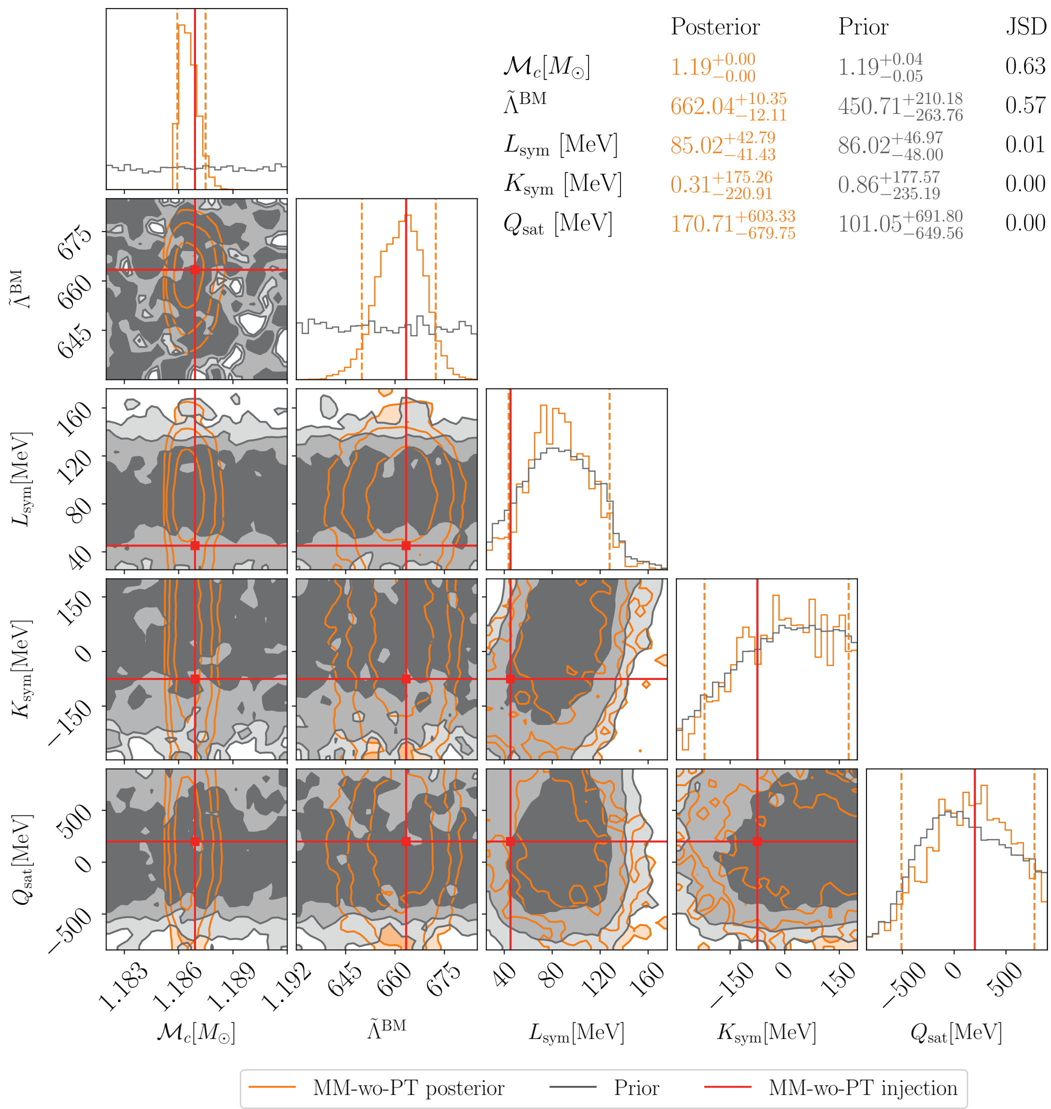

FIGURE 11.4
Corner plot of the simulated BNS Event A analyzed with ET under Gaussian-noise conditions injected and recovered with MM-wo-PT. The posterior distributions for the source-frame chirp mass $\mathcal{M}_c$, combined dimensionless tidal deformability of pure BM $\tilde{\Lambda}^{\rm BM}$ as well as nuclear parameters including $L_{\rm sym}$, $K_{\rm sym}$, and $Q_{\rm sat}$ are shown in blue. The prior is shown in gray and injected values as solid red lines. The median posterior values are reported at 90% credible interval and the JSD values are listed in the table for each parameter. Different shadings mark the 68%, 95%, and 99% confidence intervals.

other NEPs, listed in Table 11.1, resemble their respective prior distributions. Extending the analysis to the remaining BNS events yields results consistent with those obtained for Event A.

Our results indicate that next-generation GW detectors can tighten the bounds on $L_{\rm sym}$, while still leaving larger uncertainties on higher-order parameters like $K_{\rm sym}$ and $Q_{\rm sat}$. These findings are consistent with previous studies, such as [158, 357]. Comparing our results across the different EOS models, we find that constraints become more apparent when including PTs. Incorporating a PT (as in the MM-wPT model) can introduce a sharp change in the EOS above certain densities. The abrupt change in the pressure-density relation is strongly influenced by the choice of nuclear-matter parameters and affects NS properties such as the radius and tidal deformability [490]. Since GW signals are sensitive to stellar deformability, they offer the potential to place tighter constraints on the underlying nuclear parameters in the presence of a PT. On the other hand, when we do not include PTs (as in MM-wo-PT) the EOS remains nucleonic across all densities and abrupt structural changes remain absent. In addition, EOSs in this set are modeled with more free parameters as shown in Table 11.1. This extra freedom diminishes how sharply nuclear parameters show up in the tidal-deformability, leading to weaker constraints for the same data.

11.4 The dark side: constraining dark matter properties

This section examines DM-admixed BNS mergers to evaluate the potential of GW observations in constraining the DM properties considered in this study. We begin by reanalyzing the observed event GW170817 and extend our investigation to next-generation GW detectors by analyzing four simulated BNS merger events, as detailed in Subsec. 11.2.5.

11.4.1 Analyzing GW170817 assuming the presence of dark matter

To assess whether current-generation GW detectors can constrain the DM properties considered in this study, we reanalyze GW170817 under the assumption of DM presence. The analysis employs the waveform model `IMRPhenomPv2_NRTidalv2` [322, 349, 212] and utilizes GW data from the Gravitational Wave Open Science Center [649], covering the frequency range of 20 Hz to 2048 Hz to encompass the detected BNS inspiral [16]. In addition to standard BNS parameters, we sample the DM particle mass m_χ and DM fraction f_χ, with the resulting posteriors presented in Figure 11.5.
The comparison between the posterior and prior distributions of the DM particle mass and DM fraction in Figure 11.5 demonstrates that GW170817 does not impose constraints on the DM properties investigated in this study. However, the inferred BNS parameters, including the chirp mass, luminosity distance, and combined tidal deformability, are consistent with the LIGO-Virgo results reported in [10]. Given the sensitivity limitations of current-generation GW detectors, we extend our analysis to GW signals as observed with next-generation observatories to assess their potential for constraining DM properties.

11.4.2 Studying synthetic signals with next-generation detectors

To assess the potential of next-generation GW detectors to constrain DM properties, we simulate Events B–D from Table 11.2, employing both the triangular ET detector setup and a detector network composed of ET and CE, as described in Subsec. 11.2.5. All injections are generated with the aligned-spin waveform model `IMRPhenomD_NRTidalv2` [212]. In the following, we present and discuss our findings using Event D as a representative case, as the results remain unchanged for the other events listed in Table 11.2.
Figure 11.6 shows the results for Event D analyzed with ET and under zero-noise conditions. The injected values for both the source-frame chirp mass and the DM tidal deformability are tightly constrained. In contrast, the posterior distributions for the DM parameters remain largely consistent with their respective priors. This conclusion is further supported by the JSD values, listed in Figure 11.6. We repeat this analysis by injecting this signal under zero noise into a detector network assuming ET and CE. The results remain consistent with the single-detector case, indicating that the inclusion of another detector in a network does not lead to improved constraints on the DM properties.

Additionally, we performed a parameter estimation simulation for Event D using the purely baryonic

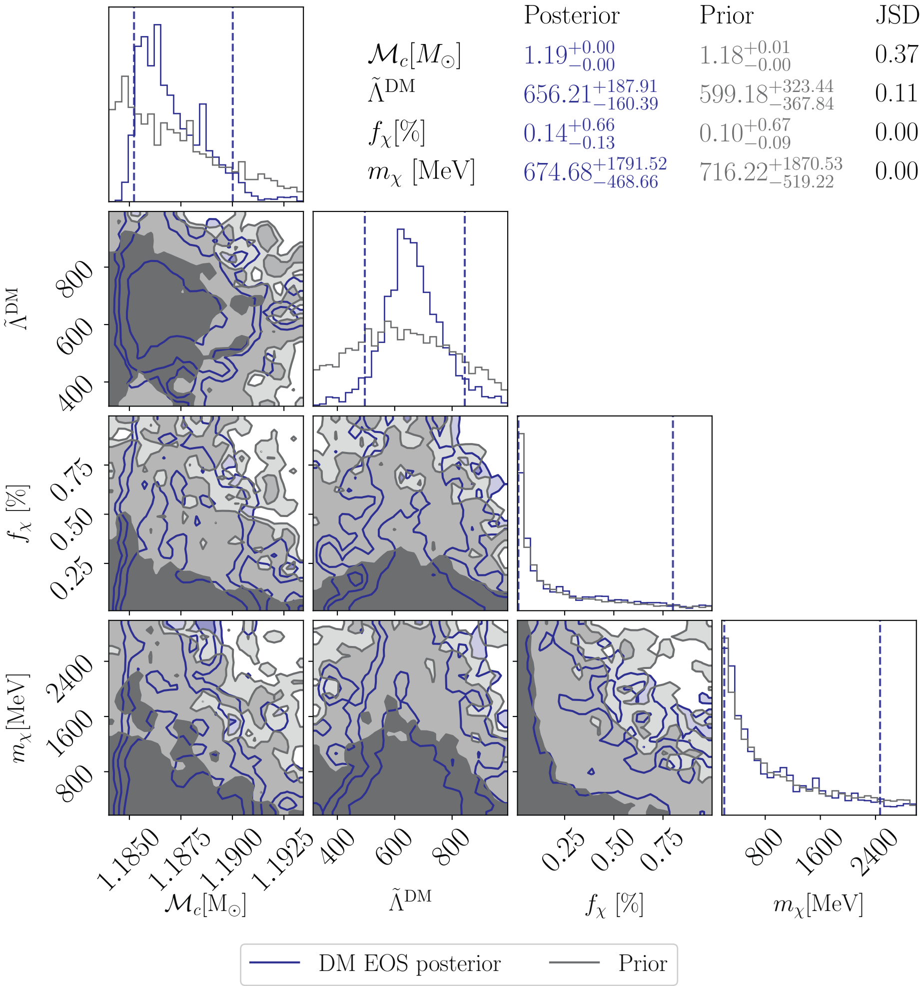

FIGURE 11.5
Corner plot of GW170817 reanalyzed under the assumption of DM during the BNS inspiral with posteriors shown in blue and priors in gray. The inferred source-frame chirp mass $\mathcal{M}_c$, luminosity distance D_L, and the combined dimensionless tidal deformability $\tilde{\Lambda}^{\rm DM}$ yield tight constraints and align with results from LIGO-Virgo [10], while no constraints are present for DM parameters, m_χ and f_χ. Vertical dashed lines denote the 90 % credible interval. Values in the table list the posterior and prior medians with uncertainties at 90 % credible interval and the JS divergence for each parameter. Different shadings mark the 68%, 95%, and 99% confidence intervals.

EOS set that served as the baseline for constructing the corresponding DM EOS set. This investigation aimed to compute the Bayes factor to assess which scenario is statistically favored by the data. To evaluate the relative plausibility of these competing hypotheses, we compute the natural logarithm of the Bayes factor, as defined in Chapter 8,

$$\ln \mathcal{B}^{\rm BM}_{\rm DM} = \ln \left(\frac{p(d|\mathbf{M}_{\rm BM})}{p(d|\mathbf{M}_{\rm DM})} \right) , \tag{11.11}$$

in which model $\mathbf{M}_{\rm BM}$ refers to the hypothesis that the BNS merger consists solely of BM, and $\mathbf{M}_{\rm DM}$ denotes the alternative scenario in which the BNS is admixed with DM. Using this definition, more negative values provide stronger support for the presence of DM in a BNS merger. Analyzing Event D

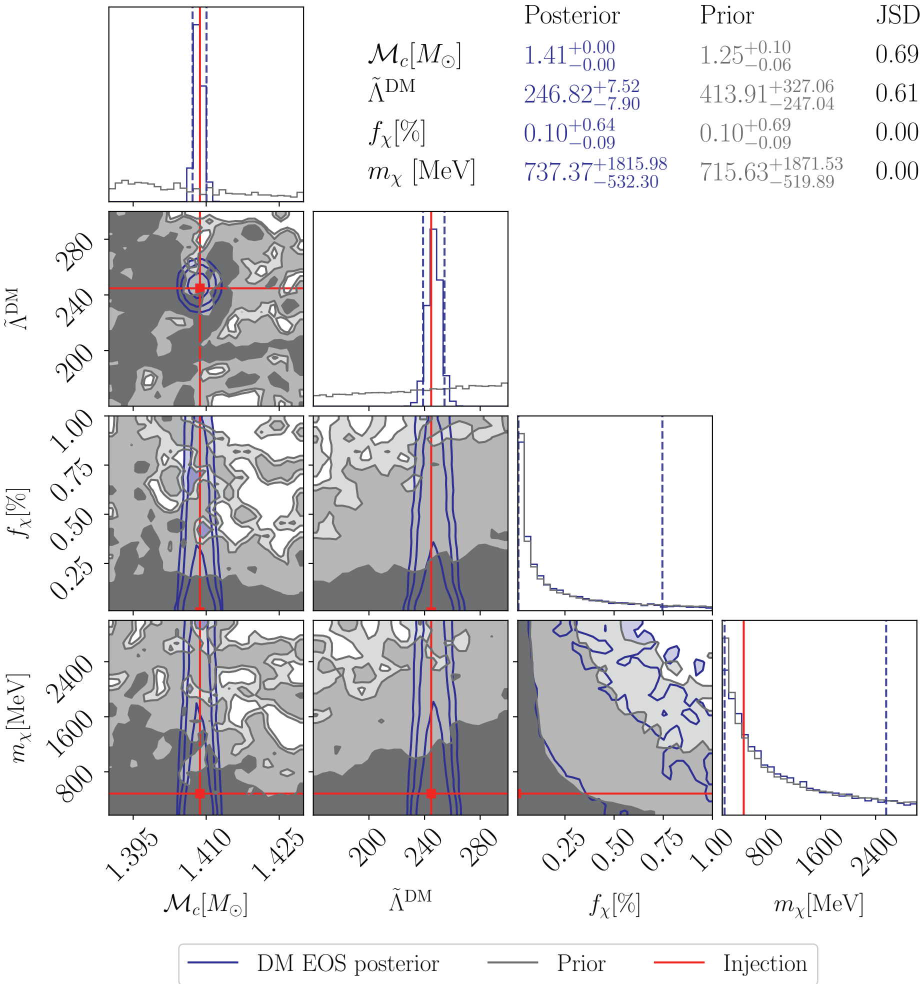

FIGURE 11.6
Corner plot of the simulated BNS Event D analyzed with ET and employing zero noise with posteriors shown in blue and priors shown in gray. The injected value for the source-frame chirp mass $\mathcal{M}_c$, DM-informed tidal deformability $\tilde{\Lambda}^{\rm DM}$, DM fraction $f_{\rm chi}$, and DM particle mass m_χ are shown as solid red lines. The median posterior values are reported at 90% credible interval and the JSD values are listed in the table for each parameter. Different shadings mark the 68%, 95%, and 99% confidence intervals.

using a detector network comprising ET and CE under zero-noise conditions yields a Bayes factor of $\ln \mathcal{B}^{\rm BM}_{\rm DM} = -0.39$, indicating no significant statistical preference for the presence of DM. Furthermore, a comparison of the posterior distributions for the BNS parameters under the purely baryonic and DM-admixed scenario reveals consistent results.

As mentioned above, we find similar results for the other events listed in Table 11.2. However, we repeat our analyses when assuming ET under Gaussian-noise conditions. Notably, the injection of Gaussian noise can introduce a measurable impact on both the Bayes factor and the inferred constraints on DM properties. For instance, analyzing Event D under an identical Gaussian noise realization with both the purely baryonic EOS set and the DM-admixed EOS set yields a Bayes factor of $\ln \mathcal{B}^{\rm BM}_{\rm DM} = -1.35$, indicating a noticeable statistical preference for the DM-admixed scenario. In this case, the posterior distributions for the DM fraction and DM particle mass show slight deviations from their priors. This outcome underscores that noise effects can induce spurious constraints on the inferred DM properties, emphasizing the necessity for caution when interpreting such results.

11.4.3 Comparison to Fisher matrix informed posteriors

We compare the results obtained by sampling additional DM properties through DM EOSs with posterior distributions derived using the Fisher matrix approximation. Specifically, we focus on two Events, B and D, drawn from one of the catalogs analyzed in the study [356] and presented in Chapter 10.

A comparison of the source-frame chirp mass posterior distributions for both events reveals consistent recovery of the injected values. The posteriors obtained by sampling DM EOSs exhibit a narrower width compared to those derived from the Fisher matrix approximation. With regard to the DM-informed tidal deformability $\tilde{\Lambda}^{\rm DM}$, the injected values are also well recovered in both events. Sampling over the DM EOSs leads to slightly tighter constraints on $\tilde{\Lambda}^{\rm DM}$, reflecting improved precision. However, as shown in Subsec. 11.4.2, the marginally improved accuracy in the DM-informed tidal deformability $\tilde{\Lambda}^{\rm DM}$ does not translate into tighter constraints on the underlying DM properties. Based on the limited number of performed simulations, our results suggest that the Fisher matrix approximation, as applied in Chapter 10, offers a reasonable approach for analyzing the considered DM-admixed BNS mergers, showing good agreement with full parameter estimation. Consequently, it appears that extending full parameter estimation to a larger population of DM-admixed BNS mergers may not lead to new insights into the DM properties considered in this study.

11.5 Concluding remarks

This work explored the potential of next-generation GW detectors to constrain both nuclear matter parameters governing the NS EOS and DM properties in BNS mergers, thereby probing both bright and dark constituents.

With regard to the bright side, initial results indicate that next-generation GW detectors can provide constraints on some nuclear parameters. While the symmetry energy slope was constrained more tightly, higher-order terms in the expansion of symmetric matter and the symmetry energy, including $K_{\rm sym}$ and $Q_{\rm sat}$, exhibited larger uncertainties. Furthermore, we find that our results are sensitive to the incorporation of PTs. Future investigations can extend the scope of this part of the analysis by including distinct nuclear-physics models, e.g. Skyrme interaction models [469] or density-dependent, relativistic-mean-field models [645, 646]. Furthermore, simulations of BM BNS mergers could be revisited using a detector network comprising ET and CE to assess whether such a network enables tighter constraints on nuclear matter parameters. Moreover, we note that our Bayesian parameter estimation framework does not sample directly over the microscopic nuclear-physics parameters that determine the EOS. As a result, some granularity is lost when inferring nuclear-physics parameters from precomputed EOS tables. Hence, tighter constraints could be achieved by performing direct sampling over microscopic parameters, an approach that has recently begun to be explored in the literature, e.g., [537].

Concerning the dark side, full parameter estimation simulations of DM-admixed BNS mergers did not reveal any constraints on the sampled DM particle mass and fraction. Moreover, the comparison between DM–informed tidal deformability posteriors obtained through full Bayesian parameter estimation and those derived via the FIM approximation revealed good agreement. This suggests that extending full parameter estimation to a larger population of DM–admixed BNS mergers is unlikely to yield additional insights into the DM properties considered in this study. Consequently, the results suggest that next-generation GW detectors may have limited capacity to identify or exclude the presence of DM within BNS mergers under the specific conditions assumed. However, it is im-

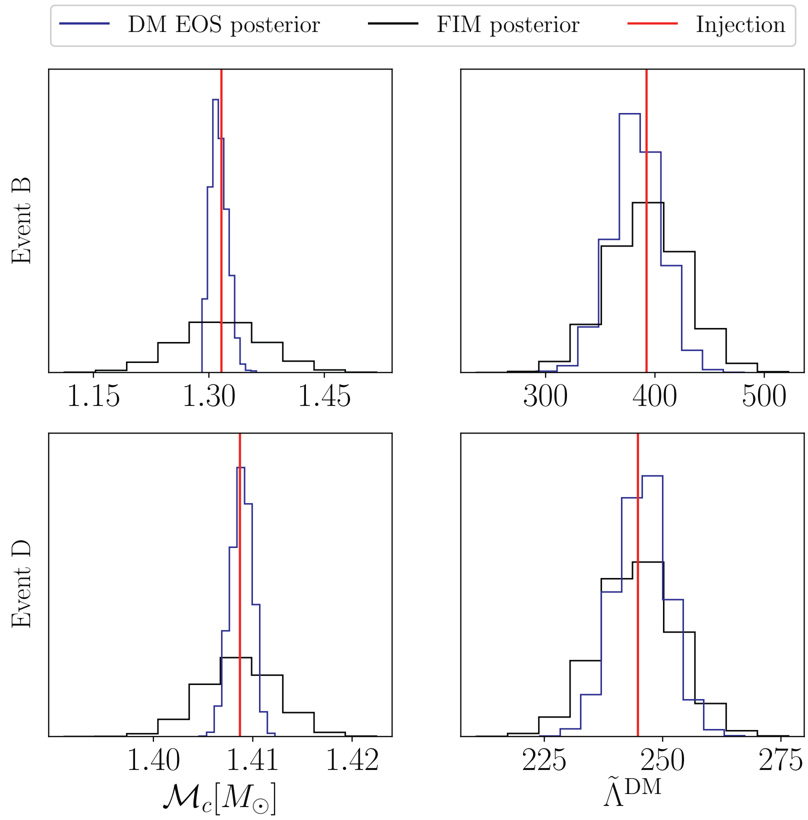

FIGURE 11.7
Comparison between posterior distributions obtained via the Fisher matrix approximation (black) and those derived from sampling of DM properties through DM EOSs (blue). Shown are the source-frame chirp mass $\mathcal{M}_c$ and the combined dimensionless tidal deformability $\tilde{\Lambda}^{\rm DM}$ when assuming the presence of DM in BNS mergers. The top panel corresponds to the lower SNR Event B, while the bottom panel displays results for the higher SNR Event D. The injected values are indicated by solid red lines.

portant to note the major assumptions underlying this analysis. First, we sampled DM properties by precomputing DM EOSs on a restricted grid of DM particle masses and fractions to estimate the DM-informed tidal deformability. This means that we expect to lose granularity to some extent as mentioned above. Second, we simulated DM-admixed BNS merger signals using existing GW models, which do not explicitly incorporate DM effects. Finally, we focused only on one specific DM type. Future work could explore a unified analysis that simultaneously accounts for both the bright and dark constituents. Such an approach would enable a systematic investigation into whether the presence of DM leads to biases in the inference of nuclear-physics parameters, such as those governing the NS EOS. Such efforts may be crucial for developing a more complete and unbiased understanding of the fundamental physics encoded in GW observations of BNS mergers.

Part VII

Conclusions

The first joint detection of a BNS merger via both gravitational and EM waves marked the beginning of a new era in multi-messenger astronomy, providing unprecedented insights across a wide spectrum of scientific disciplines. Compact binaries, particularly BNS mergers, serve as natural laboratories for multi-messenger studies, highlighting their remarkable versatility as probes of fundamental physics. Their messengers offer valuable insights into extreme gravity, dense nuclear matter, and the universe's expansion rate, positioning them as key observables in unraveling the most profound mysteries of the cosmos. Additionally, BNS mergers have been proposed as potential sites for exploring interactions with exotic matter, including hypothetical connections to dark matter, though direct evidence remains an open question.

This thesis pursued three primary objectives in the context of multi-messenger studies of compact binaries, with a particular emphasis on BNS mergers. First, it examined the impact of gravitational waveform model-dependent biases on the inference of key physical parameters, including the NS radius and the cosmic expansion rate, critical to nuclear physics and cosmology. Second, it investigated how Bayesian model selection, applied to multi-wavelength observations of GRBs, can be used to identify BNS mergers in the absence of direct GW detections. Third, it explored how future observations with next-generation detectors could constrain dense nuclear matter and DM properties, offering key insights into their fundamental nature.

The impact of gravitational waveform model systematics

Gravitational waveform models come with inherent systematic uncertainties stemming from approximations in modeling the relativistic two-body problem. With an increasing number of GW observations from BNS mergers, systematic errors are expected to grow, though the full extent remains uncertain. By simulating GW signals from 38 BNS mergers with current-generation GW detectors and analyzing them using four different waveform models, Chapter 6 and Chapter 7 investigated the impact of model-dependent biases on the inference of the NS radius and the cosmic expansion rate, respectively.

The findings in Chapter 6 showed that while the statistical uncertainty on the NS radius can shrink to about $\pm$ 250 m, systematic biases between waveform models can be up to twice as large. Incorporating EM observations from potential multi-messenger observations could further intensify these inconsistencies, stressing the urgency for more accurate waveform models. Given the substantial uncertainties in BNS detection rates and the limited number of current detections, the timescale for gravitational waveform model systematics to impact the inference remains rather uncertain.

In contrast, the findings, outlined in Chapter 7, revealed that the uncertainty in the luminosity distance arising from GW models exerts a negligible influence on the determination of the Hubble constant for current-generation GW observations. These findings are independent of the cosmic benchmark employed, i.e., the expansion rate as derived from the cosmic distance ladder by SH0ES or from the CMB radiation measured by the Planck collaboration. Still, these conclusions omit higher-order modes and assume idealized redshift measurements, implying the real-world impact may be more complex.

With next-generation detectors like ET and CE, which are expected to detect thousands of BNS merger events annually, statistical uncertainties will decrease, making the mitigation of systematic biases a key priority. Consequently, improved GW models will be essential for precise inference of NS radii and the cosmic expansion rate, which are fundamental to nuclear physics and cosmology.

Exploring progenitors: Bayesian multi-wavelength analyses of gamma-ray bursts

The limited number of observed BNS mergers motivates alternative strategies for identifying such events. This thesis explored the use of Bayesian multi-wavelength analyses of GRBs as a complementary approach for inferring compact binary mergers and demonstrated that such events can be investigated in the absence of direct GW detections, with partial characterization possible through EM observations. Applying Bayesian model selection to GRB 211211A under four scenarios, i.e., a

BNS merger, an NSBH merger, a rCCSN, and a CCSN, revealed the highest statistical evidence for a BNS merger, offering the best fit to multi-wavelength light curves and suggesting an additional emission component that is consistent with r-process nucleosynthesis. However, since the analysis only considered a limited subset of potential astrophysical origins, these findings must be interpreted cautiously, underscoring the need for further investigations encompassing a broader range of progenitor scenarios and models. Expanding this method to a broader range of astrophysical scenarios could refine our understanding of GRB progenitors and their associations with compact binaries, including BNS mergers, especially in periods when GW signals are absent.

BNS mergers as probes of nuclear and dark matter

NSs unite extreme matter and extreme gravity, making BNS mergers prime venues for probing supranuclear densities and potential DM admixtures. The NS EOS and the nature of DM remain unresolved questions. However, GW observations of BNS mergers offer a unique probe of dense nuclear matter and potentially DM, enabling constraints on nuclear-physics parameters and phenomena beyond the Standard Model of particle physics.

Chapter 9 investigated the ability to distinguish between nuclear Hamiltonians with different 3N interactions derived from chiral EFT. A Bayesian model selection study, based on an injection campaign for a BNS population, demonstrated that ET could provide strong evidence to differentiate between distinct nuclear interaction models. However, the analysis was restricted to frequencies above 30 Hz to reduce computational cost, excluding crucial mass parameter information most accessible around 5-9 Hz. Despite this limitation, the study demonstrated that future GW observations of BNS mergers could distinguish nuclear Hamiltonians and serves as a framework for constraining additional components of the Hamiltonian.

Chapter 10 explored the potential of ET measurements of the tidal deformability in DM-admixed NS mergers to constrain the baryonic EOS and to infer DM properties. Using the Fisher matrix approach, the study varied the baryonic EOS, DM particle mass, and DM fraction distribution. The results indicate that the presence of DM in NSs is disfavored. However, DM in BNS mergers can introduce a small bias in the inference of the baryonic EOS if not properly accounted for. These findings are subject to limitations, as they depend on the choice of the DM model and the assumed parameter ranges for the DM particle mass and fraction. Stronger observational GW signatures could arise under alternative DM models, higher DM fractions, different DM particle masses or with improved constraints on the baryonic EOS. Furthermore, the Fisher matrix approach provides only a lower bound on statistical uncertainties and does not account for DM-induced biases in other BNS parameters, which full Bayesian parameter estimation could reveal, along with larger uncertainties in tidal deformability measurements.

The preliminary results presented in Chapter 11 aimed to explore the potential of future GW detectors to constrain both nuclear matter parameters governing the NS EOS and DM properties in BNS mergers, thereby probing both bright and dark constituents. First results indicate moderate constraints on some nuclear parameters. Further analyses are envisioned with different microphysical models. Bayesian parameter estimation simulations of DM–admixed BNS mergers reveal no significant constraints on DM properties within the framework of the assumed model. This result suggests that next-generation gravitational-wave detectors may have limited sensitivity to test the presence of dark matter in BNS mergers. The comparison between DM-informed tidal deformability posteriors from Bayesian parameter estimation and the FIM approximation presented in Chapter 10 shows good agreement, suggesting that parameter estimation for a larger set of DM-admixed BNS mergers is unlikely to provide further insights into the examined DM properties. As in Chapter 10, these results are model-dependent, limited by assumptions on DM mass and fraction, and were conducted with existing waveform models that do not incorporate DM effects. Moreover, a main limitation extending to both analyses is that we do not directly sample over the microscopic nuclear-physics or DM parameters, but instead rely on precomputed baryonic EOSs or DM EOSs. Future work could address this limitation by implementing direct sampling methods.

Outlook

The first multi-messenger observation represents a landmark event, demonstrating the capability of BNS mergers to enhance our understanding of extreme gravity, dense nuclear matter, cosmic expansion, cosmic synthesis of heavy elements, and potentially DM. This thesis has addressed both fundamental challenges, such as waveform model biases and BNS merger studies in the absence of GW observations, as well as broader objectives, including the exploration of extreme matter, and physics beyond the Standard Model.

Looking forward, next-generation GW detectors such as CE and ET are expected to mark a transformative advancement in GW astronomy. These instruments will significantly enhance the ability to observe BNS mergers, with projected detection rates ranging from $10^4 - 10^5$ BNS events per year [538, 601, 128, 656, 241]. ET alone is expected to observe over a thousand events annually, including thousands accompanied by kilonova emission and a subset with jet-related signatures [179], thereby vastly expanding our ability to probe fundamental physics across a broad spectrum of scientific fields. CE is expected to facilitate high-precision measurements of the tidal deformability, constraining NS radii to within 0.1 km for hundreds of systems each year [241]. These observations will tightly constrain the supranuclear EOS and may reveal a PT to quark matter in NS cores. Despite these promising prospects, significant challenges remain. These include the mitigation of systematic uncertainties in waveform and noise modeling, the precise quantification of model misspecification, and the advancement of data analysis frameworks to address the limitations in current likelihood approximations and computational approaches [70].

By the time next-generation GW detectors become operational, improvements in high-precision waveform modeling, advancements in data analysis techniques, and computational methods coupled with coordinated EM follow-up campaigns will be critical for maximizing the scientific return from each BNS detection. Ultimately, the synergy of future multi-messenger observations, refined theoretical models, and advanced computational techniques will establish BNS mergers as unparalleled cosmic laboratories, where the brightest and darkest aspects of physics may be explored in unison.

List of acronyms

ADM	Arnowitt-Deser-Misner
AFDMC	auxiliary field diffusion Monte Carlo
BBH	binary black hole
BH	black hole
BL	broad-lined
BM	baryonic matter
BNS	binary neutron star
CBC	compact binary coalescence
CC	coupled-cluster
CCSN	core collapse supernova
CE	Cosmic Explorer
CLDM	compressible liquid drop model
CMB	cosmic microwave background
DM	dark matter
EFEs	Einstein field equations
EFT	effective field theory
EM	electromagnetic
EOB	effective-one-body
EOS	equation-of-state
ET	Einstein telescope
FIM	Fisher information matrix
FLRW	Friedmann-Lemaitre-Robertson-Walker
FS	forward shock
GCN	General Coordinates Network
GFMC	Green's function Monte Carlo
GPR	Gaussian Process Regression
GR	general relativity
GRB	gamma-ray burst
GW	gravitational wave
GWOSC	Gravitational Wave Open Science Center
IMR	inspiral-merger-ringdown
IR	infrared
ISM	interstellar medium
ISCO	innermost stable circular orbit
JSD	Jensen–Shannon divergence
KS	Kolmogorov-Smirnov
ΛCDM	lambda cold dark matter
LIGO	Laser Interferometer Gravitational-wave Observatory
LISA	Laser Interferometer Space Antenna
LVK	LIGO-Virgo-KAGRA
MBPT	many-body perturbation theory
MCMC	Markov chain Monte Carlo
MM	metamodel
MSE	mean squared error

NEP	nuclear empirical parameter
NICER	Neutron Star Interior Composition Explorer
NMMA	nuclear-physics and multi-messenger astrophysics
NIR	near-infrared
NN	neural network
NR	numerical relativity
NS	neutron star
NSBH	neutron star-black hole
PDF	probability density function
PP	point-particle
QCD	quantum chromodynamics
PN	post-Newtonian
PT	phase transition
ROM	reduced order model
ROQ	reduced-order-quadrature
RS	reverse shock
SCGF	self-consistent Green's function
SH0ES	supernovae, H_0, for the equation of state of dark energy
SN	supernova
SNR	signal-to-noise ratio
SPA	stationary phase approximation
SSC	synchrotron self-Compton
SVD	singular value decomposition
TOV	Tolman-Volkov-Oppenheimer
TPE	two-pion–exchange
TT	transverse-traceless
UV	ultraviolet
4PN	fourth Post-Newtonian

List of figures

List of tables

Bibliography

[1] J. Aasi et al. Advanced LIGO. *Class. Quant. Grav.*, 32:074001, 2015.

[2] A. Abac et al. New and robust gravitational-waveform model for high-mass-ratio binary neutron star systems with dynamical tidal effects. *Phys. Rev. D*, 109(2):024062, 2024.

[3] A. Abac et al. Observation of Gravitational Waves from the Coalescence of a 2.5 - 4.5 $M_\odot$ Compact Object and a Neutron Star. *Astrophys. J. Lett.*, 970(2):L34, 2024.

[4] A. Abac et al. Ultralight vector dark matter search using data from the KAGRA O3GK run. *Phys. Rev. D*, 110(4):042001, 2024.

[5] M. Abadi et al. Tensorflow: Large-scale machine learning on heterogeneous distributed systems, 2016.

[6] B. P. Abbott et al. Observation of Gravitational Waves from a Binary Black Hole Merger. *Phys. Rev. Lett.*, 116(6):061102, 2016.

[7] B. P. Abbott et al. A gravitational-wave standard siren measurement of the Hubble constant. *Nature*, 551(7678):85–88, 2017.

[8] B. P. Abbott et al. Exploring the Sensitivity of Next Generation Gravitational Wave Detectors. *Class. Quant. Grav.*, 34(4):044001, 2017.

[9] B. P. Abbott et al. Gravitational Waves and Gamma-rays from a Binary Neutron Star Merger: GW170817 and GRB 170817A. *Astrophys. J. Lett.*, 848(2):L13, 2017.

[10] B. P. Abbott et al. GW170817: Observation of Gravitational Waves from a Binary Neutron Star Inspiral. *Phys. Rev. Lett.*, 119(16):161101, 2017.

[11] B. P. Abbott et al. Multi-messenger Observations of a Binary Neutron Star Merger. *Astrophys. J. Lett.*, 848(2):L12, 2017.

[12] B. P. Abbott et al. Search for Post-merger Gravitational Waves from the Remnant of the Binary Neutron Star Merger GW170817. *Astrophys. J. Lett.*, 851(1):L16, 2017.

[13] B. P. Abbott et al. GW170817: Measurements of neutron star radii and equation of state. *Phys. Rev. Lett.*, 121(16):161101, 2018.

[14] B. P. Abbott et al. Binary Black Hole Population Properties Inferred from the First and Second Observing Runs of Advanced LIGO and Advanced Virgo. *Astrophys. J. Lett.*, 882(2):L24, 2019.

[15] B. P. Abbott et al. GWTC-1: A Gravitational-Wave Transient Catalog of Compact Binary Mergers Observed by LIGO and Virgo during the First and Second Observing Runs. *Phys. Rev. X*, 9(3):031040, 2019.

[16] B. P. Abbott et al. Properties of the binary neutron star merger GW170817. *Phys. Rev. X*, 9(1):011001, 2019.

[17] B. P. Abbott et al. Tests of General Relativity with GW170817. *Phys. Rev. Lett.*, 123(1):011102, 2019.

[18] B. P. Abbott et al. A guide to LIGO–Virgo detector noise and extraction of transient gravitational-wave signals. *Class. Quant. Grav.*, 37(5):055002, 2020.

[19] B. P. Abbott et al. GW190425: Observation of a Compact Binary Coalescence with Total Mass $\sim 3.4 M_{\odot}$. *Astrophys. J. Lett.*, 892(1):L3, 2020.

[20] B. P. Abbott et al. Model comparison from LIGO–Virgo data on GW170817's binary components and consequences for the merger remnant. *Class. Quant. Grav.*, 37(4):045006, 2020.

[21] B. P. Abbott et al. Optically targeted search for gravitational waves emitted by core-collapse supernovae during the first and second observing runs of advanced LIGO and advanced Virgo. *Phys. Rev. D*, 101(8):084002, 2020.

[22] B. P. Abbott et al. Prospects for observing and localizing gravitational-wave transients with Advanced LIGO, Advanced Virgo and KAGRA. *Living Rev. Rel.*, 23(1):3, 2020.

[23] B. P. Abbott et al. A Gravitational-wave Measurement of the Hubble Constant Following the Second Observing Run of Advanced LIGO and Virgo. *Astrophys. J.*, 909(2):218, 2021.

[24] R. Abbott et al. GW190814: Gravitational Waves from the Coalescence of a 23 Solar Mass Black Hole with a 2.6 Solar Mass Compact Object. *Astrophys. J.*, 896(2):L44, 2020.

[25] R. Abbott et al. GWTC-2: Compact Binary Coalescences Observed by LIGO and Virgo During the First Half of the Third Observing Run. *Phys. Rev. X*, 11:021053, 2021.

[26] R. Abbott et al. GWTC-2.1: Deep Extended Catalog of Compact Binary Coalescences Observed by LIGO and Virgo During the First Half of the Third Observing Run. *arXiv e-prints*, 8 2021.

[27] R. Abbott et al. Observation of gravitational waves from two neutron star–black hole coalescences. *Astrophys. J. Lett.*, 915(1):L5, jun 2021.

[28] R. Abbott et al. Open data from the first and second observing runs of Advanced LIGO and Advanced Virgo. *SoftwareX*, 13:100658, 2021.

[29] R. Abbott et al. Constraints on the Cosmic Expansion History from GWTC–3. *Astrophys. J.*, 949(2):76, 2023.

[30] R. Abbott et al. GWTC-3: Compact Binary Coalescences Observed by LIGO and Virgo during the Second Part of the Third Observing Run. *Phys. Rev. X*, 13(4):041039, 2023.

[31] R. Abbott et al. Population of Merging Compact Binaries Inferred Using Gravitational Waves through GWTC-3. *Phys. Rev. X*, 13(1):011048, 2023.

[32] R. Abbott et al. Population of Merging Compact Binaries Inferred Using Gravitational Waves through GWTC-3. *Phys. Rev. X*, 13(1):011048, 2023.

[33] T. Abdelsalhin, L. Gualtieri, and P. Pani. Post-Newtonian spin-tidal couplings for compact binaries. *arXiv: 1805.01487*, 2018.

[34] F. Acernese et al. Advanced Virgo: a second-generation interferometric gravitational wave detector. *Class. Quant. Grav.*, 32(2):024001, 2015.

[35] C. Adamcewicz and E. Thrane. Do unequal-mass binary black hole systems have larger χeff? Probing correlations with copulas in gravitational-wave astronomy. *Mon. Not. Roy. Astron. Soc.*, 517(3):3928–3937, 2022.

[36] P. A. R. Ade et al. Planck 2015 results. XIII. Cosmological parameters. *Astronomy & Astrophysics*, 594:A13, 2016.

[37] D. Adhikari et al. Accurate Determination of the Neutron Skin Thickness of ^{208}Pb through Parity-Violation in Electron Scattering. *Phys. Rev. Lett.*, 126(17):172502, 2021.

[38] D. Adhikari et al. Precision Determination of the Neutral Weak Form Factor of Ca48. *Phys. Rev. Lett.*, 129(4):042501, 2022.

[39] M. Agathos et al. Constraining the neutron star equation of state with gravitational wave signals from coalescing binary neutron stars. *Phys. Rev.*, D92(2):023012, 2015.

[40] M. Agathos et al. Inferring Prompt Black-Hole Formation in Neutron Star Mergers from Gravitational-Wave Data. *Phys. Rev. D*, 101(4):044006, 2020.

[41] G. Agazie et al. The NANOGrav 15 yr Data Set: Evidence for a Gravitational-wave Background. *Astrophys. J. Lett.*, 951(1):L8, 2023.

[42] The European Space Agency. Stellar evolution. Available at: `https://www.esa.int/ESA_Multimedia/Images/2018/03/Stellar_evolution`. (accessed: 19.12.2024).

[43] N. Aghanim et al. Planck 2018 results. VI. Cosmological parameters. *Astronomy & Astrophysics*, 641:A6, 2020. [Erratum: Astron.Astrophys. 652, C4 (2021)].

[44] T. Ahumada et al. Discovery and confirmation of the shortest gamma-ray burst from a collapsar. *Nature Astron.*, 5(9):917–927, 2021.

[45] V. Aivazyan et al. GRANDMA observations of ZTF/Fink transients during summer 2021. *Mon. Not. Roy. Astron. Soc.*, 515(4):6007–6022, 2022.

[46] P. Ajith et al. Inspiral-merger-ringdown waveforms for black-hole binaries with non-precessing spins. *Phys.Rev.Lett.*, 106:241101, 2011.

[47] S. Akcay et al. Effective-one-body multipolar waveform for tidally interacting binary neutron stars up to merger. *Phys. Rev. D*, 99(4), feb 2019.

[48] T. Akutsu et al. Overview of KAGRA: Detector design and construction history, 5 2020.

[49] M. Almualla et al. Using Neural Networks to Perform Rapid High-Dimensional Kilonova Parameter Inference. 12 2021.

[50] P. Amaro-Seoane et al. Laser Interferometer Space Antenna. February 2017. arXiv:1702.00786 [astro-ph.IM].

[51] S. Anand et al. Optical follow-up of the neutron star–black hole mergers S200105ae and S200115j. *Nature Astron.*, 5(1):46–53, 2021.

[52] S. Anand et al. Chemical Distribution of the Dynamical Ejecta in the Neutron Star Merger GW170817. 7 2023. arXiv: 2307.11080 [astro-ph.HE].

[53] I. Andreoni et al. Follow up of GW170817 and its electromagnetic counterpart by Australian-led observing programs. *Publ. Astron. Soc. Austral.*, 34:e069, 2017.

[54] I. Andreoni et al. Fast-transient Searches in Real Time with ZTFReST: Identification of Three Optically Discovered Gamma-Ray Burst Afterglows and New Constraints on the Kilonova Rate. *Astrophys. J.*, 918(2):63, 2021.

[55] E. Annala et al. Gravitational-wave constraints on the neutron-star-matter Equation of State. *Phys. Rev. Lett.*, 120(17):172703, 2018.

[56] E. Annala et al. Multimessenger Constraints for Ultradense Matter. *Phys. Rev. X*, 12(1):011058, 2022.

[57] J. Antoniadis et al. A Massive Pulsar in a Compact Relativistic Binary. *Science*, 340:6131, 2013.

[58] I. Arcavi et al. Optical emission from a kilonova following a gravitational-wave-detected neutron-star merger. *Nature*, 551:64, 2017.

[59] W. D. Arnett. Type I supernovae. I - Analytic solutions for the early part of the light curve. *Astrophys. J.*, 253:785–797, February 1982.

[60] R. L. Arnowitt, S. Deser, and C. W. Misner. Dynamical Structure and Definition of Energy in General Relativity. *Phys. Rev.*, 116:1322–1330, 1959.

[61] K. G. Arun et al. Higher-order spin effects in the amplitude and phase of gravitational waveforms emitted by inspiraling compact binaries: Ready-to-use gravitational waveforms. *Phys. Rev.*, D79:104023, 2009. [Erratum: Phys. Rev.D84,049901(2011)].

[62] K. G. Arun et al. New horizons for fundamental physics with LISA. *Living Rev. Rel.*, 25(1):4, 2022.

[63] Z. Arzoumanian et al. The NANOGrav 11-year Data Set: High-precision timing of 45 Millisecond Pulsars. *Astrophys. J. Suppl.*, 235(2):37, 2018.

[64] S. Ascenzi et al. A luminosity distribution for kilonovae based on short gamma-ray burst afterglows. *Mon. Not. Roy. Astron. Soc.*, 486(1):672–690, 2019.

[65] G. Ashton et al. Bilby: A user-friendly bayesian inference library for gravitational-wave astronomy. *Astrophys. J. Supplement Series*, 241(2):27, apr 2019.

[66] A. Askar et al. MOCCA-SURVEY Database – I. Coalescing binary black holes originating from globular clusters. *Mon. Not. Roy. Astron. Soc.*, 464(1):L36–L40, 2017.

[67] Y. Aso et al. Interferometer design of the KAGRA gravitational wave detector. *Phys. Rev. D*, 88(4):043007, 2013.

[68] L. Baiotti et al. A new three-dimensional general-relativistic hydrodynamics code. *Mem. Soc. Ast. It.*, 1:S210, 2003.

[69] L. Baiotti and L. Rezzolla. Binary neutron star mergers: a review of einstein's richest laboratory. *Reports on Progress in Physics*, 80(9):096901, jul 2017.

[70] A. M. Baker et al. Significant challenges for astrophysical inference with next-generation gravitational-wave observatories. 3 2025. arXiv:503.04073 [gr-qc].

[71] J. Baker et al. The Laser Interferometer Space Antenna: Unveiling the Millihertz Gravitational Wave Sky. 7 2019.

[72] J. G. Baker et al. Gravitational wave extraction from an inspiraling configuration of merging black holes. *Phys. Rev. Lett.*, 96:111102, 2006.

[73] C. Balazs et al. A Primer on Dark Matter. 11 2024. arXiv:2411.05062 [astro-ph.CO].

[74] A. Bandopadhyay et al. Measuring Neutron Star Radius with second and third generation Gravitational Wave Detector Networks. 2 2024. arXiv:2402.05056 [astro-ph.HE].

[75] K. Barbary. List of built-in bandpasses. Available at: `https://sncosmo.readthedocs.io/en/stable/bandpass-list.html`. (accessed: 26.12.2024).

[76] K. Barbary et al. SNCosmo. Available at: `https://zenodo.org/records/6363879`. (accessed: 11.10.2024).

[77] C. Barbieri et al. Electromagnetic counterparts of black hole-neutron star mergers: dependence on the neutron star properties. *Eur. Phys. J. A*, 56(1):8, 2020.

[78] J. Barnes et al. Radioactivity and thermalization in the ejecta of compact object mergers and their impact on kilonova light curves. *Astrophys. J.*, 829(2):110, 2016.

[79] J. Barnes and B. D. Metzger. Signatures of r-process enrichment in supernovae from collapsars. *Astrophys. J. Lett.*, 939(2):L29, nov 2022.

[80] J. Barnes and B. D. Metzger. A Collapsar Origin for GRB 211211A Is (Just Barely) Possible. *Astrophys. J.*, 947(2):55, 2023.

[81] D. Baumann et al. Sharp Signals of Boson Clouds in Black Hole Binary Inspirals. *Phys. Rev. Lett.*, 128(22):221102, 2022.

[82] T. W. Baumgarte and S. L. Shapiro. On the numerical integration of Einstein's field equations. *Phys. Rev. D*, 59:024007, 1999.

[83] A. Bauswein et al. Neutron-star radius constraints from GW170817 and future detections. *Astrophys. J.*, 850(2):L34, 2017.

[84] A. Bauswein, S. Goriely, and H. T. Janka. Systematics of dynamical mass ejection, nucleosynthesis, and radioactively powered electromagnetic signals from neutron-star mergers. *Astrophys. J.*, 773(1):78, July 2013.

[85] A. Bauswein, H. T. Janka, and R. Oechslin. Testing Approximations of Thermal Effects in Neutron Star Merger Simulations. *Phys. Rev. D*, 82:084043, 2010.

[86] G. Baym, C. Pethick, and P. Sutherland. The Ground State of Matter at High Densities: Equation of State and Stellar Models. *Astrophys. J.*, 170:299–+, December 1971.

[87] K. Belczynski et al. The first gravitational-wave source from the isolated evolution of two 40-100 Msun stars. *Nature*, 534:512, 2016.

[88] K. Belczynski et al. The origin of the first neutron star – neutron star merger. *Astronomy & Astrophysics*, 615:A91, 2018.

[89] N. F. Bell et al. Improved Treatment of Dark Matter Capture in Neutron Stars. *JCAP*, 09:028, 2020.

[90] A. M. Beloborodov. Nuclear composition of gamma-ray burst fireballs. *Astrophys. J.*, 588:931–944, 2003.

[91] P. Beniamini and P. Kumar. X-ray flares in GRBs: general considerations and photospheric origin. *Mon. Not. Roy. Astron. Soc.*, 457(1):L108–L112, 2016.

[92] S. Bera et al. Incompleteness Matters Not: Inference of H_0 from Binary Black Hole–Galaxy Cross-correlations. *Astrophys. J.*, 902(1):79, 2020.

[93] M. Berbig, J. Sudip, and A. Trautner. The Hubble tension and a renormalizable model of gauged neutrino self-interactions. *Phys. Rev. D*, 102(11):115008, 2020.

[94] V. Berezinsky, V. Dokuchaev, and Y. Eroshenko. Remnants of dark matter clumps. *Phys. Rev. D*, 77:083519, 2008.

[95] E. Berger, W. Fong, and R. Chornock. An r-process Kilonova Associated with the Short-hard GRB 130603B. *Astrophys. J. Lett.*, 774:L23, 2013.

[96] S. Bernuzzi et al. Modeling the dynamics of tidally interacting binary neutron stars up to the merger. *Phys. Rev. Let.*, 114(16), apr 2015.

[97] S. Bernuzzi, M. Thierfelder, and B. Brügmann. Accuracy of numerical relativity waveforms from binary neutron star mergers and their comparison with post-Newtonian waveforms. *Phys. Rev. D*, 85:104030, 2012.

[98] G. Bertone et al. Gravitational wave probes of dark matter: challenges and opportunities. *SciPost Phys. Core*, 3:007, 2020.

[99] G. Bertone and M. Fairbairn. Compact Stars as Dark Matter Probes. *Phys. Rev. D*, 77:043515, 2008.

[100] S. Bhattacharya et al. Can LIGO Detect Nonannihilating Dark Matter? *Phys. Rev. Lett.*, 131(9):091401, 2023.

[101] Bilby collaboration. CE power spectral density. Available at: `https://git.ligo.org/lscsoft/bilby/-/blob/master/bilby/gw/detector/noise_curves/CE_psd.txt?ref_type=heads`.

[102] Bilby collaboration. ET power spectral density. Available at: `https://git.ligo.org/lscsoft/bilby/-/blob/master/bilby/gw/detector/noise_curves/ET_D_psd.txt?ref_type=heads`.

[103] D. Bini, T. Damour, and G. Faye. Effective action approach to higher-order relativistic tidal interactions in binary systems and their effective one body description. *Phys. Rev. D*, 85:124034, 2012.

[104] T. Binnington and E. Poisson. Relativistic theory of tidal Love numbers. *Phys. Rev. D*, 80:084018, 2009.

[105] S. Birrer et al. H0LiCOW - IX. Cosmographic analysis of the doubly imaged quasar SDSS 1206+4332 and a new measurement of the Hubble constant. *Mon. Not. Roy. Astron. Soc.*, 484:4726, 2019.

[106] S. Biscoveanu, P. Landry, and S. Vitale. Population properties and multimessenger prospects of neutron star–black hole mergers following GWTC-3. *Mon. Not. Roy. Astron. Soc.*, 518(4):5298–5312, 2022.

[107] B. Biswas. Impact of PREX-II and Combined Radio/NICER/XMM-Newton's Mass–radius Measurement of PSR J0740+6620 on the Dense-matter Equation of State. *Astrophys. J.*, 921(1):63, 2021.

[108] L. Blanchet. Gravitational radiation from post-newtonian sources and inspiralling compact binaries. *Living Rev. Rel.*, 2(17), December 2014.

[109] L. Blanchet. Post-Newtonian Theory for Gravitational Waves. *Living Rev. Rel.*, 27:4, 2024.

[110] L. Blanchet et al. Gravitational radiation damping of compact binary systems to second post-Newtonian order. *Phys.Rev.Lett.*, 74:3515–3518, 1995.

[111] L. Blanchet et al. Gravitational radiation from inspiralling compact binaries completed at the third post-Newtonian order. *Phys.Rev.Lett.*, 93:091101, 2004.

[112] L. Blanchet et al. Dimensional regularization of the third post-Newtonian gravitational wave generation from two point masses. *Phys. Rev. D*, 71:124004, 2005.

[113] R. D. Blandford and C. F. McKee. Fluid dynamics of relativistic blast waves. *The physics of Fluids*, 19(8):1130–1138, 1976.

[114] R. D. Blandford and R. L. Znajek. Electromagnetic extractions of energy from Kerr black holes. *Mon. Not. Roy. Astron. Soc.*, 179:433–456, 1977.

[115] N. Blinov, G. Krnjaic, and S. W. Li. Toward a realistic model of dark atoms to resolve the Hubble tension. *Phys. Rev. D*, 105(9):095005, 2022.

[116] Z. H. Bo et al. Dark Matter Search Results from 1.54 Tonne·Year Exposure of PandaX-4T. *Phys. Rev. Lett.*, 134(1):011805, 2025.

[117] A. Bohé et al. Quadratic-in-spin effects in the orbital dynamics and gravitational-wave energy flux of compact binaries at the 3PN order. *Class. Quant. Grav.*, 32(19):195010, 2015.

[118] A. Bohé et al. Improved effective-one-body model of spinning, nonprecessing binary black holes for the era of gravitational-wave astrophysics with advanced detectors. *Phys. Rev. D*, 95(4):044028, 2017.

[119] A. Bohé, S. Marsat, and L. Blanchet. Next-to-next-to-leading order spin–orbit effects in the gravitational wave flux and orbital phasing of compact binaries. *Class. Quant. Grav.*, 30:135009, 2013.

[120] C. Bona et al. General-covariant evolution formalism for numerical relativity. *Phys. Rev. D*, 67:104005, May 2003.

[121] C. Bona et al. Symmetry-breaking mechanism for the z4 general-covariant evolution system. *Phys. Rev. D*, 69:064036, Mar 2004.

[122] N. Borghi et al. Cosmology and Astrophysics with Standard Sirens and Galaxy Catalogs in View of Future Gravitational Wave Observations. *Astrophys. J.*, 964(2):191, 2024.

[123] S. Borhanian and B. S. Sathyaprakash. Listening to the Universe with next generation ground-based gravitational-wave detectors. *Phys. Rev. D*, 110(8):083040, 2024.

[124] D. Bose and S. Sarkar. Impact of galactic distributions in celestial capture of dark matter. *Phys. Rev. D*, 107(6):063010, 2023.

[125] L. Bovard et al. r-process nucleosynthesis from matter ejected in binary neutron star mergers. *Phys. Rev. D*, 96(12):124005, 2017.

[126] J. Bramante, B. J. Kavanagh, and N. Raj. Scattering Searches for Dark Matter in Subhalos: Neutron Stars, Cosmic Rays, and Old Rocks. *Phys. Rev. Lett.*, 128(23):231801, 2022.

[127] J. Bramante and N. Raj. Dark matter in compact stars. *Phys. Rept.*, 1052:1–48, 2024.

[128] M. Branchesi et al. Science with the Einstein Telescope: a comparison of different designs. *JCAP*, 07:068, 2023.

[129] M. Breschi et al. AT2017gfo: Bayesian inference and model selection of multicomponent kilonovae and constraints on the neutron star equation of state. *Mon. Not. Roy. Astron. Soc.*, 505(2):1661–1677, 2021.

[130] D. Brethauer et al. Impact of Systematic Modeling Uncertainties on Kilonova Property Estimation. *Astrophys. J.*, 975(2):213, 2024.

[131] F. S. Broekgaarden, S. Stevenson, and E. Thrane. Signatures of Mass Ratio Reversal in Gravitational Waves from Merging Binary Black Holes. *Astrophys. J.*, 938(1):45, 2022.

[132] B. Brügmann. Binary Black Hole Mergers in 3d Numerical Relativity. *Int. J. Mod. Phys.*, D8:85, 1999.

[133] B. Brügmann et al. Calibration of Moving Puncture Simulations. *Phys. Rev. D*, 77:024027, 2008.

[134] B. Brügmann, W. Tichy, and N. Jansen. Numerical simulation of orbiting black holes. *Phys. Rev. Lett.*, 92:211101, 2004.

[135] J. Buchner et al. X-ray spectral modelling of the AGN obscuring region in the CDFS: Bayesian model selection and catalogue. *Astronomy & Astrophysics*, 564:A125, 2014.

[136] M. R. Buckley and A. DiFranzo. Collapsed Dark Matter Structures. *Phys. Rev. Lett.*, 120(5):051102, 2018.

[137] A. Buikema et al. Sensitivity and performance of the Advanced LIGO detectors in the third observing run. *Phys. Rev. D*, 102(6):062003, 2020.

[138] M. Bulla. POSSIS: predicting spectra, light curves and polarization for multi-dimensional models of supernovae and kilonovae. *Mon. Not. Roy. Astron. Soc.*, 489(4):5037–5045, 2019.

[139] M. Bulla. The critical role of nuclear heating rates, thermalization efficiencies, and opacities for kilonova modelling and parameter inference. *Mon. Not. Roy. Astron. Soc.*, 520(2):2558–2570, 2023.

[140] M. Bulla et al. Multi-Messenger Constraints on the Hubble Constant through Combination of Gravitational Waves, Gamma-Ray Bursts and Kilonovae from Neutron Star Mergers. *Universe*, 8(5):289, 2022.

[141] M. Bulla, S. A. Sim, and M. Kromer. Polarization spectral synthesis for Type Ia supernova explosion models. *Mon. Not. Roy. Astron. Soc.*, 450(1):967–981, 2015.

[142] A. Buonanno and T. Damour. Effective one-body approach to general relativistic two- body dynamics. *Phys. Rev.*, D59:084006, 1999.

[143] A. Buonanno and T. Damour. Transition from inspiral to plunge in binary black hole coalescences. *Phys. Rev.*, D62:064015, 2000.

[144] A. Buonanno et al. Comparison of post-Newtonian templates for compact binary inspiral signals in gravitational-wave detectors. *Phys. Rev. D*, 80:084043, 2009.

[145] E. M. Burbidge et al. Synthesis of the elements in stars. *Rev. Mod. Phys.*, 29:547–650, Oct 1957.

[146] M. Burgay et al. An Increased estimate of the merger rate of double neutron stars from observations of a highly relativistic system. *Nature*, 426:531–533, 2003.

[147] D. Bégué and J. M. Burgess. The anatomy of a long gamma-ray burst: A simple classification scheme for the emission mechanism(s). *Astrophys. J.*, 820(1):68, mar 2016.

[148] J. Calderón Bustillo, T. Dietrich, and P. D. Lasky. Higher-order gravitational-wave modes will allow for percent-level measurements of Hubble's constant with single binary neutron star merger observations. *Astrophys. J. Lett.*, 912(1):L10, 2021.

[149] T. A. Callister. Observed Gravitational-Wave Populations. 10 2024. arXiv:2410.19145 [astro-ph.HE].

[150] A. G. W. Cameron. Nuclear reactions in stars and nucleogenesis. *Publications of the Astronomical Society of the Pacific*, 69(408):201, jun 1957.

[151] A. G. W. Cameron. Some Nucleosynthesis Effects Associated with r-Process Jets. *Astrophys. J.*, 587(1):327–340, April 2003.

[152] M. Campanelli et al. Accurate Evolutions of Orbiting Black-Hole Binaries Without Excision. *Phys. Rev. Lett.*, 96:111101, 2006.

[153] C. D. Capano et al. Stringent constraints on neutron-star radii from multimessenger observations and nuclear theory. *Nature Astron.*, 4(6):625–632, 2020.

[154] A. Carbone et al. Self-consistent Green's functions formalism with three-body interactions. *Phys. Rev. C*, 88(5):054326, 2013.

[155] J. Carlson et al. Quantum Monte Carlo methods for nuclear physics. *Rev. Mod. Phys.*, 87:1067, 2015.

[156] M. F. Carney, L. E. Wade, and B. S. Irwin. Comparing two models for measuring the neutron star equation of state from gravitational-wave signals. *Phys. Rev. D*, 98(6):063004, 2018.

[157] S. M. Carroll. *Spacetime and Geometry: An Introduction to General Relativity.* Cambridge University Press, 7 2019.

[158] Z. Carson, A. W. Steiner, and K. Yagi. Constraining nuclear matter parameters with GW170817. *Phys. Rev. D*, 99(4):043010, 2019.

[159] J. Cehula, T. A Thompson, and B. D Metzger. Dynamics of baryon ejection in magnetar giant flares: implications for radio afterglows, r-process nucleosynthesis, and fast radio bursts. *Mon. Not. Roy. Astron. Soc.*, 528(3):5323–5345, 02 2024.

[160] E. Chabanat et al. A Skyrme parametrization from subnuclear to neutron star densities. 2. Nuclei far from stablities. *Nucl. Phys. A*, 635:231–256, 1998. [Erratum: Nucl.Phys.A 643, 441–441 (1998)].

[161] N. Chamel and P. Haensel. Physics of Neutron Star Crusts. *Living Rev. Rel.*, 11:10, 2008.

[162] H. S. Chan, M. C. Chu, and S. C. Leung. Accretion-induced Collapse of Dark Matter-admixed Rotating White Dwarfs: Dynamics and Gravitational-wave Signals. *Astrophys. J.*, 945(2):133, 2023.

[163] S. Chandrasekhar and E. A. Milne. The highly collapsed configurations of a stellar mass. *Mon. Not. Roy. Astron. Soc.*, 91(5):456–466, 03 1931.

[164] D. Chatterjee et al. Cosmology with Love: Measuring the Hubble constant using neutron star universal relations. *Phys. Rev. D*, 104(8):083528, 2021.

[165] K. Chatziioannou. Neutron star tidal deformability and equation of state constraints. *Gen. Rel. Grav.*, 52(11):109, 2020.

[166] K. Chatziioannou et al. Neutron stars and the dense matter equation of state: from microscopic theory to macroscopic observations. 7 2024. arXiv:2407.11153 [nucl-th].

[167] Katerina Chatziioannou. Uncertainty limits on neutron star radius measurements with gravitational waves. *Phys. Rev. D*, 105(8):084021, 2022.

[168] C. R. Chen and C. S. Nugroho. Detection prospects of dark matter in the Einstein Telescope. *Phys. Rev. D*, 105(8):083001, 2022.

[169] H. Y. Chen. Systematic Uncertainty of Standard Sirens from the Viewing Angle of Binary Neutron Star Inspirals. *Phys. Rev. Lett.*, 125(20):201301, 2020.

[170] H. Y. Chen, M. Fishbach, and D. E. Holz. A two per cent Hubble constant measurement from standard sirens within five years. *Nature*, 562(7728):545–547, 2018.

[171] H. Y. Chen, C. Talbot, and E. A. Chase. Mitigating the Counterpart Selection Effect for Standard Sirens. *Phys. Rev. Lett.*, 132(19):191003, 2024.

[172] W. X. Chen and A. M. Beloborodov. Neutrino-Cooled Accretion Disks around Spinning Black Hole. *Astrophys. J.*, 657:383–399, 2007.

[173] H. S. Chia. Tidal deformation and dissipation of rotating black holes. *Phys. Rev. D*, 104(2):024013, 2021.

[174] R. Chornock et al. The Electromagnetic Counterpart of the Binary Neutron Star Merger LIGO/VIRGO GW170817. IV. Detection of Near-infrared Signatures of r-process Nucleosynthesis with Gemini-South. *Astrophys. J. Lett.*, 848(2):L19, 2017.

[175] D. Clowe, A. Gonzalez, and M. Markevitch. Weak lensing mass reconstruction of the interacting cluster 1E0657-558: Direct evidence for the existence of dark matter. *Astrophys. J.*, 604:596–603, 2004.

[176] M. Coleman Miller and N. Yunes. The new frontier of gravitational waves. *Nature*, 568(7753):469–476, 2019.

[177] MUSES collaboration. A visualization of the interior of a neutron star from the muses collaboration. Available at: `https://physics.illinois.edu/research/highlights/neutronstars`. (accessed: 4.1.2025).

[178] A. Colombo et al. Multi-messenger Observations of Binary Neutron Star Mergers in the O4 Run. *Astrophys. J.*, 937(2):79, 2022.

[179] A. Colombo et al. Multi-messenger observations in the Einstein Telescope era: binary neutron star and black hole - neutron star mergers. 2 2025. arXiv:2503.00116 [astro-ph.HE].

[180] M. Colpi et al. LISA Definition Study Report. 2 2024. arXiv:2402.07571 [astro-ph.CO].

[181] M. W. Coughlin et al. Toward Rapid Transient Identification and Characterization of Kilonovae. *Astrophys. J.*, 849(1):12, 2017.

[182] M. W. Coughlin et al. Constraints on the neutron star equation of state from AT2017gfo using radiative transfer simulations. *Mon. Not. Roy. Astron. Soc.*, 480(3):3871–3878, 2018.

[183] M. W. Coughlin et al. Multimessenger Bayesian parameter inference of a binary neutron star merger. *Mon. Not. Roy. Astron. Soc.*, 489(1):L91–L96, 2019.

[184] M. W. Coughlin et al. On standardizing kilonovae and their use as standard candles to measure the Hubble constant. *Phys. Rev. Research.*, 2:022006, 2020.

[185] D. A. Coulter et al. Swope Supernova Survey 2017a (SSS17a), the Optical Counterpart to a Gravitational Wave Source. *Science*, 2017. [Science358,1556(2017)].

[186] D. A. Coulter, R. J. Foley, C. D. Kilpatrick, et al. Swope supernova survey 2017a (SSS17a), the optical counterpart to a gravitational wave source. *Science*, 358(6370):1556–1558, oct 2017.

[187] H. T. Cromartie et al. Relativistic Shapiro delay measurements of an extremely massive millisecond pulsar. *Nature Astron.*, 4(1):72–76, 2019.

[188] L. Dai, T. Venumadhav, and B. Zackay. Parameter Estimation for GW170817 using Relative Binning. *arXiv: 1806.08793*, 2018.

[189] Z. G. Dai and T. Lu. Gamma-ray burst afterglows and evolution of postburst fireballs with energy injection from strongly magnetic millisecond pulsars. *Astronomy & Astrophysics*, 333:L87, 1998.

[190] T. Damour, B. R. Iyer, and B. S. Sathyaprakash. Improved filters for gravitational waves from inspiralling compact binaries. *Phys. Rev. D*, 57:885–907.

[191] T. Damour, P. Jaranowski, and G. Schaefer. On the determination of the last stable orbit for circular general relativistic binaries at the third postNewtonian approximation. *Phys. Rev. D*, 62:084011, 2000.

[192] T. Damour, P. Jaranowski, and G. Schäfer. Dimensional regularization of the gravitational interaction of point masses. *Physics Letters B*, 513(1-2):147–155, jul 2001.

[193] T. Damour and A. Nagar. Relativistic tidal properties of neutron stars. *Phys. Rev. D*, 80(8), oct 2009.

[194] T. Damour and A. Nagar. Effective One Body description of tidal effects in inspiralling compact binaries. *Phys. Rev. D*, 81:084016, 2010.

[195] T. Damour, A. Nagar, and L. Villain. Measurability of the tidal polarizability of neutron stars in late-inspiral gravitational-wave signals. *Phys. Rev. D*, 85:123007, 2012.

[196] P. Danielewicz, R. Lacey, and W. G. Lynch. Determination of the equation of state of dense matter. *Science*, 298:1592–1596, 2002.

[197] A. Das, T. Malik, and A. C. Nayak. Dark matter admixed neutron star properties in light of gravitational wave observations: A two fluid approach. *Phys. Rev. D*, 105(12):123034, 2022.

[198] B. Dasgupta, R. Laha, and A. Ray. Low Mass Black Holes from Dark Core Collapse. *Phys. Rev. Lett.*, 126(14):141105, 2021.

[199] B. D. Day. Nuclear Saturation and Nuclear Forces. *Comments Nucl. Part. Phys.*, 11(3):115–126, 1983.

[200] S. De et al. Tidal Deformabilities and Radii of Neutron Stars from the Observation of GW170817. *Phys. Rev. Lett.*, 121(9):091102, 2018.

[201] A. de Lavallaz and M. Fairbairn. Neutron Stars as Dark Matter Probes. *Phys. Rev. D*, 81:123521, 2010.

[202] A. Del Popolo, M. Le Delliou, and M. Deliyergiyev. Neutron Stars and Dark Matter. *Universe*, 6(12):222, 2020.

[203] W. Del Pozzo. Inference of cosmological parameters from gravitational waves: Applications to second generation interferometers. *Phys. Rev. D*, 86:043011, Aug 2012.

[204] W. Del Pozzo et al. Demonstrating the feasibility of probing the neutron star equation of state with second-generation gravitational wave detectors. *Phys. Rev. Lett.*, 111(7):071101, 2013.

[205] M. Deliyergiyev et al. Dark compact objects: an extensive overview. *Phys. Rev. D*, 99(6):063015, 2019.

[206] P. Demorest et al. Shapiro Delay Measurement of A Two Solar Mass Neutron Star. *Nature*, 467:1081–1083, 2010.

[207] L. Dessart et al. Neutrino signatures and the neutrino-driven wind in Binary Neutron Star Mergers. *Astrophys.J.*, 690:1681, 2009.

[208] S. Detweiler. Pulsar timing measurements and the search for gravitational waves. *Astrophys. J.*, 234:1100–1104, December 1979.

[209] A. Dhani et al. Systematic Biases in Estimating the Properties of Black Holes Due to Inaccurate Gravitational-Wave Models. April 2024. arXiv:2404.05811 [gr-qc].

[210] T. Dietrich, S. Bernuzzi, and W. Tichy. Closed-form tidal approximants for binary neutron star gravitational waveforms constructed from high-resolution numerical relativity simulations. *Phys. Rev. D*, 96(12):121501, 2017.

[211] T. Dietrich et al. Gravitational waves and mass ejecta from binary neutron star mergers: Effect of the stars' rotation. *Phys. Rev. D*, 95(4):044045, 2017.

[212] T. Dietrich et al. Improving the NRTidal model for binary neutron star systems. *Phys. Rev. D*, 100(4):044003, 2019.

[213] T. Dietrich et al. Matter imprints in waveform models for neutron star binaries: Tidal and self-spin effects. *Phys. Rev. D*, 99(2):024029, 2019.

[214] T. Dietrich et al. Multimessenger constraints on the neutron-star equation of state and the Hubble constant. *Science*, 370(6523):1450–1453, 2020.

[215] T. Dietrich and T. Hinderer. Comprehensive comparison of numerical relativity and effective-one-body results to inform improvements in waveform models for binary neutron star systems. *Phys. Rev. D*, 95(12):124006, 2017.

[216] T. Dietrich, T. Hinderer, and A. Samajdar. Interpreting binary neutron star mergers: describing the binary neutron star dynamics, modelling gravitational waveforms, and analyzing detections. *General Relativity and Gravitation*, 53(3), mar 2021.

[217] T. Dietrich and M. Ujevic. Modeling dynamical ejecta from binary neutron star mergers and implications for electromagnetic counterparts. *Class. Quant. Grav.*, 34(10):105014, 2017.

[218] N. Domoto et al. Lanthanide Features in Near-infrared Spectra of Kilonovae. *Astrophys. J.*, 939(1):8, 2022.

[219] F. Douchin and P. Haensel. A unified equation of state of dense matter and neutron star structure. *Astronomy & Astrophysics*, 380:151–167, 2001.

[220] G. Drenkhahn and H. C. Spruit. Efficient acceleration and radiation in poynting flux powered grb outflows. *Astronomy & Astrophysics*, 391(3):1141–1153, 2002.

[221] C. Drischler et al. How Well Do We Know the Neutron-Matter Equation of State at the Densities Inside Neutron Stars? A Bayesian Approach with Correlated Uncertainties. *Phys. Rev. Lett.*, 125(20):202702, 2020.

[222] C. Drischler et al. Quantifying uncertainties and correlations in the nuclear-matter equation of state. *Phys. Rev. C*, 102(5):054315, 2020.

[223] C. Drischler, K. Hebeler, and A. Schwenk. Chiral interactions up to next-to-next-to-next-to-leading order and nuclear saturation. *Phys. Rev. Lett.*, 122(4):042501, 2019.

[224] M. R. Drout et al. Light Curves of the Neutron Star Merger GW170817/SSS17a: Implications for R-Process Nucleosynthesis. *Science*, 358:1570–1574, 2017.

[225] R. Dudi et al. Relevance of tidal effects and post-merger dynamics for binary neutron star parameter estimation. *Phys. Rev. D*, 98(8):084061, 2018.

[226] U. Dupletsa et al. Validating prior-informed Fisher-matrix analyses against GWTC data. *Phys. Rev. D*, 111(2):024036, 2025.

[227] R. B. Duran, M. B. Leng, and D. Giannios. An anisotropic minijets model for the GRB prompt emission. *Mon. Not. Roy. Astron. Soc.*, 455(1):L6–L10, 2016.

[228] W. E. East et al. Binary neutron star mergers: Effects of spin and post-merger dynamics. *Phys. Rev. D*, 100(12):124042, 2019.

[229] D. Eichler et al. Nucleosynthesis, Neutrino Bursts and Gamma-Rays from Coalescing Neutron Stars. *Nature*, 340:126–128, 1989.

[230] A. Einstein. Kosmologische Betrachtungen zur allgemeinen Relativitätstheorie. *Sitzungsberichte der Königlich Preussischen Akademie der Wissenschaften*, pages 142–152, January 1917.

[231] A. Einstein. Die Grundlage der allgemeinen Relativitätstheorie. *Annalen der Physik*, 354(7):768–822, 2016.

[232] A. Einstein. Näherunsgweise Integration der Feldgleichungen der Gravitation. *Sitzungsberichte der Königlich Preussischen Akademie der Wissenschaften Berlin*, 1:688–696, 2016.

[233] A. Ekström et al. Δ isobars and nuclear saturation. *Phys. Rev. C*, 97(2):024332, 2018.

[234] J. Ellis et al. Search for Dark Matter Effects on Gravitational Signals from Neutron Star Mergers. *Phys. Lett. B*, 781:607–610, 2018.

[235] M. Emma. Numerical Simulations of Dark Matter Admixed Neutron Star Binaries. *Particles*, 5(3):273–286, 2022.

[236] E. Epelbaum, H. W. Hammer, and U. G. Meissner. Modern Theory of Nuclear Forces. *Rev. Mod. Phys.*, 81:1773–1825, 2009.

[237] E. Epelbaum, H. Krebs, and U. G. Meißner. Improved chiral nucleon-nucleon potential up to next-to-next-to-next-to-leading order. *Eur. Phys. J. A*, 51(5):53, 2015.

[238] A. L. Erickcek and K. Sigurdson. Reheating Effects in the Matter Power Spectrum and Implications for Substructure. *Phys. Rev. D*, 84:083503, 2011.

[239] R. Essick et al. Direct Astrophysical Tests of Chiral Effective Field Theory at Supranuclear Densities. *Phys. Rev. C*, 102(5):055803, 2020.

[240] R. Essick, P. Landry, and D. E. Holz. Nonparametric Inference of Neutron Star Composition, Equation of State, and Maximum Mass with GW170817. *Phys. Rev. D*, 101(6):063007, 2020.

[241] M. Evans et al. A Horizon Study for Cosmic Explorer: Science, Observatories, and Community. 9 2021.

[242] P. A. Evans et al. Swift and NuSTAR observations of GW170817: detection of a blue kilonova. *Science*, 358:1565, 2017.

[243] J. M. Ezquiaga and D. E. Holz. Spectral sirens: Cosmology from the full mass distribution of compact binaries. *Phys. Rev. Let.*, 129(6), Aug 2022.

[244] W. M. Farr et al. The mass distribution of stellar-mass black holes. *Astrophys. J.*, 741(2):103, oct 2011.

[245] W. M. Farr et al. A Future Percent-Level Measurement of the Hubble Expansion at Redshift 0.8 With Advanced LIGO. *Astrophys. J. Lett.*, 883(2):L42, 2019.

[246] M. Favata. Systematic parameter errors in inspiraling neutron star binaries. *Phys. Rev. Lett.*, 112:101101, 2014.

[247] S. M. Feeney et al. Prospects for resolving the Hubble constant tension with standard sirens. *Phys. Rev. Lett.*, 122(6):061105, 2019.

[248] S. M. Feeney et al. Prospects for Measuring the Hubble Constant with Neutron-Star–Black-Hole Mergers. *Phys. Rev. Lett.*, 126(17):171102, 2021.

[249] R. Fernández and B. D. Metzger. Electromagnetic Signatures of Neutron Star Mergers in the Advanced LIGO Era. *Ann. Rev. Nucl. Part. Sci.*, 66:23–45, 2016.

[250] D. F. Figer. An Upper limit to the masses of stars. *Nature*, 434:192, 2005.

[251] D. Finstad, L. V. White, and D. A. Brown. Prospects for a Precise Equation of State Measurement from Advanced LIGO and Cosmic Explorer. *Astrophys. J.*, 955(1):45, 2023.

[252] M. Fishbach et al. A Standard Siren Measurement of the Hubble Constant from GW170817 without the Electromagnetic Counterpart. *Astrophys. J. Let.*, 871(1):L13, 2019.

[253] E. E. Flanagan and T. Hinderer. Constraining neutron star tidal Love numbers with gravitational wave detectors. *Phys.Rev.*, D77:021502, 2008.

[254] W. F. Fong et al. The Afterglow and Early-Type Host Galaxy of the Short GRB 150101B at $z = 0.1343$. *Astrophys. J.*, 833(2):151, 2016.

[255] W. F. Fong et al. The Optical Afterglow of GW170817: An Off-axis Structured Jet and Deep Constraints on a Globular Cluster Origin. *Astrophys. J. Lett.*, 883(1):L1, 2019.

[256] E. Fonseca et al. Refined Mass and Geometric Measurements of the High-mass PSR J0740+6620. *Astrophys. J. Lett.*, 915(1):L12, 2021.

[257] F. Foucart et al. First direct comparison of non-disrupting neutron star-black hole and binary black hole merger simulations. *Phys. Rev. D*, 88:064017, 2013.

[258] F. Foucart et al. Dynamical ejecta from precessing neutron star-black hole mergers with a hot, nuclear-theory based equation of state. *Class. Quant. Grav.*, 34(4):044002, 2017.

[259] F. Foucart, T. Hinderer, and S. Nissanke. Remnant baryon mass in neutron star-black hole mergers: Predictions for binary neutron star mimickers and rapidly spinning black holes. *Phys. Rev. D*, 98(8), Oct 2018.

[260] G. Fragione. Black-hole–Neutron-star Mergers Are Unlikely Multimessenger Sources. *Astrophys. J. Let.*, 923(1):L2, 2021.

[261] W. L. Freedman et al. The Carnegie-Chicago Hubble Program. VIII. An Independent Determination of the Hubble Constant Based on the Tip of the Red Giant Branch. *Astrophys. J.*, 882:34, 2019.

[262] C. Freiburghaus, S. Rosswog, and F.-K. Thielemann. r-process in neutron star mergers. *Astrophys. J.*, 525(2):L121, oct 1999.

[263] A. Freise et al. Triple Michelson Interferometer for a Third-Generation Gravitational Wave Detector. *Class. Quant. Grav.*, 26:085012, 2009.

[264] A. Friedmann. Über die Krümmung des Raumes. *Zeitschrift für Physik*, 10:377–386, January 1922.

[265] S. Fujibayashi et al. Comprehensive Study of Mass Ejection and Nucleosynthesis in Binary Neutron Star Mergers Leaving Short-lived Massive Neutron Stars. *Astrophys. J.*, 942(1):39, 2023.

[266] J. R. Gair et al. The Hitchhiker's Guide to the Galaxy Catalog Approach for Dark Siren Gravitational-wave Cosmology. *Astron. J.*, 166(1):22, 2023.

[267] S. Galaudage et al. Heavy Double Neutron Stars: Birth, Midlife, and Death. *Astrophys. J. Lett.*, 909(2):L19, 2021.

[268] R. Gamba and S. Bernuzzi. Resonant tides in binary neutron star mergers: Analytical-numerical relativity study. *Phys. Rev. D*, 107(4):044014, 2023.

[269] R. Gamba et al. Waveform systematics in the gravitational-wave inference of tidal parameters and equation of state from binary neutron-star signals. *Phys. Rev. D*, 103(12), jun 2021.

[270] S. Gandolfi, J. Carlson, and S. Reddy. The maximum mass and radius of neutron stars and the nuclear symmetry energy. *Phys. Rev. C*, 85:032801, 2012.

[271] S. Gandolfi et al. From the microscopic to the macroscopic world: from nucleons to neutron stars. *J. Phys. G*, 46(10):103001, 2019.

[272] H. Gao, W. H. Lei, and Z. P. Zhu. GRB 211211A: a Prolonged Central Engine under a Strong Magnetic Field Environment. *Astrophys. J. Let.*, 934(1):L12, 2022.

[273] C. García-Quirós et al. Multimode frequency-domain model for the gravitational wave signal from nonprecessing black-hole binaries. *Phys. Rev. D*, 102(6):064002, 2020.

[274] N. Gehrels et al. Correlations of Prompt and Afterglow Emission in Swift Long and Short Gamma Ray Bursts. *Astrophys. J.*, 689:1161, 2008.

[275] N. Gehrels, L. Piro, and P. J. T. Leonard. The brightest explosions in the universe. Available at: `https://personal.science.psu.edu/wnb3/astro130/articles/gehrels-GRBs-sciam-2002.pdf`. (accessed: 11.2.2025).

[276] B. Gendre. A Review of Long-Lasting Activities of the Central Engine of Gamma-Ray Bursts. *Galaxies*, 13(1):7, 2025.

[277] D. Gerosa, G. Pratten, and A. Vecchio. Gravitational-wave selection effects using neural-network classifiers. *Phys. Rev. D*, 102(10):103020, 2020.

[278] A. Gezerlis et al. Quantum Monte Carlo Calculations with Chiral Effective Field Theory Interactions. *Phys. Rev. Let.*, 111(3):032501, 2013.

[279] A. Gezerlis et al. Local chiral effective field theory interactions and quantum Monte Carlo applications. *Phys. Rev. C*, 90(5):054323, 2014.

[280] B. Giacomazzo and L. Rezzolla. WhiskyMHD: a new numerical code for general relativistic magnetohydrodynamics. *Class. Quant. Grav.*, 24:S235–S258, 2007.

[281] E. Giangrandi et al. The Effects of Self-interacting Bosonic Dark Matter on Neutron Star Properties. *Astrophys. J.*, 953(1):115, 2023.

[282] A. Goldstein et al. An Ordinary Short Gamma-Ray Burst with Extraordinary Implications: Fermi-GBM Detection of GRB 170817A. *Astrophys. J.*, 848(2):L14, 2017.

[283] B. P. Gompertz et al. The case for a minute-long merger-driven gamma-ray burst from fast-cooling synchrotron emission. *Nature Astron.*, 7(1):67–79, 2023.

[284] B. Grace, K. Wette, and S. M. Scott. Gravitational wave searches for postmerger remnants of GW170817 and GW190425. *Phys. Rev. D*, 110(8):083016, 2024.

[285] G. Grams et al. *Phys. Rev. C*, 105:035806, Mar 2022.

[286] J. Granot and T. Piran. On the lateral expansion of GRB jets. *Mon. Not. Roy. Astron. Soc.*, 421:570–587, 2012.

[287] R. Gray et al. Cosmological inference using gravitational wave standard sirens: A mock data analysis. *Phys. Rev. D*, 101(12):122001, 2020.

[288] R. Gray et al. Joint cosmological and gravitational-wave population inference using dark sirens and galaxy catalogues. *JCAP*, 12:023, 2023.

[289] R. Gray, C. Messenger, and J. Veitch. A pixelated approach to galaxy catalogue incompleteness: improving the dark siren measurement of the Hubble constant. *Mon. Not. Roy. Astron. Soc.*, 512(1):1127–1140, 02 2022.

[290] S. K. Greif et al. Equation of state sensitivities when inferring neutron star and dense matter properties. *Mon. Not. Roy. Astron. Soc.*, 485(4):5363–5376, 2019.

[291] C. Guidorzi et al. Improved Constraints on H_0 from a Combined Analysis of Gravitational-wave and Electromagnetic Emission from GW170817. *Astrophys. J. Lett.*, 851(2):L36, 2017.

[292] G. Hagen et al. Coupled-cluster calculations of nucleonic matter. *Phys. Rev. C*, 89(1):014319, 2014.

[293] A. Hajela et al. Two Years of Nonthermal Emission from the Binary Neutron Star Merger GW170817: Rapid Fading of the Jet Afterglow and First Constraints on the Kilonova Fastest Ejecta. *Astrophys. J. Let.*, 886(1):L17, 2019.

[294] A. Hajela et al. Evidence for X-Ray Emission in Excess to the Jet-afterglow Decay 3.5 yr after the Binary Neutron Star Merger GW 170817: A New Emission Component. *Astrophys. J. Lett.*, 927(1):L17, 2022.

[295] G. Halevi and P. Mösta. r-Process Nucleosynthesis from Three-dimensional Jet-driven Core-Collapse Supernovae with Magnetic Misalignments. *Mon. Not. Roy. Astron. Soc.*, 477(2):2366–2375, 2018.

[296] W. J. Handley, M. P. Hobson, and A. N. Lasenby. PolyChord: nested sampling for cosmology. *Mon. Not. Roy. Astron. Soc.*, 450(1):L61–L65, 2015.

[297] M. Hannam. Simple model of complete precessing black-hole-binary gravitational waveforms. *Phys. Rev. Let.*, 113(15), oct 2014.

[298] I. Harry and T. Hinderer. Observing and measuring the neutron-star equation-of-state in spinning binary neutron star systems. *Class. Quant. Grav.*, 35(14):145010, 2018.

[299] W. K. Hastings. Monte carlo sampling methods using markov chains and their applications. *Biometrika*, 57(1):97–109, 04 1970.

[300] K. Hebeler et al. Equation of state and neutron star properties constrained by nuclear physics and observation. *Astrophys. J.*, 773:11, 2013.

[301] K. Hebeler and A. Schwenk. Chiral three-nucleon forces and neutron matter. *Phys. Rev. C*, 82:014314, 2010.

[302] A. Heger, B. Müller, and I. Mandel. Chapter 3: Black Holes as the End State of Stellar Evolution: Theory and Simulations. pages 61–111.

[303] J. Heinzel et al. Comparing inclination dependent analyses of kilonova transients. *Mon. Not. Roy. Astron. Soc.*, 502(2):3057–3065, 2021.

[304] A. Henkel. Study of the agreement between binary neutron star ejecta models derived from numerical relativity simulations. *Phys. Rev. D*, 107(6):063028, 2023.

[305] Q. Henry, G. Faye, and L. Blanchet. Tidal effects in the gravitational-wave phase evolution of compact binary systems to next-to-next-to-leading post-Newtonian order. *Phys. Rev. D*, 102(4):044033, 2020.

[306] S. Hild et al. A Xylophone Configuration for a third Generation Gravitational Wave Detector. *Class. Quant. Grav.*, 27:015003, 2010.

[307] S. Hild et al. Sensitivity Studies for Third-Generation Gravitational Wave Observatories. *Class. Quant. Grav.*, 28:094013, 2011.

[308] T. Hinderer. Tidal Love numbers of neutron stars. *Astrophys. J.*, 677:1216–1220, 2008.

[309] T. Hinderer et al. Tidal deformability of neutron stars with realistic equations of state and their gravitational wave signatures in binary inspiral. *Phys. Rev. D*, 81(12), jun 2010.

[310] T. Hinderer et al. Effects of neutron-star dynamic tides on gravitational waveforms within the effective-one-body approach. *Phys. Rev. Let.*, 116(18):181101, 2016.

[311] T. Hinderer et al. Distinguishing the nature of comparable-mass neutron star binary systems with multimessenger observations: GW170817 case study. *Phys. Rev. D*, 100(6):06321, 2019.

[312] J. W. Holt and N. Kaiser. Equation of state of nuclear and neutron matter at third-order in perturbation theory from chiral effective field theory. *Phys. Rev. C*, 95(3):034326, 2017.

[313] K. Hotokezaka, P. Beniamini, and T. Piran. Neutron Star Mergers as sites of r-process Nucleosynthesis and Short Gamma-Ray Bursts. *Int. J. Mod. Phys. D*, 27(13):1842005, 2018.

[314] K. Hotokezaka et al. The mass ejection from the merger of binary neutron stars. *Phys. Rev. D*, 87:024001, 2013.

[315] K. Hotokezaka et al. Exploring tidal effects of coalescing binary neutron stars in numerical relativity. II. Long-term simulations. *Phys. Rev.*, D91(6):064060, 2015.

[316] K. Hotokezaka et al. Radioactive decay products in neutron star merger ejecta: heating efficiency and γ-ray emission. *Mon. Not. Roy. Astron. Soc.*, 459(1):35–43, 2016.

[317] K. Hotokezaka et al. A Hubble constant measurement from superluminal motion of the jet in GW170817. *Nature Astron.*, 2019.

[318] J. P. Hu and F. Y. Wang. Hubble Tension: The Evidence of New Physics. *Universe*, 9(2):94, 2023.

[319] Y. W. Huang et al. Impact of calibration uncertainties on Hubble constant measurements from gravitational-wave sources. *Phys. Rev. D*, 111(6):063034, 2025.

[320] E. P. Hubble. A relation between distance and radial velocity among extra-galactic nebulae. *Proceedings of the National Academy of Sciences of the United States of America*, (15):167–68, 1929.

[321] R. A. Hulse and J. H. Taylor. Discovery of a pulsar in a binary system. *Astrophys.J.*, 195:L51–L53, 1975.

[322] S. Husa et al. Frequency-domain gravitational waves from nonprecessing black-hole binaries. I. New numerical waveforms and anatomy of the signal. *Phys. Rev. D*, 93(4):044006, 2016.

[323] L. Huth et al. Analyzing the Fierz Rearrangement Freedom for Local Chiral Two-Nucleon Potentials. *Phys. Rev. C*, 96(5):054003, 2017.

[324] S. Huth et al. Constraining Neutron-Star Matter with Microscopic and Macroscopic Collisions. *Nature*, 606:276–280, 2022.

[325] F. Iacovelli et al. Forecasting the Detection Capabilities of Third-generation Gravitational-wave Detectors Using GWFAST. *Astrophys. J.*, 941(2):208, 2022.

[326] F. Iacovelli et al. GWFAST: A Fisher Information Matrix Python Code for Third-generation Gravitational-wave Detectors. *Astrophys. J. Supp.*, 263(1):2, 2022.

[327] F. Iacovelli et al. Nuclear physics constraints from binary neutron star mergers in the Einstein Telescope era. *Phys. Rev. D*, 108(12):122006, 2023.

[328] O. Ivanytskyi, V. Sagun, and I. Lopes. Neutron stars: New constraints on asymmetric dark matter. *Phys. Rev. D*, 102(6):063028, 2020.

[329] A. Jan et al. Accuracy limitations of existing numerical relativity waveforms on the data analysis of current and future ground-based detectors. *Phys. Rev. D*, 110(2):024023, 2024.

[330] G. B. Jeffery. The Field of an Electron on Einstein's Theory of Gravitation. *Proceedings of the Royal Society of London Series A*, 99(697):123–134, May 1921.

[331] H. Jeffreys. *Theory of Probability.* Oxford University Press, 1961.

[332] K. S. Jeong, L. McLerran, and S. Sen. Dynamically generated momentum space shell structure of quarkyonic matter via an excluded volume model. *Phys. Rev. C*, 101(3):035201, 2020.

[333] X. Jiménez Forteza et al. Impact of high-order tidal terms on binary neutron-star waveforms. *Phys. Rev. D*, 98(12):124014, 2018.

[334] S. J. Jin et al. Prospects for measuring the Hubble constant and dark energy using gravitational-wave dark sirens with neutron star tidal deformation. *JCAP*, 08:070, 2023.

[335] Z. P. Jin et al. The Light Curve of the Macronova Associated With the Long–short Burst GRB 060614. *Astrophys. J. Let.*, 811(2):L22, 2015.

[336] Z. P. Jin et al. Short GRBs: opening angles, local neutron star merger rate and off-axis events for GRB/GW association. *Astrophys. J.*, 857(2):128, 2018.

[337] Z. P. Jin et al. A kilonova associated with GRB 070809. *Nature Astron.*, 4:77–82, 2020.

[338] C. Jockel and L. Sagunski. Fermion Proca Stars: Vector Dark Matter Admixed Neutron Stars. *Particles*, 7(1):52–79, 2024.

[339] D. Kagan et al. Relativistic Magnetic Reconnection in Pair Plasmas and Its Astrophysical Applications. *Space Science Reviews*, 191(1-4):545–573, October 2015.

[340] J. D. Kaplan et al. The Influence of Thermal Pressure on Equilibrium Models of Hypermassive Neutron Star Merger Remnants. *Astrophys. J.*, 790:19, 2014.

[341] D. Karkevandi et al. Bosonic dark matter in neutron stars and its effect on gravitational wave signal. *Phys. Rev. D*, 105(2):023001, 2022.

[342] D. Kasen et al. Origin of the heavy elements in binary neutron-star mergers from a gravitational wave event. *Nature, 10.1038/nature24453*, 2017.

[343] D. Kasen, R. C. Thomas, and P. Nugent. Time Dependent Monte Carlo Radiative Transfer Calculations For 3-Dimensional Supernova Spectra, Lightcurves, and Polarization. *Astrophys. J.*, 651:366–380, 2006.

[344] M. M. Kasliwal et al. Infrared emission from kilonovae: the case of the nearby short hard burst GRB 160821B. *Astrophys. J. Let.*, 843(2):L34, 2017.

[345] M. M. Kasliwal et al. Spitzer mid-infrared detections of neutron star merger GW170817 suggests synthesis of the heaviest elements. *Mon. Not. Roy. Astron. Soc.*, 510(1):L7–L12, 2022.

[346] R. E. Kass and A. E. Raftery. Bayes factors. *Journal of the American Statistical Association*, 90(430):773–795, 1995.

[347] K. Kawaguchi et al. Frequency-domain gravitational waveform models for inspiraling binary neutron stars. *Phys. Rev. D*, 97(4):044044, 2018.

[348] J. Keller et al. Neutron matter at finite temperature based on chiral effective field theory interactions. *Phys. Rev. C*, 103(5):055806, 2021.

[349] S. Khan et al. Frequency-domain gravitational waves from nonprecessing black-hole binaries. II. a phenomenological model for the advanced detector era. *Phys. Rev. D*, 93(4), feb 2016.

[350] L. Kidder, H. Pfeiffer, and M. Scheel. Spectral einstein code. Available at: `https://www.black-holes.org/code/SpEC.html#introduction`.

[351] L. E. Kidder et al. SpECTRE: A Task-based Discontinuous Galerkin Code for Relativistic Astrophysics. *J. Comput. Phys.*, 335:84–114, 2017.

[352] C. D. Kilpatrick et al. Electromagnetic Evidence that SSS17a is the Result of a Binary Neutron Star Merger. *Science*, 358(6370):1583–1587, 2017.

[353] R. Kippenhahn, A. Weigert, and A. Weiss. *Stellar Structure and Evolution*. Springer Berlin, Heidelberg, 2012.

[354] S. Knirck et al. First Results from a Broadband Search for Dark Photon Dark Matter in the 44 to 52 μeV Range with a Coaxial Dish Antenna. *Phys. Rev. Let.*, 132(13):131004, 2024.

[355] S. Kobayashi and B. Zhang. GRB 021004: reverse shock emission. *Astrophys. J.*, 582(2):L75, 2002.

[356] H. Koehn et al. Impact of dark matter on tidal signatures in neutron star mergers with the Einstein Telescope. *Phys. Rev. D*, 110(10):103033, 2024.

[357] H. Koehn et al. From existing and new nuclear and astrophysical constraints to stringent limits on the equation of state of neutron-rich dense matter. *Phys. Rev. X*, 15(2):021014, 2025.

[358] K. D. Kokkotas and G. Schäfer. Tidal and tidal resonant effects in coalescing binaries. *Mon. Not. Roy. Astron. Soc.*, 275:301, 1995.

[359] O. Komoltsev et al. Equation of state at neutron-star densities and beyond from perturbative QCD. *Phys. Rev. D*, 109(9):094030, 2024.

[360] O. Komoltsev and A. Kurkela. How Perturbative QCD Constrains the Equation of State at Neutron-Star Densities. *Phys. Rev. Let.*, 128(20):202701, 2022.

[361] A. Konstantinou. The Effect of a Dark Matter Core on the Structure of a Rotating Neutron Star. *Astrophys. J.*, 968(2):83, 2024.

[362] C. Kouvaris and P. Tinyakov. Constraining Asymmetric Dark Matter through observations of compact stars. *Phys. Rev. D*, 83:083512, 2011.

[363] L. Kreidberg et al. Mass Measurements of Black Holes in X-Ray Transients: Is There a Mass Gap? *Astrophys. J.*, 757:36, 2012.

[364] C. J. Krüger and F. Foucart. Estimates for Disk and Ejecta Masses Produced in Compact Binary Mergers. *Phys. Rev. D*, 101(10):103002, 2020.

[365] T. Krüger et al. Neutron matter from chiral effective field theory interactions. *Phys. Rev. C*, 88:025802, 2013.

[366] S. R. Kulkarni. Modeling supernova-like explosions associated with gamma-ray bursts with short durations. 2005.

[367] A. Kumar et al. Magnetars as powering sources of gamma-ray burst associated supernovae, and unsupervized clustering of cosmic explosions. *Mon. Not. Roy. Astron. Soc.*, 531(3):3297–3309, 2024.

[368] P. Kumar, M. Pürrer, and H. P. Pfeiffer. Measuring neutron star tidal deformability with Advanced LIGO: a Bayesian analysis of neutron star - black hole binary observations. *Phys. Rev. D*, 95(4):044039, 2017.

[369] P. Kumar and B. Zhang. The physics of gamma-ray bursts & relativistic jets. *Phys. Rept.*, 561:1–109, 2014.

[370] N. Kunert et al. Quantifying modeling uncertainties when combining multiple gravitational-wave detections from binary neutron star sources. *Phys. Rev. D*, 105(6):L061301, 2022.

[371] A. Kurkela et al. Constraining neutron star matter with Quantum Chromodynamics. *Astrophys. J.*, 789:127, 2014.

[372] T. Kuroda et al. Magnetorotational explosion of a massive star supported by neutrino heating in general relativistic three-dimensional simulations. *Astrophys. J.*, 896(2):102, jun 2020.

[373] K. Kyutoku, K. Ioka, and M. Shibata. Anisotropic mass ejection from black hole-neutron star binaries: Diversity of electromagnetic counterparts. *Phys. Rev. D*, 88(4):041503, 2013.

[374] B. D. Lackey et al. Extracting equation of state parameters from black hole-neutron star mergers: aligned-spin black holes and a preliminary waveform model. *Phys. Rev. D*, 89:043009, 2014.

[375] B. D. Lackey et al. Surrogate model for an aligned-spin effective one body waveform model of binary neutron star inspirals using Gaussian process regression. *Phys. Rev. D*, 100(2):024002, 2019.

[376] B. D. Lackey and L. Wade. Reconstructing the neutron-star equation of state with gravitational-wave detectors from a realistic population of inspiralling binary neutron stars. *Phys. Rev. D*, 91(4):043002, 2015.

[377] D. Lai. Resonant oscillations and tidal heating in coalescing binary neutron stars. *Mon. Not. Roy. Astron. Soc.*, 270(3):611–629, 10 1994.

[378] G. P. Lamb et al. Short GRB 160821B: a reverse shock, a refreshed shock, and a well-sampled kilonova. 5 2019.

[379] G. P. Lamb et al. The optical afterglow of GW170817 at one year post-merger. *Astrophys. J. Lett.*, 870(2):L15, 2019.

[380] P. Landry. Rotational-tidal phasing of the binary neutron star waveform. 2018. arXiv:1805.01882 [gr-qc].

[381] P. Landry and E. Poisson. Tidal deformation of a slowly rotating material body. External metric. *Phys. Rev. D*, 91:104018, 2015.

[382] P. Landry and J. S. Read. The Mass Distribution of Neutron Stars in Gravitational-wave Binaries. *Astrophys. J. Lett.*, 921(2):L25, 2021.

[383] J. M. Lattimer. The nuclear equation of state and neutron star masses. *Ann. Rev. Nucl. Part. Sci.*, 62:485–515, 2012.

[384] J. M. Lattimer. Introduction to neutron stars. In *Exotic Nuclei and Nuclear/Particle Astrophysics (V) From Nuclei to Stars: Carpathian Summer School of Physics 2014*, volume 1645 of *American Institute of Physics Conference Series*, pages 61–78. AIP, February 2015.

[385] J. M. Lattimer and M. Prakash. Neutron star structure and the equation of state. *Astrophys.J.*, 550:426, 2001.

[386] J. M. Lattimer and M. Prakash. The physics of neutron stars. *Science*, 304:536–542, 2004.

[387] J. M. Lattimer and D. N. Schramm. Black-Hole-Neutron-Star Collisions. *Astrophys. J. Let.*, 192:L145, September 1974.

[388] I. Legred et al. Impact of the PSR J0740+6620 radius constraint on the properties of high-density matter. *Phys. Rev. D*, 104(6):063003, 2021.

[389] L. Lehner et al. Unequal mass binary neutron star mergers and multimessenger signals. *Class. Quant. Grav.*, 33(18):184002, 2016.

[390] G. Lemaître. Un univers homogene de masse constante et de rayon croissant rendant compte de la vitesse radiale nebuleuses extra-galactiques. *Annales de la Societe Scientifique de Bruxelles*, A(47):49–59, 1927.

[391] K. L. Leung, M. C. Chu, and L. M. Lin. Tidal deformability of dark matter admixed neutron stars. *Phys. Rev. D*, 105(12):123010, 2022.

[392] A. Levan et al. GRB 020410: A Gamma-ray burst afterglow discovered by its supernova light. *Astrophys. J.*, 624:880–888, 2005.

[393] A. Levan et al. Gamma-ray burst progenitors. *Space Sci. Rev.*, 202(1-4):33–78, 2016.

[394] L. X. Li and B. Paczynski. Transient events from neutron star mergers. *Astrophys. J.*, 507:L59, 1998.

[395] LIGO Scientific Collaboration. LIGO Algorithm Library - LALSuite. Free software (GPL), 2018.

[396] J. Lin. Divergence measures based on the shannon entropy. *IEEE Transactions on Information Theory*, 37(1):145–151, 1991.

[397] V. M. Lipunov. Astrophysical meaning of the discovery of gravitational waves. *Phys. Usp.*, 59(9):918–928, 2016.

[398] V. M. Lipunov et al. MASTER Optical Detection of the First LIGO/Virgo Neutron Star Binary Merger GW170817. *Astrophys. J.*, 850(1):L1, 2017.

[399] D. Lonardoni et al. Auxiliary field diffusion Monte Carlo calculations of light and medium-mass nuclei with local chiral interactions. *Phys. Rev. C*, 97(4):044318, 2018.

[400] D. Lonardoni et al. Nuclear and neutron-star matter from local chiral interactions. *Phys. Rev. Res.*, 2:022033, May 2020.

[401] J. E. Lynn et al. Chiral Three-Nucleon Interactions in Light Nuclei, Neutron-α Scattering, and Neutron Matter. *Phys. Rev. Lett.*, 116(6):062501, 2016.

[402] J. E. Lynn et al. Quantum Monte Carlo calculations of light nuclei with local chiral two- and three-nucleon interactions. *Phys. Rev. C*, 96(5):054007, 2017.

[403] J. E. Lynn et al. Quantum Monte Carlo Methods in Nuclear Physics: Recent Advances. *Ann. Rev. Nucl. Part. Sci.*, 69:279–305, 2019.

[404] E. Macaulay et al. First Cosmological Results using Type Ia Supernovae from the Dark Energy Survey: Measurement of the Hubble Constant. *Mon. Not. Roy. Astron. Soc.*, 486(2):2184–2196, 2019.

[405] A. MacFadyen and S. E. Woosley. Collapsars: Gamma-ray bursts and explosions in 'failed supernovae'. *Astrophys. J.*, 524:262, 1999.

[406] R. Machleidt and D. R. Entem. Chiral effective field theory and nuclear forces. *Phys. Rept.*, 503:1–75, 2011.

[407] D. J. C. MacKay. *Information Theory, Inference, and Learning Algorithms.* Cambridge University Press, 2005.

[408] M. R. Magee et al. Modelling the early time behaviour of type ia supernovae: effects of the 56ni distribution. *Astronomy & Astrophysics*, 614:A115, 2018.

[409] M. Maggiore. *Gravitational Waves. Vol. 1: Theory and Experiments.* Oxford University Press, 2007.

[410] M. Maggiore et al. Science Case for the Einstein Telescope. *JCAP*, 03:050, 2020.

[411] M. Mancarella et al. Accurate Standard Siren Cosmology with Joint Gravitational-Wave and γ-Ray Burst Observations. *Phys. Rev. Lett.*, 133(26):261001, 2024.

[412] S. Mandal et al. H0 tension in torsion-based modified gravity. *Nucl. Phys. B*, 993:116285, 2023.

[413] I. Mandel and F. S. Broekgaarden. Rates of compact object coalescences. *Living Rev. Rel.*, 25(1):1, 2022.

[414] I. Mandel, W. M. Farr, and J. R. Gair. Extracting distribution parameters from multiple uncertain observations with selection biases. *Mon. Not. Roy. Astron. Soc.*, 486(1):1086–1093, 2019.

[415] J. Mao, Y. X. Xin, and J. M. Bai. GRB 211211A: GMG upper limit. *GRB Coordinates Network*, 31232:1, December 2021.

[416] B. Margalit and B. D. Metzger. Constraining the Maximum Mass of Neutron Stars From Multi-Messenger Observations of GW170817. *Astrophys. J. Let.*, 850(2):L19, 2017.

[417] J. Margueron et al. Quarkyonic stars with isospin-flavor asymmetry. *Phys. Rev. C*, 104(5):055803, 2021.

[418] J. Margueron, R. Hoffmann Casali, and F. Gulminelli. Equation of state for dense nucleonic matter from metamodeling. I. Foundational aspects. *Phys. Rev. C*, 97(2):025805, 2018.

[419] J. Margueron, R. Hoffmann Casali, and F. Gulminelli. Equation of state for dense nucleonic matter from metamodeling. II. Predictions for neutron star properties. *Phys. Rev. C*, 97(2):025806, 2018.

[420] R. Margutti et al. The Electromagnetic Counterpart of the Binary Neutron Star Merger LIGO/VIRGO GW170817. V. Rising X-ray Emission from an Off-Axis Jet. *Astrophys. J.*, 848(2):L20, 2017.

[421] M. Markevitch et al. Direct constraints on the dark matter self-interaction cross-section from the merging galaxy cluster 1E0657-56. *Astrophys. J.*, 606:819–824, 2004.

[422] J. G. Martinez et al. Pulsar J0453+1559: A Double Neutron Star System with a Large Mass Asymmetry. *Astrophys. J.*, 812(2):143, 2015.

[423] A. Maselli, A. Sabatucci, and O. Benhar. Constraining three-nucleon forces with multimessenger data. *Phys. Rev. C*, 103(6):065804, 2021.

[424] S. Mastrogiovanni et al. On the importance of source population models for gravitational-wave cosmology. *Phys. Rev. D*, 104(6):062009, 2021.

[425] S. Mastrogiovanni et al. Joint population and cosmological properties inference with gravitational waves standard sirens and galaxy surveys. *Phys. Rev. D*, 108(4):042002, 2023.

[426] A. Matas et al. An aligned-spin neutron-star–black-hole waveform model based on the effective-one-body approach and numerical-relativity simulations. *Phys. Rev. D*, 102:043023, 2020.

[427] P. A. Mazzali and L. B. Lucy. The Application of Monte Carlo methods to the synthesis of early - time supernovae spectra. *Astronomy & Astrophysics*, 279:447, 1993.

[428] C. McCully et al. The Rapid Reddening and Featureless Optical Spectra of the optical counterpart of GW170817, AT 2017gfo, During the First Four Days. *Astrophys. J.*, 848:L32, 2017.

[429] L. McLerran and S. Reddy. Quarkyonic Matter and Neutron Stars. *Phys. Rev. Lett.*, 122(12):122701, 2019.

[430] A. Mei et al. Gigaelectronvolt emission from a compact binary merger. *Nature*, 612(7939):236–239, 2022.

[431] C. Messenger and J. Read. Measuring a cosmological distance-redshift relationship using only gravitational wave observations of binary neutron star coalescences. *Phys.Rev.Lett.*, 108:091101, 2012.

[432] P. Meszaros and M. J. Rees. Tidal heating and mass loss in neutron star binaries - Implications for gamma-ray burst models. *Astrophys. J.*, 397:570–575, 1992.

[433] P. Meszaros and M. J. Rees. Relativistic Fireballs and Their Impact on External Matter: Models for Cosmological Gamma-Ray Bursts. *Astrophys. J.*, 405:278, March 1993.

[434] N. Metropolis et al. Equation of state calculations by fast computing machines. *J. Chem. Phys.*, 21(6):1087–1092, jun 1953.

[435] B. D. Metzger. Kilonovae. *Living Rev. Rel.*, 23(1), dec 2019.

[436] B. D. Metzger et al. Electromagnetic counterparts of compact object mergers powered by the radioactive decay of r-process nuclei. *Mon. Not. Roy. Astron. Soc.*, 406(4):2650–2662, jun 2010.

[437] B. D. Metzger et al. The diversity of transients from magnetar birth in core collapse supernovae. *Mon. Not. Roy. Astron. Soc.*, 454(3):3311–3316, December 2015.

[438] B. D. Metzger and R. Fernández. Red or blue? A potential kilonova imprint of the delay until black hole formation following a neutron star merger. *Mon. Not. Roy. Astron. Soc.*, 441:3444, 2014.

[439] B. D. Metzger, E. Quataert, and T. A. Thompson. Short-duration gamma-ray bursts with extended emission from protomagnetar spin-down. *Mon. Not. Roy. Astron. Soc.*, 385(3):1455–1460, 03 2008.

[440] B. D. Metzger, T. A. Thompson, and E. Quataert. On the Conditions for Neutron-Rich Gamma-Ray Burst Outflows. *Astrophys. J.*, 676:1130, 2008.

[441] B. D. Metzger, T. A. Thompson, and E. Quataert. A magnetar origin for the kilonova ejecta in GW170817. *Astrophys. J.*, 856(2):101, mar 2018.

[442] M. Meyer and T. Petrushevska. Search for Axionlike-Particle-Induced Prompt γ-Ray Emission from Extragalactic Core-Collapse Supernovae with the *Fermi* Large Area Telescope. *Phys. Rev. Lett.*, 124(23):231101, 2020. [Erratum: Phys.Rev.Lett. 125, 119901 (2020)].

[443] Z. Q. Miao et al. Dark Matter Admixed Neutron Star Properties in the Light of X-Ray Pulse Profile Observations. *Astrophys. J.*, 936(1):69, 2022.

[444] B. Mikoczi, M. Vasuth, and L. A. Gergely. Self-interaction spin effects in inspiralling compact binaries. *Phys. Rev. D*, 71:124043, 2005.

[445] J. M. Miller et al. Full Transport Model of GW170817-Like Disk Produces a Blue Kilonova. *Phys. Rev. D*, 100(2):023008, 2019.

[446] M. C. Miller et al. PSR J0030+0451 Mass and Radius from $NICER$ Data and Implications for the Properties of Neutron Star Matter. *Astrophys. J. Lett.*, 887(1):L24, 2019.

[447] M. C. Miller et al. The Radius of PSR J0740+6620 from NICER and XMM-Newton Data. *Astrophys. J. Lett.*, 918(2):L28, 2021.

[448] C. K. Mishra et al. Ready-to-use post-Newtonian gravitational waveforms for binary black holes with nonprecessing spins: An update. *Phys. Rev. D*, 93(8):084054, 2016.

[449] C. Mondal and F. Gulminelli. Can we decipher the composition of the core of a neutron star? *Phys. Rev. D*, 105(8):083016, 2022.

[450] S. Morisaki. Accelerating parameter estimation of gravitational waves from compact binary coalescence using adaptive frequency resolutions. *Phys. Rev. D*, 104(4):044062, 2021.

[451] E. R. Most et al. New constraints on radii and tidal deformabilities of neutron stars from GW170817. *Phys. Rev. Lett.*, 120(26):261103, 2018.

[452] E. R. Most et al. Impact of high spins on the ejection of mass in GW170817. *Astrophys. J.*, 884:40, 2019.

[453] E. R. Most and A. A. Philippov. Electromagnetic precursors to gravitational wave events: Numerical simulations of flaring in pre-merger binary neutron star magnetospheres. *Astrophys. J. Lett.*, 893(1):L6, 2020.

[454] S. Mukherjee. The redshift dependence of black hole mass distribution: is it reliable for standard sirens cosmology? *Mon. Not. Roy. Astron. Soc.*, 515(4):5495–5505, 2022.

[455] S. Mukherjee et al. Accurate precision Cosmology with redshift unknown gravitational wave sources. *Phys. Rev. D*, 103(4):043520, 2021.

[456] A. Nagar et al. Time-domain effective-one-body gravitational waveforms for coalescing compact binaries with nonprecessing spins, tides, and self-spin effects. *Phys. Rev. D*, 98(10), nov 2018.

[457] A. Nagar et al. Nonlinear-in-spin effects in effective-one-body waveform models of spin-aligned, inspiralling, neutron star binaries. *Phys. Rev. D*, 99(4):044007, 2019.

[458] A. Nagar and P. Rettegno. Efficient effective one body time-domain gravitational waveforms. *Phys. Rev. D*, 99(2):021501, 2019.

[459] T. Nakamura, K. Oohara, and Y. Kojima. General relativistic collapse to black holes and gravitational waves from black holes. *Progress of Theoretical Physics Supplement*, 90:1–218, 01 1987.

[460] E. Nakar. Short-hard gamma-ray bursts. *Phys. Rept.*, 442:166–236, 2007.

[461] E. Nakar and T. Piran. Early afterglow emission from a reverse shock as a diagnostic tool for gamma-ray burst outflows. *Mon. Not. Roy. Astron. Soc.*, 353(2):647–653, 2004.

[462] R. Narayan, B. Paczynski, and T. Piran. Gamma-ray bursts as the death throes of massive binary stars. *Astrophys. J.*, 395:L83–L86, 1992.

[463] T. Narikawa and N. Uchikata. Follow-up analyses of the binary-neutron-star signals GW170817 and GW190425 by using post-Newtonian waveform models. *Phys. Rev. D*, 106(10):103006, 2022.

[464] T. Narikawa, N. Uchikata, and T. Tanaka. Gravitational-wave constraints on the GWTC-2 events by measuring the tidal deformability and the spin-induced quadrupole moment. *Phys. Rev. D*, 104(8):084056, 2021.

[465] P. Navratil et al. Recent developments in no-core shell-model calculations. *J. Phys. G*, 36:083101, 2009.

[466] V. Nedora et al. Mapping dynamical ejecta and disk masses from numerical relativity simulations of neutron star mergers. *Class. Quant. Grav.*, 39(1):015008, 2022.

[467] A. Nelson, S. Reddy, and D. Zhou. Dark halos around neutron stars and gravitational waves. *JCAP*, 07:012, 2019.

[468] I. Newton. *Philosophiæ Naturalis Principia Mathematica.* England, 1687.

[469] W. G. Newton et al. Ensembles of unified crust and core equations of state in a nuclear-multimessenger astrophysics environment. *Eur. Phys. J. A*, 58(4):69, 2022.

[470] M. Nicholl and I. Andreoni. Electromagnetic follow-up of gravitational waves: review and lessons learned. *Phil. Trans. Roy. Soc. Lond. A*, 383(2294):20240126, 2025.

[471] M. Nicholl et al. Tight multimessenger constraints on the neutron star equation of state from GW170817 and a forward model for kilonova light-curve synthesis. *Mon. Not. Roy. Astron. Soc.*, 505(2):3016–3032, 2021.

[472] N. Nishimura et al. The intermediate r-process in core-collapse supernovae driven by the magneto-rotational instability. *Astrophys. J. Lett.*, 836(2):L21, feb 2017.

[473] G. Nordström. On the Energy of the Gravitation field in Einstein's Theory. *Koninklijke Nederlandse Akademie van Wetenschappen Proceedings Series B Physical Sciences*, 20:1238–1245, January 1918.

[474] J. A. Nousek et al. Evidence for a canonical GRB afterglow light curve in the Swift/XRT data. *Astrophys. J.*, 642:389–400, 2006.

[475] M. Obergaulinger and M. Á. Aloy. Magnetorotational core collapse of possible GRB progenitors. III. Three-dimensional models. *Mon. Not. Roy. Astron. Soc.*, 503(4):4942–4963, 2021.

[476] R. Oechslin, H. T. Janka, and A. Marek. Relativistic neutron star merger simulations with non-zero temperature equations of state. 1. Variation of binary parameters and equation of state. *Astronomy & Astrophysics*, 2006.

[477] M. Oguri. Measuring the distance-redshift relation with the cross-correlation of gravitational wave standard sirens and galaxies. *Phys. Rev. D*, 93:083511, Apr 2016.

[478] J. H. Oort. The force exerted by the stellar system in the direction perpendicular to the galactic plane and some related problems. *Bulletin of the Astronomical Institutes of the Netherlands*, 6:249, August 1932.

[479] J. R. Oppenheimer and H. Snyder. On continued gravitational contraction. *Phys. Rev.*, 56:455–459, Sep 1939.

[480] J. R. Oppenheimer and G. M. Volkoff. On massive neutron cores. *Phys. Rev.*, 55:374–381, 1939.

[481] R. W. O'Shaughnessy et al. Constraining population synthesis models via empirical binary compact object merger and supernovae rates. *Astrophys. J.*, 672:479–488, 2008.

[482] T. Otsuka et al. Three-body forces and the limit of oxygen isotopes. *Phys. Rev. Let.*, 105:032501, 2010.

[483] C. B. Owen et al. Waveform accuracy and systematic uncertainties in current gravitational wave observations. *Phys. Rev. D*, 108(4):044018, 2023.

[484] C. Pacilio et al. Ranking Love Numbers for the Neutron Star Equation of State: The Need for Third-Generation Detectors. *Phys. Rev. Let.*, 128(10):101101, 2022.

[485] B. Paczynski. Gamma-ray bursters at cosmological distances. *Astrophys. J.*, 308:L43, sep 1986.

[486] B. Paczynski. Cosmological gamma-ray bursts. *Acta Astron.*, 41:257–267, 1991.

[487] B. Paczyński. Are Gamma-Ray Bursts in Star-Forming Regions? *Astrophys. J. Lett.*, 494(1):L45–L48, February 1998.

[488] C. Palenzuela et al. Gravitational and electromagnetic outputs from binary neutron star mergers. *Phys. Rev. Let.*, 111:061105, 2013.

[489] A. Palmese et al. Standard siren measurement of the Hubble constant using GW170817 and the latest observations of the electromagnetic counterpart afterglow. *Phys. Rev. D*, 109(6):063508, 2024.

[490] P. T. H. Pang et al. Parameter estimation for strong phase transitions in supranuclear matter using gravitational-wave astronomy. *Phys. Rev. Res.*, 2(3):033514, 2020.

[491] P. T. H. Pang et al. Nuclear Physics Multimessenger Astrophysics Constraints on the Neutron Star Equation of State: Adding NICER's PSR J0740+6620 Measurement. *Astrophys. J.*, 922(1):14, 2021.

[492] P. T. H. Pang et al. An updated nuclear-physics and multi-messenger astrophysics framework for binary neutron star mergers. *Nature Commun.*, 14(1):8352, 2023.

[493] P. Pani, L. Gualtieri, and V. Ferrari. Tidal Love numbers of a slowly spinning neutron star. *Phys. Rev. D*, 92(12):124003, 2015.

[494] N. Pankov et al. GRB 211211A: AbAO optical observations. *GRB Coordinates Network*, 31233:1, December 2021.

[495] A. Patel et al. Direct Evidence for r-process Nucleosynthesis in Delayed MeV Emission from the SGR 1806-20 Magnetar Giant Flare. *Astrophys. J. Let.*, 984(1):L29, 2025.

[496] A. Patel et al. r-process Nucleosynthesis and Radioactively Powered Transients from Magnetar Giant Flares. *Astrophys. J.*, 985(2):234, 2025.

[497] F. Pedregosa et al. Scikit-learn: Machine Learning in Python. *Journal of Machine Learning Research*, 12:2825–2830, October 2011.

[498] A. Perego et al. Neutrino-driven winds from neutron star merger remnants. *Mon. Not. Roy. Astron. Soc.*, 443:3134, 2014.

[499] L. Perivolaropoulos and F. Skara. Challenges for ΛCDM: An update. *New Astron. Rev.*, 95:101659, 2022.

[500] D. A. Perley et al. GRB 080503: Implications of a Naked Short Gamma-Ray Burst Dominated by Extended Emission. *Astrophys. J.*, 696:1871–1885, 2009.

[501] P. Petrov et al. Data-driven Expectations for Electromagnetic Counterpart Searches Based on LIGO/Virgo Public Alerts. *Astrophys. J.*, 924(2):54, 2022.

[502] E. Pian et al. Spectroscopic identification of r-process nucleosynthesis in a double neutron star merger. *Nature*, 2017.

[503] M. Piarulli et al. Benchmark calculations of pure neutron matter with realistic nucleon-nucleon interactions. *Phys. Rev. C*, 101(4):045801, 2020.

[504] A. Pierce, K. Riles, and Y. Zhao. Searching for Dark Photon Dark Matter with Gravitational Wave Detectors. *Phys. Rev. Let.*, 121(6):061102, 2018.

[505] G. Pierra, S. Mastrogiovanni, and S. Perriès. The spin magnitude of stellar-mass black holes evolves with the mass. *Astronomy & Astrophysics*, 692:A80, 2024.

[506] T. Piran et al. Jets in gamma-ray bursts. *Astrophys. J.*, 519(1):L17, 1999.

[507] M. Ponce et al. Interaction of misaligned magnetospheres in the coalescence of binary neutron stars. *Phys. Rev. D*, 90(4):044007, 2014.

[508] S. F. Portegies Zwart et al. The Formation of massive black holes through collision runaway in dense young star clusters. *Nature*, 428:724, 2004.

[509] S. Postnikov, M. Prakash, and J. M. Lattimer. Tidal Love Numbers of Neutron and Self-Bound Quark Stars. *Phys. Rev. D*, 82:024016, 2010.

[510] V. Poulin, T. L. Smith, and T. Karwal. The Ups and Downs of Early Dark Energy solutions to the Hubble tension: A review of models, hints and constraints circa 2023. *Phys. Dark Univ.*, 42:101348, 2023.

[511] G. Pratten et al. Setting the cornerstone for a family of models for gravitational waves from compact binaries: The dominant harmonic for nonprecessing quasicircular black holes. *Phys. Rev. D*, 102(6):064001, 2020.

[512] G. Pratten et al. Computationally efficient models for the dominant and subdominant harmonic modes of precessing binary black holes. *Phys. Rev. D*, 103(10):104056, 2021.

[513] G. Pratten, P. Schmidt, and T. Hinderer. Gravitational-Wave Asteroseismology with Fundamental Modes from Compact Binary Inspirals. *Nature Commun.*, 11(1):2553, 2020.

[514] G. Pratten, P. Schmidt, and N. Williams. Impact of Dynamical Tides on the Reconstruction of the Neutron Star Equation of State. *Phys. Rev. Lett.*, 129(8):081102, 2022.

[515] F. Pretorius. Evolution of binary black hole spacetimes. *Phys. Rev. Lett.*, 95:121101, 2005.

[516] D. Price and S. Rosswog. Producing ultra-strong magnetic fields in neutron star mergers. *Science*, 312:719, 2006.

[517] A. Puecher et al. Unraveling information about supranuclear-dense matter from the complete binary neutron star coalescence process using future gravitational-wave detector networks. *Phys. Rev. D*, 107(12):124009, 2023.

[518] A. Puecher, A. Samajdar, and T. Dietrich. Measuring tidal effects with the Einstein Telescope: A design study. *Phys. Rev. D*, 108(2):023018, 2023.

[519] M. Punturo, M. Abernathy, F. Acernese, B. Allen, N. Andersson, et al. The Einstein Telescope: A third-generation gravitational wave observatory. *Class.Quant.Grav.*, 27:194002, 2010.

[520] M. Punturo et al. The einstein telescope: a third-generation gravitational wave observatory. *Class. Quant. Grav.*, 27(19):194002, sep 2010.

[521] M. Pürrer. Frequency domain reduced order models for gravitational waves from aligned-spin compact binaries. *Class. Quant. Grav.*, 31(19):195010, 2014.

[522] M. Pürrer. Frequency domain reduced order model of aligned-spin effective-one-body waveforms with generic mass-ratios and spins. *Phys. Rev. D*, 93(6):064041, 2016.

[523] Y. Z. Qian and S. E. Woosley. Nucleosynthesis in neutrino driven winds: 1. The Physical conditions. *Astrophys. J.*, 471:331–351, 1996.

[524] G. Raaijmakers et al. Constraints on the Dense Matter Equation of State and Neutron Star Properties from NICER's Mass–Radius Estimate of PSR J0740+6620 and Multimessenger Observations. *Astrophys. J. Let.*, 918(2):L29, 2021.

[525] G. Raaijmakers et al. The Challenges Ahead for Multimessenger Analyses of Gravitational Waves and Kilonova: A Case Study on GW190425. *Astrophys. J.*, 922(2):269, 2021.

[526] D. Radice and L. Dai. Multimessenger Parameter Estimation of GW170817. *Eur. Phys. J.*, A55(4):50, 2019.

[527] D. Radice et al. Dynamical Mass Ejection from Binary Neutron Star Mergers. *Mon. Not. Roy. Astron. Soc.*, 460(3):3255–3271, 2016.

[528] D. Radice et al. Binary Neutron Star Mergers: Mass Ejection, Electromagnetic Counterparts and Nucleosynthesis. *Astrophys. J.*, 869(2):130, 2018.

[529] D. Radice et al. GW170817: Joint Constraint on the Neutron Star Equation of State from Multimessenger Observations. *Astrophys. J.*, 852(2):L29, 2018.

[530] D. Radice and L. Rezzolla. THC: a new high-order finite-difference high-resolution shock-capturing code for special-relativistic hydrodynamics. *Astronomy & Astrophysics*, 547:A26, 2012.

[531] C. A. Raithel. Constraints on the Neutron Star Equation of State from GW170817. *Eur. Phys. J. A*, 55(5):80, 2019.

[532] C. E. Rasmussen and C. K. I. Williams. *Gaussian Processes for Machine Learning.* MIT Press, 2006.

[533] J. C. Rastinejad et al. A kilonova following a long-duration gamma-ray burst at 350 Mpc. *Nature*, 612(7939):223–227, 2022.

[534] V. Raymond and W. M. Farr. Physically motivated exploration of the extrinsic parameter space in ground-based gravitational-wave astronomy. 2 2014. arXiv:1402.0053 [gr-qc].

[535] J. S. Read. Waveform uncertainty quantification and interpretation for gravitational-wave astronomy. *Class. Quant. Grav.*, 40(13):135002, 2023.

[536] J. S. Read et al. Constraints on a phenomenologically parameterized neutron- star equation of state. *Phys. Rev. D*, 79:124032, 2009.

[537] B. T. Reed et al. Toward Accelerated Nuclear-physics Parameter Estimation from Binary Neutron Star Mergers: Emulators for the Tolman–Oppenheimer–Volkoff Equations. *Astrophys. J.*, 974(2):285, 2024.

[538] T. Regimbau et al. A Mock Data Challenge for the Einstein Gravitational-Wave Telescope. *Phys. Rev. D*, 86:122001, 2012.

[539] M. Reichert et al. Nucleosynthesis in magneto-rotational supernovae. *Mon. Not. Roy. Astron. Soc.*, 501(4):5733–5745, 2021.

[540] H. Reissner. Über die Eigengravitation des elektrischen Feldes nach der Einsteinschen Theorie. *Annalen der Physik*, 355(9):106–120, January 1916.

[541] D. Reitze et al. Cosmic Explorer: The U.S. Contribution to Gravitational-Wave Astronomy beyond LIGO. *Bull. Am. Astron. Soc.*, 51(7):035, 2019.

[542] L. Rezzolla, E. R. Most, and L. R. Weih. Using gravitational-wave observations and quasi-universal relations to constrain the maximum mass of neutron stars. *Astrophys. J.*, 852(2):L25, 2018.

[543] L. Rezzolla and O. Zanotti. *Relativistic Hydrodynamics*. Oxford University Press, Oxford, 2013.

[544] J. E. Rhoads. How to tell a jet from a balloon: a proposed test for beaming in gamma-ray bursts. *Astrophys. J.*, 487(1):L1, 1997.

[545] J. E. Rhoads. The dynamics and light curves of beamed gamma-ray burst afterglows. *Astrophys. J.*, 525(2):737, 1999.

[546] A. G. Riess et al. Large Magellanic Cloud Cepheid Standards Provide a 1% Foundation for the Determination of the Hubble Constant and Stronger Evidence for Physics beyond ΛCDM. *Astrophys. J.*, 876(1):85, 2019.

[547] T. E. Riley et al. A NICER View of PSR J0030+0451: Millisecond Pulsar Parameter Estimation. *Astrophys. J. Let.*, 887(1):L21, 2019.

[548] T. E. Riley et al. A NICER View of the Massive Pulsar PSR J0740+6620 Informed by Radio Timing and XMM-Newton Spectroscopy. *Astrophys. J. Let.*, 918(2):L27, 2021.

[549] L. F. Roberts et al. Electromagnetic transients powerred by nuclear decay in the tidal tails of coalescing compact binaries. *Astrophys. J. Lett.*, 736(1):L21, jul 2011.

[550] S. Robles. Improved treatment of dark matter capture in compact stars. *SciPost Phys. Proc.*, 12:057, 2023.

[551] C. L. Rodriguez et al. Inadequacies of the Fisher Information Matrix in gravitational-wave parameter estimation. *Phys. Rev. D*, 88(8):084013, 2013.

[552] R. W. Romani et al. Psr j0952-0607: The fastest and heaviest known galactic neutron star. *Astrophys. J. Let.*, 934(2):L17, jul 2022.

[553] H. Rose et al. Revealing the strength of three-nucleon interactions with the proposed Einstein Telescope. *Phys. Rev. C*, 108(2):025811, 2023.

[554] A. Rossi et al. The Peculiar Short-duration GRB 200826A and Its Supernova*. *Astrophys. J.*, 932(1):1, 2022.

[555] S. Rosswog. The multi-messenger picture of compact binary mergers. *Int. J. Mod. Phys.*, D24(05):1530012, 2015.

[556] S. Rosswog et al. Mass ejection in neutron star mergers. *Astronomy & Astrophysics*, 341:499–526, 1999.

[557] S. Rosswog and M. Liebendoerfer. High resolution calculations of merging neutron stars. 2: Neutrino emission. *Mon. Not. Roy. Astron. Soc.*, 342:673, 2003.

[558] N. Roth and D. Kasen. Monte Carlo Radiation Hydrodynamics with Implicit Methods. *Astrophys. J. Suppl.*, 217(1):9, 2015.

[559] P. Routaray et al. Radial oscillations of dark matter admixed neutron stars. *Phys. Rev. D*, 107(10):103039, 2023.

[560] V. C. Rubin and W. K. Ford, Jr. Rotation of the Andromeda Nebula from a Spectroscopic Survey of Emission Regions. *Astrophys. J.*, 159:379–403, 1970.

[561] M. H. Ruffert, H. T. Janka, and G. Schäfer. Coalescing neutron stars: A step towards physical models. I: Hydrodynamic evolution and gravitational- wave emission. *Astronomy & Astrophysics*, 311:532–566, 1996.

[562] M. Ruiz, S. L. Shapiro, and A. Tsokaros. GW170817, General Relativistic Magnetohydrodynamic Simulations, and the Neutron Star Maximum Mass. *Phys. Rev. D*, 97(2):021501, 2018.

[563] P. Russotto et al. Results of the ASY-EOS experiment at GSI: The symmetry energy at suprasaturation density. *Phys. Rev. C*, 94(3):034608, 2016.

[564] H. R. Rüter et al. Quasiequilibrium configurations of binary systems of dark matter admixed neutron stars. *Phys. Rev. D*, 108(12):124080, 2023.

[565] N. Rutherford et al. Constraining bosonic asymmetric dark matter with neutron star mass-radius measurements. *Phys. Rev. D*, 107(10):103051, 2023.

[566] G. Ryan et al. Gamma-ray burst afterglows in the multimessenger era: Numerical models and closure relations. *Astrophys. J.*, 896(2):166, jun 2020.

[567] A. Sabatucci et al. Sensitivity of neutron star observations to three-nucleon forces. *Phys. Rev. D*, 106(8):083010, 2022.

[568] V. Sagun et al. How does dark matter affect compact star properties and high density constraints of strongly interacting matter. *EPJ Web Conf.*, 274:07009, 2022.

[569] V. Sagun et al. What Is the Nature of the HESS J1731-347 Compact Object? *Astrophys. J.*, 958(1):49, 2023.

[570] M. Saleem et al. The science case for LIGO-India. *Class. Quant. Grav.*, 39(2):025004, 2022.

[571] A. Samajdar and T. Dietrich. Waveform systematics for binary neutron star gravitational wave signals: Effects of the point-particle baseline and tidal descriptions. *Phys. Rev. D*, 98(12), dec 2018.

[572] A. Samajdar and T. Dietrich. Waveform systematics for binary neutron star gravitational wave signals: effects of the point-particle baseline and tidal descriptions. *Phys. Rev. D*, 98(12):124030, 2018.

[573] A. Samajdar and T. Dietrich. Waveform systematics for binary neutron star gravitational wave signals: Effects of spin, precession, and the observation of electromagnetic counterparts. *Phys. Rev. D*, 100(2):024046, 2019.

[574] L. Santamaria et al. Matching post-Newtonian and numerical relativity waveforms: systematic errors and a new phenomenological model for non-precessing black hole binaries. *Phys. Rev. D*, 82:064016, 2010.

[575] R. Sari, T. Piran, and R. Narayan. Spectra and light curves of gamma-ray burst afterglows. *Astrophys. J. Let.*, 497:L17, 1998.

[576] N. Sarin and P. D. Lasky. The evolution of binary neutron star post-merger remnants: a review. *Gen. Rel. Grav.*, 53(6):59, 2021.

[577] B. Sathyaprakash et al. Scientific Objectives of Einstein Telescope. *Class. Quant. Grav.*, 29:124013, 2012. [Erratum: Class.Quant.Grav. 30, 079501 (2013)].

[578] B. S. Sathyaprakash and S. V. Dhurandhar. Choice of filters for the detection of gravitational waves from coalescing binaries. *Phys. Rev. D*, 44:3819–3834, 1991.

[579] F. Schianchi et al. M1 neutrino transport within the numerical-relativistic code BAM with application to low mass binary neutron star mergers. *Phys. Rev. D*, 109(4):044012, 2024.

[580] E. F. Schlafly and D. P. Finkbeiner. Measuring Reddening with Sloan Digital Sky Survey Stellar Spectra and Recalibrating SFD. *Astrophys. J.*, 737(2):103, August 2011.

[581] K. E. Schmidt and S. Fantoni. A quantum Monte Carlo method for nucleon systems. *Phys. Lett. B*, 446:99–103, 1999.

[582] P. Schmidt and T. Hinderer. Frequency domain model of f-mode dynamic tides in gravitational waveforms from compact binary inspirals. *Phys. Rev. D*, 100(2):021501, 2019.

[583] B. Schutz. Determining the Hubble constant from gravitational wave observations. *Nature*, 323:310–311, 1986.

[584] K. Schwarzschild. Über das Gravitationsfeld einer Kugel aus inkompressibler Flüssigkeit nach der Einsteinschen Theorie. In *Sitzungsberichte der Königlich Preussischen Akademie der Wissenschaften zu Berlin*, pages 424–434, March 1916.

[585] K. Schwarzschild. Über das Gravitationsfeld eines Massenpunktes nach der Einsteinschen Theorie. *Sitzungsberichte der Königlich Preussischen Akademie der Wissenschaften*, pages 189–196, January 1916.

[586] S. Sen and L. Sivertsen. Mass and Radius Relations of Quarkyonic Stars Using an Excluded-volume Model. *Astrophys. J.*, 915(2):109, 2021.

[587] P. A. Seoane et al. Astrophysics with the Laser Interferometer Space Antenna. *Living Rev. Rel.*, 26(1):2, 2023.

[588] S. L. Shapiro and S. A. Teukolsky. *Black holes, white dwarfs and neutron stars. The physics of compact objects.* 1983.

[589] B. J. Shappee et al. Early Spectra of the Gravitational Wave Source GW170817: Evolution of a Neutron Star Merger. *Science*, 358:1574, 2017.

[590] M. Shibata. Gravitational waves induced by a particle orbiting around a rotating black hole: spin orbit interaction effect. *Phys. Rev. D*, 48:663–666, 1993.

[591] M. Shibata et al. Constraint on the maximum mass of neutron stars using GW170817 event. *Phys. Rev. D*, 100(2):023015, 2019.

[592] M. Shibata and K. Hotokezaka. Merger and Mass Ejection of Neutron-Star Binaries. *Ann. Rev. Nucl. Part. Sci.*, 69:41–64, 2019.

[593] M. Shibata and T. Nakamura. Evolution of three-dimensional gravitational waves: Harmonic slicing case. *Phys. Rev. D*, 52:5428–5444, Nov 1995.

[594] M. Shibata, K. Taniguchi, and K. Uryu. Merger of binary neutron stars of unequal mass in full general relativity. *Phys. Rev. D*, 68:084020, 2003.

[595] M. Shrestha et al. Impact of jets on kilonova photometric and polarimetric emission from binary neutron star mergers. *Mon. Not. Roy. Astron. Soc.*, 523(2):2990–3000, 2023.

[596] D. M. Siegel. GW170817–the first observed neutron star merger and its kilonova: implications for the astrophysical site of the r-process. *Eur. Phys. J. A*, 55(11):203, 2019.

[597] D. M. Siegel. r-Process nucleosynthesis in gravitational-wave and other explosive astrophysical events. *Nature Rev. Phys.*, 4(5):306–318, 2022.

[598] D. M. Siegel, J. Barnes, and B. D. Metzger. Collapsars as a major source of r-process elements. *Nature*, 569:241, 2019.

[599] D. M. Siegel and B. D. Metzger. Three-dimensional general-relativistic magnetohydrodynamic simulations of remnant accretion disks from neutron star mergers: Outflows and r-process nucleosynthesis. *Phys. Rev. Lett.*, 119:231102, Dec 2017.

[600] D. Singh et al. Constraining properties of asymmetric dark matter candidates from gravitational-wave observations. *Phys. Rev. D*, 107(8):083037, 2023.

[601] N. Singh et al. Exploring compact binary populations with the Einstein Telescope. *Astronomy & Astrophysics*, 667:A2, 2022.

[602] J. Skilling. Nested sampling. In *AIP Conference Proceedings*. AIP, 2004.

[603] J. Skilling. Nested sampling for general bayesian computation. *Bayesian Anal.*, 1(4):833–859, 12 2006.

[604] A. Smith. Tolman–Oppenheimer–Volkoff stars. Available at: `https://www.as.utexas.edu/astronomy/education/spring13/bromm/secure/TOC_Supplement.pdf`. (accessed: 13.12.2024).

[605] R. Smith et al. Fast and accurate inference on gravitational waves from precessing compact binaries. *Phys. Rev. D*, 94(4):044031, 2016.

[606] R. Smith et al. Massively parallel Bayesian inference for transient gravitational-wave astronomy. *Mon. Not. Roy. Astron. Soc.*, 498(3):4492–4502, 2020.

[607] A. Sneppen. On the Blackbody Spectrum of Kilonovae. *Astrophys. J.*, 955(1):44, 2023.

[608] A. Sneppen et al. Spherical symmetry in the kilonova AT2017gfo/GW170817. *Nature*, 614(7948):436–439, 2023.

[609] R. Somasundaram, I. Tews, and J. Margueron. Investigating signatures of phase transitions in neutron-star cores. *Phys. Rev. C*, 107(2):025801, 2023.

[610] K. Somiya. Detector configuration of KAGRA: The Japanese cryogenic gravitational-wave detector. *Class. Quant. Grav.*, 29:124007, 2012.

[611] J. S. Speagle. dynesty: a dynamic nested sampling package for estimating Bayesian posteriors and evidences. *Mon. Not. Roy. Astron. Soc.*, 493(3):3132–3158, 2020.

[612] D. Spolyar, K. Freese, and P. Gondolo. Dark matter and the first stars: a new phase of stellar evolution. *Phys. Rev. Lett.*, 100:051101, 2008.

[613] K. Z. Stanek et al. Spectroscopic discovery of the supernova 2003dh associated with GRB 030329. *Astrophys. J.*, 591(1):L17–L20, jun 2003.

[614] C. L. Steinhardt, A. Sneppen, and B. Sen. Effects of Supernova Redshift Uncertainties on the Determination of Cosmological Parameters. *Astrophys. J.*, 902(1):14, 2020.

[615] J. Steinhoff et al. Dynamical Tides in General Relativity: Effective Action and Effective-One-Body Hamiltonian. *Phys. Rev. D*, 94(10):104028, 2016.

[616] J. Steinhoff et al. Spin effects on neutron star fundamental-mode dynamical tides: Phenomenology and comparison to numerical simulations. *Phys. Rev. Res.*, 3(3):033129, 2021.

[617] S. Stevenson et al. Formation of the first three gravitational-wave observations through isolated binary evolution. *Nature Commun.*, 8:14906, 2017.

[618] K. Stovall et al. PALFA Discovery of a Highly Relativistic Double Neutron Star Binary. *Astrophys. J.*, 854(2):L22, 2018.

[619] D. Suárez-Fontanella et al. Gravitational wave emission in binary neutron star early post-merger within a dark environment. *Phys. Lett. B*, 862:139358, 2025.

[620] A. G. Suvorov, H. J. Kuan, and K. D. Kokkotas. Quasi-periodic oscillations in precursor flares via seismic aftershocks from resonant shattering. *Astronomy & Astrophysics*, 664:A177, 2022.

[621] Y. Suwa et al. On the minimum mass of neutron stars. *Mon. Not. Roy. Astron. Soc.*, 481(3):3305–3312, 2018.

[622] M. Tanaka. Kilonova/Macronova Emission from Compact Binary Mergers. *Adv. Astron.*, 2016:6341974, 2016.

[623] M. Tanaka et al. Systematic Opacity Calculations for Kilonovae. *Mon. Not. Roy. Astron. Soc.*, 496(2):1369–1392, 2020.

[624] N. R. Tanvir et al. A kilonova associated with short-duration gamma-ray burst 130603B. *Nature*, 500:547, 2013.

[625] N. R. Tanvir et al. The Emergence of a Lanthanide-Rich Kilonova Following the Merger of Two Neutron Stars. *Astrophys. J.*, 848(2):L27, 2017.

[626] A. Taracchini et al. Effective-one-body model for black-hole binaries with generic mass ratios and spins. *Phys. Rev. D*, 89(6):061502, 2014.

[627] T. M. Tauris et al. Formation of Double Neutron Star Systems. *Astrophys. J.*, 846(2):170, 2017.

[628] I. Tews. Spectrum of shear modes in the neutron-star crust: Estimating the nuclear-physics uncertainties. *Phys. Rev. C*, 95(1):015803, 2017.

[629] I. Tews et al. Neutron matter at next-to-next-to-next-to-leading order in chiral effective field theory. *Phys. Rev. Let.*, 110(3):032504, 2013.

[630] I. Tews et al. Constraining the speed of sound inside neutron stars with chiral effective field theory interactions and observations. *Astrophys. J.*, 860(2):149, 2018.

[631] I. Tews et al. On the Nature of GW190814 and Its Impact on the Understanding of Supranuclear Matter. *Astrophys. J. Let.*, 908(1):L1, 2021.

[632] I. Tews et al. Nuclear Forces for Precision Nuclear Physics: A Collection of Perspectives. *Few Body Syst.*, 63(4):67, 2022.

[633] I. Tews, J. Margueron, and S. Reddy. Critical examination of constraints on the equation of state of dense matter obtained from GW170817. *Phys. Rev. C*, 98(4):045804, 2018.

[634] M. Thierfelder, S. Bernuzzi, and B. Brügmann. Numerical relativity simulations of binary neutron stars. *Phys. Rev. D*, 84:044012, 2011.

[635] J. E. Thompson et al. Modeling the gravitational wave signature of neutron star black hole coalescences: PhenomNSBH. *Phys. Rev. D*, 101(12):124059, 2020.

[636] E. Thrane and C. Talbot. An introduction to Bayesian inference in gravitational-wave astronomy: parameter estimation, model selection, and hierarchical models. *Publ. Astron. Soc. Austral.*, 36:e010, 2019. [Erratum: Publ.Astron.Soc.Austral. 37, e036 (2020)].

[637] R. C. Tolman. Static solutions of Einstein's field equations for spheres of fluid. *Phys. Rev.*, 55:364–373, 1939.

[638] R. C. Tolman, J. Robert Oppenheimer, and G. M. Volkoff. On massive neutron cores. *Physical Review*, 55(4):374–381, 1939.

[639] E. Troja et al. A luminous blue kilonova and an off-axis jet from a compact binary merger at z=0.1341. *Nature Commun.*, 9:4089, 2018.

[640] E. Troja et al. A year in the life of GW 170817: the rise and fall of a structured jet from a binary neutron star merger. *Mon. Not. Roy. Astron. Soc.*, 489(2):1919–1926, 2019.

[641] E. Troja et al. The afterglow and kilonova of the short GRB 160821B. *Mon. Not. Roy. Astron. Soc.*, 489(2):2104–2116, 2019. [Erratum: Mon.Not.Roy.Astron.Soc. 490, 4367 (2019)].

[642] E. Troja et al. A nearby long gamma-ray burst from a merger of compact objects. *Nature*, 612(7939):228–231, 2022.

[643] S. Tsuchida et al. Dark Matter Signals on a Laser Interferometer. *Phys. Rev. D*, 101(2):023005, 2020.

[644] C. Turski et al. Impact of modelling galaxy redshift uncertainties on the gravitational-wave dark standard siren measurement of the Hubble constant. *Mon. Not. Roy. Astron. Soc.*, 526(4):6224–6233, 2023.

[645] S. Typel, G. Ropke, T. Klahn, D. Blaschke, and H. H. Wolter. Composition and thermodynamics of nuclear matter with light clusters. *Phys. Rev. C*, 81:015803, 2010.

[646] S. Typel and H. H. Wolter. Relativistic mean field calculations with density dependent meson nucleon coupling. *Nucl. Phys. A*, 656:331–364, 1999.

[647] Y. Utsumi et al. J-GEM observations of an electromagnetic counterpart to the neutron star merger GW170817. *Publ. Astron. Soc. Jap.*, 69(6):101, 2017.

[648] S. Valenti et al. The discovery of the electromagnetic counterpart of GW170817: Kilonova AT 2017gfo/DLT17ck. *Astrophys. J.*, 848(2):L24, oct 2017.

[649] M. Vallisneri. Use and abuse of the Fisher information matrix in the assessment of gravitational-wave parameter-estimation prospects. *Phys. Rev. D*, 77:042001, 2008.

[650] H. J. van Eerten et al. Gamma-ray burst afterglows from trans-relativistic blast wave simulations. *Mon. Not. Roy. Astron. Soc.*, 403:300, 2010.

[651] H. J. van Eerten, W. Q. Zhang, and A. MacFadyen. Off-Axis Gamma-Ray Burst Afterglow Modeling Based On A Two-Dimensional Axisymmetric Hydrodynamics Simulation. *Astrophys. J.*, 722:235–247, 2010.

[652] J. Veitch et al. Parameter estimation for compact binaries with ground-based gravitational-wave observations using the LALInference software library. *Phys. Rev. D*, 91(4):042003, 2015.

[653] V. A. Villar et al. The Combined Ultraviolet, Optical, and Near-Infrared Light Curves of the Kilonova Associated with the Binary Neutron Star Merger GW170817: Unified Data Set, Analytic Models, and Physical Implications. *Astrophys. J.*, 851(1):L21, 2017.

[654] J. Vines, E. E. Flanagan, and T. Hinderer. Post-1-Newtonian tidal effects in the gravitational waveform from binary inspirals. *Phys. Rev. D*, 83:084051, 2011.

[655] L. Wade et al. Systematic and statistical errors in a bayesian approach to the estimation of the neutron-star equation of state using advanced gravitational wave detectors. *Phys. Rev. D*, 89(10), may 2014.

[656] K. Walker et al. Precision constraints on the neutron star equation of state with third-generation gravitational-wave observatories. *Phys. Rev. D*, 110(4):043013, 2024.

[657] H. Wang and D. Giannios. Multimessenger parameter estimation of GW170817: from jet structure to the Hubble constant. *Astrophys. J.*, 908(2):200, 2021.

[658] D. Watson et al. Identification of strontium in the merger of two neutron stars. *Nature*, 574(7779):497–500, 2019.

[659] E. Waxman and T. Piran. Stability of Fireballs and Gamma-Ray Bursts. *Astrophys. J. Let.*, 433:L85, October 1994.

[660] S. Weinberg. Nuclear forces from chiral Lagrangians. *Phys. Lett. B*, 251:288–292, 1990.

[661] S. Weinberg. Effective chiral Lagrangians for nucleon - pion interactions and nuclear forces. *Nucl. Phys. B*, 363:3–18, 1991.

[662] S. Weinberg. Three body interactions among nucleons and pions. *Phys. Lett. B*, 295:114–121, 1992.

[663] H. Weyl. Zur Gravitationstheorie. *Annalen der Physik*, 359(18):117–145, January 1917.

[664] J. C. Wheeler et al. Asymmetric Supernovae, Pulsars, Magnetars, and Gamma-Ray Bursts. *Astrophys. J.*, 537(2):810–823, July 2000.

[665] F. Wienholtz et al. Masses of exotic calcium isotopes pin down nuclear forces. *Nature*, 498(7454):346–349, 2013.

[666] C. Winteler et al. Magnetorotationally Driven Supernovae as the Origin of Early Galaxy r-process Elements? *Astrophys. J. Let.*, 750(1):L22, May 2012.

[667] M. T. Wolff et al. NICER Detection of Thermal X-Ray Pulsations from the Massive Millisecond Pulsars PSR J0740+6620 and PSR J1614–2230. *Astrophys. J. Let.*, 918(2):L26, 2021.

[668] R. T. Wollaeger et al. Impact of ejecta morphology and composition on the electromagnetic signatures of neutron star mergers. *Mon. Not. Roy. Astron. Soc.*, 478(3):3298–3334, 2018.

[669] S. E. Woosley. Gamma-Ray Bursts from Stellar Mass Accretion Disks around Black Holes. *Astrophys. J.*, 405:273, March 1993.

[670] S. E. Woosley. Bright Supernovae from Magnetar Birth. *Astrophys. J. Let.*, 719(2):L204–L207, August 2010.

[671] S. E. Woosley, A. Heger, and T. A. Weaver. The evolution and explosion of massive stars. *Rev. Mod. Phys.*, 74:1015–1071, 2002.

[672] Y. Y. Wu and A. MacFadyen. Constraining the Outflow Structure of the Binary Neutron Star Merger Event GW170817/GRB170817A with a Markov Chain Monte Carlo Analysis. *Astrophys. J.*, 869(1):55, 2018.

[673] D. Wysocki et al. Inferring the neutron star equation of state simultaneously with the population of merging neutron stars. 1 2020. arXiv:2001.01747 [gr-qc].

[674] S. Xiao et al. The Peculiar Precursor of a Gamma-Ray Burst from a Binary Merger Involving a Magnetar. *Astrophys. J.*, 970(1):6, 2024.

[675] W. J. Xie and B. A. Li. Bayesian Inference of the Symmetry Energy of Superdense Neutron-rich Matter from Future Radius Measurements of Massive Neutron Stars. *Astrophys. J.*, 899(1):4, 2020.

[676] T. Yamamoto, M. Shibata, and K. Taniguchi. Simulating coalescing compact binaries by a new code SACRA. *Phys. Rev. D*, 78:064054, 2008.

[677] B. Yang et al. A possible macronova in the late afterglow of the long-short burst GRB 060614. *Nature Commun.*, 6:7323, June 2015.

[678] J. Yang et al. A long-duration gamma-ray burst with a peculiar origin. *Nature*, 612(7939):232–235, 2022.

[679] C. Ye and M. Fishbach. Inferring the Neutron Star Maximum Mass and Lower Mass Gap in Neutron Star–Black Hole Systems with Spin. *Astrophys. J.*, 937(2):73, 2022.

[680] B. Zhang. *The Physics of Gamma-Ray Bursts*. Cambridge University Press, 2018.

[681] B. Zhang et al. Physical processes shaping GRB x-ray afterglow lightcurves: Theoretical implications from the SWIFT XRT observations. *Astrophys. J.*, 642:354–370, 2006.

[682] B. Zhang, S. Kobayashi, and P. Mészáros. Gamma-ray burst early optical afterglows: implications for the initial lorentz factor and the central engine. *Astrophys. J.*, 595(2):950, 2003.

[683] B. Zhang and P. Meszaros. Gamma-ray burst afterglow with continuous energy injection: Signature of a highly magnetized millisecond pulsar. *Astrophys. J. Let.*, 552:L35–L38, 2001.

[684] B. B. Zhang et al. A peculiarly short-duration gamma-ray burst from massive star core collapse. *Nature Astron.*, 5(9):911–916, 2021.

[685] H. M. Zhang et al. Fermi-LAT Detection of a GeV Afterglow from a Compact Stellar Merger. *PoS*, ICRC2023:887, 2024.

[686] N. B. Zhang and B. A. Li. Extracting Nuclear Symmetry Energies at High Densities from Observations of Neutron Stars and Gravitational Waves. *Eur. Phys. J. A*, 55(3):39, 2019.

[687] J. P. Zhu et al. Population properties of gravitational-wave neutron star–black hole mergers. *Astrophys. J.*, 928:167, 04 2022.

[688] F. Zwicky. Die Rotverschiebung von extragalaktischen Nebeln. *Helv. Phys. Acta*, 6:110–127, 1933.

[689] F. Zwicky. On the Masses of Nebulae and of Clusters of Nebulae. *Astrophys. J.*, 86:217–246, 1937.

[690] F. Özel et al. The black hole mass distribution in the galaxy. *Astrophys. J.*, 725(2):1918–1927, dec 2010.

[691] F. Özel and P. Freire. Masses, Radii, and Equation of State of Neutron Stars. *Ann. Rev. Astron. Astrophys.*, 54:401, 2016.

Curriculum vitae

In compliance with the university's publication requirements, all personal data have been removed from the curriculum vitae. The remaining content consists solely of the list of publications.

Publication list

Peer-reviewed articles

- Hauke Koehn, Henrik Rose, Peter T. H. Pang, Rahul Somasundaram, Brendan T. Reed, Ingo Tews, Adrian Abac, Oleg Komoltsev, **Nina Kunert**, Aleksi Kurkela, Michael W. Coughlin, Brian F. Healy, Tim Dietrich. *An overview of existing and new nuclear and astrophysical constraints on the equation of state of neutron-rich dense matter.* Phys. Rev. X 15 (2025) 2, 021014.

- Hauke Koehn, Edoardo Giangrandi, **Nina Kunert**, Rahul Somasundaram, Violetta Sagun, Tim Dietrich. *Impact of dark matter on tidal signatures in neutron star mergers with Einstein Telescope.* Phys.Rev.D, doi: 10.1103/PhysRevD.110.103033

- **Nina Kunert**, Jonathan Gair, Peter T. H. Pang, Tim Dietrich. *Impact of gravitational waveform model systematics on the measurement of the Hubble constant.* Phys.Rev.D 110 (2024) 4, 043520.

- **Nina Kunert**, Sarah Antier, Vsevolod Nedora, Mattia Bulla, Peter T. H. Pang, Shreya Anand, Michael Coughlin, Ingo Tews, Jennifer Barnes, Thomas Hussenot-Desenonges, Brian Healy, Theophile Jegou du Laz, Meili Pilloix, Weizmann Kiendrebeogo, Tim Dietrich, *Bayesian model selection for GRB 211211A through multiwavelength analyses.* Mon. Not. Roy. Astron. Soc., 527(2):3900–3911, 2024. doi: 10.1093/mnras/stad3463.

- R. Weizmann Kiendrebeogo, Amanda M. Farah, Emily M. Foley, Abigail Gray, **Nina Kunert**, Anna Puecher, Andrew Toivonen, R. Oliver VandenBerg, Shreya Anand, Tomás Ahumada, Viraj Karambelkar, Michael W. Coughlin, Tim Dietrich, S. Zacharie Kam, Peter T. H. Pang, Leo P. Singer, Niharika Sravan. *Updated Observing Scenarios and Multimessenger Implications for the International Gravitational-wave Networks O4 and O5.* Astrophys. J., 958(2):158, 2023. doi: 10.3847/1538-4357/acfcb1.

- Henrik Rose, **Nina Kunert**, Tim Dietrich, Peter T. H. Pang, Rory Smith, Chris Van Den Broeck, Stefano Gandolfi, and Ingo Tews. *Revealing the strength of three-nucleon interactions with the proposed Einstein Telescope.* Phys. Rev. C, 108(2):025811, 2023. doi: 10.1103/PhysRevC.108.025811.

- Peter T. H. Pang, Tim Dietrich, Michael W. Coughlin, Mattia Bulla, Ingo Tews, Mouza Almualla, Tyler Barna, Ramodgwendé Weizmann Kiendrebeogo, **Nina Kunert**, Gargi Mansingh, Brandon Reed, Niharika Sravan, Andrew Toivonen, Sarah Antier, Robert O. VandenBerg, Jack Heinzel, Vsevolod Nedora, Pouyan Salehi, Ritwik Sharma, Rahul Somasundaram, Chris Van Den Broeck.

An updated nuclear-physics and multi-mes-senger astrophysics framework for binary neutron star mergers. Nature Communications, 14(1):8352, 2023. doi: 10.1038/s41467-023-43932-6.

- **Nina Kunert**, Peter T. H. Pang, Ingo Tews, Michael W. Coughlin, and Tim Dietrich. *Quantifying modeling uncertainties when combining multiple gravitational-wave detections from binary neutron star sources.* Phys. Rev. D, 105(6):L061301, 2022. doi: 10.1103/ PhysRevD.105.L061301.

Published collaboration papers

- D. A. Kann, S. Agayeva, V. Aivazyan, S. Alishov, C. M. Andrade, S. Antier, A. Baransky, P. Bendjoya, Z. Benkhaldoun, S. Beradze, D. Berezin, M. Boër, E. Broens, S. Brunier, M. Bulla, O. Burkhonov, E. Burns, Y. Chen, Y. P. Chen, M. Conti, M. W. Coughlin, W. W. Cui, F. Daigne, B. Delaveau, H. A. R. Devillepoix, T. Dietrich, D. Dornic, F. Dubois, J.-G. Ducoin, E. Durand, P.-A. Duverne, H.-B. Eggenstein, S. Ehgamberdiev, A. Fouad, M. Freeberg, D. Froebrich, M. Y. Ge, S. Gervasoni, V. Godunova, P. Gokuldass, E. Gurbanov, D. W. Han, E. Hasanov, P. Hello, T. Hussenot-Desenonges, R. Inasaridze, A. Iskandar, N. Ismailov, A. Janati, T. Jegou du Laz, S.M. Jia, S. Karpov, A. Kaeouach, R. W. Kiendrebeogo, A. Klotz, R. Kneip, N. Kochiashvili, **N. Kunert**, A. Lekic, S. Leonini, C. K. Li, W. Li, X. B. Li, J. Y. Liao, L. Logie, F. J. Lu, J. Mao, D. Marchais, R. Ménard, D. Morris, R. Natsvlishvili, V. Nedora, K. Noonan, K. Noysena, N. B. Orange, P. T. H. Pang, H. W. Peng, C. Pellouin, J. Peloton, T. Pradier, O. Pyshna, Y. Rajabo, S. Rau, C. Rinner, J.-P. Rivet, F. D. Romanov, P. Rosi, V. A. Rupchandani, M. Serrau, A. Shokry, A. Simon, K. Smith, O. Sokoliuk, M. Soliman, L. M. Song, A. Takey, Y. Tillayev, L. M. Tinjaca Ramirez, I. Tosta e Melo, D. Turpin, A. de Ugarte Postigo, S. Vanaverbeke, V. Vasylenko, D. Vernet,Z. Vidadi, C. Wang, J. Wang, L. T. Wang, X. F. Wang, Shaolin L. Xiong, Y. P. Xu, W. C. Xue, X. Zeng, S. N. Zhang, H. S. Zhao, X. F. Zhao. *GRANDMA and HXMT Observations of GRB 221009A: The Standard Luminosity Afterglow of a Hyperluminous Gamma-Ray Burst*, In Gedenken an David Alexander Kann. Astrophys. J. Lett., 948(2):L12, 2023. doi: 10.3847/2041-8213/acc8d0.

Pre-print articles

- Shreya Anand, Peter T. H. Pang, Mattia Bulla, Michael W. Coughlin, Tim Dietrich, Brian Healy, Thomas Hussenot-Desenonges, Theophile Jegou du Laz, Mansi M. Kasliwal, **Nina Kunert**, Ivan Markin, Kunal Mooley, Vsevolod Nedora, and Anna Neuweiler. *Chemical distribution of the dynamical ejecta in the neutron star merger GW170817.* arXiv:2307.11080.

- Edoardo Giangrandi, Hannes Rüter, **Nina Kunert**, Mattia Emma, Adrian Abac, Ananya Adhikari, Wolfgang Tichy, Violetta Sagun, Tim Dietrich, Constança Providência. *Numerical Simulations of Dark Matter admixed Neutron Stars.* arXiv:2504.20825.

Articles in preparation

- **Nina Kunert**, Edoardo Giangrandi, Guilherme Grams, Anna Puecher, Hauke Koehn, Violetta Sagun, and Tim Dietrich. *The Bright and the Dark: Exploring nuclear-physics and dark matter constraints with binary neutron star mergers.*

Acknowledgements

Embarking on the journey of this dissertation has been an extraordinary adventure. Much like my passion for traveling, exploring new places, and diving in the ocean, multi-messenger astronomy has offered me a unique way to discover fascinating phenomena throughout the universe, to meet inspiring researchers from diverse scientific fields, and to deepen my understanding in countless ways.

I am profoundly grateful to Prof. Dr. Tim Dietrich for his exceptional guidance, invaluable insights, and unwavering support throughout these past years. His mentorship has been a cornerstone in shaping my academic journey, and I deeply appreciate his dedication and encouragement. I am thankful for the freedom to explore new topics that sparked my curiosity.

I am grateful for being part of the nuclear-physics and multi-messenger astrophysics community, where I have had the opportunity to collaborate with passionate researchers including Dr. Peter Pang, Prof. Dr. Michael Coughlin, Dr. Sarah Antier, Prof. Dr. Mattia Bulla, Dr. Ingo Tews, and many more. Furthermore, I am grateful to my second supervisor Prof. Dr. Philipp Richter and my mentor Dr. Jonathan Gair for their insightful guidance.

I extend my gratitude to our numerical-relativity group members, including Ivan, Henrique, Anna, Federico, and Edoardo, for their invaluable contributions in introducing me to sophisticated numerical methods for modeling compact binary mergers. I will never forget cry-laughing with Edoardo as we uncovered the Matryoshka-like nesting of SGRID folders endlessly unfolding on our machines.

I am grateful to my 'sunny office' mates, Ivan and Edoardo, whose friendly and cheerful presence made our workspace truly enjoyable. I will always remember our ambitious shopping trip, driven by the bold vision of transforming our office into a vibrant, sunlit jungle.

I would also like to express my gratitude to all my colleagues at the University of Potsdam who have contributed to making these past years truly memorable, including Federico, Hauke, Henrik, both Annas, Sophia, and all the other past and recently joined group members. Furthermore, a special thanks goes out to all the proofreaders of this work which include Guilherme, Ivan, Adrian, Anna P., Henrik, Hauke, and Vsevolod.

I will always remember Andrea's and Conni's tireless help in handling all the paperwork and bureaucracy, and appreciate the financial support that I received from University Potsdam.

Von Herzen danke ich meiner Familie, meinem Partner und meinen Freunden für ihre bedingungslose Unterstützung. Ohne eure Ermutigung, Geduld und Liebe wäre dieser Weg nicht derselbe gewesen. Eure Unterstützung bedeutet mir mehr, als Worte ausdrücken können.

Declaration of authorship

Hereby, I declare that the thesis I am submitting does not exhibit any resemblance to any other work, either in its entirety or in part, and has been completed solely by me. I am aware of the University's regulations concerning plagiarism and confirm that I have cited all sources used in this thesis and listed them accordingly, giving proper credit to the original authors. Furthermore, I declare that this work has not been submitted to any other institution of higher education and acknowledge the financial support received from the PhD completion scholarship of the University of Potsdam.

Potsdam, March 25, 2025 Nina Kunert